Looking for a Physical Basis of Rainfall Multifractality

Victor Manuel Peñaranda Vélez

Universidad Nacional de Colombia
Geophysical and Environmental Department
Medellín, Colombia
2019

Looking for a Physical Basis of Rainfall Multifractality

Victor Manuel Peñaranda Vélez

A thesis submitted to the Geophysical and Environmental Department at Universidad Nacional of Colombia in partial fulfillment of the requirements for the degree of

Doctor of Engineering - Water Resources

Advisor:
Ph.D. Óscar José Mesa Sánchez

Line of Work:
Hydrological Systems and Hydroclimatology

Research Group:
Posgrado en Aprovechamiento de Recursos Hidráulicos

Universidad Nacional de Colombia
Geoscience and Environmental Research
Ciudad, Colombia
2019

To my dear Manuel Felipe who gave me all the inspiration to go ahead and to pursuit my dreams.

Wisdom takes care of those who look for her; she raises them to greatness... At first, Wisdom will lead you along difficult paths... (Sirach 4).

Acknowledgment

This research would not have been possible without the help and patience of some relatives, close friends and colleagues. The author express his gratitude and kindness to:

Dr. Óscar José Mesa Sánchez Ph.D. Full professor of the Geophysical and Environmental Department at Universidad Nacional de Colombia. Advisor and Grandmaster of this research.

Dr. Carlos E. Puente Ph.D. Full professor of the Department of Land, Air and Water Resources at University of California, Davis.

Dr. Carlos D. Hoyos Ph.D. Professor of the Geophysical and Environmental Department at Universidad Nacional de Colombia.

Dr. Jorge A. Ramirez Ph.D. Full Professor of the Department of Civil and Environmental Engineering at Colorado State University.

Dr. German Poveda Ph.D. Full professor of the Geophysical and Environmental Department at Universidad Nacional de Colombia.

Dr. Edward Waymire Ph.D. Emeritus Professor of the Department of Mathematics at Oregon State University.

All my professors and colleagues from Universidad Nacional de Colombia.

The Administrative Department of Science, Technology and Innovation (COLCIENCIAS).

My friends Carlos Saldarriaga, Alejandro Jaramillo, Ricardo Monroy, Francisco Guerrero and Melanie Place for sharing with me their passion for science and for giving me your kindly support.

My wife Nancy who supports me to get ahead of this challenge.

My family for giving me support and cheers all the time.

Those people who somehow cooperate with the development of this research.

Resumen

El estudio de la precipitación responde a la necesidad inherente por conocer las dinámicas climáticas de corto y largo plazo, como también sus afectaciones en el contexto de las prácticas de ingeniería. La presente investigación se delimitó al estudio de la precipitación tropical y se orientó a la exploración conceptual del mecanismo físico que explica la emergencia de las propiedades de escalamiento multifractal del campo de precipitación. Partiendo del análisis de registros espacio–temporales de precipitación y de patrones simulados por computador se agruparon evidencias que ratifican la existencia de la multifractalidad en la precipitación y que tal propiedad estadística puede también ser identificada en modelo de base física. La exploración conceptual realizada en la investigación se apoyó en los principios de conservación provenientes de la física clásica y en las teorías modernas que han dado lugar a lo que hoy en día es conocido como fenómenos críticos. Entre los hallazgos encontrados, se concibe la multifractalidad como una manifestación inherente de la inestabilidad atmosférica por procesos de convección. Las inestabilidades y consecuentemente la multifractalidad son subproductos inducidos por un mecanismo difusivo en la atmósfera terrestre. Bajo condiciones especiales del sistema dinámico asociado a los procesos de convección, las inestabilidades inducidas por difusión dan lugar a la concentración de estructuras espaciales en el campo de precipitación y la organización de estas estructuras se describen a través de la multifractalidad. Aún cuando se mantienen algunas preguntas abiertas sobre la física de la multifractalidad en la precipitación, esta investigación establece una ruta para la consolidación de una teoría general y el desarrollo de nuevas herramientas de diseño en el marco de la ingeniería.

Palabras clave: precipitación, convección tropical, fractales, multifractales, fenómenos críticos, formación de patrones, difusión, escalamiento.

Abstract

The study of rainfall arises from the necessity for knowing large and short–term climatic dynamics, as well as their affectations in the context of engineering practices. This research focus on the study of tropical rainfall and it was guided toward the conceptual exploration of the physical mechanism that explains how the multifractal scaling properties emerges in the rainfall field. On the basis of space–time rainfall records and model outputs analysis, it was possible to collect evidence that confirm rainfall multifractality exists and such a statistical property can be also identified in physically–based model outputs. The conceptual exploration that was developed in this research based on either classic–physics conservation principles or modern theories related to the study of the well-known critical phenomena. Among the findings, multifractality is understood as an essential reflection of the atmospheric instability by convection processes. Either instabilities or their resulting multifractality are sub–products of a diffusive mechanism which takes effect in the atmosphere. Under particular conditions of the dynamical system representing the convection processes, diffusion–driven instabilities give rise to the concentration of spatial structures in the rainfall field, and the organization of such structures is described by multifractality. Although open questions remain about the physics of rainfall multifractality, this work sets up a path for building a general theory and to promote innovative engineering design tools.

Keywords: Rainfall, tropical convection, fractals and multifractals, critical phenomena, patterns formation, diffusion, scaling.

Contents

List of Figures

List of Tables

Symbols and Nomenclature

In this section general symbols (either Latin or Greek letters), subscripts, superscripts, and abbreviation, used along this document, are exhibited. Every element on these lists are organized in alphabetic order following their first letter.

Latin Letters Symbols

Symbol	Name	SI Units	Definition
A	Area	m^2	$\int\int dxdy$
A_k	Random variable (r.v.)	$\dim(A_k)$	$\cdots$
d	Euclidean dimension	1	$\cdots$
$C(\gamma)$	Codimension function	1	Eq. 2-11
c	Condensation rate	kJ kg^{-1} s^{-1}	$\cdots$
∂_t	Time partial derivative	t^{-1}	$\frac{\partial}{\partial t}$
$\partial_{\mathbf{x}}$	Spatial partial derivative	x^{-1}	$\frac{\partial}{\partial \mathbf{x}}$
$\mathrm{E}[X]$	Mathematical expectation	$\dim(X)$	$\int x f(x) dx$
e	Evaporation rate	kJ kg^{-1} s^{-1}	$\cdots$
$f(\alpha)$	Fractal dimension	1	Eq. 2-6
$f_X(x)$	Probability density function	$\dim(X)$	$\frac{d}{dx}F_X(x)$
$F_X(x)$	Probability distribution function	$\dim(X)$	$\mathbb{P}_{\mathrm{r}}\{X \leq x\}$
H	Dynamic scaling exponent	1	$\cdots$
H	Anisotropy scaling exponent	1	$\cdots$
I_v	Vertically integrated moisture content	$\mathrm{kg\ m}^{-2}$	$\int_{Z_0}^{Z} \rho_v \, dz$
$K(q)$	Moment scaling function	1	Eq. 2-10
$\mathbf{k}$	Wavenumber vector	1	$\cdots$
L	Characteristic length	$\dim(L)$	$\cdots$
L	Latent heat	J kg^{-1} K^{-1}	$\cdots$
M_X^q	q–order moment of the variable X	$\dim(X)$	$\mathrm{E}[X^q]$
M	Mass flux	$\mathrm{kg\ m}^{-2}$ s^{-1}	$\rho \, \lvert\mathbf{u}\rvert$

Symbol	Name	SI Unit	Definition
m	mass	kg	DF
∇	Gradient vector	m^{-1}	$\sum_{i=1}^{n} \partial_{\mathbf{x}_i}$
P	Precipitation rate	kg m^{-2} d^{-1}	$\cdots$
p	Atmospheric pressure	Pa, psi	$\cdots$
$\mathbb{P}_{\mathrm{r}}\{X\}$	Probability	$\dim(X)$	$\cdots$
Q_R	Radiative heating rate	kJ kg^{-1} s^{-1}	$\cdots$
q	Vertically integrated moisture content	kg m^{-2}	$\int_{Z_0}^{Z} \rho_v \, dz$
$\mathbf{R}$	Rainfall field	mm h^{-1}	$\cdots$
s	Dry static energy	kJ kg^{-1}	$s = c_p \, T + g \, z$
T	Temperature	C, K	$\cdots$
t	Time	s, min, h, d	$\cdots$
x	Spatial position	m, km	$\cdots$
$\mathbf{x}$	Spatial position vector	m, km	$\cdots$
X	Random variable (r.v.)	$\dim(X)$	$\cdots$
V	Volume	m^3	$\int \int \int dxdydz$
$\mathbf{V}_i$	Random variable (r.v.)	$\dim(\mathbf{V}_i)$	$\cdots$
$\mathbf{u}$	Velocity vector	m s^{-1}	$\frac{dx}{dt}$
w	vertically integrated water vapor	kg m^{-2}	$\int_{z_B}^{z_T} \rho_v dz$
w	Upward (or downward) velocity	m s^{-1}	$\cdots$
W_j	Random variable (r.v.)	$\dim(W_j)$	$\cdots$
$\mathbf{W}$	Random variable (r.v.)	$\dim(\mathbf{W})$	$\cdots$
W_n	Contractile affine map	1	Eq. 2-24
y	Spatial position	m, km	$\cdots$

Greek Letters Symbols

Symbol	Name	SI Units	Definition
α	Singularity exponent	1	$\cdots$
α	Multifractality index	1	$\cdots$
χ_T	Susceptibility function	$\dim(T)$	$\cdots$
Δ	Laplacian	m^{-2}	$\frac{\partial^2}{\partial \mathbf{x}^2} \equiv \partial_{xx}$

Symbol	Name	SI Units	Definition
δ	Density	kg m^{-3}	$\frac{dm}{dV}$
$\delta(x)$	Delta function	$\dim(x)$	$\int_{-\infty}^{\infty} \delta(x) = 1$
ϵ	Measure density	1	$\cdots$
ϵ	Mean energy dissipation rate	m^2 s^{-3}	v_λ^3/λ
η	Passive scalar	$\dim(\eta)$	$\cdots$
γ	Local singularity exponent	1	$\cdots$
γ	Scaling exponent	1	$\cdots$
Γ	Lapse rate	°C, °K	$\partial T/\partial z$
λ	Spatial scale	m, km	$\cdots$
μ_i	Normalized rainfall measure	1	$R_i / \sum R_i$
θ	Potential temperature	C, K	$T\left(\frac{p_0}{p}\right)^k$

Subscripts

Subscripts	Name
c	Critical value
i	Component identifier
j	Component identifier
k	Component identifier
max	Maximum
min	Minimum
n	Component identifier
q	Order of the moment
v	Water vapor
X	Random variable
∞	Limit to infinity

Superscripts

Superscripts	Name
q	Order of the moment
’	Perturbation

Abbreviation and Acronyms

Abbreviation	Name
CAPE	Convective available potential energy
CIN	Convective inhibition
CRM	Cloud–resolving model
dCAPE	Downdraft CAPE
DALR	Dry–adiabatic lapse rate
EL	Equilibrium level
FM	Fractal – Multifractal
FCA	Fractional cloud area
IPCC	Intergovernmental Panel of Climate Change
LFC	Level of free Convection
LNB	Level of neutral buoyancy
MSE	Moist static energy
SALR	Saturated–adiabatic lapse rate
SOC	Self-organized criticality
SST	Sea surface temperature
TRMM	Tropical Rainfall Measurement Missions

1. Introduction

The accelerated growth of the global population and the economy of countries have rapidly increased the demand for water, which makes it more urgent to understand the behavioral patterns of water resources and to predict their future dynamic scenarios. Rainfall as one of the fundamental components of the hydrological cycle and the global climate system, participates in the composition and dynamic of the atmosphere, firstly by its important optical and energetic properties associated to the release of latent heat, pressure changes by phase transitions, and the greenhouse effect associated to water vapor. Furthermore, it also affects indirectly the transport and removal of aerosols and soluble gases [Mesa, 2007]. Considering that rainfall plays an important role for life and the environment, it should be studied over a broad thematic framework to respond to social and economic interests of all regions in the planet.

According to the final report submitted by the Intergovernmental Panel of Climate Change (IPCC), since 1951, there is an increase in the frequency and intensity of heavy rainfall over various regions of the planet [Intergovernmental Panel on Climate Change, 2013, p. 2-162]. Moreover, in the tropical region (defined as the territorial strip 30°S–30°N), a positive trend in the annual precipitation anomalies is identified in the mid 90s [Intergovernmental Panel on Climate Change, 2013, p. 2-162]. Studies by Mesa et al. [1997] for Colombia, found positive trends in the annual and semi-annual cycles of 151 rain-gauges records. These and other results have been understood as the intensification of extreme hydrological events that finally result in human and economic losses, and water stress. Mesa et al. [1997] suggest that Colombia must take actions diligently to develop climate studies that anticipate the negative consequences of hydro–meteorological processes, since their benefits are reflected not only in science but also in society. For instance, the majority of methodologies in hydrological engineering design are based on the hypothesis of stationarity (and homogeneity) and consequently it is assumed that the historical records of any measurements at a given location can be used to statistically infer the future hydrological behavior and the operation of structures. In principle, a simple adjustment to those design methodologies is not possible, because current they are not directly based on scientific but rather empirical knowledge.

From a global point of view, there have been some attempts to combine scientific efforts to provide answers to some of the questions being born from the study of precipitation processes. The National Council of American Research [NRC, 1991] pointed out two important scientific challenges with respect to precipitation that still apply nowadays: i) How can we aggregate the dynamic behavior of hydrologic processes at various space and time scales in the presence of great natural heterogeneity? and ii) How can we establish the links between deterministic and stochastic rainfall models? The results of multiple hydrological publica-

tions highlight the limitations in modeling nonlinear physical processes, emphasizing among them the theoretical idealization of a *uniform space–time*. This has led to an incorrect use of measurement (or surrogated physical parameters) extrapolations in ungauged regions and consequently to the development of ineffective engineering designs.

Hydrological science has formulated questions about the quantitative relationship of physical processes at disparate spatial or temporal scales. For such situations, the NRC's committee [1991] has defined the scaling of hydrological processes as a priority research subject. If we could achieve a physical and mathematical theory of rainfall which explains its inverse problem (i.e. in this context as disaggregating rainfall fields from large scales to small ones), the meteorological parameterizations and hydrological models will be optimized. This would allow scientists, engineers and practitioners to obtain better predictions of short and long term of water quantity and quality models and re-normalized procedures in engineering designs [NRC, 1991]. If this last happened, either economical infrastructure projects or sustainable development of cities would be feasible.

This research deals with one of the most complex physical phenomena found in the hydrological cycle: *rainfall*. Its interpretations span from simple to extremely complex conceptual approaches [Mesa & Peñaranda, 2015]. So far, in the scientific community there is not a consensus about how to describe, to model and to predict rainfall from physical basis. Furthermore, the classic physics that explains how rainfall processes work does not explain how multifractal patterns emerge. Based on the aforementioned arguments, the main objective of this research is to investigate what physical mechanism is directly responsible for the multifractal properties of space–time rainfall fields.

In the methodology of this research the literature survey is the first activity in it and although it is an intrinsic or essential part of the research it is always worth mentioning which bibliographic sources were consulted. Every inquiry related to this research has been initially made by using available institutional information sources (e.g. SINAB[1], Repositories, Databases[2]), public–domain bibliographic databases and Internet search engines. All the bibliographic sources come from a large collection of materials on physics, math, hydrology, meteorology and related topics to this research, furthermore they include conference proceedings and monographs that will help to get an outlook of current scientific developments. The selected bibliographic references were collected and managed by EndNote™ which allows to export the bibliography in a suitable format for LaTeXusers. The research subject is highly wide and the literature review required to be delimited to those documentation related to multifractal rainfall models and physical-based models whose outcomes depict fractals features.

The scope of this research was bound geographically by the *tropical region*. This region

[1] National System of Libraries at Universidad Nacional – Sistema Nacional de Bibliotecas de la Universidad Nacional

[2] EBSCO Host, JSTOR, Nature Journal, Scielo, Science Direct, Springer Journal, Springer Books, Taylor & Francis, Water Resources Research, Geophysical Review Letters and Wiley Online Library.

has an important connotation for the world since it is the center of convective activity from which energy by latent heat is released influencing the Colombian hydrometeorology and several global circulation processes [Poveda & Mesa, 1997]. Furthermore, this region is also characterized, onshore and offshore, by a high humid content input into the troposphere from which a large amount of mesoscale convective complexes evolve [Mapes et al., 2003]. The local study area is Colombia, since it represents an important location to understand the social implications associated to weather and climate changes. Furthermore, among data that were used for the research purposes, some of them were recorded in two locations of Colombia i.e. Bogotá and Medellín.

Data used in this study are classified into two groups: observational records and model outputs. Observational records correspond to punctual data of high–resolution rainfall intensities, weather–radar reflectivity and satellite rainfall intensities. High–resolution rainfall intensities data came from raingauges observations located at Bogotá (Colombia). Weather radar reflectivity data came from SIATA[3] observations. Satellite rainfall data came from the Tropical Rainfall Measurement Mission products (3B42, version 7). All available data are distributed in several spatial and time scale resolutions according to its origin, and they were studied under the same methodologies for multifractal analysis. Techniques implemented by Gómez & Poveda [2008] and Peñaranda [2008] to analyze Colombia's rainfall datasets[4] have been also used for the data sets here explored. The theory about multifractal-analysis techniques will be briefly presented in the next section 3.1. Further details about the research methodology can be consulted in the following works: Lovejoy & Schertzer [2013], Roux et al. [2009], Lopes & Betrouni [2009], Peñaranda [2008], Gómez & Poveda [2008], Roux et al. [2000], Feder [1988].

It is highlight that model outputs correspond to simulated fields from three selected models: Nordstrom & Gupta's model [2003], Craig & Mack's model [2013], Hottovy & Stechmann's model [2015] and Raymond & Zeng's model [2005]. The models that were studied here correspond to those formulated with a minimal amount of hypotheses and conceived as *parsimonious* models. An special emphasis was put on Craig & Mack's model [2013] and Hottovy & Stechmann's model [2015] because their physical characteristics and connectivi-ty with observational results are very attractive to explore and understand. For instance, Craig & Mack's model [2013] is an approach for assessing the moisture budget of the free troposphere and it is supported on three physical considerations: subsidence drying, convective moistening and horizontal mixing. Former results obtained from this model exhibit a self–organization mechanism and dynamical scaling properties [Craig & Mack, 2013]. For this research, the criteria for assessing the model performance were based on: i) *correspondence*: the model capacity for reproducing statistical properties of real observations i.e. multifractality, ii) *consistency*: a suitable mathematical and physical formulation, iii) *parsimonia*: a minimal amount of hypotheses and parameters to describe the physical system, and *funcionality*: the model capacity for adapting to engineering purposes.

[3]Medellín and Valle de Aburra's Early Warning System - Sistema de Alerta Temprana de Medellín y el Valle de Aburra.

[4]i.e. the moment method, Chhabra & Jensen method.

The conceptual integration was one of the most difficult task of this research because the difficulties to tackle the diversity of theories from physics and modern mathematics. Nevertheless, through years Prof. Óscar Mesa and I have studied several theories related to the subjects: tropical convection, critical phenomena and rainfall multifractality, in order to get a technical contribution to the understanding of rainfall multifractality. Thus, the goal of this document is to provide a unifying framework for all the observational and numerical evidence, analyses and conceptual contributions that helped to achieve the overall objective of this research.

The thesis is organized in five chapter; the first one is an introduction to developed work and it presents the (theoretical and practical) origins of the research subject, its objectives, scopes, limitations and an overview of the research methodology. The second chapter is a literature review which was built to define the theoretical framework explored by the author and how was addressed the exploration of rainfall multifractality under physical basis. The third chapter shows some proof of the existence of multifractality in either rainfall observation or physically–based model outputs. The fourth chapter shows the conceptual integration responding to where the physics of rainfall multifractality is identified and what physical mechanisms explains the emergence of it. This chapter is introduced by some physical aspect of the large–scale atmospheric thermodynamic to connect with ideas explaining why rainfall is concentrated over the spatial domain, and how such a theory could explain the physical origin of multifractality. The fifth and last chapter presents a summary of the results and some direction for future works.

2. Literature Review

In this section a literature review about some important theoretical formulations built to understand precipitation processes are briefly presented. It begins with a short summary about the pioneer models of rainfall which are designed as a stochastic process. The next generation of rainfall models, presented here, include self-similarity properties and furthermore, they depict the multifractal structure found in observations. Current rainfall models include some physical properties of the atmosphere. Some of these model are discussed briefly in the next subsection and the purpose to deal with them is to get an insight about the most recent interpretations of precipitation processes and how multifractality is connected to their outcomes.

2.1. Multifractality: the Geometry of Rainfall

Rainfall in time and space is depicted by irregular patterns that look random, however, through *multifractal analysis*, a statistical structure is identified in those patterns that relates the large and small scales. Such structure is known as a *self-similarity* property which characterizes objects by the translation and scaling invariance [Feder, 1988]. Actually, several researches have determined that rainfall has multifractal scale invariance in the range from a few minutes to several days (for time) and from below 1 km to 100 km (for space) [Lovejoy & Schertzer, 2013, Peñaranda, 2008, Venugopal et al., 1999, Foufoula-Georgiou, 1998, Lovejoy & Schertzer, 1995, Marzan et al., 1996, Over & Gupta, 1996, Over, 1995, Gupta & Waymire, 1993].

The starting point in the application of multifractal theory over physical systems was born in the study of turbulence phenomena [Zybin & Sirota, 2013, Meneveau & Sreenivasan, 1991, 1987, Frisch & Parisi, 1985] and its techniques were applied subsequently to describe geophysical patterns. Rainfall patterns have been characterized through multifractal techniques and some studies have suggested that the multifractal (scaling) properties of rainfall are inherited from the atmospheric turbulence [Lovejoy & Schertzer, 1995, 2013]. So far, the turbulence closure problem still remains and the interactions between turbulence and precipitation processes are open problems either; therefore, the hypothesis about how rainfall inherits the multifractal properties from the atmospheric turbulence is a research subject for the next years.

How is *multifractality* defined? Based on the former studies about turbulence, multifractality is defined through the structure function[1] and its scaling exponents. If the exponents

[1] In Frisch [1995] the structure function is defined as $S_q(\ell) = \langle(\delta v(r,\ell))^q\rangle$, where $\delta v(r,\ell) = [v(r+\ell) - v(r)]$

of the structure function θ_q depicts a non-linear behavior in the plane $q - \theta_q$, there could be a multifractal description of quantities representing the physical process [Frisch, 1995, Anselmet et al., 1984]. For instance, Figure 2-1 shows an example of multifractality for a rainfall data set. The left panel of Figure 2-1 shows a plot of the q–order moments $M_X^q(T) = \mathrm{E}[X^q(T)]$ for a rainfall data set $X(T)$ at scale T. For every q–order moment there exists a value of θ_q which represents the average slope of the dots describing the relation between the moment $M_X^q(T)$ and the time scale T. The right panel of Figure 2-1 exhibits a plot of the function θ_q vs q. If, for example, this time series was a mono–fractal set (i.e. represented by a simple scaling), the scaling dependence between θ_q and q would be linear (see the dash blue line in Figure 2-1). For the selected rainfall data set, the function $\theta(q)$ shows a non–linear dependence since it grows in a sub–linear manner as q increases. The turbulence theory defines such a behavior as an evidence of multifractality and since the data exhibited in Figure 2-1 correspond to rainfall data, one can think that the statistical structure of rainfall is also multifractal. It is highlighted that in some turbulence models the function θ_q can be depicted by a broken straight line but only two scaling exponents can be estimated by such a function. So, multifractality will always require a broad number of scaling exponents organized in a non-linear manner.

It is worth noting how the scaling properties can be associated to the physics of some phenomena. Among the group of physical models, the Burgers' equation ($\partial_t v + \partial_x v = \nu\, \partial_{xx} v$) is known as a bi–fractal model in the turbulence theory. The solution of Burgers's equation for smooth initial data and considering a vanishing viscosity ($\nu \to 0$), generates isolated shocks connected to smooth ramps in the velocity field. Either shocks or ramps are representing the two possible scaling-exponent $\{\alpha_1, \alpha_2\}$ with dimensions $\{f(\alpha_1), f(\alpha_2)\} \equiv \{D_1, D_2\}$ (see Frisch [1995], She et al. [1992] for more details), which are embedded in the geometry of the physical space and they describe the behavior of the velocity field. On the other hand, the scaling properties of Navier–Stokes equations ($\partial_t v_i + v_j\, \partial_j v_i = \partial_i p + \nu\, \partial_{jj} v_i$) are represented by infinite many scaling groups if the viscous term vanishes[2] [Frisch, 1995].

Based on turbulence theory and its advances in the identification and characterization of multifractality, one can have some special considerations for rainfall analysis: i) the physics of rainfall is as complex as turbulence and physical models designed to describe rainfall physics and its scaling properties can either be implicitly implied in Navier-Stokes equations as a sub-process of the turbulence physics or be an independent physical process that interacts with the turbulence and as a consequence describe multifractality, and ii) observational evidence for rainfall show that there exists a local scale-invariance property which determines the existence of a bound range of scaling exponents [Lovejoy & Schertzer, 2013, Peñaranda, 2008, Venugopal et al., 1999, Over & Gupta, 1996, Over, 1995, Gupta & Waymire, 1993],

is the velocity increment and q is the order of the moment. This structure function follows a power-law in the inertial range of a turbulent flow of the form $S_q(\ell) \propto \ell^{\zeta_q}$, where ζ_qs are denominated exponents of the structure function.

[2] If the symmetry property $g_\lambda : t,\, r,\, v \to \lambda^{1-h} t,\, \lambda r,\, \lambda^h v$ is applied to Navier-Stokes equation the first three terms are multiplied by λ^{2h-1} and the viscosity term by λ^{h-2}. The last term in negligible at very high Reynolds numbers and only in that case there could be infinitely many scaling groups.

therefore the property of infinite many scaling groups given by the Navier-Stokes equations for describing turbulent flows is not necessary to be satisfied in the same way as rainfall.

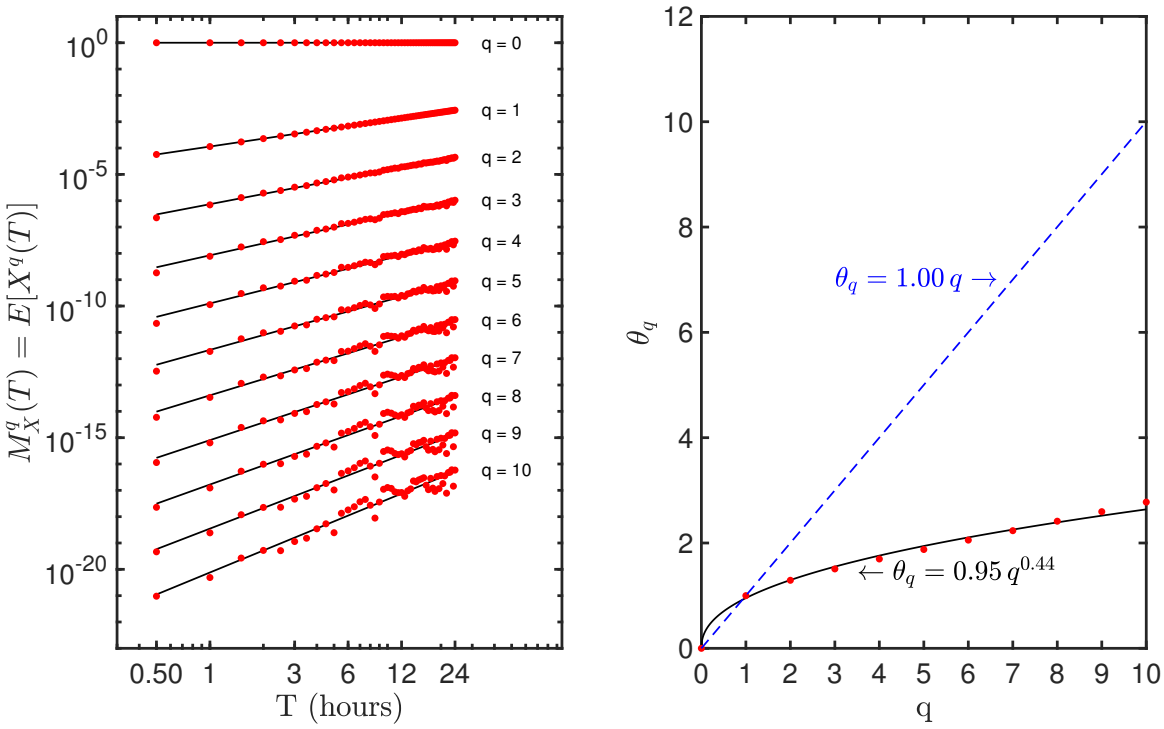

Figure 2-1: (Left panel) Graph of the first ten (10) statistical moments ($M_X^q(T)$, for $q = \{1, 2, \ldots, 10\}$) of the rainfall time series registered at Bosa Barreno (Bogotá) rain-gauge over the span of 1995 to 1999. These moments were obtained after a normalization of time series in each time aggregation scale ($T = 30\,\text{min}, 60\,\text{min}, 3\,\text{h}, 6\,\text{h}, 12\,\text{h}, 24\,\text{h}$). (Right panel) Graph of the function θ_q vs q. Conceptually, a field is multifractal if for an arbitrary moment the power-law $M_X^q(T) \sim T^{\theta_q}$ is satisfied. Here, θ_q represents a scaling function for all statistical moments which characterize the field variability for different time aggregation scales. The curved form of the function θ_q for the selected data set (red dots in the right panel) proves the existence of a multifractal structure into the rainfall field for the range of scales that is indicated here. In contrast, the dash blue line drawn in the right panel identified what a mono-fractal measure would be. In this case, a linear behavior of the function θ_q characterizes mono-fractal measures.

A formal definition of multifractality determines that a rainfall field **R** of measures $\{\mu_i\}$ will be multifractal if there exists a range of scaling exponents $H_\alpha = (\alpha_{min}, \alpha_{max})$ defined on a fractal set whose dimension $f(\alpha)$ depends on the scaling exponent α. As the scale $\lambda \to 0$, the measures $\{\mu_i\}$ defined on **R**, satisfy the following power-law relationship: $\mu_\alpha \sim \lambda^\alpha$, where the α-exponents are known as singularity exponents of order α, the function $f(\alpha)$ as the *multifractal spectrum*, and the rainfall fluctuations as *multifractal measures* [Veneziano

et al., 2006, Frisch, 1995, Feder, 1988].

The former definition has a geometrical restriction; the existence of a local singularity exponent α for every point in the measure function $M(x)$. Based on this restriction, the definition of multifractality has a *probabilistic* connotation. Following a conceptualization alike to that given by Frisch [1995], be $f(\mu)$ the probability density function (p.d.f.) of the (random) measures $\{\mu_i\}$ defined on $\mathbf{R}$, the statistical moments of measures $\mu = \{\mu_i\}$ are then given by:

$$M_{\mu}^{q}(\lambda) = \mathrm{E}[\mu^q(\lambda)] = \int_{\mathbb{R}} \mu^q(\lambda) f(\mu)\, d\mu \tag{2-1}$$

Considering that $\mu_\alpha \sim \lambda^\alpha$ is the power–law relationship is satisfied for multifractal measures and the probability of having $\mu_\alpha \sim \lambda^\alpha$ should be proportional to $\lambda^{d-f(\alpha)}$ [3] [4], the integral at equation 2-1 is redefined over the range I of scaling exponents as:

$$M_{\mu_\alpha}^{q}(\lambda) = \int_I \lambda^{q\,\alpha+d-f(\alpha)}\, d\mu_\alpha = \int_I \lambda^{q\,\alpha+C(\alpha)}\, d\mu_\alpha \tag{2-2}$$

where $d - f(\alpha) = C(\alpha)$ is the codimension function.

In the limit when $\lambda \to 0$, the smallest exponents of the power law into the integral 2-2 dominate and by the steepest–descent method, equation 2-2 is solved to give:

$$\lim_{\lambda\to 0} \frac{\ln M_{\mu}^{q}(\lambda)}{\ln \lambda} = \theta_q \qquad \text{where} \quad \theta_q = \inf_{\alpha} \left[q\,\alpha + d - f(\alpha)\right] \tag{2-3}$$

Thus, equation 2-3 can be now re-written as:

$$M_{\mu}^{q}(\lambda) \sim \lambda^{\theta_q} \tag{2-4}$$

where θ_q is the Legendre transformation of the codimension C_α as follows:

$$\theta_q = \inf_{\alpha}\{q\,\alpha + C_\alpha\} = \inf_{\alpha}\{q\,\alpha + d - f(\alpha)\} \tag{2-5}$$

$$f(\alpha) = \inf_{\alpha}\{q\,\alpha + d - \theta_q\} \tag{2-6}$$

According to the last results, $f(\alpha)$ should be concave in order to get a unique value $\alpha(q)$ such that $df(\alpha)/d\alpha = q$. Into the probabilistic definition, multifractality exists if there is a function $f(\alpha)$ which maps real scaling exponents α to scaling dimension $D \leq d$, and satisfies for every α:

$$\lim_{\lambda\to 0} \frac{\ln \mathbb{P}_{\mathrm{r}}\{\mu > \lambda^\alpha\}}{\ln \lambda} = d - f(\alpha) \tag{2-7}$$

[3] This probability represents the probability of a ball at the scale λ of being into the set $\mathscr{C}_\alpha$ with dimension $f(\alpha)$ and Euclidean embedding dimension d.

[4] $d = 1$ for measures on a line, $d = 2$ for measures on a plane, and $d = 3$ for measures on a volume.

where $\mathbb{P}_{\mathrm{r}}\{\mu > \lambda^{\alpha}\}$ denotes the survival function obtained from the probability distribution function of the (random) measures $\{\mu_i\}$ and represents the tail distribution. This probability definition of multifractality has been widely used by researchers to understand rainfall multifractality and to predict extreme values for practical purposes [Veneziano et al., 2006, Veneziano & Furcolo, 2002, Tessier et al., 1996, Bendjoudi et al., 1997, Hubert et al., 1993]. In the framework of what is called *Universal Multifractals* [Lovejoy & Schertzer, 2013, 1995, 1990], some scaling relations have been derived for the exceedance probability of stationary multifractal measures. If it is considered the average measure density ϵ_r at the resolution r in a cube of side length $1/r$, the following property is satisfied:

$$\mathbb{P}_{\mathrm{r}}\{\epsilon_r > r^{\gamma}\} \propto r^{-C(\gamma)} \tag{2-8}$$

where $C(\gamma)$ is the codimension function of ϵ_r (or exponent that measure the fraction of the space occupied by the set defined by $\{\epsilon_r > r^{\gamma}\}$) and γ is the local singularity exponent. From this definition and as $r \to \infty$, the moments of ϵ_r scale as

$$\mathrm{E}[\epsilon^q] \propto r^{K(q)} \tag{2-9}$$

where $K(q)$ is the moment scaling function and it is related to $C(\gamma)$ through the following Legendre transform:

$$K(q) = \sup_{\gamma}\{q\,\gamma - C(\gamma)\} \tag{2-10}$$

$$C(\gamma) = \sup_{\gamma}\{q\,\gamma - K(q)\} \tag{2-11}$$

In this context, if the moment scaling function $K(q)$ has a non-linear behavior, the measure is multifractal. If the moment scaling function $K(q)$ has a linear behavior and does not pass through the origin, the measure is mono-fractal, but if it pass through the origin, the measure if self-similar. In Figure 2-2 is presented an example of the moment scaling function $K(q)$ (continuous black line with red dots) for a rainfall data set, moreover, its codimension function is also exhibited at the right panel of the figure. The function $K(q)$ presents a suitable potential fitting (black continuous line) which indicates the existence of a multifractal structure. In addition, the left panel shows in dash blue line the tendency curve for a self-similar structure in order to compare with observations. On the other hand, the right panel shows the codimension function $C(\gamma)$ which was estimated through the Legendre transform (see equation 2-10).

The codimension function $C(\gamma)$ is a statistical scaling exponent that characterizes how the probability changes with the scale [Lovejoy & Schertzer, 2013]. Among its properties, one of them is that this functions is a increasing monotone function $dC(\gamma)/d\gamma > 0$. Moreover, when its derivative is evaluated at γ_1, i.e. the singularity associated to the mean (at $q = 1$), then $dC(\gamma_1)/d\gamma = 1$. This means that $C(\gamma_1) \equiv C_1 = \gamma_1 = dK(q = 1)/dq$ and $C(\gamma_1)$ is denominated the *codimension of the mean*. Moreover, there exists a parameter of curvature α^* that characterizes the degree of multifractality. This parameter is associated to the radius of curvature R_c of the codimension function when it is evaluated at C_1. For $\alpha^* = 0$ there

exists a mono-fractal set whose singularities all have the same fractal dimension, and for $\alpha^* = 2$, the maximum degree of multifractality is obtained. For the example exhibited in Figure 2-2, the codimension C_1 approximates to ≈ 0.65 and the curvature parameter α^* approximates to ≈ 1.25 (unconditionally hard multifractal processes).

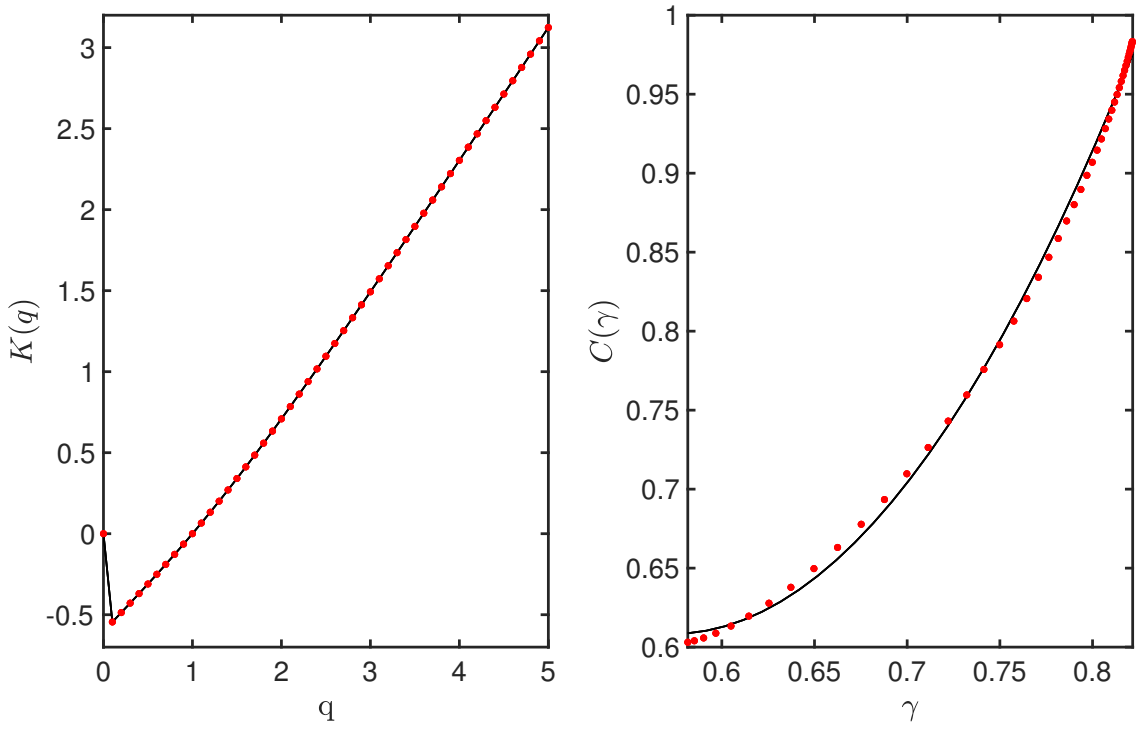

Figure 2-2: (Left panel) Graph of the moment scaling function $K(q)$ ($M_X^q(T)$, for $q = \{0.0, 0.1, \ldots, 5.0\}$) for a rainfall time series registered at Bosa Barreno (Bogotá) rain-gauge over the span of 1995 to 1999. (Right panel) Graph of the codimension function $C(\gamma)$ depending on the singularity exponent γ. The codimension function was obtained from the Legendre transform indicated at equation 2-10. The curved form of the moment scaling function $K(q)$ confirms that the rainfall data set is indeed multifractal.

Another aspect to consider in the multifractal theory developed by Lovejoy & Schertzer is the divergence of statistical moments ($\epsilon_\lambda^q \to \infty$). Lovejoy & Schertzer [1987b, 2013] identified that for a multifractal process there exists a critical value q_c of q in which the statistical moments diverge[5] i.e. the largest values exceed a critical value when γ^+ exceeds the embedding dimension d. For instance, if a multiplicative random cascade is developed to the small–scale limit (i.e. $\lambda \to \infty$), the mass is concentrated in a sparse fractal set whose measures equal to zero (respect to the Lebegue measure) and the magnitude diverge so as to keep a fixed mean. In order to deal with the problem of divergence, the integration of the set formed at the small scale limit or the truncation of the multiplicative process are proposed.

[5]Also called statistical phase transition in analogy with thermodynamic phase transition.

For un-integrated (or bared[6]) cascades the moments are finite because $\lambda < \infty$, whereas for integrated (or dressed) cascades the moments generally diverge for the order of the moment $q > q_c$, where $q_c > 1$ is the critical order of the moment and it can be computed through the moment scaling function as $K(q_c) = q_c - 1$ [Lovejoy & Schertzer, 2013, Veneziano & Furcolo, 2002, Schertzer & Lovejoy, 1987b]. The former implies that the divergence of statistical moments of densities $\epsilon_\lambda^q \to \infty$ at $q \geq q_c$ and such a diverge can be also understood through the codimension function $C(\gamma)$; a linear behavior of $C(\gamma)$ suggests a power–law tail on the probability distribution $\mathbb{P}_\mathrm{r}\{\epsilon_\lambda > s\} \sim s^{-q_c}$ for a large enough threshold s.

In the last 25 years or more, several multifractal techniques and theories have been developed for describing and modeling rainfall [Lovejoy & Schertzer, 1995, 2013, Veneziano et al., 2006, Veneziano & Furcolo, 2002, Over & Gupta, 1996, Over, 1995, Gupta & Waymire, 1993, Schertzer & Lovejoy, 1987a,b]. The first conceptual models for rainfall apply the phenomenology of multiplicative random cascades. For the general case[7], suppose that there is a dyadic interval $I^k = I_{\beta_1\,\beta_2\,\ldots\,\beta_k}$ which is selected randomly. The random sequence of digits $\beta_1\,\beta_2\,\ldots\,\beta_k$ could be 0 or 1 with probability $\frac{1}{2}$. For instance, the probabilities for the first digit are $\Pr\{\beta_1 = 0\} = \Pr\{\beta_1 = 1\} = \frac{1}{2}$, for the second digit are $\Pr\{\beta_2 = 0\} = \Pr\{\beta_2 = 1\} = \frac{1}{2}$ and so on. The measures in the dyadic interval are estimated as:

$$\mu(I^k) = \mu(I_{\beta_1\,\beta_2\ldots\beta_k}) = \prod_{i=1}^{k} m_{\beta_i} \tag{2-12}$$

where m_{β_i} is a random variable whose possible values are either m_0 or m_1. In equation 2-12, the measure μ is the result of the product of k independent and identically distributed random variables m_i whose possible values are m_0 or m_1 with probability $\mathbb{P}_\mathrm{r}\{m_0\} = \mathbb{P}_\mathrm{r}\{m_1\} = \frac{1}{2}$. The singularity exponent α of the sequence at the dyadic interval I^k is computed as follows:

$$\alpha_k(\beta_1\,\beta_2\ldots\beta_k) = \frac{\log\prod_{i=1}^{k} m_{\beta_i}}{\log 2^{-k}} = -\frac{1}{k}\sum_{i=1}^{k}\log_2 m_{\beta_i} = -\frac{1}{k}\sum_{i=1}^{k} v_{\beta_i} \tag{2-13}$$

where v_{β_i} is a random variable with distribution $\Pr\{v_0 = -\log_2 m_0\} = \Pr\{v_1 = -\log_2 m_1\} = \frac{1}{2}$. Hence, the singularity exponent α for the sequence in the dyadic interval I^k is a random variable, such that:

$$A_k = \frac{1}{k}\sum_{i=1}^{k}\mathbf{V}_i \tag{2-14}$$

equals to the sample average of k independent random variables $\mathbf{V}_i$ whose possible values are v_0 or v_1. The expected value for the random variable A_k is computed as:

$$\mathrm{E}[A_k] = \frac{1}{2}v_0 + \frac{1}{2}v_1 = -\frac{\log m_0 + \log m_1}{2\,\log 2} = \alpha_0 \qquad \text{(binomial measure)} \tag{2-15}$$

[6]This term is used to express that the cascade quantities do not take into account the small scale interactions.

[7]For further details of the arguments here presented see the manuscripts done by Evertsz & Mandelbrot [1992] and Mesa [2016].

where α_0 represents the singularity exponent of the *support* of the measure. It can be equal to 1 when the measure is defined over a unit interval. On the other hand, if the strong law of large numbers is applied to previous results, the sample average A_k will converge, almost surely, to the expected value $\mathrm{E}\, A_k$ for $k \to \infty$, i.e.

$$\mathbb{P}_\mathrm{r}\left\{\lim_{k\to\infty}\frac{1}{k}\sum_{i=1}^{k}\mathbf{V}_i = \mathrm{E}[A_k] = \alpha_0\right\} = 1 \tag{2-16}$$

This result means that the binary expansion $\beta_1\,\beta_2\ldots\beta_k$, selected randomly in the unit interval $[0, 1]$, has the same frequency of zeros and ones with probability 1. However, this result can not be always attained because it only holds pointwise. In the case where there exists a large number of finite size 2^k, there will be a range spanning from α_{min} to α_{max}. So, deviations from the expected value become significant depending on the value of k.

Assuming that the random variable $\mathbf{V}_i$ has a finite first and second moment (e.g. in the binomial case: $\mathrm{E}[\mathbf{V}] = \frac{1}{2}(v_0 + v_1)$ and $\mathrm{E}[\mathbf{V}^2] = \frac{1}{2}(v_0^2 + v_1^2)$), the central limit theorem states that the distribution of the re-scaled random variable

$$\mathbf{Y}_k = \frac{\sum_{i=1}^{k}\mathbf{V}_i - k\ \mathrm{E}[\mathbf{V}_i]}{\sigma\sqrt{k}} = \frac{(A_k - \alpha_0)}{\sigma/\sqrt{k}} \tag{2-17}$$

converges to the Gaussian distribution with zero mean and variance $\sigma^2 = \mathrm{E}[\mathbf{V}^2] - (\mathrm{E}[\mathbf{V}])^2$, for $k \to \infty$, i.e.

$$\lim_{k\to\infty}\ \mathbb{P}_\mathrm{r}\left\{\mathbf{Y}_k \le \xi\right\} = \int_{-\infty}^{\xi}\frac{1}{2\,\pi}\exp\left\{-\frac{1}{2}x^2\right\} = \int_{-\infty}^{\xi} G(x)dx \tag{2-18}$$

where $G(x)$ is the reduced Gaussian probability density. If the coarse Hölder exponent is approximated as $A_k \approx Y_k/\sqrt{k} + \alpha_0$ in order to get a variance defined as:

$$\mathrm{Var}[A_k] = \frac{\sigma^2}{\sqrt{k}} \approx \frac{(\alpha_{max} - \alpha_{min})^2}{4\,\sqrt{k}} \tag{2-19}$$

the function $f(\alpha)$ can be approximated for α near to α_0 as follows:

$$f(\alpha) = d + C(\alpha) = 1 - \frac{\ln p_k(\alpha)}{\ln 2^k} \approx 1 - \frac{2}{\ln 2}\left(\frac{\alpha - \alpha_0}{\alpha_{max} - \alpha_{min}}\right)^2 \tag{2-20}$$

where $p_k(\alpha)$ is a Gaussian approximation of the probability density of α. Equation 2-20 is a suitable approximation for $f(\alpha)$ near to the exponent α_0, but for larger deviations from α_0 the equation 2-20 should be re-defined. Actually, some new approximations using the *large deviation theory*[8] are discussed by Veneziano et al. [2006], Veneziano & Furcolo [2002],

[8] The large deviation principle defines that the probability of a random function A_k satisfy the large deviation principle if the limit $\lim_{k\to\infty} -\frac{1}{k}\ln\mathbb{P}_\mathrm{r}\{A_k \in B\} = r_B$ exists for a rate $r_B > 0$ (also known as Cramér function).

Frisch [1995], Evertsz & Mandelbrot [1992]. One the main results allows to compute the tail distribution of the coarse Hölder exponent, as follows:

$$\lim_{k\to\infty} -\frac{1}{k}\ln\{A_k \geq \alpha\} = \sup_{t>0}\{q\,\alpha - \lambda(q)\} \tag{2-21}$$

where $\lambda(t) = \ln \mathrm{E}[e^{q\,\mathbf{V}_i}]$ is the cumulant generating function of the random function $\mathbf{V}_i$ [Mesa, 2016]. Moreover, Evertsz & Mandelbrot [1992] showed that for multinomial measures, the functions $f(\alpha)$ can be computed as $f(\alpha) = C(\alpha) + 1 = \Gamma(\alpha) + 1$, where $\Gamma(\alpha)$ is the moment generating function of the coarse Hölder exponent α. Another important remark about the application of the large deviation theory for the study of multifractality is that the function $f(\alpha)$ is related to the structure function through the Legendre transform [Touchette, 2009, Frisch, 1995] , therefore the importance of understand multifractality should be comprehended as a tool for understanding the statistical structure of rare events in either rainfall or any other geophysical process.

2.2. Rainfall Models

2.2.1. Stochastic Rainfall Models

As it is evidenced in observational records, rainfall is characterized by a strong variability in space and time [Mesa & Peñaranda, 2015]. Rainfall is a process that comes from a non–linear deterministic system in which its patterns can be understood as outcomes of a random processes [Rodríguez-Iturbe, 1991]. The first attempts to describe rainfall consisted in looking for a suitable random process that adjusted to all observed data sets [Wilks, 1998, Rodríguez-Iturbe et al., 1984, Waymire & Gupta, 1981a,b,c]. The first stochastic rainfall models used Markov chains to simulate the occurrence of wet and dry periods of rainfall [e.g. Gabriel & Neumann, 1962] and they were evolving to what was known as parametric empirical–statistical model which were employed to simulate daily data sequences because it is the time scale with greater available observations [Wilks, 1998]. However, the main pro-blems of this kind of models is that the atmospheric physical processes are related implicitly into the model and they are point-processes (or model for a single location) and even if these model are used simultaneously at multiple points (e.g. multi–site models), the model parameters can not be related and there is not any spatial correlation between them. It is highlighted, multi-site models simulate smooth spatial patterns, therefore, they have limited applications, for instance, they can not be used for modeling rainfall extremes.

Space–time stochastic models trying to solve the space–dependence of rainfall events [e.g. Cox & Isham, 1988, Smith & Karr, 1985, Waymire et al., 1984, Gupta & Waymire, 1979] but their mathematical abstraction raises some difficulties; among them, i) the inabili-ty to integrate outcomes on a range of space–time scales (e.g. applications on downscaling problems), ii) the relative inaccessibility of solving the equations analytically for the most complex models [e.g. Waymire et al., 1984, Waymire & Gupta, 1981a,b,c], besides the over-parametrization associated to these models makes difficult the calibration procedure, and

iii) the lack of a straightforward connection with precipitation physics still persists. Despite some of the space–time stochastic models capture anisotropy, their capability for representing complex spatial rainfall patterns and the dynamics of rainfall processes are still immature. There exists a marked variability of observations in both spatial and temporal scales[9], and the estimation of a unique random process has not been possible.

In spite of the intrinsic shortcomings in stochastic modeling, new models have been proposed to improve some of the problems found in their predecessors. Models based on the theory of random fields have been used for the representation of rainfall at the mesoscale. Through non-linear transformation of Gaussian random fields, including fractional Gaussian noise and Hurst–Kolmogorov processes, rainfall field can be simulated improving the representation of large fluctuation into the field [Koutsoyiannis et al., 2011]. On the other hand, Paschalis et al. [2013] developed a stochastic model capable of reproducing essential features of the statistical structure of rainfall in the space-time for a wide range of scales. This model, known as STREAP[10], considers that space–time rainfall is a stochastic process with various subprocesses: i) a storm arrival process, ii) a process for the temporal evolution of areal precipitation properties and iii) a process to describe the space-time evolution of the storm. In spite of the conceptual structure for representing spatial features and statistics of the rainfall field the STREAP model preserves limitations alike to early stochastic models, i.e. difficulties for a direct estimation of parameters and the lack of a physical interpretation in its parameters.

It is underlined that the complexity of stochastic models increases when the ability for describing processes is extended. This possibly implies a major number of parameters and more difficulties for direct estimation. Moreover, these models turn out to be more efficient for describing patterns in smaller time scales and less functional with the estimations based on scale transformations [Rodríguez-Iturbe et al., 1987, 1984]. It is noteworthy that the implementation of stochastic models for describing temporal rainfall patterns in Colombia could not be suitable for the resolution of rainfall data. The majority of the rain–gauges records daily measurements, thus the reliability of the results arising from these models is limited. Based on the aforementioned arguments, an stochastic explanation for rainfall is still incomplete because these models are not completely functional to explain the space–time heterogeneity on all scales and its parameters are not always coupled to physical principles.

2.2.2. Models Based on Multifractal Theory

Up to date, many mathematical models have been developed and applied in order to understand and model rainfall multifractality in time, space and space-time [Puente & Obregon, 1996, Puente, 1995, Over & Gupta, 1996, Marzan et al., 1996, Over, 1995, Schertzer & Lovejoy, 1987a, Frisch & Parisi, 1985]. One of the pioneer multifractal models was introduced by Gupta & Waymire [1993] and later implemented by Over & Gupta [1994, 1996]. In this model, random cascades are constructed as a result of the subdivisions of a d–dimensional

[9] For rainfall these scales is also referred to as aggregation scales.
[10] STREAP: Space-Time Realizations of Areal Precipitation

cube $[0, L_0]^d$ into b^n sub-cubes. For a embedding dimension $d = 2$ and a branching number $b = 4$, $b^n = 4^n$ represents the number of subdivisions in each step of the cascade. The i-th sub-cube after n subdivisions is denoted by Δ_n^i. The length $L_n = L_0^{-b^n}$ of each side of the sub cube Δ_n^i in the level n represents the spatial scale.

The construction of the rainfall field begins when a cube $[0, L_0]^d$ adopts an initial mass $R_0 L_0^d$ and the i-th sub-cube of the first subdivision Δ_1^i consequently adopt the mass $R_0 L_0^d W_1^i b^{-1}$ for $i = \{1, \ldots, b\}$. Here W_1^i is a mutually independent random variable. Thus, for every subdivision Δ_n^i of the cascade, the mass is estimated as follows:

$$\mu(\Delta_n^i) = \frac{R_0 L_0^d}{b^n} \prod_{j=1}^{n} W_j^i \tag{2-22}$$

The limiting mass μ_∞ is obtained by letting $n \to \infty$ (small–scale limit), so that $\mu_\infty = \mu(\Delta_n^i) Z_\infty(i)$, where:

$$Z_\infty(i) = \frac{\mu_\infty([0, L_0]^d)}{R_0 L_0^d} \tag{2-23}$$

is an independent and identically distributed random variable which is employed to designate a high frequency (or small scale) component, and $\mu(\Delta_n^i)$ to designate a low frequency (or large scale) component in the random cascade. One important aspect in the construction of canonical random fields is to maintain the ensemble mean $\mathrm{E}[\mathbf{W}] = 1$ of the random variable $\mathbf{W} = \{W_n^i\}$, thus the mass preservation is guaranteed for all scales. As an example of the possible outcomes from this model, in Figure 2-3 is illustrated four realizations of the random cascade algorithm implemented by Over & Gupta [1994, 1996]. All realizations were simulated for $R_0 = 1.00$ mm/h, 7 subdivisions for the high–frequency component and 4 subdivisions for the low frequency component.

An advantage of this random cascade model is it requires few parameters to describe the spatial pattern, however, the model foundations are based on the theory of random functions and for this reason, there are some difficulties for validating the hypotheses related to the choice of a universal class of random generator with which multiplicative cascades are developed. On the other hand, Paschalis et al. [2013] and Kang & Ramírez [2010] highlight that a characteristic of random cascade models is that simulations generate blockiness[11] in the spatial patterns. Although there exist several methods for reducing the anomalous effect of blockiness after the model generates the output, Kang & Ramírez [2010] suggest that further research is required for improving the reduction of blockiness from the model itself.

[11] This means a concentration of the mass in blocks into the spatial patterns.

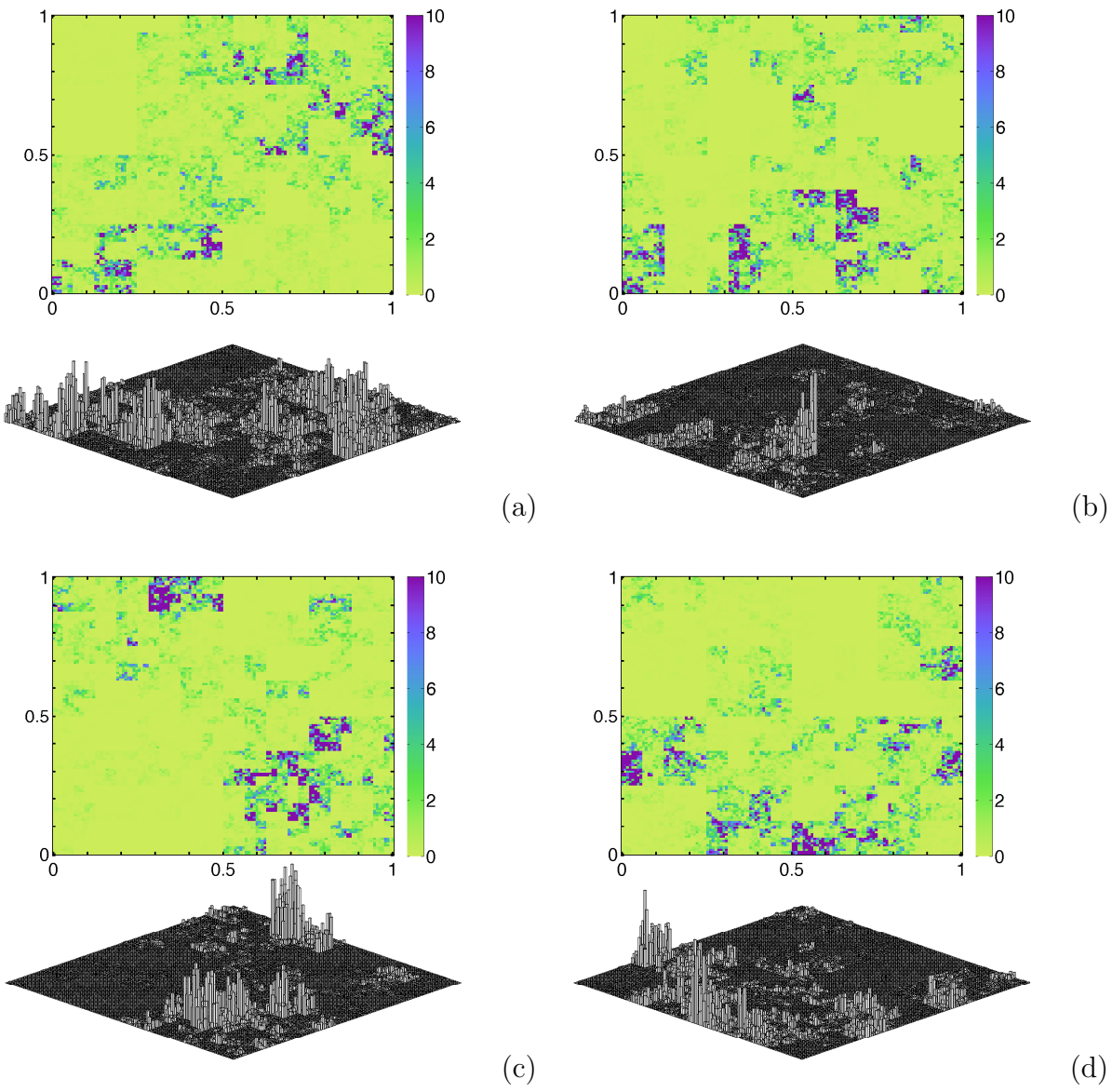

Figure 2-3: Rainfall fields simulated with the random cascade algorithm suggested by Over & Gupta [1994]. All fields were simulated for an average precipitation rate $R_0 = 1.00$ mm/h, 7 subdivisions for the high–frequency component and 4 subdivisions for the low frequency component. In every plot is shown a planar view of the generated field (top plot) and a three dimensional view (bottom plot). All rainfall fields exhibited here are canonical cascades (i.e. there exists conservation of the mass on average) and preserve the same statistical structure.

Another model using the multifractal theory but its mathematical structure is entirely deterministic is the Fractal–Multifractal (FM) approach which was introduced by Puente [1995] and developed by Maskey et al. [2017, 2016], Huang et al. [2013], Cortis et al. [2010], Peñaranda [2011, 2008], Puente & Sivakumar [2007], Puente & Obregon [1996]. In this

model the observed patterns are built from a fractal interpolation function[12]. In the original FM approach, a combination of linear functions of the form $W_n(\mathbf{x}) = A_n\,\mathbf{x} + B_n$ (affine transformations) are employed to interpolate (in a fractal way) a set of points in $\mathbb{R}^N$ and by mean of projections (derived distributions) of the graph obtained from the fractal interpolation functions the multifractal measures are achieved. For instance, at $\mathbb{R}^2$, the FM approach requires a set of 2 contractile affine maps for modeling patterns in a plane, i.e.

$$W_n \begin{pmatrix} x \\ y \end{pmatrix} = \begin{pmatrix} a_n & 0 \\ c_n & d_n \end{pmatrix} \begin{pmatrix} x \\ y \end{pmatrix} + \begin{pmatrix} e_n \\ f_n \end{pmatrix} = Ax + t, \quad n = 1, ..., N \tag{2-24}$$

subject to these restrains:

$$W_n \begin{pmatrix} x_0 \\ y_0 \end{pmatrix} = \begin{pmatrix} x_{n-1} \\ y_{n-1} \end{pmatrix}, \quad W_n \begin{pmatrix} x_N \\ y_N \end{pmatrix} = \begin{pmatrix} x_n \\ y_n \end{pmatrix}, \quad 0 \leq d_n < 1, \quad n = 1, ..., N \tag{2-25}$$

where a_n, c_n, e_n, f_n are the parameter of the FM approach in $\mathbb{R}^2$ which are estimated directly from the restrains indicated above, and d is the vertical scaling factor[13] in the transformation W_n. Consequently, all affine transformations $W_n(\cdot)$ become contractile if for all n is satisfied that $0 \leq d_n < 1$. When all these conditions are gathered, a unique fixed point exists, i.e. a fractal interpolation function $f : x \to y$, such that $G = \{(x, f(x))|x \in [0, 1]\}$, should satisfy that $G = \bigcup_{n=1}^{N} W_n(G)$ [Barnsley, 1993].

During the construction of the fractal interpolation function in $\mathbb{R}^2$, two probability measures are generated by counting the frequency of points with coordinates x and y. Under a suitable parameter configuration, both generated measures are multifractal objects but only one is highly intermittent and resembles geophysical patterns[14] [Puente, 1995]. On the other hand, if for all points at coordinates x and y a rotation θ is applied, the original FM approach increases its complexity, i.e. enhances its space of possibilities for generating more complex fractal patterns. The concept of projections of multifractal measures that are supported over a fractal interpolation function are indeed transformations $W_n(x) : \mathbb{R}^2 \to \mathbb{R}^2$, where the matrix A_n in $W_n(x) = A_n\,x + t_n$ is re–written as follows:

$$A_n = \begin{pmatrix} a_n & 0 \\ c_n & d_n \end{pmatrix} \to A_n = \begin{pmatrix} \cos\theta & -\sin\theta \\ \sin\theta & \cos\theta \end{pmatrix} \begin{pmatrix} a_n & 0 \\ c_n & d_n \end{pmatrix}^T \tag{2-26}$$

where the matrix A_n transforms the relative space with rotations or contractions, the vector t specify a linear displacement of the map [Barnsley, 1993]. Earlier applications of the FM

[12]The fractal interpolation function was originally worked by Barnsley [1993]. These functions $f : x \to y$ are developed to find a fractal curve of a given dimension passing through $N + 1$ order points $\{(x_n.y_n)|x_0 < x_1 < \cdots < x_N\}$ on the plane ($\mathbb{R}^2$). By choosing transformations of the form $W_n(\mathbf{x}) = A_n\mathbf{x} + B_n$, the order points will be mapped in order to get a self-affine function with a graph passing through the order points [Falconer, 1990].

[13]For $d_n = 0$, $n = 1, 2, \ldots, N$, is obtained a linear interpolation function.

[14]Some model outputs look alike to those seen in rainfall. Puente & Obregon [1996] and Huang et al. [2013] show some results for the description of rainfall patterns.

approach for rainfall modeling were made by Puente & Obregon [1996] and Huang et al. [2013] who analyzed a high-resolution rainfall data of a storm developed in Boston (USA), and by Peñaranda [2008] who used the FM approach for describing Bogotá's hourly rainfall time series. These works concluded that the FM approach is suitable model for describing rainfall time series in a parsimonious way. Furthermore, the statistical properties of simulated patterns are comparable to rainfall patterns.

Some examples of the FM approach in $\mathbb{R}^2$ and $\mathbb{R}^3$ can be observed in the Figures 2-4 and 2-5. In Figure 2-4 is illustrated two unidimensional patterns generated with the FM approach. Each figure is composed by two graphs. The left graph shows a fractal interpolation function and over it measures obtained from a binomial cascade. The right graph shows the projection (or illumination) of those multifractal measures for a specific rotation angle θ. Figure 2-4b resembles a high-resolution rainfall patterns registered at Boston in Octuber 25 of 1980 which was previously studied by Huang et al. [2013], Puente & Obregon [1996]. In Figure 2-5 is observed spatial patterns derived from the FM approach in $\mathbb{R}^3$. This figure shows six graphs: i) a $3D$ view of the fractal interpolation function into a cube, ii) three planar projections of the fractal interpolation function: x–$f(x)$, y–$f(y)$, z–$f(z)$, iii) a projection of the fractal interpolation function over the $x - y$ plane in order to get a simulated spatial pattern, and iv) a $3D$ view of the simulated spatial pattern. These kind of patterns can be used to simulate rainfall fields, groundwater fluxes, and other spatial geophysical patterns. Applications about the application of FM approach for modeling spatial patterns can be observed in the works of Cortis et al. [2010], Puente et al. [2001], Puente [1995].

It is highlighted that the FM approach has some drawbacks. The geometrical pattern derived from the FM approach is not always easy to obtain by regular procedures employed in hydrology for solving the inverse problem, therefore, it is necessary to continue improving the methodology for solving the inverse problem. On the other hand, there is not a significant advance in the application of the FM approach for modeling the evolution (or dynamic) of patterns. Puente [1995] suggests that a FM dynamic approach may take place if the evolution of parameters is studied, nevertheless, there still exists some difficulties for coding observed patterns in a non-dynamic approach. Huang et al. [2013] determined that there is not a unique code for a set of observed data and therefore, a dynamic approach as suggested by Puente [1995] may not be still feasible.

2.2.3. Physically–Based Models

The first models introduced by hydrologists for describing rainfall patterns were not designed from the physics of precipitation processes, instead they were conceived from mathematical basis in order to get suitable statistical estimations in comparison to historical records [Over & Gupta, 1994, Gupta & Waymire, 1993, Puente, 1995, Schertzer & Lovejoy, 1987a]. However, questions around the physics of rainfall were addressed to explain statistical properties of the rainfall field in connection with the dynamic of precipitation processes [Mesa & Peñaranda, 2015, Cortis et al., 2014, Nordstrom & Gupta, 2003, Marzan et al., 1996]; particularly what is related to the multifractal properties observed in rainfall patterns.

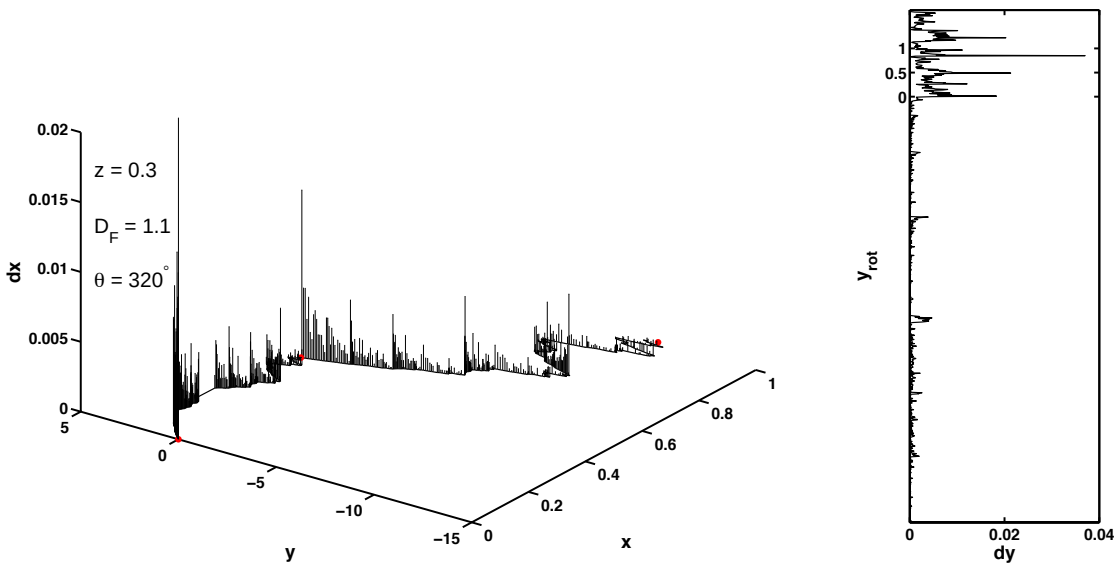

(a)

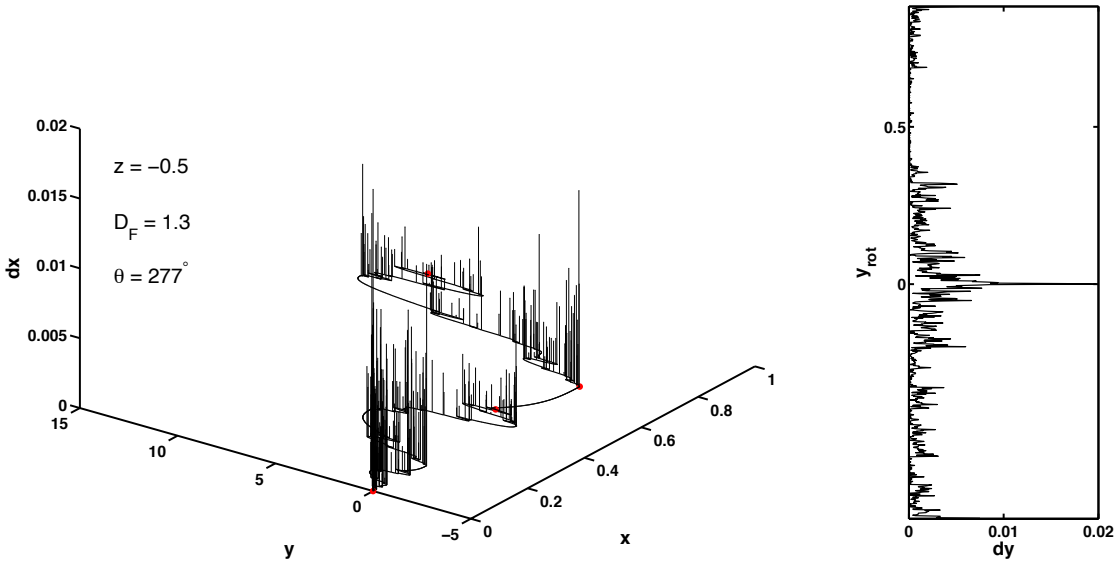

(b)

Figure 2-4: The FM approach for $\mathbb{R}^2$ is described through three constitutive elements that can be observed in the images: the fractal interpolation function (over the plane x–y), the multifractal measure (supported on the fractal interpolation function) and the derived measure (in the plane y_{rot}–dy). The original idea of *projections* proposed by Puente & Obregon [1996] and Puente [1995] is understood as multifractal measures supported on the path of a fractal interpolation function which are illuminated over a rotated plane in $\mathbb{R}^2$ in order to get patterns alike to those observed in rainfall.

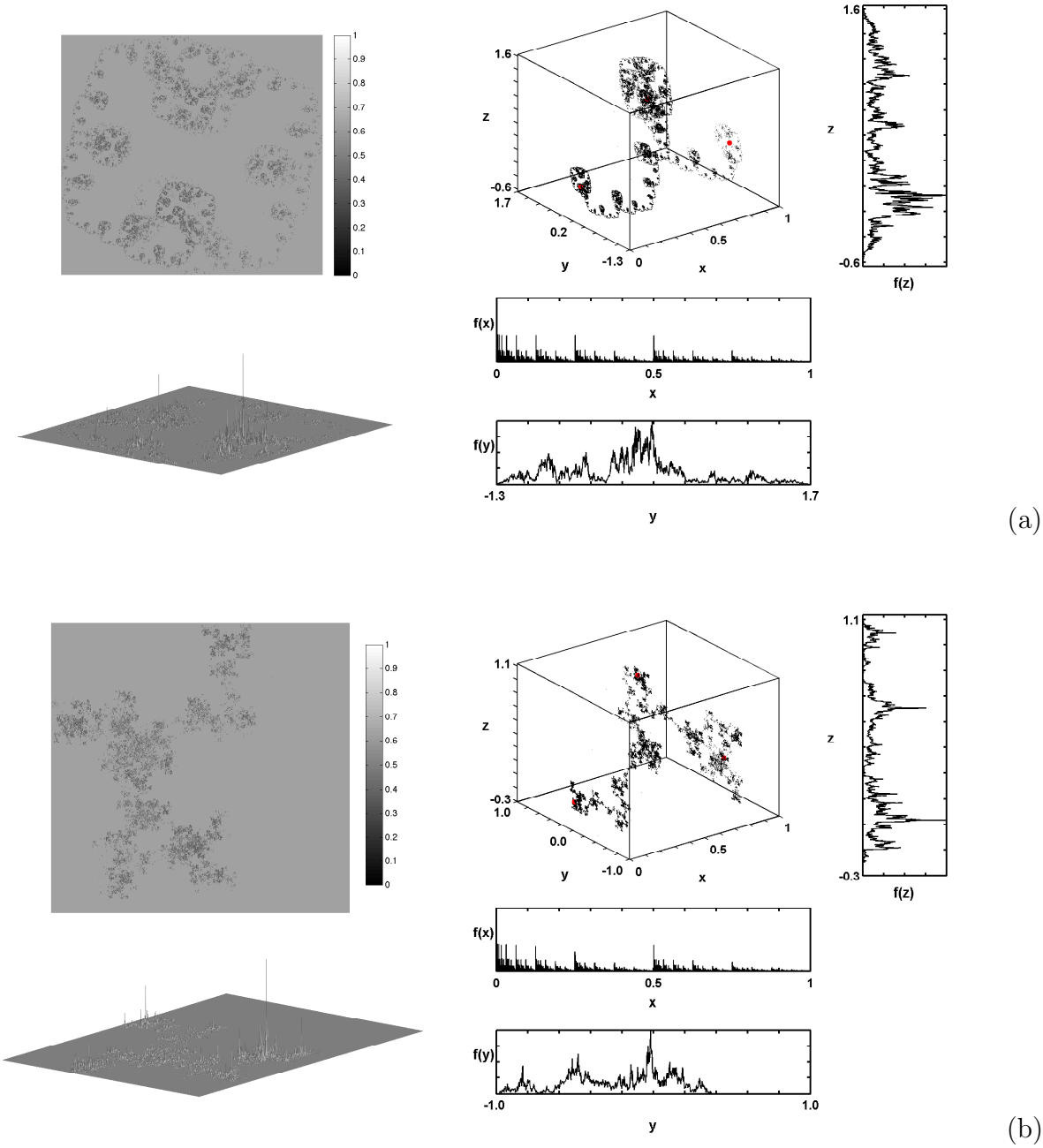

Figure 2-5: Example of two rainfall fields simulated by a $\mathbb{R}^3$–version of the FM approach. Here the fractal interpolation function is built over a tridimensional domain (top center of the picture). Three planar projections are derived from the fractal interpolation function: x–$f(x)$, y–$f(y)$, z–$f(z)$. These planes allow us to distinguish three unidimensional multifractal measures. The projections over the x–y plane constitute the simulated rainfall field. By a modification of the projection angle parameter, the mass of the fields changes from more distributed in (a), to more concentrated in (b). The FM algorithm employed here can be found at Huang et al. [2013], Peñaranda [2008] and Puente [1995].

Although big efforts have been carried out to build the foundation of a theory of rainfall multifractality, there is not yet a coupling among the proposed ideas, furthermore, the prevalence of complex models used in meteorology do not allow the simple comprehension of either the precipitations processes or the integration of theories about rainfall multifractality. Briefly, It will be discussed below some general aspect about how the physics of rainfall multifractality has been envisioned and which paths have been identified for getting answers to the problem of establishing a successful theory. It is recalled the models that will be presented in this document were selected under the criteria of having a parsimonious mathematical structure and a linkage with the fractal theory; therefore, the entire universe of physically-based models will not be here discussed.

Causal Space–Time Multifractal Processes

One of first physically-based rainfall model was proposed by Marzan et al. [1996]. This model considers rainfall acts as a passive scalar into the atmospheric turbulence, therefore it must preserve the scaling properties of the turbulence environment. If the atmospheric turbulence can be well represented by the Navier–Stokes equations for large Reynolds number, there should be symmetries between the rainfall field properties and the turbulence ones. Recalling the Navier–Stokes equations:

$$\partial_t \mathbf{u} + (\mathbf{u}\cdot\nabla)\,\mathbf{u} = -\frac{1}{\rho}\nabla p + \nu\,\Delta\,\mathbf{u} \tag{2-27}$$

$$\nabla\,\mathbf{u} = 0 \tag{2-28}$$

where $\mathbf{u}$ is the velocity vector, ρ the fluid density, $\mathbf{p}$ the pressure, and ν the fluid viscosity. The scaling symmetries of Navier–Stokes are [Frisch, 1995, Marzan et al., 1996]:

$$g_\lambda^{scal} : t, \mathbf{x}, \mathbf{u}, \nu \mapsto \lambda^{1-H} t, \lambda\,\mathbf{x}, \lambda^H\,\mathbf{u}, \lambda^{H+1}\nu \tag{2-29}$$

which are obtained if all the terms in Navier-Stokes equations are multiplied by λ^{2H-1}. Similarly, the equation for describing a passive scalar η is:

$$\partial_t \eta + \mathbf{u}\cdot\nabla\eta = \kappa\Delta\eta \tag{2-30}$$

where κ is a molecular diffusivity for the passive scalar η. The scaling symmetries for the passive scalar equation are:

$$g_\lambda^{scal} : t, \mathbf{x}, \eta, \kappa \mapsto \lambda^{1-H} t, \lambda\,\mathbf{x}, \lambda^{H^*}\eta, \lambda^{H+1}\kappa \tag{2-31}$$

All the aforementioned scaling symmetries for either the Navier–Stokes equations or the passive scalar equation depend on the scaling exponent H. The research developed by Marzan et al. [1996] just focused in the space–time symmetries and in the empirical determination of the scaling exponent H. In order to have a reference framework about the magnitude of the scaling exponent H, the phenomenology of turbulence gives some clues about it. Kolmogorov

[1941] suggests that the eddy turnover time[15] (or circulation time) t_λ for a structure of size λ can be computed as follows [Frisch, 1995, p. 102]:

$$t_\lambda \sim \epsilon^{-1/3}\lambda^{2/3} \tag{2-32}$$

where $\epsilon \sim v_\lambda^3/\lambda$ is the mean energy dissipation rate for a typical value of the velocity v_λ associated to the scale λ. Equations 2-32 shows a space–time symmetry for turbulence processes where the scaling exponent H should be equal to $H = 1/3$. According to Marzan et al. [1996], this space–time symmetry should be hold for rainfall since it acts a passive scalar into the atmospheric turbulence.

In the model introduced by Marzan et al. [1996], the rainfall field is modeled as a multiplicative multifractal process with scaling anisotropy exponent $H > 0$. The space–time cascades are usually generated considering one axis for the spatial domain and another for the time domain. In order to introduce a space–time anisotropy with scaling exponent H, in each cascade step there will be $\lambda \times \lambda^{1-H}$ structures of size $l_n^x = L\lambda^{-n}$ into the spatial axis and $l_n^t = L\lambda^{n(H-1)}$ into the time axis. For instance, if $H = 1/3$, the smallest number of structures equals to 8×4 structures, since $\lambda = 8$ (for the spatial domain) and $\lambda^{1-H} = 4$ (for the time domain). For discrete cascades, all the structures at scale l_n are separated by a distance $|\Delta\,\mathbf{x}| > l_n$ and they are offspring of structures at scale $l_m = |\Delta\,\mathbf{x}|$. Marzan et al. [1996] suggest rainfall intensities can be computed as follows:

$$\epsilon_n(\mathbf{x}) = \epsilon_m(\mathbf{x}) \prod_{i=m+1}^{n} \mu\epsilon_i(\mathbf{x}) \tag{2-33}$$

$$\epsilon_n(\mathbf{x}+\Delta\,\mathbf{x}) = \epsilon_m(\mathbf{x}) \prod_{i=m+1}^{n} \mu\epsilon_i(\mathbf{x}+\Delta\,\mathbf{x}) \tag{2-34}$$

where $\mu\epsilon_i$ is a random variable statistically independent with respect to the scaling index i and spatial location $\mathbf{x}$, with distribution $\langle \mu\epsilon^q \rangle = \lambda^{K(q)}$, where $K(q)$ is the moment scaling function. In the case of continuous cascades, the multiplication of random fields is replaced by an additive process if quantities are applied a logarithmic transformation. Therefore, if the multifractal field of ϵ_λ is built taking into account a generator Γ_λ at resolution λ, each ϵ_λ should respect the moment distribution $\langle \mu\epsilon_\lambda^q \rangle = \lambda^{K(q)}$ and thus, $\langle e^{q\,\Gamma_\lambda} \rangle \sim e^{K(q)\,\ln\lambda}$. In the framework of universal multifractals [Lovejoy & Schertzer, 1990], the generator Γ_λ for generating the multifractal field is the infinite limit of the sum of independent stable (Levy) random variables and the subgenerator γ_λ is equivalent to an stochastic process with Levy distribution, so γ_λ can be represented as:

$$g_\lambda(\mathbf{x},t) * \Gamma_\lambda(\mathbf{x},t) = \gamma_\lambda(\mathbf{x},t) \tag{2-35}$$

$$\left[\partial_{t^{\xi_1}} + (-\Delta)^{\xi_2}\right]^{H_\alpha} \Gamma_\lambda(\mathbf{x},t) = \gamma_\lambda(\mathbf{x},t); \qquad H_\alpha = D/\alpha'; \qquad \frac{1}{\alpha} + \frac{1}{\alpha'} = 1 \tag{2-36}$$

[15] The eddy turnover time is the typical time of a structure of size λ to undergo a significant due to the relative motion os its components [Frisch, 1995]. It also means a typical time to transfer energy from scales λ to smaller ones.

where $g_\lambda(\mathbf{x}, t)$ is a impulse–response function[16], $*$ is a convolution operator, $D = 3$ is the dimension of the space–time and α is the Lévy noise index, and equation 2-36 represents an (anomalous) diffusion equation. This last mathematical representation defines a causal process in the space–time for modeling rainfall.

In Marzan et al.'s research [1996], the scaling exponent H is directly estimated from rainfall records by mean of the space–time rainfall–field energy spectrum (or space–time Fourier spectrum). Marzan et al. [1996] defines the space–time energy spectra as follows:

$$P(\mathbf{k}, \omega) \sim \|(\mathbf{k}, \omega)\|^{-d_{el}+K(2)} \tag{2-37}$$

where $d_{el} = d + 1 - H$, d is the topological dimension, H the scaling exponent and $K(2)$ is the value of the moment scaling function evaluated for the second moment ($q = 2$). For $\omega = 0$, the spatial energy spectrum can be approximated as

$$P(k) \sim k^{-d_{el}+K(2)} = k^{-s_k} \tag{2-38}$$

and for $k = 0$, the time energy spectrum can be approximated as

$$P(\omega) \sim \omega^{\frac{-d_{el}+K(2)}{1-H}} = \omega^{-s_w} \tag{2-39}$$

Therefore, H can be estimated through the relationship between the slopes s_k and s_ω, as follows:

$$H = 1 - \frac{s_k}{s_\omega} \tag{2-40}$$

If $H \neq 0$, the rainfall field is isotropic in the space–time domain, i.e. the structures evolves almost identical in either time or space. However, if $H > 0$, there exists space–time anisotropy and there should be a dynamic scaling in the rainfall field for describing how the structures change in the space–time. Based on Marzan et al.'s model simulations, they found a stronger decorrelation rate at smaller scales of the spectra which means that smaller structures posses shorter lifetime compared to bigger ones.

Dynamic Scaling of Rainfall

In the same direction of Marzan et al. [1996], the hypothesis of a dynamic scaling in rainfall is also studied by Venugopal et al. [1999]. They tried to understand and to quantify the space–time dependencies in rainfall for several scales via dynamic scaling[17] which has been evidenced in evolving physical systems far from equilibrium [Goldenfeld, 1992]. The employed research methodology consisted in study the rainfall intensity evolution of a particular point (i, j) into the rainfall field, i.e. how much the intensity of the field averaged

[16] Also known as *propagator* or Green's function.

[17] A function depending on time and space $f(x, t)$ exhibits dynamic scaling if satisfies the following relation: $f(x, t) \sim t^{-\alpha} x^{-\beta} g(x/t^z) \sim t^{-\theta} \Phi(x/t^z)$, where the variables x and t denote space and time variables correspondingly; α, β, and θ are dynamic scaling exponents and Φ is a scaling function [Vicsek & Family, 1984].

over a box of size $L \times L$ and centered around (i, j) changes during a time interval t. Employing this methodology for different spatial and temporal scales, Venugopal et al. [1999] collected several statistics of the space–time structure of the rainfall. Moreover, they looked for relations of the form:

$$\frac{t_1}{t_2} = f\left(\frac{L_1}{L_2}\right); \quad \frac{t_1}{t_3} = f\left(\frac{L_1}{L_3}\right); \quad \frac{t_1}{t_3} = \frac{t_1}{t_2}\frac{t_2}{t_3} = f\left(\frac{L_1}{L_2}\right) f\left(\frac{L_2}{L_3}\right) \tag{2-41}$$

and non-linear relations as follows:

$$\frac{t_1}{t_2} = f\left(\frac{L_1}{L_2}\right)^z; \tag{2-42}$$

where z is the scaling dynamic exponent. The temporal rainfall evolution at the point (i, j) was measured through fluctuations as follows:

$$\Delta \ln I_{i,j,t}(L, t) = \ln I^L_{i,j}(t + \tau) - \ln I^L_{i,j}(t) \tag{2-43}$$

where $I^L_{i,j}(\tau + t)$ is the non-zero rainfall intensity at location (i, j), at instant $\tau + t$, and spatial scale L, and τ is the time-lag over which the rainfall evolution is measured. Venugopal et al. [1999] computed $\Delta \ln I_{i,j,t}(L, t)$ for different time-lags τ (i.e. $10, 20, 30, \ldots, 80$ min) and for all the point of the rainfall field. Equation 2-43 represents the intensity change of the field over a time lag τ and its application suppose the existence of an additive random process where the increments are independent and identically distributed random variables.

By means of the study of the probability density functions (PDF) of $\Delta \ln I_{i,j,t}(L, t)$ is checked if these increments remains invariant under space-time transformations and particularly, the invariance of second moment. Selecting pairs of t and L values and following a criteria of constancy in the standard deviation of their PDFs for selected (stationary) regions, the scaling dynamic is identified[18]. For the tropical convective storms at Darwin[19] (Australia) which were studied by Venugopal et al. [1999], it was found that the dynamic scaling exists for the selected stationary regions, therefore, the intensity rate of rainfall stays invariant under space–time transformations and the statistical dynamic structure of rainfall can be expressed through the scaling dynamic exponent z. The value of z range between 0.6 and 0.7 for those regions where the mean rainfall intensity and the fraction of rainy areas decrease. On the other hand, the value of z range between 0.8 and 1.2 for those regions where the mean rainfall intensity and the fraction of rainy areas increase. According to those results, Venugopal et al. [1999] could not determine clearly if the value of z changes with the dynamics of the rainfall field and they suggest to study the dependence of z with the space-time dynamics.

[18] Venugopal et al. [1999] considered that the log–log linearity of the iso-standard deviation lines suggest a scaling dynamic and their slope were traduced as the scaling dynamic exponent z.

[19] Venugopal et al. [1999] used weather radar data with spatial resolution of 2 km and temporal resolution of 10 min. The storms analyzed correspond to the days December 28th of 1993, December 30th of 1993 and January 4th of 1994.

An important fact to mention is that the research developed by Venugopal et al. [1999] was not oriented directly to explain the underlying physic mechanism of rainfall dynamics, instead to identify a mechanism for study the space-time structure of rainfall simultaneously. The main finding of this research was found in an empirical proof of the space-time transformation $t \sim L^z$, where $z \approx 0.6$, but there is not any physical connection to explain such a value. However, Venugopal et al. [1999] consider that the exponent z keeps a resemblance to the anisotropy scaling exponent H introduced by Marzan et al. [1996]. They suspect that there could be an approximation of the form $z \approx 1 - H$. Moreover, they suggest the physics of the scaling dynamic can be only studied through numerical simulations of mesoscale weather models since the difficulties for getting physical observations at the same space–time resolution of rainfall records.

Another research about the identification of dynamic scaling in rainfall patterns was developed by De-Michele and Bernardara [2005]. Taking into account that in the spectral theory is found that those point stochastic processes exhibiting time scale invariance, the spectral density function S scales with frequency ω as $S \propto \omega^{-\gamma}$, where γ is a scaling exponent. De-Michele and Bernardara [2005] also used the spectral theory to identify dynamic scaling exponents as Marzan et al. [1996] did for their research. For De-Michele and Bernardara [2005], the spectral density function is represented as follows:

$$S(\omega_x, \omega_y, \omega_t) \propto \left(\alpha^2 \omega_x^{2\epsilon_{xt}} + \beta^2 \omega_y^{2\epsilon_{yt}} + \omega_t^2\right)^{-\frac{\delta+1}{2}} \tag{2-44}$$

where ω_x and ω_y are wave numbers in a $\mathbb{R}^2$–space, ω_t is the frequency, δ, ϵ_{xt} and ϵ_{yt} are dynamic scaling exponents, α and β are two constants called multiplicative coefficients[20] which take into account the non-homogeneity of the space–time [Hardy & Beier, 1994]. Moreover, from the two exponents ϵ_{xt} and ϵ_{yt} is derived an spacial anisotropic exponent ϵ_{xy}, such as follows:

$$\epsilon_{xy} = \frac{\epsilon_{xt}}{\epsilon_{yt}} \tag{2-45}$$

where $\epsilon_{xy} \approx 1$ will represent an isotropic spatial behavior of the studied process. The exponent δ at equation 2-44 has a relationship with the fractal dimension D, such that $D = d + (3 - \delta)/2$ for $1 \leq \delta \leq 3$ (where d represents the Euclidean dimension). On the other hand, α and β are considered as *lacunarity*[21] indexes; large values of α and β are related to high lacunarity which means that rainfall would be concentrated in small portions of the spatial domain.

De-Michele and Bernardara [2005] applied least–squared techniques for estimating the parameters δ, ϵ_{xt}, ϵ_{yt}, α and β of equation 2-44 for some radar–based rainfall data sets that belong to GATE[22] campaign. Their results shows there exist a dynamic scaling for rainfall whose mean values for δ, ϵ_{xt}, ϵ_{yt}, ϵ_{xy}, α and β are ≈ 1.54, $\epsilon_{xt} \approx 1.26$, $\epsilon_{yt} \approx 1.06$, $\epsilon_{xy} \approx 1.22$,

[20] For an isotropic spatial behavior $\epsilon_{xt} = 1$ and $\epsilon_{yt} = 1$.
[21] Lacunarity is a texture–fractal measure associated to the gaps into a fractal set [Mandelbrot, 1982].
[22] Global Atmospheric Research Program - Atlantic Tropical Experiment.

68 and 46, respectively. In connection with the results obtained by Marzan et al. [1996], the former results can be also seen as $H_x = 0.26$ and $H_y = 0.06$, which describe either a spatial anisotropy of the rainfall field or a value of the dynamic scaling exponent different to the results found in turbulence theory, i.e. $H \sim 1/3$. From the aforementioned arguments, one could conclude that rainfall is not acting as a passive scalar in the atmospheric turbulence; instead, rainfall is interacting with turbulent processes in an unknown fashion.

Scaling in the Atmospheric Convection

An starting point in the study of the relationship between atmospheric convection and rainfall scaling properties was the research developed by Perica & Foufoula-Georgiou [1996]. In this research, they found empirical relationships between statistical scaling properties of rainfall fluctuations[23] and thermodynamic properties of the atmosphere during rainfall events[24]. Perica & Foufoula-Georgiou [1996] considered that rainfall fluctuations components $\{X'_{m,i}\}$ for $i = 1, 2, 3$ exhibit *simple scaling* (or self-similarity), therefore, the following scaling property should be satisfied:

$$\{X'_{m,i}\} \stackrel{\mathrm{d}}{=} \{(2^{m-1})^{H_i} X'_{1,i}\} \tag{2-46}$$

where H_i are scaling exponents. Equation 2-46 means that the marginal distribution function of $X'_{m,i}$ at all scales m should be of the same type for all the components i if there exists self-similarity. On the other hand, Perica & Foufoula-Georgiou [1996] used a symmetric stable distribution[25] for analyzing the variability of the empirical density probability functions (pdf). For these distributions, the scaling condition at equation 2-46 should be satisfied as follows:

$$c_{m,i} = 2^{(m-1)^{H_i}} c_{1,i} \tag{2-47}$$

where $c_{m,i}$ are the scale parameters of the stable distribution for each fluctuation components $i = 1, 2, 3$ and scales m. In equation 2-47, the scaling exponent H_i represents the rate of variability of $c_{m,i}$ over all the scales m. For the studied stratiform systems, Perica & Foufoula-Georgiou [1996] found H_i is in the range 0.14–0.18 and $c_{m,i}$ is in the range 0.30–0.40. In the case of convective systems, H_i is in the range 0.20–0.45 and $c_{m,i}$ is in the range 0.10–0.35. Although these results show the scaling properties change with the spatial pattern type[26], Perica & Foufoula-Georgiou [1996] found the scaling parameters depended more on convective instability of the atmospheric environment before starting the storm instead the spatial pattern type.

[23] Rainfall fluctuations were obtained from the application of the Haar wavelet transform to the spatial rainfall field.

[24] The data used for this research came from radar and sounding observations of the measurement campaign over Oklahoma and Kansas (USA) called PRE-STORM. The objective of this campaign was to study the structure and dynamics of mesoscale convective systems over Oklahoma and Kansas.

[25] A stable distribution $S(x : \alpha, \beta, \delta, c)$ will be symmetric if the skewness parameter β equals zero.

[26] i.e. linear (squall line), occluding, or chaotic systems [Blanchard, 1990].

Among the thermodynamic and kinematic variables that Perica & Foufoula-Georgiou [1996] studied, the Convective Available Potential Energy (CAPE) is the best predictor of the scaling properties of rainfall fluctuations. Perica & Foufoula-Georgiou [1996] show the following linear relationship:

$$\bar{H} = 0.05 + 0.96\,\mathrm{CAPE} \times 10^{-4} \tag{2-48}$$

$$\bar{c} = 0.38 - 0.60\,\mathrm{CAPE} \times 10^{-4} \tag{2-49}$$

High values of CAPE represent high intensities in the rainfall field and there exists a strong spatial dependence of rainfall rates (i.e. high intensities are more likely to occur in the neighborhood of high rainfall intensity points.). The higher the rainfall rate is, the smaller the scaling parameter $\bar{c}$ becomes but the converse happens with the scaling parameter H, i.e. for higher rainfall rate, H becomes higher. The former results suggest that for areas of higher convective potential energy, the scaling parameter H will be high and the parameter $\bar{c}$ will be small.

Dynamic Equations of Convection

With the idea of looking for physical basis to scaling properties of rainfall, Nordstrom & Gupta [2003] proposed a physically-based model for describing tropical convective rainfall. In this model does not exist statistical and cloud micro–physics considerations to describe atmospheric convection processes, however its mathematical structure represents some of the main features of convection physics. Furthermore, this model is able to simulate patterns alike to rainfall ones in a parsimonious way.

The model phenomenology takes into account the triggering effect produced by a cold pool (also known as outflow) in the development of convection. It supposes the existence of a region below of the level of free convection[27] (LFC) where both cold and warm air masses are found in a state of conditional stability. The incident air packets will ascend to the level of neutral buoyancy[28] (LNB) if there exists enough energy for pushing the air packet. Such an energy is referred in the phenomenology as triggering energy and it is interpreted as the *convective inhibition*[29] (CIN). On the other hand, the energy stored into the air packets for their ascents after reaching the LFC is known as *convective available potential energy* (CAPE). During the ascension of air packets, the cooling by evaporation of cloud droplets allows the creation of a *downdraft*. This downdraft is colder and denser than its surroundings and that helps to sustain the convection.

In Nordstrom & Gupta's model (2003), the dynamics of the cold–pool depth $h(\mathbf{x}, t)$ is described by an advection – diffusion equation as follows:

$$\partial_t h(\mathbf{x}, t) + \mathbf{u} \cdot \nabla h(\mathbf{x}, t) = \nu_a \, \Delta h(\mathbf{x}, t) \tag{2-50}$$

[27] This the high at which the moist air becomes positively buoyant [Nordstrom & Gupta, 2003].

[28] The height at which the moist air is in dynamic equilibrium with its surrounding [Nordstrom & Gupta, 2003].

[29] Convective Inhibition (CIN) is associated to the inhibition degree of convection because the existence of a inversion layer at the top of the planetary boundary layer [Wallace & Hobbs, 2006].

where $\mathbf{u}$ is the velocity of the cold pool propagation and ν_a is a diffusion coefficient for the air into the cold pool. The heating of the cold pool is accounted through the reduction of its depth, thus:

$$h(\mathbf{x}, t + \delta t) = h(\mathbf{x}, t) \times (1 - F) \tag{2-51}$$

where F is a reduction factor for every time step. The ascent of incident moist air is represented as follows:

$$v_a = U \cdot \nabla h = |U|\,|\nabla h| \cos(\theta_h) = \frac{|U|\,|\nabla h|}{\sqrt{1 + |\nabla h|^2}} \tag{2-52}$$

where U is the incident wind which is parallel to the surface, ∇h is the gradient of the cold pool and θ_h is the angle between the vectors U and ∇h. Low values of the relation $u_a/|U|$ represents an incident wind tangent to the gradient of the cold pool and therefore, is not likely to get an upward wind into the field. On the other hand, high values of the relation $u_a/|U|$ represents a direct entry of the winds into the pool. Because these conditions, u_a should be into a threshold range $[b_1, b_2]$ for existing ascent of air. In the conceptual model, b_1 is a parameter that depends on the CIN and $b_2 > b_1$ depends on the density difference between the cold pool and the incident wind.

The model also describes a cloudiness field $C(\mathbf{x}, t)$ by mean of a Heaviside function $\Theta(\kappa)$ as follows:

$$\partial_t C(\mathbf{x}, t) = c\,\Theta(\kappa) \tag{2-53}$$

where c is a constant value which indicates the position of cloud packets into the atmosphere and κ is the triggering energy for the deep convection which is computed as:

$$k(\mathbf{x}, t) = (U \cdot \nabla h - b_1)(b_2 - U \cdot \nabla h) \tag{2-54}$$

In the phenomenology of Nordstrom & Gupta's model (2003), cloudy regions of higher mass should rain more quickly than those of lower mass. Therefore, the way for representing the downdraft of convective clouds is through a local time scale τ for the ascent and fallout, thus:

$$\tilde{t} = \frac{1}{N(\mathbf{x}, t)} \sum_{i=1}^{N(\mathbf{x},t)} t_i \Theta(\kappa(t_i)) \tag{2-55}$$

where $t_i = t_i(\mathbf{x})$ is the time associated to the convective event i, $N(\mathbf{x}, t)$ is the number of convective events at the location $\mathbf{x}$. If $\tilde{t} < t - \tau$ rainfall will start and it will be computed as:

$$R(\mathbf{x}, t) = r\,C(\mathbf{x}, t) \tag{2-56}$$

where r is a constant value of rainfall intensity. After computing rainfall, the update values for cloudiness and depth of the cold pool are:

$$\partial_t C(\mathbf{x}, t) = - R(\mathbf{x}, t) \tag{2-57}$$

$$\partial_t h(\mathbf{x}, t) = + R(\mathbf{x}, t) \tag{2-58}$$

In Figure 2-6 are exhibited some simulations obtained with the Nordstrom & Gupta's model (2003). For these simulations a cold pool is previously defined a cold pool at the level of 1000 m and including a Gaussian perturbation over the cold pool field. By means of tuning the parameter b_1 to three specific values, three different spatial patterns of the rainfall field $R(\mathbf{x}, t)$ were obtained (right panels of figure 2-6). Clearly, for lower values of b_1 the higher rainfall rate prevails. Nordstrom & Gupta [2003] have considered b_1 as a tuning parameter. For getting output patterns exhibiting multifractal scaling structure, b_1 should reach a critical value. Moreover, during the critical state of the parameter b_1 rainfall patterns are highly variable alike to those generated by random cascade models and therefore the scaling properties of the field exhibit multifractality. Certainly, the simulated outputs of the Nordstrom & Gupta's model (2003) are highly complex, although not completely similar to real rainfall fields. The most important feature of the model is the existence of a tuning parameter which can reach a critical state in order to get statistical (multifractal) scaling of the rainfall field. This statistical feature is also found in non-linear dynamic models [Strogatz, 1994] and in those from the statistical mechanics which exhibit second–order phase transitions.

Vieira [2006] applied the Nordstrom & Gupta's model (2003) to understand the development of precipitation patterns over the Colombian Pacific ocean in three different atmospheric sceneries and comparing with observations recorded by the mission TRMM[30]. The results from this research state strong limitations in the use of the model because its parameters should be selected in a bound range for obtaining coherent outputs. In spite of the good statistical results that are proved by the model (i.e. multifractal scaling), the dynamical representation needs modifications to capture completely the geometry of observed rainfall fields. Further work must be done around the conceptual structure of the model in order to explain the behavior of its parameters and their connectivity with the physics of convective processes.

In recent years Holloway & Neelin [2010, 2009], Muller et al. [2009], Peters & Neelin [2009, 2006] NS Bretherton et al. [2004] have identified a new conceptual formulation for understanding rainfall using the critical phenomena theory. As a first approach and example of criticality is exhibited in the quantity of integral–column water vapor. It seems to play a role of a tuning parameter in the convection development, since the formation of strong precipitation when a critical value in the quantity of integral–column water vapor is reaches. Peters & Neelin [2006] suggest that the process leading to a critical transition to strong precipitation could be understood as a self-organized critical (SOC) system.

[30]TRMM: Tropical Rainfall Measurement Mission.

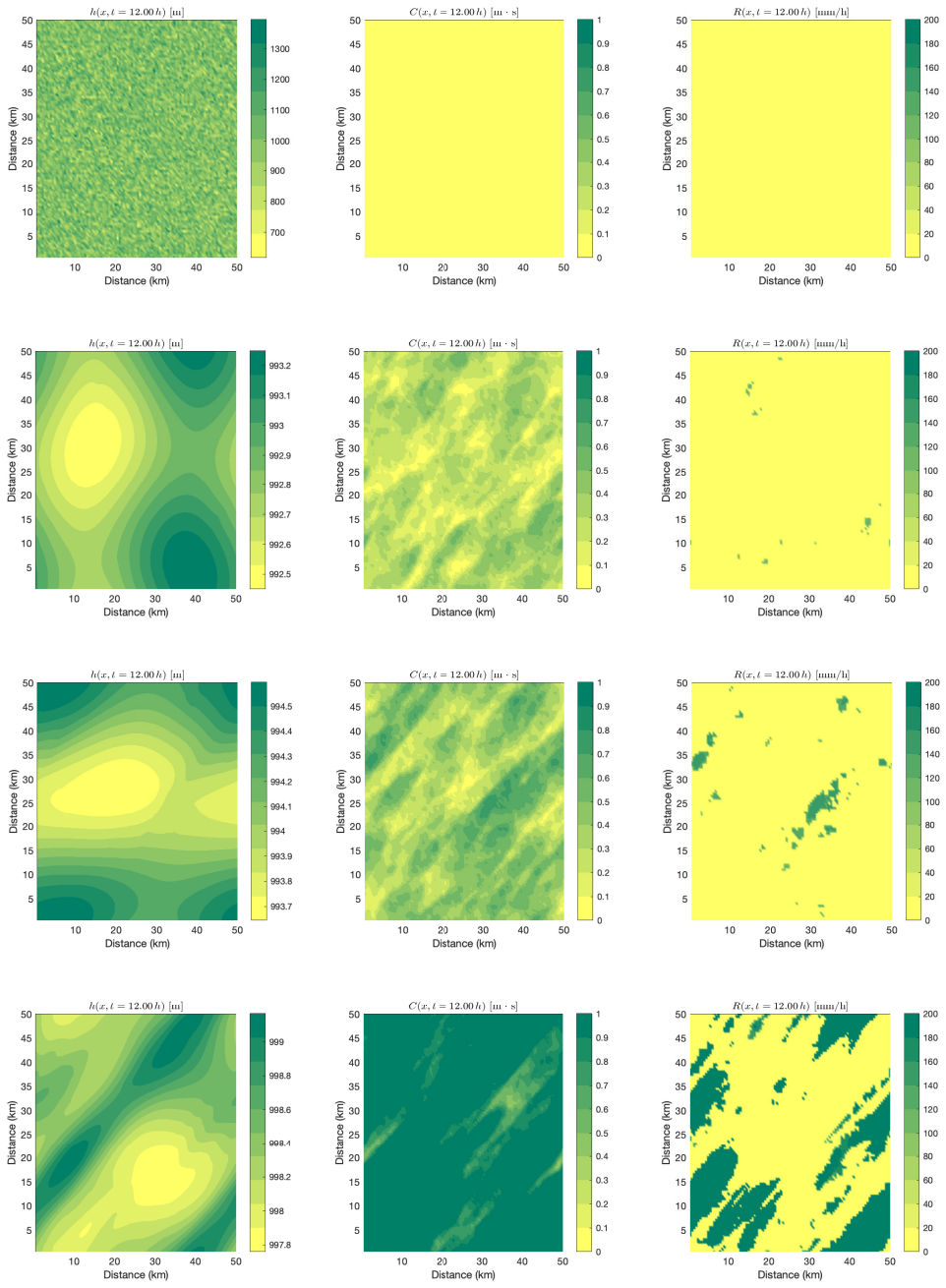

Figure 2-6: Example of simulated rainfall fields with the Nordstrom & Gupta's model [2003]. In every row of the figure there are three graphs. The left one is representing the depth of the pool cold field $h(\mathbf{x}, t)$, the centered one the cloudiness field $C(\mathbf{x}, t)$ and the right one the rainfall field $R(\mathbf{x}, t)$. In the row (a) is showing the initial conditions for the fields $h(\mathbf{x}, t)$, $C(\mathbf{x}, t)$, and $R(\mathbf{x}, t)$. The simulations parameters are: $\Delta t = 5$ s, $\Delta x = 500$ m, $\mathbf{u} = 10\,\hat{i} + 10\,\hat{j}$ (m s^{-1}), and $a = 1 \times 10^5$ m^2 s^{-1}, $U = 10\,\hat{i} + 10\,\hat{j}$ (m s^{-1}) and the time lapse for the simulation was 12 h. In the row (b), the parameter $b_1 = 0.3$ m s^{-1}. In the row (c), the parameter $b_1 = 0.2$ m s^{-1}. In the row (d), the parameter $b_1 = 0.1$ m s^{-1}.

Peters & Neelin [2009, 2006] support their interpretation in the fact they found some typical characteristics of SOC systems: power–law fit between precipitation and water vapor content, maximum variance near critical point in this relationship, spatial scaling of rainfall and so on. However, Muller et al. [2009] state an opposition considering that the empirical evidence of SOC found by Peters & Neelin [2009, 2006] is essentially circumstantial because there is not still a physical mechanism that proves how SOC comes out. As seen in the scientific literature, SOC is understood as the result of a slow forcing applied to systems that exhibit phase transitions. Evidences of SOC in physical systems are illustrated by scale invariance, cooperation and spontaneous organization [Dickman et al., 2000]. Nevertheless, If criticality does not happen spontaneously and if there is not a mechanism explaining how this critical state is maintained, therefore SOC does not exist but a conventional phase transition. In the last 20 years, several parsimonious models describing the organizational pattern of convective systems have envisioned the inclusion of SOC for describing rainfall [e.g Nagel & Raschke, 1992, Nordstrom & Gupta, 2003, Craig & Mack, 2013, Hottovy & Stechmann, 2015]. However, the evidence offered by those models is premature and only shows a phenomenology where the atmosphere acts near to a critical threshold during the formation of either convective clouds [Nagel & Raschke, 1992] or high–intensity rainfall areas [Nordstrom & Gupta, 2003, Craig & Mack, 2013, Hottovy & Stechmann, 2015].

Following the discussion about parsimonious dynamic models for describing convection, there exists another model to be introduced in this section. The model known as Craig & Mack's model [2013] is a new proposal for understanding convective rainfall. This model represents a moisture budget of the free troposphere including three physical processes associated to the convection: subsidence drying by radiative cooling (moisture is sinked into the subcloud layer), convective moistening (transport of moisture from the subcloud layer) and horizontal mixing (turbulence effect). Craig & Mack [2013] consider that the location of convection is determined by the moisture content of the lower troposphere and its dynamics can be represented as a bistable system in which a feedback process leads to dry regions becoming drier and moist regions moister. The physical mechanism for representing a bistable system is known as *coarsening*. Imaging a stable mixture of two regions with different phase in where one of the regions grows in size over time to get a stable condition. For describing this physical process, Allen & Cahn [1979] suggested a mathematical model for anti–phase domain coarsening in Fe-Al alloys, thus:

$$\partial_t \eta = -\alpha\, \partial_\eta V(\eta) + \nu\, \Delta\eta \tag{2-59}$$

where η represents a long-range non-conserved order parameter, α is a positive kinetic coefficient, V is a potential function representing the free energy difference between the order–parameter values in the homogeneous state η and the state of minimal free energy η_e, and ν is a diffusion coefficient. Equation 2-59 describes the evolution of the field η for any initial condition of η and this kind of equation is known as a reaction–diffusion equation [Turing, 1952]. Suppose the potential function V have two minima; in this case there would be two equilibrium values of η (bi-stability). The coarsening process is characterized by dynamical scaling of the structures and a power–law property for the correlation length[31] [Craig & Mack, 2013].

[31] For conserved field η the length scale increases proportional to the cubic root of the time scale, i.e. $L \propto t^{1/3}$,

In Craig & Mack's model [2013], the moisture budget is taken over the oceanic tropospheric region in radiative–convective equilibrium[32] (RCE) where convection is driven by radiative cooling over a sea with horizontally uniform temperature. The rate of cooling $\dot{\theta}_R$ is considered constant in time and therefore the spatial–average precipitation rate $\langle P \rangle$ resulting from a radiative balance is also constant and estimated as:

$$\langle P \rangle = \frac{c_p}{L_v} \int_{z_{SCL}}^{z_T} \dot{\theta}_R \left(\frac{p}{p_0} \right)^k \rho_v \, dz \tag{2-60}$$

where c_p is the heat capacity fo air at constant pressure, L_v is the latent heat of condensation, ρ_v is the water vapor density, $k = R/c_p$ is the adiabatic constant, R is the gas constant for dry air, and p_0 is a reference pressure. Equation 2-60 is integrated from the top of the subcloud layer[33] z_{SCL} to the top of the tropopause z_T. This formulation has not considered the effect of other surface fluxes and the horizontal transport of moisture in the subcloud layer. On the other hand, the vertically integrated moisture I_v at the free troposphere is computed as:

$$I_v(\mathbf{x}, t) = \int_{z_{SCL}}^{z_T} \rho_v(\mathbf{x}, t) \, dz \tag{2-61}$$

where $\rho_v(\mathbf{x}, t)$ is the water vapor density at the planar location $\mathbf{x}$ and time t. Tropospheric budget of I_v is then evaluated as follows:

$$\partial_t \, I_v(\mathbf{x}, t) = S(\mathbf{x}, t) + C(\mathbf{x}, t) + T(\mathbf{x}, t) \tag{2-62}$$

where $S(\mathbf{x}, t)$ represents the subsidence drying, $C(\mathbf{x}, t)$ the convective moistening and $T(\mathbf{x}, t)$ the horizontal transport of humidity at the horizontal location $\mathbf{x}$ and time t. If by the effect of subsidence the water vapor density ρ_v changes between the cloud base and the top of the tropopause, then:

$$\partial_t \rho_v = -w \, \partial_z \rho_v \tag{2-63}$$

where w is a subsidence velocity associated to a radiative cooling velocity and it is constant between the cloud base and the top of the tropopause. Assuming a vertical exponential distribution of the water vapor:

$$\rho_v \approx \rho_0 \, e^{-\frac{z}{H_v}} \tag{2-64}$$

where H_v is a scale height (≈ 2 km). Thus, the rate of change of water vapor density is now:

and for non–conserved field η, the length scale increases proportional to the square root of the time scale, i.e. $L \propto t^{1/2}$ [Bray, 1994].

[32] Radiative–Convective Equilibrium is the equilibrium state of an atmospheric column for which any net loss or gain of radiant energy is balanced by the vertical transport of latent or sensible heat [AMS, 2019a].

[33] The subcloud layer is the portion of the boundary layer extending from the surface to the average altitude of the base of clouds with updrafts originating in the boundary layer [AMS, 2019b].

$$\partial_t \rho_v = -\alpha\, \rho_v \tag{2-65}$$

where $\alpha = w/H_v$. After integrating equation 2-65, the subsidence rate S is computed as:

$$S(\mathbf{x}, t) = \int_{z_{SCL}}^{z_T} -\alpha\, \rho_v\, dz = -\alpha\, I_v \tag{2-66}$$

The moisture transported up from the subcloud layer is related to precipitation through the precipitation efficiency ϵ, as follows:

$$\epsilon = \frac{P}{P + C} \tag{2-67}$$

where C represents the moistening rate and P represents the precipitation rate. Following the empirical evidence that shows precipitation rate P increases as tropospheric moisture I_v increases [Neelin et al., 2009, Peters & Neelin, 2009, 2006, Bretherton et al., 2004], precipitation is approximated by Craig & Mack [2013] as:

$$P(\mathbf{x}, t) = a(t)\, \left[\exp\left(b\, \frac{I_v(\mathbf{x}, t)}{I_v^*}\right) - 1\right] = a(t)\, \phi(\mathbf{x}, t) \tag{2-68}$$

where b is a scaling exponent, I_v^* is the saturation integrated water vapor, $\phi(I_v) = \exp(b\, \frac{I_v}{I_v^*}) - 1$ and $a(t)$ is step-time constrain representing the relation between the spatial averages of variables P and $\phi(I_v)$ and it can be computed as:

$$a(t) = \frac{\langle P(\mathbf{x}, t) \rangle}{\langle \phi\, I_v(\mathbf{x}, t) \rangle} \tag{2-69}$$

Taking into account the last expressions, the moistening rate C is computed as:

$$C(\mathbf{x}, t) = \left(\frac{1 - \epsilon}{\epsilon}\right)\, P(\mathbf{x}, t) \tag{2-70}$$

where the precipitation efficiency is considered as a direct function of moisture I_v, furthermore, Craig & Mack [2013] adopted an efficiency expressed in terms of the relationship $\epsilon = \beta(I_v/I_v^*)$. Finally, the process denominated horizontal transport of moisture is represented through a down–gradient diffusive flux as follows:

$$T(\mathbf{x}, t) = \nu\, \Delta I_v(\mathbf{x}, t) \tag{2-71}$$

where ν is the eddy diffusivity which is derived as the product of the typical horizontal velocity $v_0 \approx 10$ m s^{-1} and the length scale associated to convective motion $L \approx 10$ km, so $\nu \approx 10^5$ m^2 s^{-1}. Summing up, the tropospheric budget of moisture I_v is then:

$$\partial_t I_v(\mathbf{x}, t) = -\alpha\, I_v + \left(\frac{1 - \epsilon}{\epsilon}\right)\, a(t)\, \phi(I_v(\mathbf{x}, t)) + \nu\, \Delta I_v(\mathbf{x}, t) \tag{2-72}$$

where the potential term V_n for Craig & Mack's reaction–diffusion equation [2013] is:

$$V(I_v) = \int_0^{I_v} \alpha\, I_v - \left(\frac{1-\epsilon}{\epsilon}\right) a(t)\, \phi(I_v)\, dI_v \tag{2-73}$$

The aforementioned model for representing the tropospheric moisture budget is alike to Allen–Cahn equation (Eq. 2-59), therefore, the model could also be expressed as:

$$\partial_t I_v = -\xi\, \partial_{I_v} V(I_v) - \nu\, \Delta I_v \tag{2-74}$$

where $\xi = 1$ would be a kinetic coefficient for the tropospheric moisture budget. In Figure 2-7 is shown an example of a simulation with the Craig & Mack's model [2013]. In this simulation, the moisture distribution is initialized by a spatially uncorrelated noise. During the time evolution, strong spatial gradients in the moisture field are rapidly removed by diffusion (*diffusive stage*) and the emergence of large–scale structures characterizes the moisture field evolution. After 5 d of simulations a further growth of the structures can be seen and the range of moisture values has broadened in the whole domain (*coarsening stage*) and after 27 d the spatial distribution of the moisture field $I_v(\mathbf{x}, t)$ exhibits a concentration of the moisture at an specific region of the spatial domain (*droplet stage*).

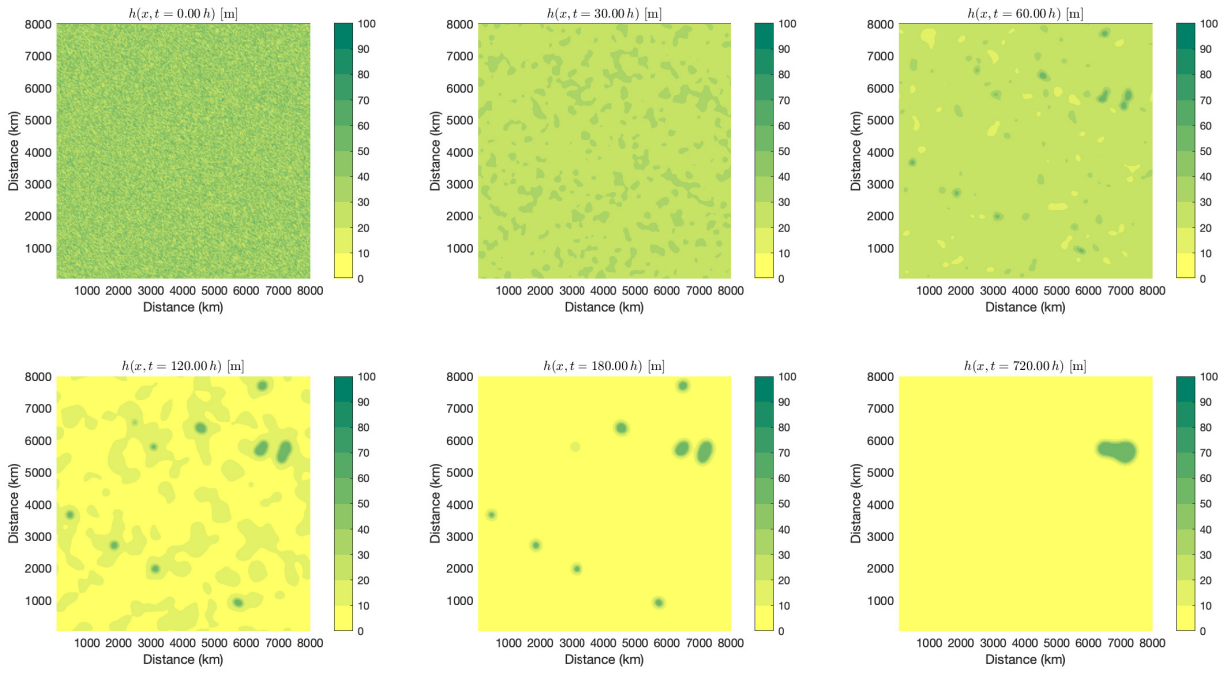

Figure 2-7: Example of simulated rainfall fields with the Craig & Mack's model (2013). In every panel is shown the moisture field $I_v(\mathbf{x}, t)$ (in kg m^{-2}) for the times t indicated on top of each panel. The model parameters are: $\Delta t = 1$ h, $\Delta x = 40$ km, $P_{av} = 8$ kg m^{-2} d^{-1}, and $\alpha = 5 \times 10^{-6}$ s^{-1}, $I_v^* = 57$ kg m^{-2} and the time lapse for the simulation was 50 d.

The model results shows a *self–organization mechanism* for the moisture field (and the precipitation field). In Figure 2-8 is exhibited three plots of the time evolution of the moisture content frequency for three different values of the saturation integrated water vapor I_v^*. Each simulation the moisture content of large–structures converges to a value approximated equal to I_v^*.

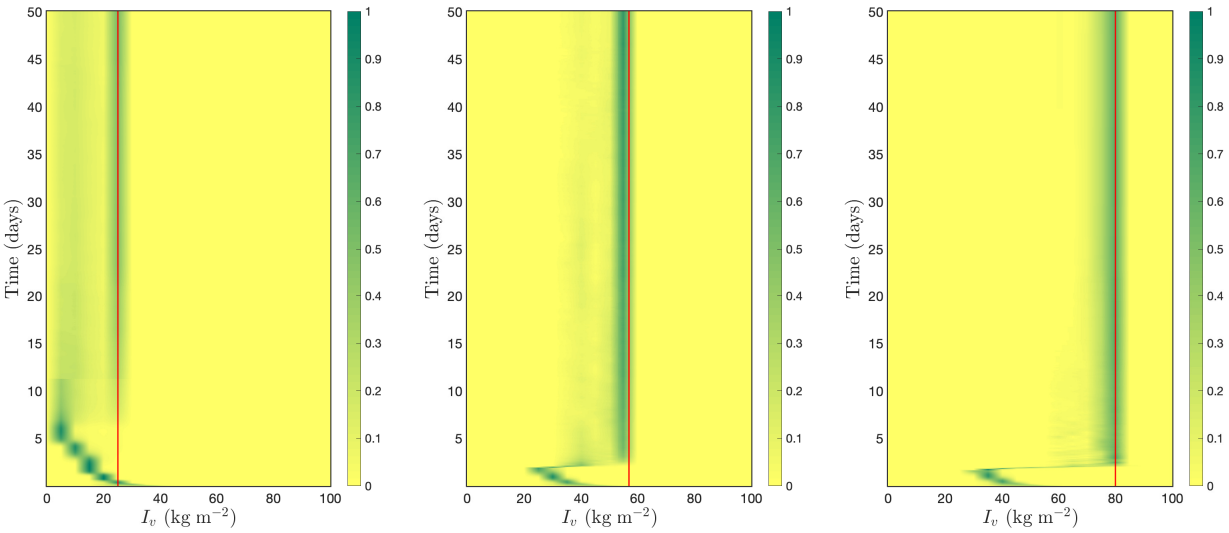

Figure 2-8: Time evolution of the larger–structure moisture content frequency for three simulations of the Craig & Mack's model (2013) with saturation integrated water vapor I_v^* equal to 25 kg m^{-2} (left panel), 57 kg m^{-2} (central panel) and 80 kg m^{-2} (right panel). For all simulations, the model parameters were: $\Delta t = 1$ h, $\Delta x = 40$ km, $P_{av} = 8$ (kg m^{-2} d^{-1}), and $\alpha = 5 \times 10^{-6}$ s^{-1}, and a time lapse of 50 d. The color bar shows the intensity of the relative frequency of I_v which is more intense at the end of every simulation.

Another remarkable aspect to highlight about the model outputs is that during the coarsening process exhibits a dynamic scaling i.e. the spatial scale of structures grows according to a power law such as $L \sim t^{1/2}$. All the aspects indicated above resemble some properties of rainfall and they suggest that Craig & Mack's model (2013) could be give an insight about the physics of rainfall multifractality and a conceptual evidence about a SOC process. In the same direction of the last discussed model, Hottovy & Stechmann [2015] proposed a model for the description of water vapor dynamic over tropical regions. This model is expressed as follows:

$$\partial_t q(\mathbf{x}, t) = \left[-\frac{1}{\tau}(q(\mathbf{x}, t) - q*) + F(\mathbf{x}, t) \right] + b_0 \, \Delta q(\mathbf{x}, t) + D_* \dot{W}(\mathbf{x}, t) \tag{2-75}$$

where $q(\mathbf{x}, t)$ is the integrated column water vapor (mm) at horizontal location $\mathbf{x}$ and time t, τ is a relaxation time, q^* is a threshold water vapor content to switch to convection, $F(\mathbf{x}, t)$ is a external force, b_0 is a diffusion coefficient, D_* is a stochastic forcing variance, and $\dot{W}(\mathbf{x}, t)$

is an independent white noise random variable. In Hottovy & Stechmann's model [2015], the water vapor mass concentration evolves according to the following expression:

$$\partial_t q + \big[(\bar{u}\bar{q})_x + (\bar{v}\bar{q})_y\big] + \big[(u'q')_x + (v'q')_y\big] = \bar{S} \tag{2-76}$$

where $\bar{u}$ and $\bar{v}$ are the large scale components of the velocity vector $\mathbf{u}$, u' and v' are the small scale components of the velocity vector $\mathbf{u}$, $\bar{q}$ represents a vertical average of the integrated column water vapor q, q' represents the small scale component of q, and $\bar{S}$ represents a source or sink of water vapor. In Hottovy & Stechmann's model [2015], the small scale flux convergence is modeled as an eddy diffusion process:

$$-\big[(u'q')_x + (v'q')_y\big] = b_0\,\Delta q(\mathbf{x}, t), \tag{2-77}$$

The non–linear turbulent effect is modeled as a turbulent damping and a stochastic forcing:

$$-\big[(\bar{u}\bar{q})_x + (\bar{v}\bar{q})_y\big] = -\frac{1}{\tau}\big[q(\mathbf{x}, t) - q_*\big] + D_*\dot{W}(\mathbf{x}, t) \tag{2-78}$$

and the effect of precipitation or evaporation $\bar{S}$ is modeled through a deterministic forcing F. Cloudiness, in Hottovy & Stechmann's model (2015), is represented through a Heaviside function as follows:

$$\sigma(\mathbf{x}, t) = \Theta(q - q_*) \tag{2-79}$$

Here, $\sigma(\mathbf{x}, t)$ is a cloud indicator function equal to one if strong convection is developed $q(\mathbf{x}, t) > q_*$. In this model the rainfall rate is a function of the integrated column water vapor content, therefore, the precipitation rate $r(\mathbf{x}, t)$ can be computed as:

$$r(\mathbf{x}, t) = f\big(\,[q(\mathbf{x}, t) - q_*]\;\sigma(\mathbf{x}, t)\big) \tag{2-80}$$

In figures 2-9 and 2-10 are shown the outputs of a run with Hottovy & Stechmann's model [2015]. Every row of the figure is conformed by three panels. The left one is representing the integrated–column water vapor ($q(\mathbf{x}, t) \equiv IWV(\mathbf{x}, t)$), the central panel shows the cloudiness field $\sigma(\mathbf{x}, t)$, and the right one shows the rainfall field $r(\mathbf{x}, t)$. Figures 2-9 and 2-10 show three snapshots of the variables indicated above for the times 0 d, 14 d and 28 d. Figure 2-10 is zooming a region of the fields shown at Figure 2-9 in order to show more details about the spatial patterns. Clearly, these plots exhibit high complexity and resembles to real ones; moreover, a dynamic coarsening process is depicted in these figures. The spatial scale selected for the numerical simulation was 5000 km × 5000 km in order to create a scenery approximately alike to that found in satellite observations. The spatial evolution of the integrated column water vapor field $q(\mathbf{x}, t)$ starts as a random field with a spatial average equal to 50 mm h^{-1} to get a spatial average equal to 65 mm h^{-1}, whose value is the threshold for the beginning of strong convection according to the model phenomenology. According to these results the spatial mean of simulations is defined as $\mathrm{E}[q(\mathbf{x}, t] \equiv \langle q(\mathbf{x}, t)\rangle = q_*$.

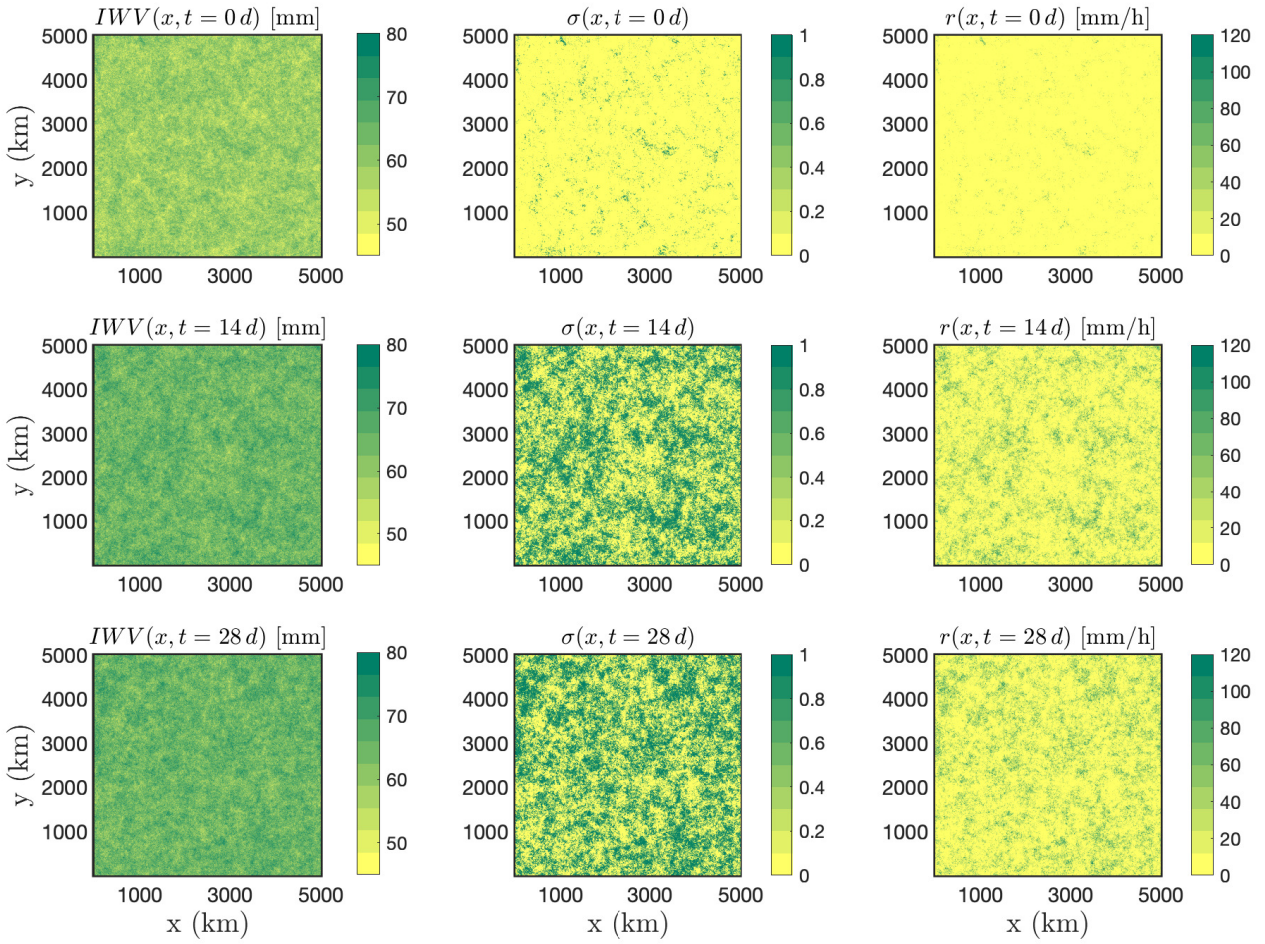

Figure 2-9: Example of simulated rainfall fields with the Hottovy & Stechmann's model [2015]. Each row has three panel indicating three outputs of the model. The first panel shows the integrated column water vapor $IWV(\mathbf{x}, t)$, the second one the cloudiness $\sigma(\mathbf{x}, t)$ and the third one the rainfall rate field $r(\mathbf{x}, t)$. For getting this results, the model parameters were the followings: $\Delta t = 0.01$ h, $\Delta x = 5$ km, $\tau = 96$ h^{-1}, and $q_* = 65$ mm, $b_0 = 750$ km^2 h^{-1}, $D_* = 0.15$ mm h^{-1} and the time lapse for the simulation was 28 d.

The results shown by Hottovy & Stechmann's model [2015], set up that there is either a phase transition or a self-organized criticality process to describe rainfall evolution. Their results shows a fast grow of the mean precipitation as the critical integrated-column water vapor is reached (i.e. $q^* = 65$ mm). This last was also observed by Peter & Neelin's research [2006].

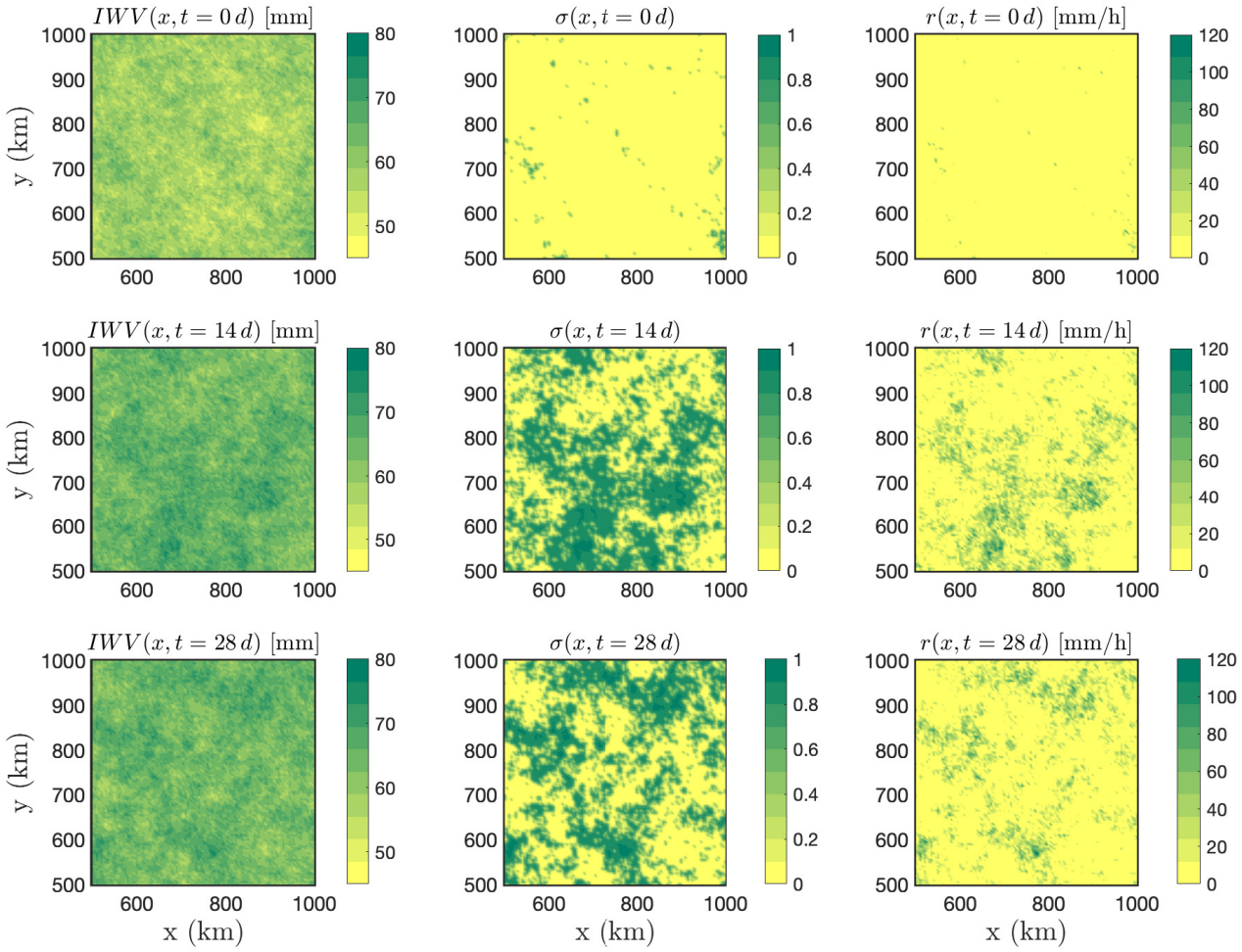

Figure 2-10: Example of simulated rainfall fields with the Hottovy & Stechmann's model [2015]. Each row has three panel indicating three outputs of the model. The first panel shows the integrated column water vapor $IWV(\mathbf{x}, t)$, the second one the cloudiness $\sigma(\mathbf{x}, t)$ and the third one the rainfall field $r(\mathbf{x}, t)$. All plots represents a spatial fraction of the simulated fields shown at figure 2-9, therefore every panel show a horizontal distance of 500 km in each orthogonal direction. For getting this results, the model parameters were the followings: $\Delta t = 0.01$ h, $\Delta x = 5$ km, $\tau = 96$ h^{-1}, and $q_* = 65$ mm, $b_0 = 750$ km^2 h^{-1}, $D_* = 0.15$ mm h^{-1} and the time lapse for the simulation was 28 d.

Among the variety of characteristics of Hottovy & Stechmann's model [2015], the existence of SOC process for representing convection is highlighted. On the other hand, the model's thermodynamic is limited to the analysis of the variable $q(\mathbf{x}, t)$ which neglects the effect of a vertical structure in the atmosphere. Moreover, either rainfall or evaporation are represented by the model through a linear function of $q(\mathbf{x}, t)$ and τ. Despite the model simplifications, it is able to represent a phase transition and a self–organization mechanism which are evidenced in observations [Peters & Neelin, 2006, Neelin et al., 2009].

Cloud–Resolving Models

Among the variety of known models for the meteorological analysis, those so–called Cloud–Resolving models (CRMs) have acquired a well acknowledged for their capacities to describe surface rainfall processes [Guichard & Couvreux, 2017, Muller, 2013, Muller & Held, 2012, Li & Gao, 2012]. These kind of models are designed with a fine horizontal resolution grid to simulate individual clouds, radiative processes, cloud microphysics and so on. Although CRMs are not categorized as parsimonious models, some brief details are consigned in this document about them and focused to the research context.

The origins of CRMs came from the work developed by Soong & Ogura [1980], Soong & Tao [1980] and Sui et al. [1994] who wanted to study tropical convection at time scales less than a day. As an example of a typical set of equations in CRMs is shown as follows:

1. The potential temperature θ is expressed as:

$$\frac{\theta}{T} = \left(\frac{p_0}{p}\right)^k \tag{2-81}$$

   where T is the air temperature, p is the atmospheric pressure, p_0 is a reference pressure, $k = R_d/c_p$ is the adiabatic constant, R_d is the universal gas constant for the dry air and c_p is the the specific heat coefficient. If the potential temperature of a mass of air is constant, the mass is subject to an adiabatic change, and the converse is also true [Wallace & Hobbs, 2006].

2. The continuity equation is represented as:

$$\rho_r \frac{\partial \bar{u}_j}{\partial x_j} + \bar{w}\frac{\rho_r}{\partial z} = 0 \tag{2-82}$$

   where ρ_r is the water vapor density under an anelastic assumption and $\bar{u}_j$ are the average components of the velocity vector.

3. The dynamic equation is represented as:

$$\frac{\partial \bar{u}_i}{\partial t} = -\frac{1}{\rho_r}\frac{\partial\left(\rho_r \overline{u_i\, u_j}\right)}{\partial x_j} - \frac{1}{\rho_r}\frac{\partial p}{\partial x_i} + \frac{g}{\theta_r}\left(\overline{\theta_{vl}} - \theta_r\right)\,\delta_{i,3} - \frac{1}{\rho_r}\frac{\partial\left(\rho_r \overline{u_i'\, u_j'}\right)}{\partial x_j} - 2\epsilon_{i,j,k}\Omega_j \overline{u_k} \tag{2-83}$$

   where θ_{vl} is the virtual potential temperature and $\overline{u_i'\, u_j'}$ is the turbulence flux of u_j'.

4. The thermodynamic equation is represented as:

$$\frac{\partial \bar{\theta}}{\partial t} = -\frac{1}{\rho_r}\frac{\partial\left(\rho_r \overline{u_j\, \theta}\right)}{\partial x_j} - \frac{1}{\rho_r}\frac{\partial\left(\rho_r \overline{u_j'\, \theta'}\right)}{\partial x_j} + Q_{rad} + Q_{m\Phi} \tag{2-84}$$

   where Q_{md} is the radiative heating rate and $Q_{m\Phi}$ is the heating rate associated to mycrophysical processes (i.e. condensation, evaporation, precipitation, freezing, etc.).

5. The prognostic equation for water vapor is represented as:

$$\frac{\partial \bar{r_x}}{\partial t} = -\frac{1}{\rho_r}\frac{\partial\left(\rho_r \overline{u_j\, r_x}\right)}{\partial x_j} - \frac{1}{\rho_r}\frac{\partial\left(\rho_r \overline{u'_j\, r''_x}\right)}{\partial x_j} + S_x \tag{2-85}$$

where r_x is the mixing ratio of each hydrometeor specie x (e.g. liquid droplets, rain drops, ice, or snow) and S_x is the sum of the microphysical processes affecting r_x.

For the solution of this set of equations, finite difference or spectral methods are usually employed. The typical size of the grid for simulations is defined between 50 to 100 meters either in the horizontal or the vertical direction. Although CRMs possess more physical considerations for representing atmospheric processes, the large number of parametrization and idealized settings for modeling could be a problem for practitioners and even for scientists. All CRMs made some asumptions about the thermodynamics and nowadays the CRMs are tested to verify the likelihood of such assumptions.

In the literature is reported that CRMs have been employed for understanding the space–time variability in different scales and to associate the scaling parameters to the atmospheric thermodynamic. For instance, Parodi et al. [2011] studied some aspects of the moist–convection micro–physics in order to obtain a physical meaning of the rainfall statistics. Parodi et al. [2011] employed the Weather Research and Forecasting (WRF) model for developing high–resolution simulations of an atmosphere under radiative–convective equilibrium. The model was run on a domain size of 200 km representing an horizontally homogeneous ocean. The horizontal spatial resolution is 2 km and the vertical resolution is 100 m near the bottom and 500 m near the top boundary. Among the thermodynamics assumptions, the run was executed considering a constant radiative cooling rate Q_{rad} equal to -4 K d^{-1} and the initial ocean temperature T_s is constants over the whole domain whose value equal to 300.15 K.

Among the results obtained by Parodi & Emanuel [2009], the drop size distribution (DSD), the terminal velocity and some statistics of the rainfall field are related. Having into account that small terminal velocity values are representing small and light raindrops, and large terminal velocity values are representing large and heavy raindrops, the terminal velocity determines the drop size distribution (DSD). Parodi et al. [2011] found a power–law scaling relationship between the mean cell size $\langle A_c \rangle$ and the raindrop terminal velocity V_T, such as:

$$\langle A_c \rangle = k\, V_T^{\gamma} \tag{2-86}$$

where,

$$k = 130, \quad \gamma = -0.71, \quad \text{for } 1 < V_T \leq 5\,\text{m s}^{-1} \tag{2-87}$$

$$k = 69, \quad \gamma = -0.32, \quad \text{for } 5 < V_T \leq 15\,\text{m s}^{-1} \tag{2-88}$$

On the other hand, when the terminal velocity is large, the convective cells are isolated and smaller in size, but when terminal velocity is small, the rainfall field exhibits an uniform

spatial pattern. Under a spectral analysis, the spectral slopes of 3 h and 24 h accumulated rainfall fields are approximately to -1 for raindrop velocity larger than 5 m s^{-1} and approximately to -3 for raindrop velocity smaller than 5 m s^{-1}. The former suggests there exists a power law scaling regime depending on the terminal raindrop velocity.

Parodi et al. [2011] also studied the dependence of the scaling exponent H and the raindrop terminal velocity, in the same way as Perica & Foufoula-Georgiou [1996] studied the relationship between H and the convective available potential energy (CAPE). They found a strong dependence ($R^2 \approx 0.9$) between H and V_T for the accumulated rainfall fields of durations 6, 12, and 24 hours and a weaker dependence ($0.2 \lesssim R^2 \lesssim 0.5$) for 3 h accumulated rainfall fields. These results identify the raindrop terminal velocity V_T as a variable explaining the statistical structure of rainfall.

Others important works related to applications of CRMs for understanding how rainfall patterns are formed and how they are connected to atmospheric conditions, have been developed by Wing & Emanuel [2014], Muller & Held [2012], Khairoutdinov & Emanuel [2010], and Bretherton et al. [2005]. These researches show a mode of spatial organization of oceanic tropical convection which is referred as *self–aggregation*[34] can be simulated via CRMs. Under a self–aggregation state, the atmospheric conditions are described by convectively active moist regions surrounded by a dry region with strong radiative cooling. These researches also suggest the atmosphere could have two equilibrium states. A first equilibrium state where there exists a random distribution of convective areas, and a second one where convection is aggregated in a specific region of the space domain [Khairoutdinov & Emanuel, 2010]. It is unclear which atmospheric conditions and feedbacks lead to the instability of the radiative–convective equilibrium and the resulting development of self-aggregation. Khairoutdinov and Emanuel's simulations [2010] show a phase transition between the two equilibrium states depending on the sea surface temperature (SST); for higher values of SST, the aggregated state is triggered.

The CRM model used by Bretherton et al. [2005], Khairoutdinov & Emanuel [2010], Muller & Held [2012] and Wing & Emanuel [2014] is denominated as System for Atmospheric Modeling (SAM). This CRM was developed by Khairoutdinov & Randall [2003] and it solves the anelastic continuity, momentum, and tracer conservation equations. The prognostic variables of SAM are liquid/ice water static energy, total precipitating and non-precipitating water. In Muller and Held's simulations [2012], two different domains were studied (198 km and 510 km) and for the smaller one, the radiative–convective equilibrium was reached in about 30 d and the spatial pattern exhibits a random distribution of convective areas. For the larger domain, i.e. 510 km, self-aggregation is reached in a term of a few days and such a simulation shows a state of disorganized radiative–convective equilibrium. The aforementioned arguments indicate that self-aggregation depends on the domain size.

In the model, the frozen moist static energy (MSE) is conserved during moist adiabatic

[34]Self-aggregation is the process observed in the tropical convection in which convective structures are spontaneously aggregated into one single region [Muller & Held, 2012].

processes, i.e.

$$\text{MSE} \equiv c_p\, T + g\, z + L_v\, q_v - L_f\, q_i = C \tag{2-89}$$

where c_p is the isobaric specific heat of dry air, T is the temperature, g is the gravitational acceleration, z is the height, L_v is the latent heat of evaporation, q_v is the water vapor mixing ratio, L_f is the latent heat of freezing, and q_i is the mixing ratio of all ice phase condensates. The vertically integrated moist static energy budget is defined as:

$$\frac{\partial}{\partial t}\text{MSE} = \text{LHF} + \text{SHF} + \Delta Q_{rad} + C_{\text{MSE}} \tag{2-90}$$

where LHF is the latent heat fluxes at the surface, SHF is the sensible heat fluxes at the surface, ΔQ_{rad} is the radiative cooling lost by the atmospheric column at the top of the atmosphere and at the surface, and C_{MSE} is the vertically integrated horizontal convergence of MSE. In the simulations made by Muller & Held [2012] over the smaller spatial domain, there is a down-gradient horizontal transport of MSE, i.e. there is a flux from high-energy columns to low-energy columns. Conversely, simulations developed over the larger spatial domain (where self-aggregation emerges), there is a up-gradient horizontal transport of MSE, i.e. there is flux of energy from low-energy columns to high-energy columns.

In order to understand which feedback could be responsible of self-aggregation some physical interactions were turned off. The interaction between convection and surface fluxes was turned off homogenizing the horizontal surface fluxes in every time step of the model. Similarly, the interaction between convection and the radiative cooling was turned off homogenizing the horizontal longwave (or shortwave) radiative cooling in every time step of the model. The process of homogenize the surface fluxes or the shortwave radiative cooling do not prevent the development of self-aggregation, but to homogenize the longwave radiative cooling did prevent self-aggregation regarless the domain size or resolution. Therefore, longwave interactions are responsible for self-aggregation.

Muller & Held [2012] suggest the mechanism for self-aggregation is due to the presence of low clouds in the dry regions which produce longwave cooling near their top and induce the horizontal flux of low-energy air from dry regions to high-energy moist regions, i.e. low-level radiative cooling in dry regions produces a secondary circulation that is responsible for the up-gradient transport of MSE. The relevance of understanding the convective self-aggregation is due to its association with the physical mechanism of rainfall multifractality. Both processes could be coupled and they represent an explanation of the space–time rainfall organization. The author reiterates that CRMs applications are not in the focus of this research, however the physical bases of these model can give some clues for identifying a simplified explanation of the nature of rainfall multifractality.

3. Evidence of Rainfall Multifractality

In this chapter is reported some empirical evidence of rainfall multifractality for some selected data sets. Some mathematical techniques were chosen, adapted and applied to identify statistical properties evoking multifractality in rainfall patterns. As an extension of the empirical evidence, some data sets that correspond to model outputs were also studied in order to identify any concurrence between multifractal properties of model outputs and the physical basis of selected models.

3.1. Methods for Data Analysis

In this document is reported the study of five methods for analyzing the statistical structure of rainfall fields. These methods were chosen from the scientific literature and they were adapted to the data type and the purposes of this research. The first selected method is denominated "multifractal spectrum via moment method" which has been widely applied for describing multifractal processes through the estimation of the function $f(\alpha)$ [Bacry et al., 1993, Feder, 1988]. The next two studied methods are denominated "cumulant–based magnitude coefficients" and "two–point correlation functions". They were suggested by Roux et al. [2009] for identifying scaling properties and measures of non–linearity in rainfall time series. For this research these methods were adapted for the analysis of 2D rainfall fields and they are part of the main contribution of this research. The fourth method is a new approach denominated "incremental similarity" which was introduced by Barndorff–Nielsen et al. [2015, 2004] to analyzed intermittent patterns such as those identified turbulence processes. The fifth method is an application of the methodology suggested by Marzan et al. [1996] for the estimation of dynamic scaling exponents. In the following section is summarized the description of these methodologies, some of their limitations and goals according to this research.

3.1.1. Multifractal Spectrum Via Method of Moments

The multifractal spectra is a tool for analyzing multifractal measures through the Hölder exponent spectrum $f(\alpha)$ (also called singularity spectrum) [Bacry et al., 1993, Feder, 1988]. In this method, the mass on rainfall records is defined as $\mu_i = R_i / \sum_{i=1}^{N} R_i$, where the subindex represents the i-th cell of a rainfall record, and the measure is then defined as:

$$M_d(q,\delta) = \sum_{i=1}^{N} \mu_i^q \, \delta^d = N(q,\delta)\, \delta^d \xrightarrow[\delta \to 0]{} \begin{cases} 0, & d > \tau(q) \\ \infty, & d < \tau(q) \end{cases} \tag{3-1}$$

where N is the number of observations in the rainfall record, q is the order of the moment, δ is the observation scale, $N(q,\delta)$ is a partition function defined by the statistical moments of order q, and $d = \tau(q)$ is the q-dependent mass exponent for which the measure neither vanished nor diverge as $\delta \to 0$. In equation 3-1, the partition functions $N(q,\delta)$ is defined as follows:

$$N(q,\delta) = \sum_{i=1}^{N} \mu_i^q \sim \delta^{-\tau(q)} \tag{3-2}$$

From this partition function, the sequence of mass exponents $\tau(q)$, can be computed as:

$$\tau(q) = -\lim_{\delta \to 0} \frac{\ln N(q,\delta)}{\ln \delta} \tag{3-3}$$

As one can evidence, equation 3-2 and 3-3 show that mass exponents $\tau(q)$ have a direct relationship with the statistical moments of observations and the shape of the function $\tau(q)$ allows to identify the existence of multifractal structures. On the other hand, singular measures are characterized by singularity exponents[1] α, which are defined as follows:

$$\alpha = \lim_{\delta \to 0} \frac{\ln \mu(\delta)}{\ln \delta} \tag{3-4}$$

If the mass exponent $\tau(q)$ and the singularity exponent α are known, the multifractal spectrum $f(\alpha)$ can be computed through a Legendre's transform, such as:

$$\alpha(q) = -\frac{d}{dq}\tau(q) \tag{3-5}$$

$$f(\alpha(q)) = q\,\alpha(q) + \tau(q) \tag{3-6}$$

where $f(\alpha)$ represents the fractal dimension of every singularity exponent α. Statistically, the number of occurrences of a particular value of α defines the multifractal (or singularity) spectrum $f(\alpha)$. The multifractal spectra have many properties, some of them were studied in this research to characterized the rainfall field. One of the main properties is the fractal dimension of the support D_0 which is defined as the maximum value of the function $f(\alpha)$, i.e. $\max\{f(\alpha)\} = D_0$ [Feder, 1988] and it provides information about the frequency of rainfall events [Peñaranda, 2008]. D_0 could be equal to the embedding (Euclidean) dimension D if the measure is defined over an Euclidean space, i.e. for 2D rainfall fields the possible maximum dimension is $f(\alpha) = 2$ and for rainfall time series, $f(\alpha) = 1$. Another important property of $f(\alpha)$ is given in the point where a line defined as $f(\alpha) = \alpha$ is tangent to the multifractal spectrum $f(\alpha)$, i.e. $df(\alpha)/d\alpha = 1$. The fractal dimension of the singularity defined where the former condition is satisfied, is known as information dimension or dimension where the measure is concentrated and such a dimension is represented as $f(\alpha) = D_1$ [Feder, 1988, Mandelbrot, 1982].

[1] Also known as Lipschitz–Hölder exponents [Feder, 1988, Mandelbrot, 1982].

3.1.2. Cumulant–Based Magnitude Coefficients

For every rainfall observations R exists a probability density function $\mathcal{P}(R)$, a characteristic function $\hat{\mathcal{P}}(k)$, a cumulant generating function c_q and a n-th order moment m_q. The moments m_q of the probability density function $\mathcal{P}(R)$ can be computed through successive derivatives of the characteristic function at $k = 0$, such as:

$$m_q = (-1)^q \frac{d^q}{dk^q} \hat{\mathcal{P}}(k) \tag{3-7}$$

The cumulant generating function c_q of rainfall observations R can be computed through successive derivatives of the logarithm of the characteristic function at $k = 0$, such as:

$$c_q = (-1)^q \frac{d^q}{dk^q} \ln \hat{\mathcal{P}}(k) \Big|_{k=0} \tag{3-8}$$

Thus, a cumulant c_q is a combination of moments m_p of order $p \leq q$. For instance, the first 5 cumulants are estimated as follows:

$$\begin{aligned}
c_1 &= m_1 \\
c_2 &= m_2 - m_1^2 \\
c_3 &= m_3 - 3m_2m_1 + 2m_1^3 \\
c_4 &= m_4 - 4m_3m_1 - 3m_2^2 + 12m_2m_1^2 - 6m_1^4 \\
c_5 &= m_5 - 5m_4m_1 - 10m_3m_2 + 20m_3m_1^2 + 30m_2^2m_1 + 60m_2m_1^3 + 24m_1^5
\end{aligned} \tag{3-9}$$

The partition function $N(q, \delta)$ that was introduced at equation 3-2, is related to the cumulant expansion c_q through the following expression [Roux et al., 2009, Delour et al., 2001]:

$$-\ln N(q, \delta) = \tau(q) \ln(\delta) \sim -D_0 \ln(\delta) + \sum_{n=1}^{\infty} c_n(\delta) \frac{q^n}{n!} \tag{3-10}$$

or equivalently,

$$\tau(q) \sim -D_0 \frac{q^0}{0!} + \sum_{n=1}^{\infty} \frac{c_n(\delta)}{\ln(\delta)} \frac{q^n}{n!} \tag{3-11}$$

$$= -D_0 + \sum_{n=1}^{\infty} C_n(\delta) \frac{q^n}{n!} \tag{3-12}$$

$$= -C_0 + C_1 q - C_2 \frac{q^2}{2} + C_3 \frac{q^3}{3!} + \cdots \tag{3-13}$$

where $C_0 \equiv D_0$ is the fractal dimension of the support, c_n are cumulants of $\mu_i(\delta)$, and the coefficients C_n are cumulant–based magnitude coefficients which are estimated by means of a linear–log regression between $c_n(\delta)$ vs $\ln(\delta)$ for $n = 1, 2, 3, \ldots$. After finding the cumulant–based magnitude coefficients, the function $\tau(q)$ can be computed with equation 3-11. If there exists a non–linear behavior of the function $\tau(q)$, there could be a multifractal description in the statistical structure of the studied pattern.

3.1.3. Two-point Correlation Functions

The two-point correlation is a statistical technique designed for identifying dependence among scales of the studied process and it was originally proved in the study of cascade processes [Arneodo et al., 1998]. The two-point correlation function $C(\delta, \Delta x)$ of rainfall records R_i is assessed through the following expression [Roux et al., 2009]:

$$C(\delta, \Delta x) = \langle (\ln R(x) - \langle R(x) \rangle)((\ln R(x + \Delta x) - \langle R(x) \rangle)) \rangle \tag{3-14}$$

where δ represents the scale of data and $\Delta x > \delta$ is the time (or space) lag. Equation 3-14 provides information about the time–scale (or space–scale) structure of the multifractal process. A linear behavior of $C(\delta, \Delta x)$ vs $\ln \Delta x$ is characteristic of scale–invariant cascades for which the random weights are uncorrelated. Conversely, a non–linear behavior of $C(\delta, \Delta x)$ vs $\ln \Delta x$ is characteristic of a broken scale-invariant cascades where their weights are not identically distributed and have an explicit scale dependence. Furthermore, there could be a power–law decrease of the correlation function.

Summing up, if $C(\delta, \Delta x)$ decreases to zero rapidly, such a result indicates the non–existence of a long–range correlation and possibly there is not a multifractal description of the studied pattern. On the other hand, if $C(\delta, \Delta x)$ is logarithmic in Δx and independent of scale δ, then it suggests a long–range dependence and possibly there exists an evidence of multifractality.

3.1.4. Incremental Similarity

The incremental similarity (IS) was introduced by Barndorff-Nielsen & Schmiegel [2015] as a statistical property of turbulence processes and finance time series. During the study of high–frequency recordings of velocity, Barndorff-Nielsen & Schmiegel [2015] found that the incremental similarity property is preserved for the velocity increments and the normal inverse Gaussian (NIG) distribution describes suitably the statistical distribution of them. There exists a hypothesis that the incremental similarity property may be characteristic of other intermittent and singular data sets such as occur in rainfall time series and therefore incremental similarity will be considered as a property of multifractal patterns.

In order to define what incremental similarity means, let's consider two real-valued random processes X and Y indexed by the positive real number line $\mathbb{R}^+$. Then X will be incrementally similar to Y and denoted by

$$X \overset{\mathbf{IS}}{\preceq} Y \tag{3-15}$$

if for any $t, u \in \mathbb{R}^+$ exist a $s, v \in \mathbb{R}^+$ such that the probability distribution of the increment $\Delta_{s,v}(Y) = Y(s+v) - Y(s)$ is the same as that of the increments $\Delta_{t,u}(X) = X(t+u) - X(t)$:

$$\Delta_{t,u}(Y) \overset{\text{dist}}{=} \Delta_{s,v}(X) \tag{3-16}$$

The symbol $\preceq$ is used in referring to partially ordered sets[2]. On the other hand, it will say that X and Y are (mutually) incrementally similar, if the following condition is satisfied:

$$X \overset{\mathbf{IS}}{=} Y \quad \text{if} \quad X \overset{\mathbf{IS}}{\preceq} Y \ \wedge \ Y \overset{\mathbf{IS}}{\preceq} X. \tag{3-17}$$

As it was previously mentioned, Barndorff-Nielsen et al. [2004] showed the laws of turbulent velocity differences can be fitted by the normal inverse Gaussian (NIG) distribution. Such a distribution is described by four parameters: α, β, μ and δ and is denoted as $\mathrm{NIG}(\alpha, \beta, \mu, \delta)$. This distribution is defined under the following probability density function:

$$p(x; \alpha, \beta, \mu, \delta) = a(\alpha, \beta, \mu, \delta)\, q\left(\frac{x-\mu}{\delta}\right)^{-1} K_1\left\{\delta\, \alpha\, q\left(\frac{x-\mu}{\delta}\right)\right\} = \mathrm{NIG}(\alpha, \beta, \mu, \delta) \tag{3-18}$$

where,

$$q(x) = \sqrt{1+x^2}, \tag{3-19}$$

$$a(\alpha, \beta, \mu, \delta) = \frac{\alpha}{\pi} \exp\left\{\delta\sqrt{\alpha^2-\beta^2}\right\}, \tag{3-20}$$

and K_1 is the modified Bessel function of the third kind of order $\nu = 1$. In the NIG distribution $\mu \in \mathbb{R}$ represents a location parameter, $\delta \in \mathbb{R}_+$ is a scale parameter, β is an asymmetry parameter defined in the range $0 \leq |\beta| \leq \alpha$, and α is a tail-heaviness parameter. Among the attributes of the NIG distribution, it is should be considered that:

- If the sequence $\{X_i\}$ (for $i = 1, \ldots, m$) is described by independent NIG random variables with common parameters $\alpha_i = \alpha$ and $\beta_i = \beta$ but with local parameters δ_i and μ_i (for $i = 1, \ldots, m$); then $x_i = x_+$ (for $i = 1, \ldots, m$) is described by an Inverse Gaussian Law, with parameters α, β, μ_+, δ_+.

- If X is a random variable with distribution $\mathrm{NIG}(\alpha, \beta, \mu, \delta)$ its cumulant generating function $\mathrm{C}(\theta; \alpha, \beta, \mu, \delta) = \log \mathrm{E}[e^{\theta X}]$ is defined as follows:

$$\mathrm{C}(\theta; \alpha, \beta, \mu, \delta) = \delta\left\{\sqrt{\alpha^2-\beta^2} - \sqrt{1-\alpha^2-(\beta+\theta)^2}\right\} + \mu\,\theta \tag{3-21}$$

  where the first four cumulants of the NIG distribution are:

$$\begin{aligned} C_1 &= \mu + \frac{\delta\,\rho}{(1-\rho^2)^{1/2}}, \quad C_2 = \frac{\delta}{\alpha(\sqrt{1-\rho^2})^{3/2}} \\ C_3 &= \frac{3\delta\rho}{\alpha^2(\sqrt{1-\rho^2})^{5/2}}; \quad C_4 = \frac{3\delta(1+4\,\rho^2)}{\alpha^3(\sqrt{1-\rho^2})^{7/2}} \quad \rho = \frac{\beta}{\alpha} \end{aligned} \tag{3-22}$$

[2]In the set theory, If two elements a, $b \in \Omega$ are comparable, then $a \preceq b$ or $b \preceq a$.

- The parameters of the NIG distribution can be estimated considering the first raw moment (mean), the second central moment (variance) and the third and fourth standardized moments (skewness and kurtosis), as follows:

$$\begin{aligned} \text{mean} &= \mu + \frac{\delta\,\beta}{\gamma} \\ \text{variance} &= m_2 = c_2 = \frac{\delta\alpha^2}{\gamma^3} \\ \text{skewness} &= \frac{m_3}{m_2^{3/2}} = \frac{c_3}{c_2^{3/2}} = \frac{3\,\beta}{\alpha\sqrt{\delta\gamma}} \\ \text{kurtosis} &= \frac{m_4}{m_2^2} = \frac{c_4}{c_2^2} = \frac{3\,(\alpha^2 + 4\beta^2)}{\alpha^2\,\delta\,\gamma} \end{aligned} \tag{3-23}$$

  where $\gamma = \sqrt{\alpha^2 - \beta^2}$ and m_i represents a central moment of order i.

Since the NIG distribution is a well statistical descriptor of the velocity increments in a turbulent flow; in this research, the incremental similarity property it will be adopted as an evidence of multifractality if such a property is satisfied. For further details about the theory of incremental similarity is suggested to follow the references: Barndorff-Nielsen & Schmiegel [2015] and Barndorff-Nielsen et al. [2004].

3.1.5. Dynamic Scaling Exponents

Under the phenomenology of turbulent cascades suggested by Marzan et al. [1996], each spatial structures (or eddies) defined over the scale λ has a lifetime t_λ depending on its scale, thus:

$$t_\lambda \sim \lambda^{1-H} \tag{3-24}$$

The time t_λ defines the necessary time for the creation of new structures coming from the scale λ to smallest scale and H is the space–time anisotropy scaling exponent (also known as dynamic scaling exponent). If rainfall exhibits a scaling invariance behavior in the space-time domain, then its spectral density function scales with the angular frequency ω and the angular wave number k, thus:

$$P(k,\omega) \sim \|(k,\omega)\|^{-\xi} \tag{3-25}$$

For a scale invariance anisotropic rainfall field in a space–time domain the spectral density is here represented as:

$$P(k,\omega) \sim \left(a\,k + b\,\omega^{1/(1-H)}\right)^{-\xi} \tag{3-26}$$

Thus, $P(k,\omega) \sim a\,k^{-\xi}$ for $\omega = 0$ and $P(k,\omega) \sim b\,\omega^{-\frac{\xi}{1-H}}$ for $k = 0$. Therefore, the spectral slopes $\beta_k = -\xi$ for the space cut at $\omega = 0$ and $\beta_\omega = -\xi/(1-H)$ for the time cut at $k = 0$, allow the estimation of the dynamic scaling exponent H as:

$$H = 1 - \frac{\beta_k}{\beta_\omega} \tag{3-27}$$

In the case that rainfall is acting as passive scalar in the atmospheric turbulence, one would expect H is expected to be near to $\sim 1/3$ and a scaling dynamic will also be valid. However, if H is non–zero there exists an space–time anisotropy denoting a dynamic scaling, such that the following functional form could be satisfied:

$$\mathbf{R}(\mathbf{x},t) \sim t^{\theta}\phi\left(\frac{\mathbf{x}}{t^{z}}\right) \tag{3-28}$$

where $\mathbf{R}(\mathbf{x},t)$ is the rainfall field, the exponents θ and $z \sim 1-H$ are non–dimensional exponents that satisfy the dimensional relations $[t^{\theta}] = [R(\mathbf{x},t)]$ and $[t^{z}] = [\mathbf{x}]$, and $\phi(\cdot)$ is a scaling function [Hassan et al., 2011, Family & Vicsek, 1985].

The analysis of 2D spatial rainfall fields required a dimensional reduction during the construction of space–time fields. For every frame of the field $\mathbf{R}(\mathbf{x},t) \equiv R_{ijz}$, there are two sub–fields $R_x^t \equiv R_{iz} \equiv \sum_j R_{ijz}$ and $R_y^t \equiv R_{jz} \equiv \sum_i R_{ijz}$ which result from averaging the field $\mathbf{R}(\mathbf{x},t)$ in either zonal (i) or meridional (j) directions. By means of collecting the vectors $R_x^{t_0}, R_x^{t_1}, \ldots R_x^{t_n}$, the space–time fields $\mathbf{R}(x,t)$ (for zonal direction) and $\mathbf{R}(y,t)$ (for meridional direction) are build. These two fields describe the space–time dynamics of the rainfall field. Intuitively, if the equivalence $\mathbf{R}(x,t) = \mathbf{R}(y,t)$ is true, the studied rainfall field could be considered an isotropic field, therefore, the scaling exponents H_x and H_y derived from the fields $\mathbf{R}(x,t)$ and $\mathbf{R}(y,t)$ will be equals, i.e. $H_x = H_y = H$. The dimensional–reduction procedure of the field $\mathbf{R}(\mathbf{x},t)$ has as a consequence that the intermittency of the rainfall field be smoothed, furthermore, the spatial structures could be disassembled or reduced from the original field. The aforementioned arguments state H_x and H_y are indeed marginal values of H and represent how the average spatial structures change in time.

3.2. Observational Analysis

Through some selected rainfall data sets of different kind of measurements, multifractality will be identified and analyzed through the techniques indicated at section 3.1. These analyses will be extended to rainfall simulations in order to establish a feasible physical parametrization of rainfall multifractality.

3.2.1. High–Resolution Rainfall Records

The first rainfall data set to be studied are punctual observations. In Table 3-1 are exhibited a set formed by 17 rain-gauge stations taken from the hydrological measurement network of Bogotá (Colombia) which is managed by the drinking and wastewater system operator EAAB[3]. In the appendix B are depicted the rainfall time series that were selected for studying in this research. The time resolution of these time series is 30 min and their registers were organized from the summer solstice of the year 1995 to the summer solstice of the year 1999, so that four years of 17 high–resolution rainfall data sets were available for the analysis. Although these records might not give straightforward information about the

[3]EAAB: Empresa de Acueducto, Alcantarillado y Aseo de Bogotá.

space–time structure of Bogotá's rainfall, the comparison between two or more rain-gauge data sets can give some clues about the spatial heterogeneity of the rainfall field and how its multifractal structure changes in the space-time.

The first data analysis corresponded to the construction of local multifractal spectra for each selected rain-gauges data. At Figure 3-1 are depicted such multifractal spectra which give evidence of a non–linear statistical structure of the rainfall field. The singularities measures are evidenced in the range of $0.4 \leq \alpha < 1.0$ and non–singular measures in the range $1.0 \leq \alpha < 1.2$. The fractal dimension of the support D_0 is indeed similar among the computed spectra and its average value is approximately $D_0 \sim 0.74$. In Table 3-2 are exhibited the statistics of some descriptors of the multifractal spectrum. They are the singularity exponents α_{min}, α_{max}, α_0, α_1 and α_2, and their corresponding fractal dimensions $f(\alpha_0) = D_0$, $f(\alpha_1) = D_1$, and $f(\alpha_2) = D_2$. As one can evidence in Table 3-2, α_{min} and α_{max} are almost the same for all spectra. Their average values are $\alpha_{min} \approx 0.45$ and $\alpha_{max} \approx 1.13$; thus, the average spectral width is $H_\alpha \approx 0.68$. The average spectrum is centered at $\alpha_0 = 0.81$ and $D_0 = 0.74$ as it was mentioned above. The singularity exponent for the concentrated measure is $\alpha_1 = D_1 = 0.67$ and the average correlation dimension D_2 which presents higher variability among the other fractal descriptors, equals to $D_2 \approx 0.53$.

The spatial variability of multifractal dimensions is almost regular over the space domain[4]. In the case of dimension D_0, its average variability is approximately equal to $|\partial D_0/\partial \mathbf{x}| \approx 1.98$ km^{-1}, for dimension D_1 is $|\partial D_1/\partial \mathbf{x}| \approx 0.29$ km^{-1}, and for dimension D_2 is $|\partial D_2/\partial \mathbf{x}| \approx 0.34$ km^{-1}. The greater variability in D_0 is given between closer stations, e.g. RG-11 vs RG-14 where $\Delta x = 8.89$ km, and the lower variability in D_0 is given between isolated stations, e.g. RG-09 vs RG-13 where $\Delta x = 31.32$ km. Similarly, the greater variability in D_1 is given between near stations, e.g. RG-11 vs RG-14 where $\Delta x = 8.89$ km, and the lower variability in D_1 is given between isolated stations, e.g. RG-06 vs RG-11 where $\Delta x = 23.67$ km. These results make sense if one supposes that there exists a spatial correlation decaying in the rainfall field, and rainfall intermittency (associated to singular measures) is mainly manifested at the local scale.

The function $\tau(q)$ was estimated for all selected rainfall punctual observations following the methodology that was indicated in section 3.1.2. Figure 3-2 shows the plot of the function $\tau(q)$ for every rain–gauges data and Table 3-3 exhibits the first five cumulant–based magnitude coefficients. These cumulant–based magnitude coefficients were used for computing the function $\tau(q)$ and every frame at Figure 3-2 shows the plot of two lines. The red one corresponds to the function $\tau(q)$ for a data set that exhibits a linear behavior (or non–multifractal), and the solid black line corresponds to the function $\tau(q)$ for the selected rainfall data set. As shown in Figure 3-2, there exists a non–linear structure for all the studied rainfall records. All estimated $\tau(q)$–functions for the rainfall records exhibit a departure from the linear behavior (i.e. solid red line) which is more noticeable for large order of the moments. However, the patterns that correspond to the rain–gauges: Hato, La Regadera and Une, do

[4]See numerical results at Tables B-2, B-3 and B-4

Table 3-1: List of the selected rain–gauge from Bogota and surrounding locations for multifractal analysis.

Gauge Number	IDEAM ID	Gauge Name	Geo. Coordinates East	Geo. Coordinates North	Elevation (msnm)	Type	Location
1	2120154	Bosa Barreno	1001915	988072	2550	PG	Bogotá
2	2120569	Camavieja	1003580	998480	2680	CO	Bogotá
3	2120013	El Delirio	994730	1002120	3000	PG	Bogotá
4	2120020	El Hato	976829	988920	3150	PG	Bogotá
5	2120547	Fontibón	1007180	992500	2518	CO	Bogotá
6	2120531	La Caro	1028994	1005739	2560	CO	Chía
7	2120509	La Regadera	978751	992782	3050	PG	Bogotá
8	2120211	Las Huertas	999100	981400	2572	PG	Bogotá
9	2120205	Quiba	992305	989998	3000	PG	Bogotá
10	2120008	San Francisco Salitre	999200	1004500	3047	PG	Bogotá
11	2120040	San Luís	1005380	1004130	2300	PG	Bogotá
12	2120052	Santa Lucía	997550	995080	2630	PG	Bogotá
13	2120202	Serrezuela	1018613	1007000	2800	PG	Bogotá
14	2120199	Teusacá	1007100	1012850	2750	PG	La Calera
15	3502042	Une	979000	1005800	2430	PG	Bogotá
16	2120111	Usaquen Santa Ana	1010242	1005804	2647	PG	Bogotá
17	2120524	Vitelma	997682	1000642	2800	CO	Bogotá

show a weak non–linear structure and the higher values of the dimension D_0. The time series for the rain–gauges: Hato, La Regadera and Une, exhibit less intermittency as compared to other rainfall time series; furthermore, rainfall events during the observational window are more frequent in these rain–gauges than others.

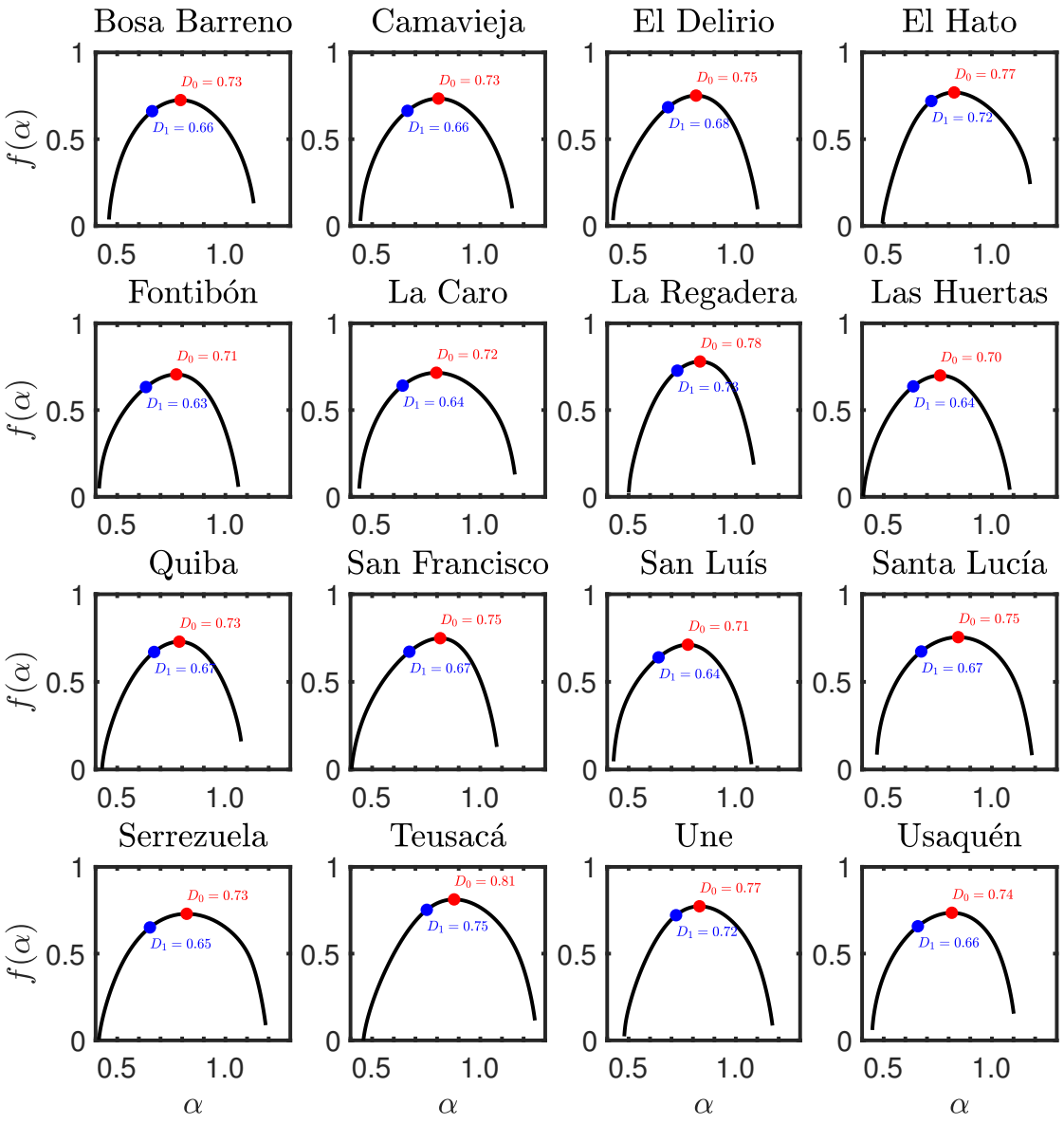

Figure 3-1: Graphs of multifractal spectra for the rainfall punctual observations measured at Bogotá over the span defined between the winter solstices of the years 1995 to 1999. In every plot is depicted a multifractal spectrum and the location of its descriptors D_0 and D_1.

Table 3-2: Main multifractal parameters obtained from the rainfall data sets. The selected rainfall data sets are exhibited at Table 3-1.

Gauge Number	IDEAM ID	Gauge Name	α_{min}	α_{max}	α_0	α_1	α_2	D_0	D_1	D_2
1	2120154	Bosa Barreno	0.46	1.13	0.79	0.66	0.57	0.73	0.66	0.54
2	2120569	Camavieja	0.46	1.15	0.81	0.66	0.56	0.73	0.66	0.51
3	2120013	El Delirio	0.43	1.10	0.81	0.68	0.55	0.75	0.68	0.49
4	2120020	El Hato	0.49	1.18	0.83	0.72	0.65	0.77	0.72	0.62
5	2120547	Fontibón	0.42	1.06	0.77	0.63	0.52	0.71	0.63	0.47
6	2120531	La Caro	0.44	1.16	0.80	0.64	0.55	0.72	0.64	0.51
7	2120509	La Regadera	0.50	1.08	0.83	0.73	0.65	0.78	0.73	0.61
8	2120211	Las Huertas	0.41	1.08	0.76	0.64	0.53	0.70	0.64	0.48
9	2120205	Quiba	0.43	1.07	0.79	0.67	0.57	0.73	0.67	0.52
10	2120008	San Francisco Salitre	0.41	1.08	0.81	0.67	0.53	0.75	0.67	0.46
11	2120040	San Luís	0.43	1.07	0.78	0.64	0.53	0.71	0.64	0.48
12	2120052	Santa Lucía	0.47	1.19	0.84	0.67	0.57	0.75	0.67	0.53
13	2120202	Serrezuela	0.42	1.19	0.82	0.65	0.55	0.73	0.65	0.51
14	2120199	Teusacá	0.46	1.25	0.88	0.75	0.64	0.81	0.75	0.58
15	3502042	Une	0.48	1.17	0.83	0.72	0.63	0.77	0.72	0.59
16	2120111	Usaquen Santa Ana	0.45	1.10	0.81	0.66	0.55	0.74	0.66	0.51
17	2120524	Vitelma	0.45	1.08	0.82	0.67	0.57	0.74	0.67	0.52
$\bar{P}$	Mean	(mm)	0.45	1.13	0.81	0.67	0.57	0.74	0.67	0.53
σ	Std. Deviation	(mm)	0.03	0.05	0.03	0.04	0.04	0.03	0.04	0.05
CV	Coef. Variation	(%)	6.56	4.87	3.60	5.24	7.58	4.00	5.24	9.11

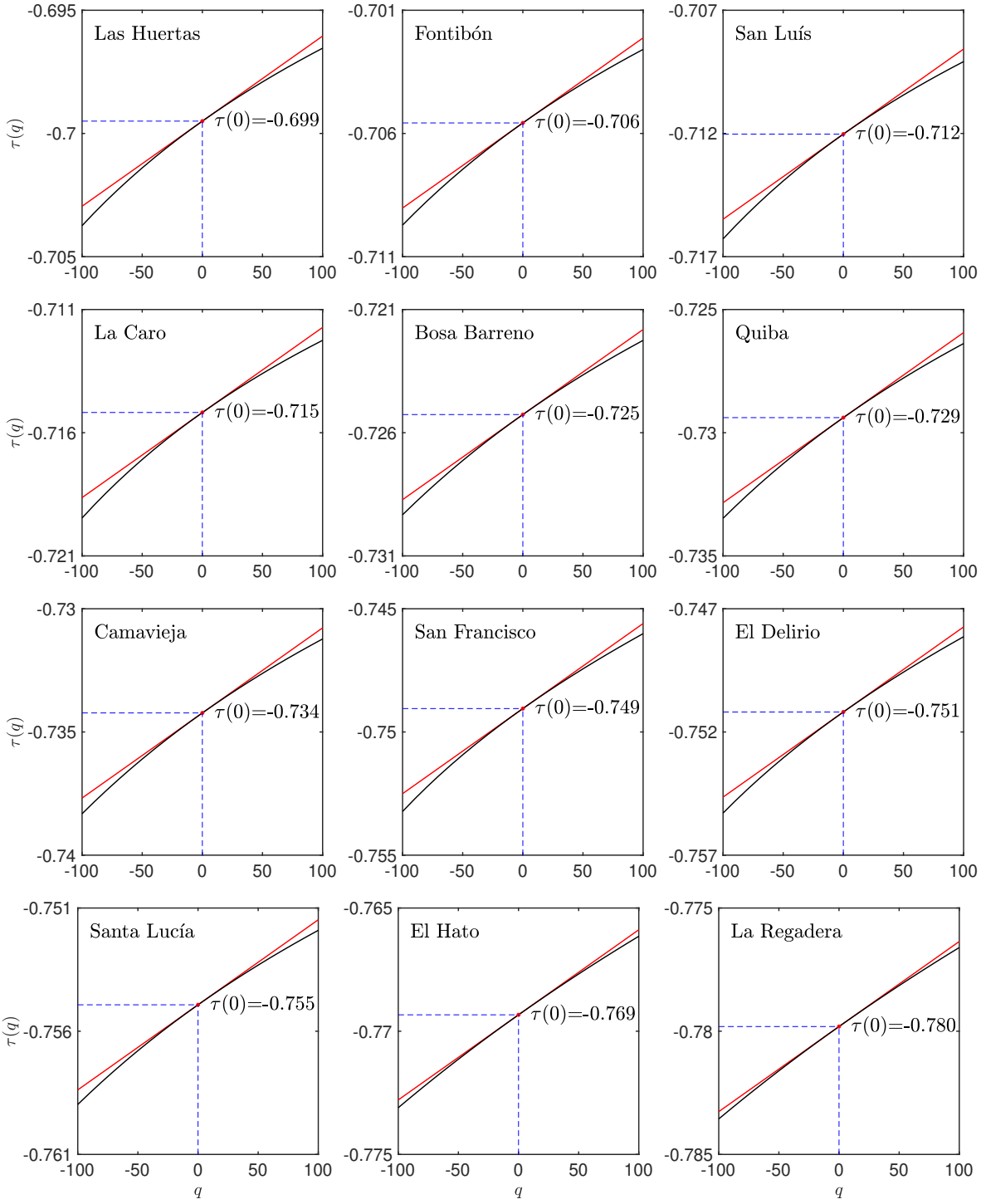

Figure 3-2: Graph of function $\tau(q)$ for the selected rainfall time series registered at Bogotá's rain–gauges over the span defined by the winter solstices of the years 1995 to 1999. The solid red line shown in every frame corresponds to the behavior of a $\tau(q)$–function whose pattern exhibits a linear structure. The solid black line describes the behavior of $\tau(q)$–function for the rainfall data set.

The location of $\tau(0)$ into the domain states a geometrical hierarchy among rain-gauges. It is almost straightforward to see that lower values of $\tau(0) = D(0)$ describe patterns with less frequency of rainfall events and more intermittency, whereas higher values of $\tau(0)$ describe patterns with more frequency of rainfall events and less intermittency. Table 3-3 summed up the first five cumulant–based magnitude coefficients, i.e. $\{C_0, C_1, \ldots, C_5\}$. This magnitude coefficients were computed as the slope of the linear–log relationship between the cumulants $c_n(\delta)$ and the aggregation scales $\ln(\delta)$.

Table 3-3: Values of the first five cumulant–based magnitude coefficients which were estimated for the rainfall data indicated at Table 3-1.

Gauge Number	IDEAM ID	Gauge Name	C_0	C_1 ($\times 10^{-5}$)	C_2 ($\times 10^{-7}$)	C_3 ($\times 10^{-9}$)	C_4 ($\times 10^{-11}$)
1	2120154	Bosa Barreno	0.725	-5.185	-1.701	-0.881	-0.576
2	2120569	Camavieja	0.734	-5.185	-1.789	-1.048	-0.800
3	2120013	El Delirio	0.751	-5.185	-1.624	-1.223	-1.603
4	2120020	El Hato	0.769	-5.185	-1.030	-0.343	-0.159
5	2120547	Fontibón	0.706	-5.185	-1.824	-1.121	-0.918
6	2120531	La Caro	0.715	-5.185	-2.197	-1.640	-1.593
7	2120509	La Regadera	0.780	-5.185	-0.961	-0.326	-0.159
8	2120211	Las Huertas	0.699	-5.185	-2.024	-1.515	-1.651
9	2120205	Quiba	0.729	-5.185	-1.877	-1.171	-0.952
10	2120008	San Francisco Salitre	0.749	-5.185	-1.814	-1.502	-1.922
11	2120040	San Luís	0.712	-5.185	-2.119	-1.596	-1.550
12	2120052	Santa Lucía	0.755	-5.185	-1.692	-0.911	-0.614
13	2120202	Serrezuela	0.730	-5.185	-2.084	-1.519	-1.477
14	2120199	Teusacá	0.813	-5.185	-0.856	-0.329	-0.246
15	3502042	Une	0.773	-5.185	-1.151	-0.465	-0.267
16	2120111	Usaquén Santa Ana	0.735	-5.185	-1.807	-1.037	-0.793
17	2120524	Vitelma	0.744	-5.185	-1.707	-0.939	-0.651
Mean		(·)	0.742	-5.185	-1.662	-1.033	-0.937
Std. Deviation		(·)	0.029	0.000	0.414	0.453	0.587
Coef. Variation		(%)	3.964	0.000	24.910	43.809	62.635

Statistics about the magnitude coefficient C_1 do show a kind of uniformity, but the converse for the others magnitude coefficients. Table 3-3 shows that the computed magnitude coefficient C_1 seems to be the same for all rainfall data sets ($\approx -5.19 \times 10^{-5}$), but such a results means that all rainfall data sets were normalized and the average value of the studied rainfall patterns is almost the same for all possible scales. Since the magnitude coefficients of order larger than one ($n > 1$) are smaller in magnitude than C_1, a linear component predominates

in the statistical structure of rainfall patterns. However, there exists a non-linear component which can be evidenced for larger order of the moments, therefore the multifractal structure of rainfall should be explored in large order statistics. Based on the statistical results shown in Table 3-3, the lack of regularity among statistics could be interpreted as the non–existence of universality in the description of rainfall multifractality.

Figures B-5, B-6, B-7 and B-8 show two–point correlation functions in a linear–log domain which were computed for every studied rainfall time series. Every plot in these figures shows the relation between the correlation function $C(\delta, \Delta t)$ and the logarithm of the scale $\ln(\Delta t)$ for four aggregation scales (i.e. 30 min, 1 h, 3 h and 6 h). Moreover, each plot shows results of two curve fitting using regression methods. The computed regression coefficients are exhibited in Table 3-4. For the power model its mathematical expression is $C(\delta, \Delta t) = m\,(\Delta t)^k$ whose parameters are m and k, and for the exponential model, its mathematical expression is $C(\delta, \Delta t) = a + \exp(b\,\Delta t)$ whose parameters are a and b. As evidenced in Table 3-4, the best fit is achieved with the power model which describes a power–law decay in the correlation function as the scale increases ($\Delta t > \delta$). Figures B-5 to B-8 show evidence of scale independence for large enough time lags ($\Delta t \gg \delta$). Since the computed two–point correlation function $C(\delta, \Delta t)$ does not changes linearly with $\ln \Delta t$, there is not a long–range dependence as evidenced in random multiplicative cascades, therefore, the multifractal structure of the studied rainfall patterns is not the same those derived from random multiplicative cascades.

Comparing the two–point correlation functions of the rain–gauges: La Regadera (third frame at Figure B-6) and San Luís (second frame at Figure B-7), the second one decays faster than that observed in La Regadera rain–gauge. It is recalled the fractal correlation dimensions D_2 for San Luís and La Regadera are 0.48 and 0.61, correspondingly. It seems D_2 is associated to the velocity of the correlation decay. The faster $C(\delta, \Delta t)$ declines, the lower value of D_2 becomes. As shown in the reported results, D_2–values are prone to be higher in rainfall observations whose function $C(\delta, \Delta t)$ declines slowly, and the converse is also true.

The incremental similarity analysis begins with the assessment of empirical probability density functions (PDFs) of the increments $\Delta_{t,u}$. Figures B-9 to B-25 show a logarithm representation of PDFs for seventeen normalized–rainfall–increments data sets. Red dots in every plot are indicating the empirical PDF and the black solid line represents the PDF of an estimated Normal Inverse Gaussian (NIG) distribution for the chosen data set. In each plot is also shown the validity of the fitting to the PDF via Kolmogorov–Smirnov test (i.e. $H_0 = 0$ for acceptance and $H_0 = 1$ for rejection of the fitting), and the variance of increments $\mathrm{Var}(\Delta_{t,u})$.

For the results obtained in this research, punctual rainfall records have a highly resemblance to the statistical behavior to that found in turbulent flows. All data sets that were analyzed through of incremental similarity (IS) analysis can be described by a NIG distribution with exception of a few rainfall records. Different time lags were used for the IS analysis and for all of them the increments $\Delta_{t,u}$ can be suitably described by a NIG distribution and an specific variance $\mathrm{Var}(\Delta_{t,u})$. As the positive time lag u increases the variance is also augmented

Table 3-4: Curve–fitting regression coefficients for the power and exponential models the description of two–point correlation function for the studied rainfall time series. The selected rainfall time series belonging to the rain–gauges identified at Table 3-1.

Gauge Number	IDEAM ID	Gauge Name	m	k	R^2	RMSE	a	b	R^2	RMSE
1	2120154	Bosa Barreno	0.613	-1.308	0.996	0.047	1.009	-0.622	0.960	0.141
2	2120569	Camavieja	0.629	-1.428	0.994	0.063	0.984	-0.624	0.974	0.114
3	2120013	El Delirio	0.613	-1.423	0.998	0.040	1.031	-0.662	0.976	0.117
4	2120020	El Hato	0.869	-1.069	0.988	0.086	1.048	-0.413	0.981	0.064
5	2120547	Fontibón	0.315	-1.507	0.968	0.155	0.599	-0.759	0.932	0.230
6	2120531	La Caro	0.646	-1.429	0.964	0.158	0.970	-0.595	0.996	0.044
7	2120509	La Regadera	0.850	-1.195	0.992	0.080	1.066	-0.457	0.984	0.066
8	2120211	Las Huertas	0.437	-1.294	0.998	0.037	0.667	-0.576	0.960	0.132
9	2120205	Quiba	0.695	-1.153	0.992	0.061	1.016	-0.512	0.986	0.068
10	2120008	San Francisco Salitre	0.452	-1.197	0.987	0.078	0.644	-0.518	0.893	0.201
11	2120040	San Luís	0.481	-1.555	0.985	0.109	0.872	-0.733	0.994	0.062
12	2120052	Santa Lucía	0.633	-1.255	0.999	0.025	0.973	-0.568	0.972	0.107
13	2120202	Serrezuela	0.711	-1.508	0.976	0.133	1.160	-0.662	0.998	0.032
14	2120199	Teusacá	0.745	-0.983	0.994	0.057	0.935	-0.404	0.961	0.091
15	3502042	Une	0.968	-1.171	0.951	0.192	1.050	-0.403	0.992	0.039
16	2120111	Usaquen Santa Ana	0.556	-1.394	0.996	0.049	0.934	-0.657	0.951	0.166
17	2120524	Vitelma	0.650	-1.514	0.996	0.057	1.161	-0.719	0.975	0.130
$\bar{P}$	Mean	(mm)	0.639	-1.317	0.987	0.084	0.948	-0.581	0.970	0.106
σ	Std. Deviation	(mm)	0.166	0.170	0.014	0.049	0.166	0.115	0.027	0.057
CV	Coef. Variation	(%)	25.938	-12.946			17.540	-19.820		

its value but such a variance is bound for large enough time lag u, therefore an asymptotic behavior is evidenced for the variance. For instance, at Bosa Barreno – RG1 (see Figure B-9) the asymptotic value for the variance of the increments $\Delta_{t,u}$ is ≈ 0.46 and at El Hato – RG4 (see Figure B-12) the asymptotic value for the variance of the increments $\Delta_{t,u}$ is ≈ 0.33. It seems the variance of the increments grow from 2 to 3 times between $\mathrm{Var}(\Delta_{t,1})$ and $\mathrm{Var}(\Delta_{t,u_\infty})$, where u_∞ represents a large enough time lag. It is highlighted that the difference $\Delta V = \mathrm{Var}(\Delta_{t,u_\infty}) - \mathrm{Var}(\Delta_{t,1})$ seem to be related to the fractal dimension D_0. For higher values of ΔV, higher values of D_0 are reached. As an example of this premise can be observed in the rainfall records of Fontibón (RG5) and San Luís (RG11) have a $\Delta V \approx 1.8$ and their fractal dimension $D_0 \sim 0.71$; conversely, the rainfall records of La Regadera (RG7) and Une (RG15) have a $\Delta V \approx 3.7$ and their fractal dimension $D_0 \sim 0.78$. Thus, the last remarks are indicating that the power of the intermittency is associated to the fractal dimension of the support D_0.

In Table 3-5 is shown the statistic of NIG–distribution parameters for the rainfall time series recorded at Bogotá. The second column of the Table 3-5 exhibits a value for the variance of the increment $\Delta_{t,u}$ which is estimated for different lags u. Only the set of data that satisfy the relation $\mathrm{Var}(\Delta_{t,u}) \approx \mathrm{Var}(\Delta_{t,u+s})$ were selected for the statistical description with NIG distribution. From the fourth to seventh column of the Table 3-5, the empirical estimation of NIG parameters are exhibited and they are lumped in quartiles in order to analyze the parametric variability. For the selected data there is not a significant difference among the parameter whose empirical variance is held to a single value and the only change associated to the variance are the tail-heaviness parameter α and the scaling parameter δ. However, the parameter α presents a remarkable consideration in the data analysis. As it is shown in Table 3-5, for a large variance it is expected to have a small value in the tail-heaviness parameter and a better statistical fit to the NIG distribution (e.g. the comparison between the results for the rain-gauges RG1 and RG11). In Figure B-9 the tails of the NIG distribution do not fit to the observations whose stable variance approximates to ≈ 0.46 ($\alpha \approx 0.17$), whereas in Figure B-19 the converse is obtained; here the variance approximates to ≈ 1.75 ($\alpha \approx 0.07$) and a good fit of data is observed in the tails of the distribution. In other words, for larger intensity in the intermittency of the rainfall records, the NIG distribution describes better their statistical law.

Albeit there exists an suitable statistical description of rainfall increments $\Delta_{t,u}$ with the NIG distribution, for punctual observations measured at points i and j, the equivalence relation

$$R_i \overset{\mathbf{IS}}{=} R_j \qquad \text{or equivalently,} \quad \Delta_{t,u}(R_i) \overset{\text{dist}}{=} \Delta_{t,v}(R_j) \tag{3-29}$$

could be valid. From the available data, there is not similarities among the obtained parameters of the NIG distribution; clearly, the stable variance of the increments $\Delta_{t,u}$ is not exactly the same for all the punctual observations, however, for those observations whose variances are closed to an specific value, their tail–heaviness and scaling parameters are different.

For instance, the variance of the rainfall increments at the rain–gauges RG1 and RG9 is approximated to ≈ 0.5 (low intermittency) and their parameters are $\alpha \approx 0.17$, $\beta \approx 0.00$,

Table 3-5: Estimates of NIG distribution parameters for the increments of rainfall time series with stable variance.

Gauge	$\mathrm{Var}(\Delta_{t,u})$	Quartile	α	β	μ	δ
RG1	0.455	Q1	0.173	0.000	0.000	0.079
		Q2	0.174	0.001	0.000	0.079
		Q3	0.174	0.001	0.000	0.079
RG2	1.218	Q1	0.087	0.000	0.000	0.106
		Q2	0.087	0.000	0.000	0.106
		Q3	0.087	0.000	0.000	0.106
RG5	1.138	Q1	0.070	0.000	0.000	0.080
		Q2	0.070	0.000	0.000	0.080
		Q3	0.070	0.000	0.000	0.080
RG6	0.592	Q1	0.127	-0.001	0.000	0.075
		Q2	0.127	0.000	0.000	0.075
		Q3	0.127	0.000	0.000	0.075
RG8	0.610	Q1	0.094	0.000	0.000	0.057
		Q2	0.094	0.000	0.000	0.057
		Q3	0.094	0.000	0.000	0.057
RG9	0.479	Q1	0.124	0.000	0.000	0.059
		Q2	0.124	0.000	0.000	0.060
		Q3	0.125	0.000	0.000	0.060
RG10	1.673	Q1	0.051	0.000	0.000	0.085
		Q2	0.051	0.000	0.000	0.085
		Q3	0.051	0.000	0.000	0.085
RG11	1.745	Q1	0.065	0.000	0.000	0.113
		Q2	0.065	0.000	0.000	0.113
		Q3	0.065	0.000	0.000	0.113
RG12	0.724	Q1	0.127	0.000	0.000	0.092
		Q2	0.128	0.000	0.000	0.092
		Q3	0.128	0.000	0.000	0.093
RG13	0.932	Q1	0.087	0.001	-0.001	0.081
		Q2	0.087	0.001	-0.001	0.081
		Q3	0.087	0.001	-0.001	0.081
RG16	1.445	Q1	0.082	0.000	0.000	0.118
		Q2	0.082	0.000	0.000	0.118
		Q3	0.082	0.000	0.000	0.118
RG17	1.255	Q1	0.096	0.000	0.000	0.120
		Q2	0.096	0.000	0.000	0.120
		Q3	0.096	0.000	0.000	0.120

$\mu \approx 0.00$, $\delta \approx 0.08$ (with cumulants: $C_1 \approx 0$, $C_2 \approx 0.5$, $C_3 \approx 0$, $C_4 \approx 45$) for RG1 and $\alpha \approx 0.12$, $\beta \approx 0.00$, $\mu \approx 0.00$, $\delta \approx 0.06$ (with cumulants: $C_1 \approx 0$, $C_2 \approx 0.5$, $C_3 \approx 0$, $C_4 \approx 94$) for RG9. Another example is observed between the rain–gauges RG10 and RG11, whose variance of the rainfall increments is approximated to ≈ 1.7 (high intermittency) and their parameters are $\alpha \approx 0.05$, $\beta \approx 0.00$, $\mu \approx 0.00$, $\delta \approx 0.09$ (with cumulants: $C_1 \approx 0$, $C_2 \approx 1.7$, $C_3 \approx 0$, $C_4 \approx 1922$) for RG10 and $\alpha \approx 0.07$, $\beta \approx 0.00$, $\mu \approx 0.00$, $\delta \approx 0.11$ (with cumulants: $C_1 \approx 0$, $C_2 \approx 1.7$, $C_3 \approx 0$, $C_4 \approx 1739$) for RG9. Summing up, the incremental similarity (equation 3-29) seems to be valid for those signals having a more intermittent (multifractal) structure.

3.2.2. Reflectivity Fields from Weather Radar

For this research, some reflectivity observations recorded by the weather radar located at Santa Elena's town, at the East of Medellín (CO). This C–band weather radar is operated by Early Warning System of Medellín and Aburrá's Valley (SIATA[5]) and a set of observations were selected and used for the multifractal analysis and the description of a typical tropical storm. In Figure 3-3 are shown some snapshots of the weather radar base reflectivity recorders from 00:00 h to 14:00 h of May 18th of 2015. This data set was selected for the research purposes. The time resolution of reflectivity observations is $\Delta t = 5$ min, the spatial resolution is $\Delta x \approx 250$ meters and the spatial range is 119.94 km for a PPI[6] sweep fixed angle of $\approx 1.0°$.

Figure 3-4 exhibited the time evolution of the mean spatial value, the maximum spatial value, the standard deviation of observations and the fractional wet area (FWA) of the reflectivity field measured by the SIATA's weather radar on May 18th of 2015 from 00:00 h to 14:00 h. The mean value of the reflectivity field seems to have a smooth decay during the time evolution of the rainfall field, but the maximum value of this field seems to be constant over time. The standard deviation is also decaying as the time progresses but not so fast as the mean value does. The fractional wet area increases between the 00:00 h (FWA= 6.1 %) to the 08:25 h (FWA= 28.0 %) and decreases between the 08:25 h to 14:00 h (FWA= 3.2 %). In the FWA peak the mean value of the field is $\langle R_i \rangle \approx \overline{R} \approx 16.8$ dBZ, the max value of the field is ≈ 52 dBZ and the variance $\sigma_i^2 \approx 70.2$ dBZ.

The multifractal spectrum of reflectivity observations is depicted in Figure 3-5 for some selected snapshots in order to get a prime of how multifractal spectra look like. For all reflectivity observations, the empirical multifractal spectrum depicts a regular convex function made up by non–singular scaling exponents. Some statistical characteristics of the multifractal spectra can be represented in the time arrow as seen in Figure 3-6. This figure shows how some specific points in the multifractal spectra evolve in time. Clearly, the multifractal variables seem to have a characteristic pattern alike to that of the FWA exhibits; since the multifractal variables α_0, α_1, α_2, D_0, D_1 and D_2 grow to get a maximum value at the same time where FWA does.

[5]Sistema de Alertas Tempranas de Medellín y el Valle de Aburrá
[6]i.e. Plan Position Indicator.

[H]

Figure 3-3: Weather radar based reflectivity fields (Z) of the rainfall event on May 18th of 2015. Each frame into the figure shows an instantaneous plot of the reflectivity field (Z) observed by the Early Warning System of Medellín and Aburrá's Valley (SIATA) in decibels (dBz) units from 00:00 to 14:00 h (GMT-5). The weather radar is located at Medell'in in geographical coordinates Lat: 6.19° N, Lon: 75.53° W.

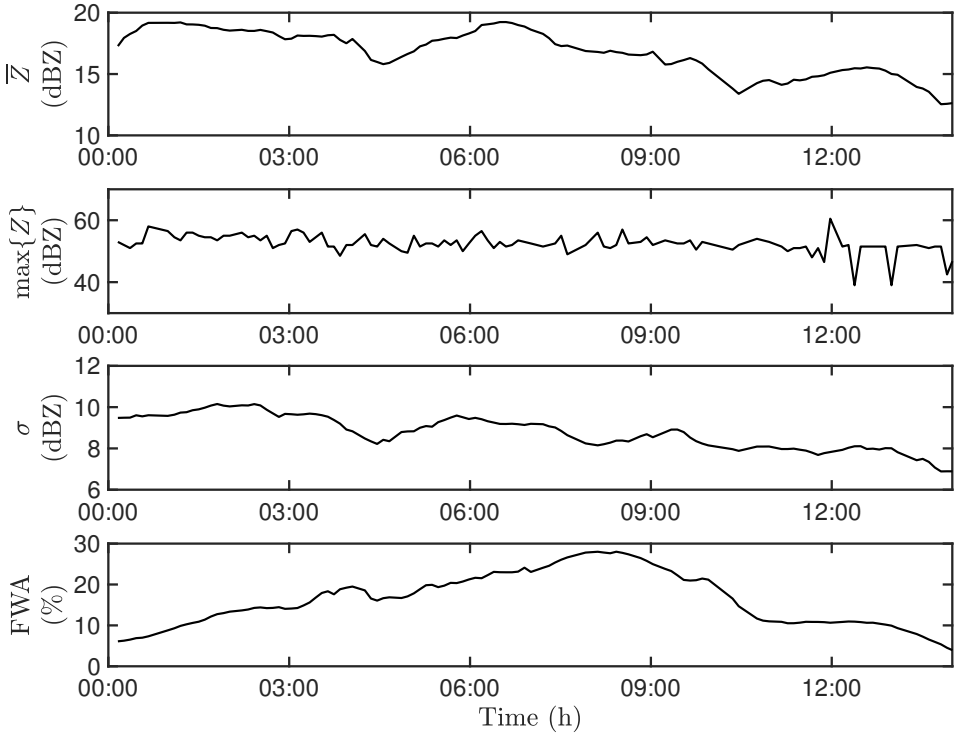

Figure 3-4: Time variation of the mean ($\overline{Z}$), maximum observed value (max$\{Z\}$), standard deviation (σ) and the fractional wet area for the based reflectivity fields observed by the Early Warning System of Medellín and Aburra's Valley (SIATA) from 00:00 to 14:00 h (GMT-5) on May 18th of 2015.

A first conclusion about the behavior of the time structure of multifractal statistics is that there is a kind of modulation of the spatial organization of rainfall patterns by the FWA, and this modulation also applies for the statistical structure of the field. Actually, previous researches have identified such a connection. Indeed, FWA represents a scaling property of the rainfall field which has been widely used as a parameter for the construction of random cascades [Over & Gupta, 1994, 1995, 1996]. On the other hand, the time evolution of multifractal variables indicates that as the storm spatial cover grows to a maximum value of FWA, measures are moving away of singularity (i.e. $\alpha > 1$), so, the spatial quantities of rainfall are apparently more regular in the space.

The statistics about the variables of the multifractal spectrum, exhibited in Table 3-6, show that $\alpha_{min} \equiv \min\{\alpha\} \approx 1.16 \pm 0.09$ and $\alpha_{max} \equiv \max\{\alpha\} \approx 2.23 \pm 0.27$, thus the spectral width is estimated as ≈ 1.0. For the the support of the measure, the singularity exponent $\alpha_0 \approx 1.69$ and its associated fractal dimension $D_0 \approx 1.65$. The average fractal dimension of the concentrated measure $D_1 \approx 1.61$ is nearly closed to the value obtained for D_0, so the concavity of the multifractal spectra seen from its slopes, grows (or decays) almost linearly at the beginning (or the end) of the function $f(\alpha)$.

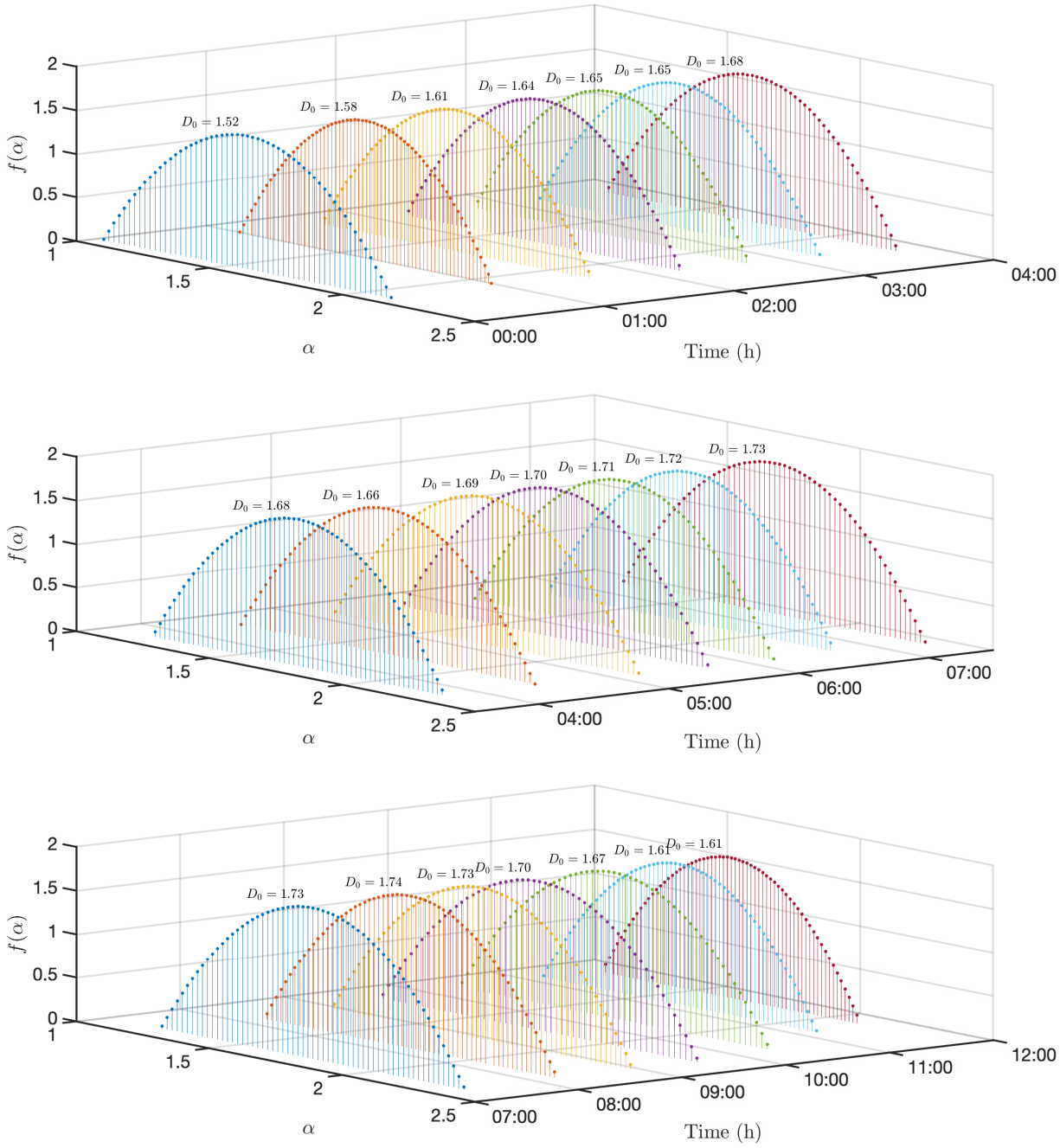

Figure 3-5: Time evolution of the estimated multifractal spectrum to the based reflectivity fields (Z) measured by the Early Warning System of Medellín and Aburra's Valley (SIATA) from 00:00 to 14:00 h (GMT-5) on May 18th of 2015.

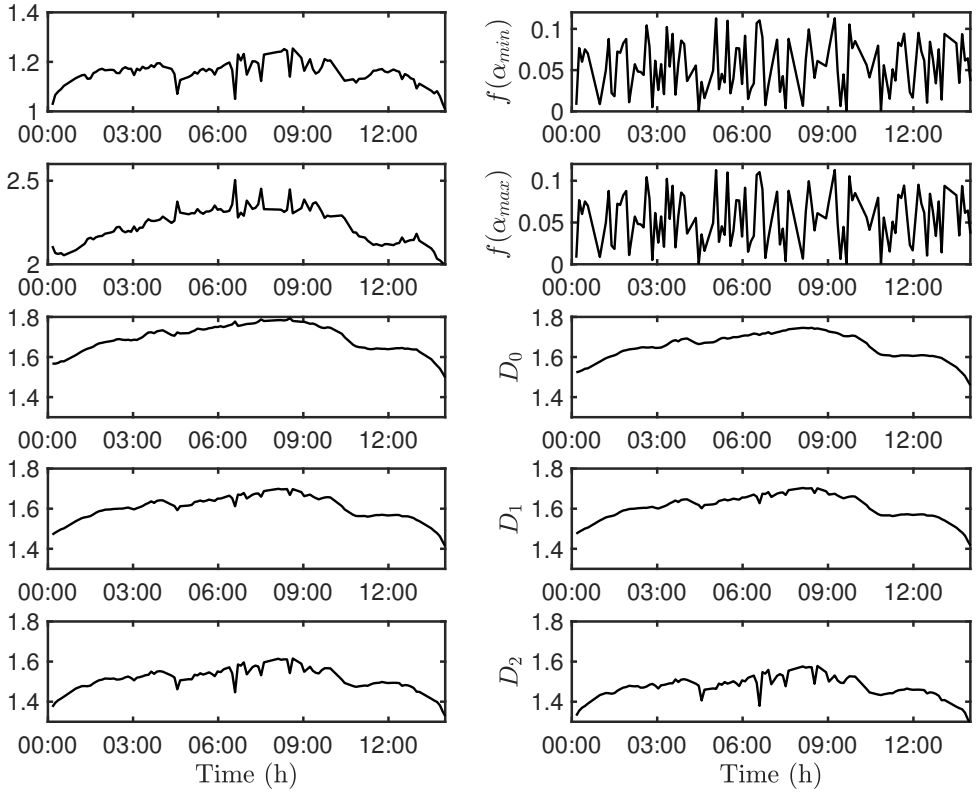

Figure 3-6: Time variation of the multifractal variables: α_{min}, α_{max}, α_0, α_1, α_2, $f(\alpha_{min})$, $f(\alpha_{max})$, $D_0 = f(\alpha_0)$, $D_1 = f(\alpha_1)$, and $D_2 = f(\alpha_2)$. All these variables were obtained from the computed multifractal spectra of the based reflectivity fields (Z) which is measured by the Early Warning System of Medellín and Aburra's Valley (SIATA) from 00:00 to 14:00 h (GMT-5) on May 18th of 2015.

Table 3-6: Statistics of the multifractal variables: α_{min}, α_{max}, α_0, α_2, $f(\alpha_{min})$, $f(\alpha_{max})$, $D_0 = f(\alpha_0)$, $D_1 = f(\alpha_1) = \alpha_1$, and $D_2 = f(\alpha_2)$, for the empirical multifractal spectrum of the based reflectivity fields (Z) measured by the Early Warning System of Medellín and Aburra's Valley (SIATA) from 00:00 to 14:00 h (GMT-5) of May 18th of 2015.

	α_{min}	α_{max}	α_0	α_2	D_0	D_1	D_2
Minimum	0.98	1.96	1.47	1.30	1.43	1.39	1.26
Mean	1.16	2.23	1.69	1.51	1.65	1.61	1.47
Maximum	1.25	2.50	1.79	1.62	1.75	1.70	1.58
σ	0.05	0.11	0.07	0.06	0.07	0.06	0.06
CV (%)	4.10	4.77	4.03	3.80	3.96	3.87	3.86
γ	-0.84	-0.10	-0.67	-0.85	-0.74	-0.81	-0.85

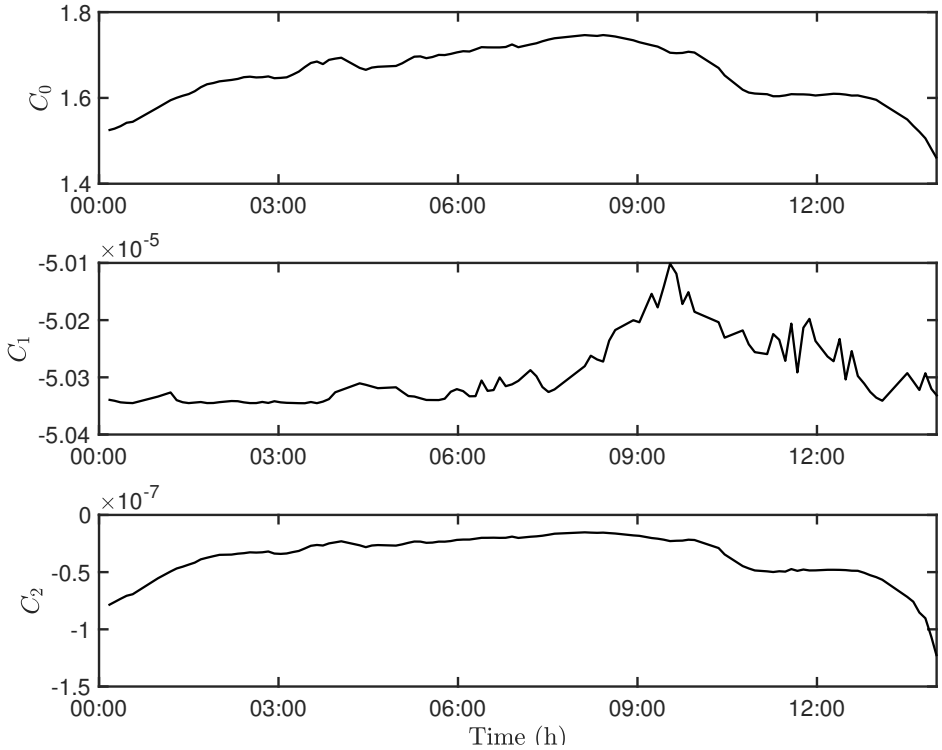

Figure 3-7: Time variation of the coefficients C_0, C_1 and C_2 which were estimated for reflectivity fields (Z) measured by the Early Warning System of Medellín and Aburra's Valley (SIATA) on May 18th of 2018 from 00:00 to 14:00 h (GMT-5) of May 18th of 2015. These coefficients were estimated via linear regression as the slope the relationship of $c_n(\delta)$ vs $\ln(\delta)$ for $n = 1, 2, 3, \ldots$ and $C_0 = D_0$.

The cumulant–based magnitude coefficients C_0, C_1 and C_2 were studied in the time domain. These coefficients were estimated for every observation during the evolution of the storm and results are exhibited in Figure 3-7. As it was mentioned above, the time dynamic of $C_0 \equiv D_0$ is similar to that observed in the fractional wet area (FWA); so, there exists a concave shape of the function $C_0(t)$ during the storm duration and its peak is given at 08:25 h. The behavior of C_1 and C_2 seems not be very numerically significant because their values are close to zero and one would expect to find a quasi–linear structure of the function $\tau(q)$ for the order of the moments near to $q = 0$. Under this result, the analysis of cumulant–based magnitude coefficients states that the multifractal structure of the studied reflectivity fields is not conclusive.

In Figure 3-8 are exhibited the plots of the two–point correlation functions for SIATA's reflectivity fields. Every plot shows the correlation function $C(\delta, \Delta x)$ for the spatial scales $\delta = 125$ m (Figure 3-8 (a)), $\delta = 250$ m (Figure 3-8 (b)), $\delta = 375$ m (Figure 3-8 (c)), and $\delta = 500$ m (Figure 3-8 (d)). Furthermore, every plot include a linear–fitting to the relationships: $\max\{C(\delta, \Delta t)\}$ vs $\ln(\Delta x)$ and $C(\delta, \Delta t)$ vs $\ln(\Delta x)$.

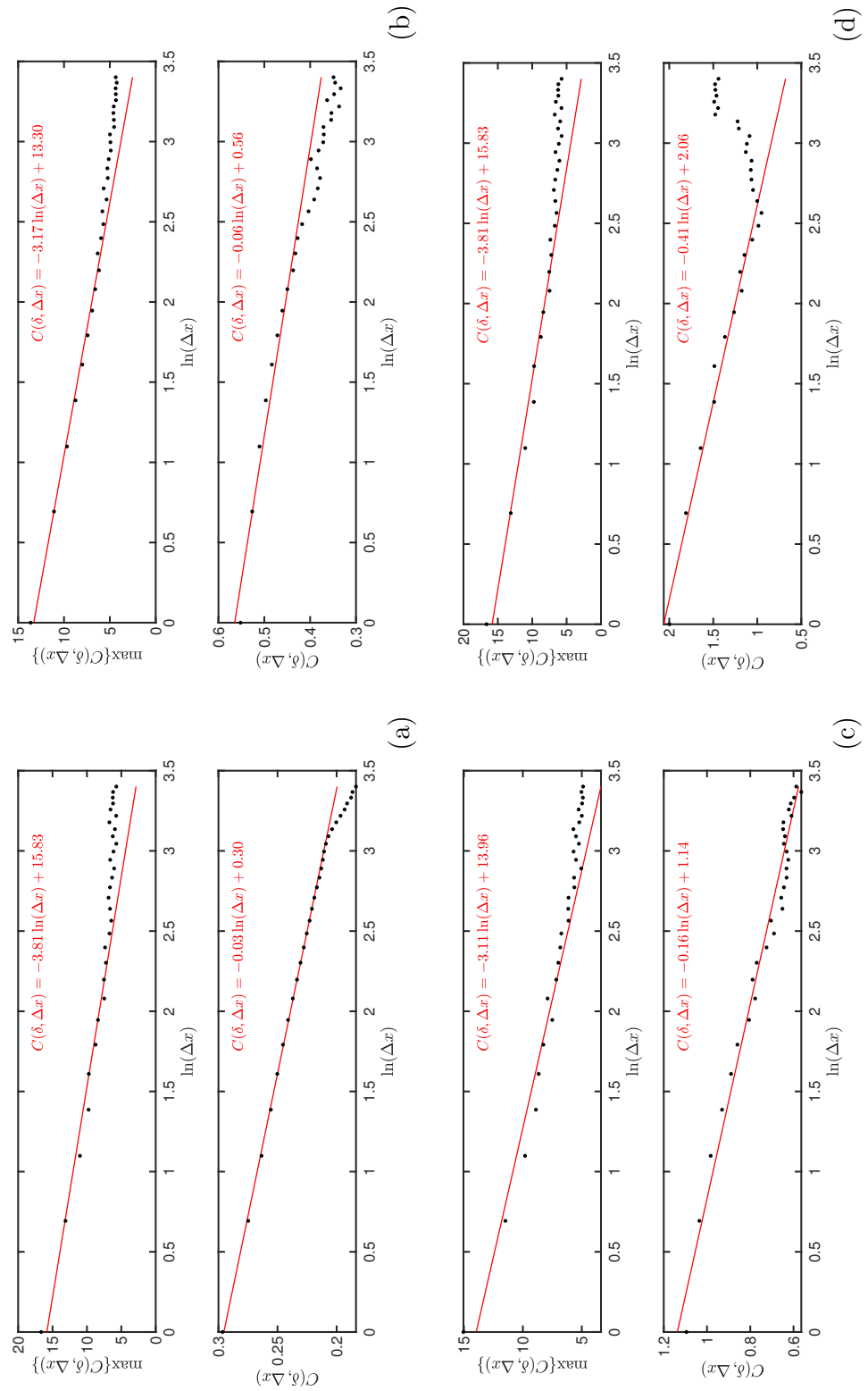

Figure 3-8: Maximum value of the two-point correlation field ($\max\{C(\delta,\Delta x)\}$ vs $\ln(\Delta x)$) and average value of the two-point correlation field ($C(\delta,\Delta x)$ vs $\ln(\Delta x)$) obtained from the reflectivity fields (Z) measured by the Early Warning System of Medellín and Aburrá's Valley (SIATA) in May 18th of 2018 from 00:00 to 14:00 h (GMT-5). In this plot the two-point correlation analysis is developed for the scales $\delta = \Delta x = 125$ meters (a), $\delta = 2\,\Delta x$ (b), $\delta = 3\,\Delta x$ (c), and $\delta = 4\,\Delta x$ (d).

It is to highlight that the correlation function was estimated for every record at time t as:

$$C_t(\delta, \Delta x) = \langle (\ln R(t,x) - \langle R(t,x) \rangle)((\ln R(t, x+\Delta x) - \langle R(t,x) \rangle)) \rangle \tag{3-30}$$

where $R(t,x)$ represents the reflectivity field observed at time t, $\langle R(t,x) \rangle$ represents the spatial average of the reflectivity field observed at time t, and $R(t, x+\Delta x)$ represents the reflectivity field observed at time t with a spatial shift of magnitude Δx. This shift was computed in four orthogonal direction (i.e. $R_{i,j+\Delta x}$, $R_{i+\Delta x,j}$, $R_{i-\Delta x,j}$, $R_{i,j-\Delta x}$) and their results were integrated in a single matrix in order to evaluate either the spatial average or the maximum value of the correlation function of the reflectivity field recorded at time t.
As one can observe in Figure 3-8, the correlation function $C(\delta, \Delta x)$ is linear in $\ln(\Delta x)$ for $\Delta x > \delta$, so there exists a long–range dependence for the reflectivity field which is also exhibited in multifractal patterns derived from multiplicative cascade. Actually, the non–zero value of the coefficient m in the expressions $C(\delta, \Delta x) = m\ \ln(\Delta x) + b$, suggests the presence of multifractality. Furthermore, the linear decay in the relationship $C(\delta, \Delta x)$ vs $\ln(\Delta x)$ indicates that multifractality can be described by a scale–invariant multiplicative cascade[7] as evidenced by Arneodo et al. [1998]. Another observation in the correlation function is the independence of the scale δ in the relationship $C(\delta, \Delta x)$ vs $\ln(\Delta x)$; for the scales $\delta = 125$ m and $\delta = 500$ m, the correlation function can be represented as $C(\delta, \Delta x) \sim 3.81\ \ln(\Delta x)$, so for the selected scales the long–range dependence and the scale–invariance are evidence of a multifractal multiplicative process.

The incremental similarity analysis was also applied to SIATA's reflectivity fields and the results will be summarized below. In Figure 3-9 are presented the PDFs of the increments $\Delta_{t,u}$ which were computed for the reflectivity field recorded by the Early Warning System of Medellín and Aburra's valley on May 18th of 2018. In contrast of the incremental similarity analysis over punctual observations whose increments are defined in time, for the reflectivity fields the increment are taken over the space, i.e. $\Delta^t_{x,u}(Z) = Z(t, x+u) - Z(t,x)$. In Figure 3-9 the PDF of the increments $\Delta^t_{x,u}(Z)$ is identified with red dots and all PDFs were depicting for the spatial lag $u = \{\Delta x, 2\,\Delta x, 3\,\Delta x, \ldots, 400\,\Delta x\}$ with $\Delta x = 150$ m. Moreover, for all spatial lags there exist either an empirical PDF of the increments $\Delta^t_{x,u}(Z)$ and the fitting to the NIG distribution (solid black line). As one can evidence in Figure 3-9, neither the empirical PDF of $\Delta^t_{x,u}(Z)$ fits to the NIG distribution nor the variance σ^2 gets a stable value as the spatial lags increase, i.e. the variance is an increasing function depending on the spatial lag. Therefore, this last states that

$$\mathrm{Var}\{\Delta^t_{x,u}(Z)\} \neq \mathrm{Var}\{\Delta^t_{x,v}(Z)\} \tag{3-31}$$

and

$$\Delta^t_{x,u}(R) \overset{\text{dist}}{\neq} \Delta^t_{x,v}(R) \tag{3-32}$$

[7] In scale–invariant multiplicative cascades, $c_{\epsilon_1,\ldots,\epsilon_j} = c_0 \prod_{i=1}^{j} W_{\epsilon_j}$, the random weights W_{ϵ_j} are uncorrelated [Arneodo et al., 1998].

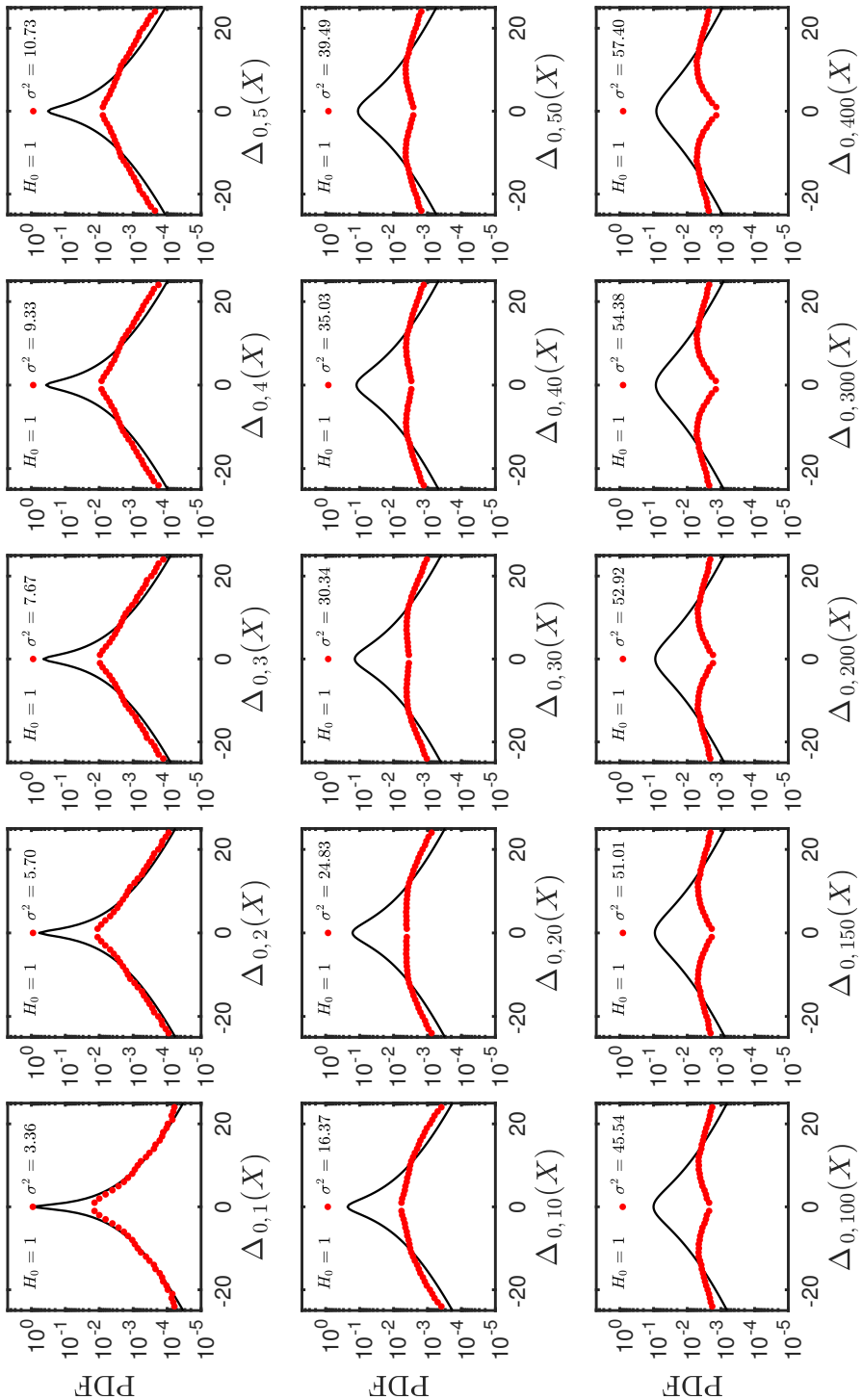

Figure 3-9: Probability density function of the increments $\Delta_{t,u}$ of the reflectivity fields (Z) measured by the Early Warning System of Medellín and Aburra's Valley (SIATA) on May 18th of 2018. The increments were obtained taking as a pivot point, the maximum observation recorded at 11:58 (GMT-5) and for $u = \{\Delta x, 2\Delta x, 3\Delta x, 4\Delta x, 5\Delta x, 10\Delta x, 20\Delta x, 30\Delta x, 40\Delta x, 50\Delta x, 100\Delta x, 150\Delta x, 200\Delta x, 300\Delta x, 400\Delta x\}$ where $\Delta(x) = 125$ m. In every plot, the red dots represent the empirical PDF and the solid line represents the normal inverse Gaussian distribution fitted to the rainfall observations. In each frame is indicated the value of null hypothesis H_0 (zero for the acceptance of H_0 and one for the rejection of H_0; both values for a 5% of significance level α). The null hypothesis states data come from a normal inverse Gaussian distribution.

In this sense, the disagreement between the empirical PDF and the NIG distribution determines that observations are not building by intermittent measures as seen in punctual observations (see section 3.2.1). However, Figure 3-9 shows that the NIG distribution represents adequately the tails of the empirical PDFs for the increments $\Delta^t_{x,u}(Z)$ when the spatial lag $u \leq 10\,\Delta x$. There also exists a kind of geometric similarity between empirical PDFs when $u \geq 30\,\Delta x$. Summing up, the incremental similarity analysis over the reflectivity field Z do show reflectivity fields are not made by intermittent measures which would explain the lack of singularity scaling exponents in multifractal spectra. The statistical structure for the selected reflectivity fields could be qualified as that of a weak multifractality process exists for generating patterns.

As a final test to verify the non–linear (multifractal) structure of the reflectivity field, the identification of dynamic scaling in such observations was looked into. In Figure C-1, one can observe a space–time plot, also known as Hövmoller diagram[8], based on reflectivity observations recorded on May 18th of 2018 from 00:00 to 14:00 h (GMT-5) by SIATA's weather radar. The space–time plot shown in Figure C-1 was build by means of averaging every reflectivity field in both orthogonal directions (i.e. East–West (left panel of Figure C-1) and North-South (right panel of Figure C-1). In the upper panels of Figure 3-10 are shown the isocorrelation contours of the 2D Fourier space for the reflectivity field Z. Left upper panel represents the Fourier space for the x–t section (South–North direction average) and the right upper panel represents the Fourier space for the y–t section (East–West direction average). In the upper panels are indicated two orthogonal lines that representing two cuts in the Fourier space, when $\omega \approx 0$ or $k_{x,y} \approx 0$. The slope values of these lines are shown in the lower panels with the same colors as they were drawn into the Fourier space, i.e. the red dashed line is representing the cut for $\omega \approx 0$ and $P(k_{x,y})$ and the blue dashed line is representing the cut for $k_{x,y} \approx 0$ and $P(\omega)$. Moreover, the lower panels of Figure 3-10 identify the slopes as β_k for the cut in the wavenumber domain and β_ω for the cut in the frequency domain.

The computed slopes β_k and β_ω are used for estimating the dynamic scaling (or anisotropy) exponent H, as indicated in equation 3-27. The scaling dynamic exponent for the averaged values of the reflectivity field is approximated $H \approx 1/2$ for both orthogonal directions. Initially, this result is representing a homogeneous reflectivity field Z and a particular space–time symmetry. A dynamic scaling exponent equals to $H \approx 1/2$ disagrees to that expected in the turbulence theory, $H \approx 1/3$ [Marzan et al., 1996], however, this value is alike to that of the non–conservative scalar fields exhibit (e.g. Allen–Cahn equation) and it suggests a growth law based on non–conserved dynamics [Bray, 1994]. This last means that after time t there will be no domains smaller than $t^{1/2}$, thus the characteristic domain size is $L \sim t^{1/2}$.

[8] In this diagram the information is organized in either time or space. The vertical axis is commonly selected for time and the horizontal axis for space. Figures C-1 show the time axis is defined every 5 min from 00:00 h to 14:00 h, and the spatial axis is defined by the observational spatial range of the SIATA's weather radar, i.e. 119.94 km with a spatial resolution of 250 m approximately.

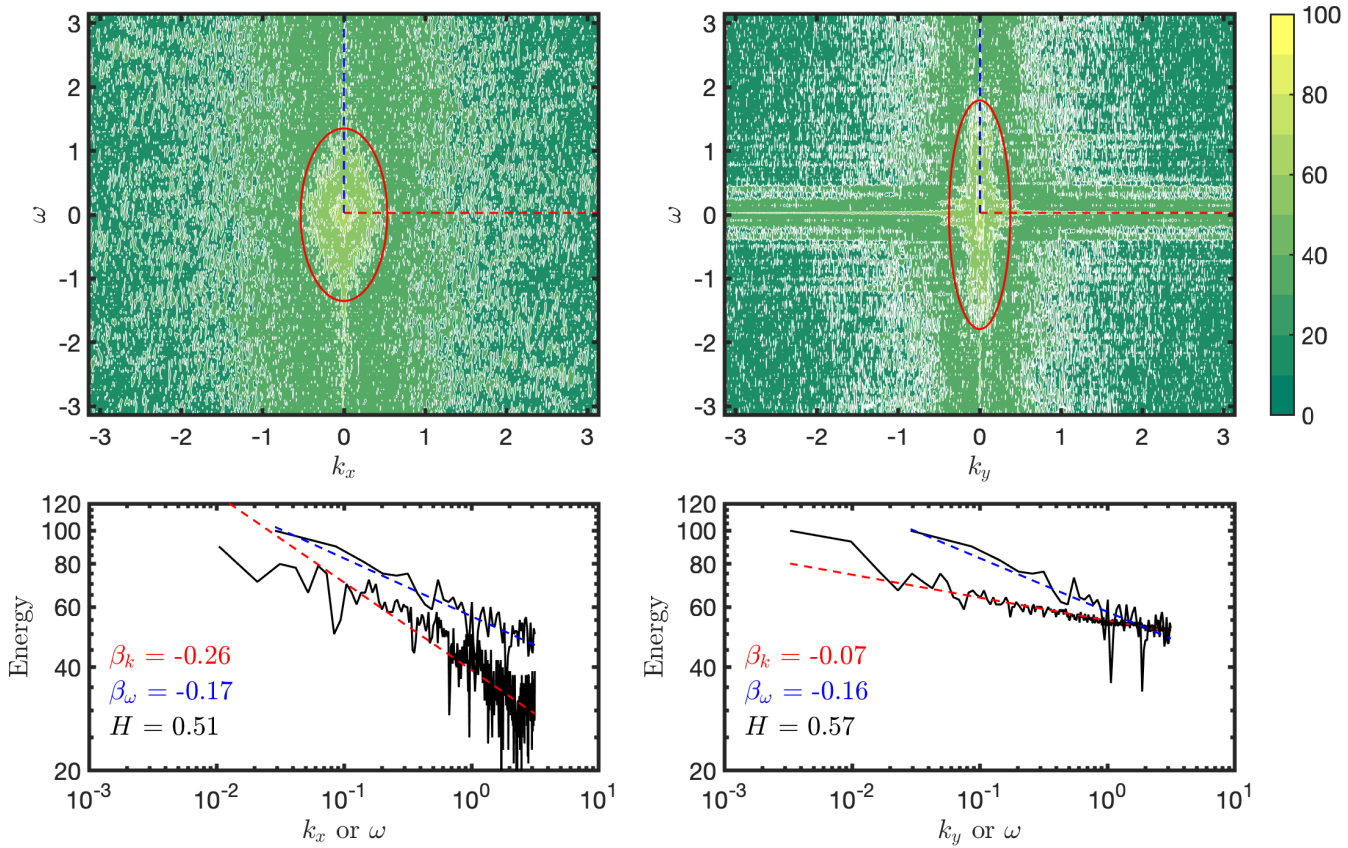

Figure 3-10: Isocorrelation contours in the 2D Fourier space for the x–t section (upper left panel) and the y–t section (upper right panel) of the averaged values of reflectivity fields (Z) measured by the Early Warning System of Medellín and Aburra's Valley (SIATA) on May 18th of 2018 from 00:00 to 14:00 h (GMT-5). The lower panels are representing two cuts in the $2D$ Fourier spectra in the wavelength direction ($k.$) and frequency direction $f.$. In the lower panels are indicated the slopes β of each cuts in the Fourier spectra and besides the scaling anisotropy exponent H is computed from these values. The ellipse indicated in the upper panel is identifying the geometry of one contour in the $2D$ Fourier spectra. The ellipse in the upper left panel have a length of $0.43\,\pi$ and width of $0.17\,\pi$ and the ellipse in the upper right panel have a length of $0.57\,\pi$ and width of $0.12\,\pi$.

3.2.3. Satellite Rainfall Fields

From the product 3B42 (version 7) of the Tropical Rainfall Measuring Mission (TRMM[9]) has been selected some satellite rainfall fields. Product 3B42 v7 [TRMM, 2011] provides SG–merged precipitation estimates at Level 3 (L3), i.e. records every 3 hour with spatial resolution $0.25° \times 0.25°$ quasi–global (50° North–South) gridded SG–rainfall database, resulting from the mean of satellite rainfall estimates (S) and gauge data (G) [Huffman et al., 2007]. For the purpose of this research, the records of the year 2015 were selected. This data set were re–organized in four groups following an specific time definition, i.e. a first group (Gr1) from January 1st to March 31st, a second group (Gr2) from April 1st to June 30th, a third group (Gr3) from July 1st to September 30th and a four group (Gr4) from October 1st to December 31st. In Figures D-1 to D-4, one can observe a spatial plot of the average field, the maximum field and the standard deviation field for the selected four–group of data. These plots were framed in the latitudes 30° S to 30° N.

Figures 3-11 to 3-14 show the spatial estimates of the spatial average values for ($\overline{R}$), maximums ($\max\{R\}$), and standard deviations σ. Furthermore, the fractional wet area (FWA) of TRMM precipitation which were obtained for the latitudes 30° S – 30° N and longitudes 180° E – 180° W, is also exhibited in Figures 3-11 to 3-14. In the group Gr1, the mean precipitation is below 1.5 mm/h most of the time and no important peaks are observed in the maximum records, so this time period represents a dry season in the year 2015. In groups Gr2 and Gr3, there exists a more dynamic averaged–precipitation time series and a more active season of strong rainfall events, so these time periods represent a wet season in the year 2015. The group Gr4 does not exhibit the same quality in the precipitation statistics of the other groups, however, it is characterized by having more peaks (or events) of strong precipitation and its averaged precipitation is near to ≈ 1.5 mm/h. It is to highlight that the precipitation variability in indeed more unstable in the selected precipitation seasons. In Gr1 is observed that the precipitation variability is $\sigma \approx 2$ mm/h in the months of January and February, and it changes to $\sigma \approx 1.7$ at the end of the season. In Gr2, the precipitation variability is approximately $\sigma \approx 2$ mm/h in the months of April and May, and it increases to $\sigma \approx 2.3$ in June. In Gr3, the precipitation variability is above of 2 mm/h in the months of July, August and September and it is almost $\sigma \approx 2$ at the end of the season. Another remark about the precipitation statistics in the selected seasons is how the fractional wet area (FWA) changes over time. During the dry season (Gr1) the FWA is almost 9% and during the wet season (Gr2 and Gr3), the FWA slightly decreases apart from 9%., which indicates the development of cloud clustering and isolated rainfall events in the tropical region.

[9]The Tropical Rainfall Measuring Mission (TRMM) is a joint NASA–JAXA satellite mission to monitor the rainfall in the tropical region. TRMM was launch on November 27 of 1997 from the Tanegashima Space Center in Japan. TRMM satellite is equipped with 5 instruments: a Precipitation Radar (PR), an electronically scanning radar operating at 13.8 GHz; a TRMM Microwave Image (TMI), a nine-channel passive microwave radiometer; and Visible and Infrared Scanner (VIRS) [GES DISK, 2017].

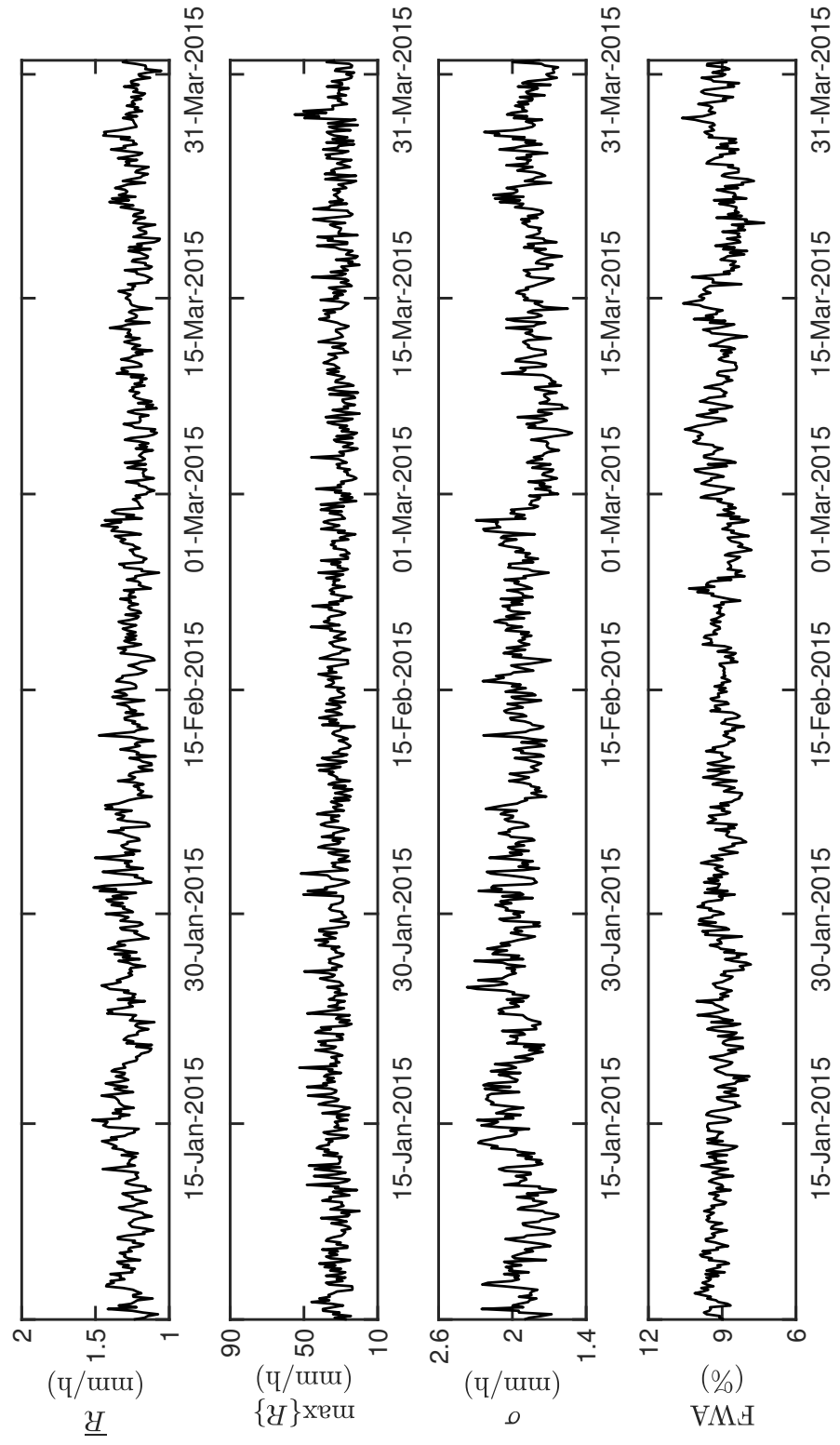

Figure 3-11: Time variation of the mean ($\overline{R}$), maximum observed value ($\max\{R\}$), standard deviation (σ) and the fractional wet area for the rainfall intensity fields observed by the TRMM satellite mission from January 1st of 2015 at 00:00 h to April 1st of 2015 at 00:00 h (GMT-5).

Figure 3-12: Time variation of the mean ($\overline{R}$), maximum observed value ($\max\{R\}$), standard deviation (σ) and the fractional wet area for the rainfall intensity fields observed by the TRMM satellite mission from April 1st of 2015 at 00:00 h to July 1st of 2015 at 00:00 h (GMT-5).

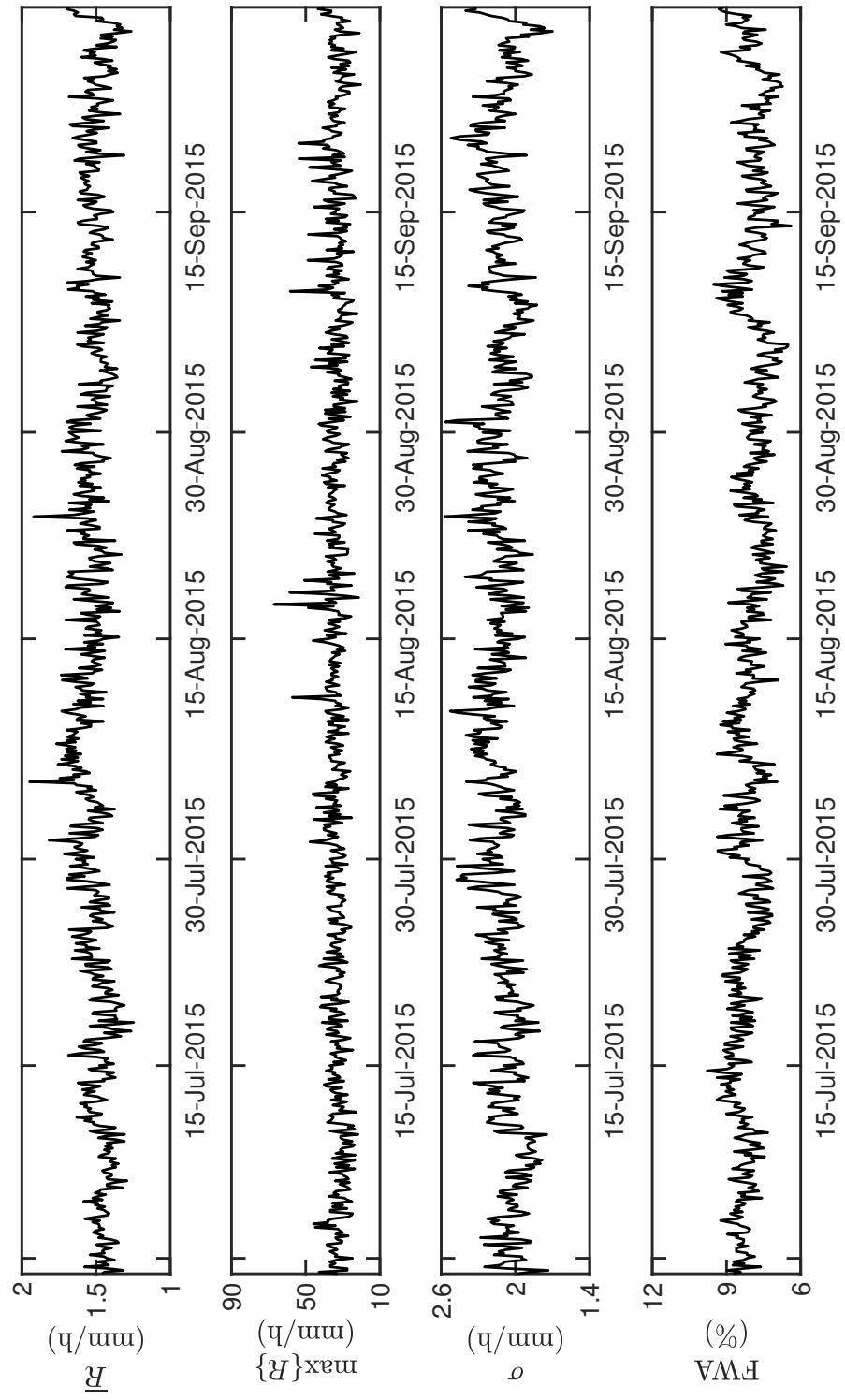

Figure 3-13: Time variation of the mean ($\overline{R}$), maximum observed value ($\max\{R\}$), standard deviation (σ) and the fractional wet area for the rainfall intensity fields observed by the TRMM satellite mission from Jule 1st of 2015 at 00:00 h to October 1st of 2015 at 00:00 h (GMT-5).

Figure 3-14: Time variation of the mean ($\overline{R}$), maximum observed value ($\max\{R\}$), standard deviation (σ) and the fractional wet area for the rainfall intensity fields observed by the TRMM satellite mission from October 1st of 2015 at 00:00 h to January 1st of 2016 at 00:00 h (GMT-5).

The multifractal spectra of TRMM–precipitation records are exhibited in Figure 3-15. They do not seem to change over time and to be influenced by seasonal atmospheric conditions, however, some remarks can be derived from estimated spectra. They are indicating the measures (recovered by the TRMM–precipitation records) are not singular since $\alpha > 1$ and such a condition is described by spatial patterns of low intermittency. The atmosphere as a whole seems to be in equilibrium over time which is represented by its quasi–constant fractal dimension of the support D_0 whose value is approximately ≈ 1.48. The spectral width, $H_\alpha = \alpha_{max} - \alpha_{min}$, could be defined as an identifier of the season, such that for the dry season (Gr1) the spectral width is $H_\alpha \approx 1.8$, and for the wet seasons (Gr2 and Gr3) the spectral width is $H_\alpha \approx 1.7$. So, for higher values of H_α, the rainfall events are less frequent and it means there could be a dry season in the time where data were recorded.

Table 3-7 show a summary of the statistics of some multifractal descriptors in accordance to the observation season. Clearly, the multifractal descriptors are nearly the same for the wet seasons (Gr2 and Gr3) and they are slightly different to those observed in the dry season (Gr1). As it was aforementioned, the value of D_0 is higher in the dry season than in wet season, however, the value of D_2 (the correlation dimension) is higher in the wet season than in the dry season. The value of D_2 connects with the existence or not of a long–range correlation; during the wet season where the value of D_2 is higher, therefore it is expected to find rainfall events highly correlated among them. The dynamic of the multifractal descriptors can be depicted in Figures 3-16 to 3-19. In the dry season the singularity exponent α_{min} seems to fluctuate around ≈ 0.73 during January to March, and after March it starts to grow. The wet season which stars in early April and ends in late August, the singularity exponent α_{min} seems to fluctuate around ≈ 0.77. The fractal dimension associated to the singularity exponent α_{min} looks rather random but bound in the range $\{0.0, 0.2\}$. The singularity exponent α_{max} fluctuates around ≈ 2.54 during the months of January to March, and after March it starts to decay around the mean value of $\alpha_{max} \approx 2.51$. In the wet season, the singularity exponent α_{max} fluctuates around ≈ 2.43. In similar manner, the fractal dimension associated to the singularity exponent α_{max} looks rather random and it is also bound in the range $\{0.0, 0.2\}$.

Since January to early April, α_0 is decaying from $\alpha_0 \approx 1.64$ to $\alpha_0 \approx 1.60$, and after mid April to late December, α_0 fluctuates around ≈ 1.60. The dimension D_0 is roughly stable throughout the year whose value is approximately ≈ 1.48, nonetheless, D_0 tends to be slightly higher during the dry season than in the wet season. Furthermore, D_0 fluctuates more in the wet season than in the dry season, thus is suspected that D_0 could be associated to the atmospheric stability. The singularity exponents α_1 and α_2 behave in a similar way to α_0, furthermore, their associated fractal dimensions seems to behave alike to them. As one can evidence in the plots, throughout the year, α_1 fluctuates between 1.35 and 1.36, being slightly higher in the wet season (Gr2 and Gr3) and highly fluctuating in the transition season Gr4. The behavior of α_2 is characterized by jumps in different time points. In early March, it is observed a change of value from $\alpha_2 \approx 1.02$ to $\alpha_2 \approx 1.08$ and in mid April from $\alpha_2 \approx 1.05$ to $\alpha_2 \approx 1.11$. This last value is quite steady until late August, then it decays to $\alpha_2 \approx 1.09$ in late December.

The multifractal descriptors here indicated in time series, characterize the dynamic of the rainfall field, albeit the representation of such a dynamic should be understood through small changes in their quantities but not in their gross statistics. As shown in Table 3-7, the multifractal descriptors are rather stable throughout the year, the highest values of the coefficient of variability is 3.47% for D_2 and 3.22% for α_{min}, therefore, the gross statistics of the multifractal descriptors describes an equilibrium in the physical processes associated to rainfall dynamics. These results suggest that only t fluctuations in the multifractal descriptor could help to understand space–time dynamics of the rainfall field.

Table 3-7: Statistics of the multifractal variables: $\alpha_{min} \equiv \min\{\alpha\}$, $\alpha_{max} \equiv \max\{\alpha\}$, α_0, α_2, $f(\alpha_{min})$, $f(\alpha_{max})$, $D_0 = f(\alpha_0)$, $D_1 = f(\alpha_1) = \alpha_1$, and $D_2 = f(\alpha_2)$, which were obtained from the TRMM satellite mission observations of rainfall intensity in the year 2015. Observations were bound to the the latitudes 30°S and 30°N.

	From January 1st of 2015 to April 1st of 2015							From April 1st of 2015 to July 1st of 2015						
	α_{min}	α_{max}	α_0	α_2	D_0	D_1	D_2	α_{min}	α_{max}	α_0	α_2	D_0	D_1	D_2
Minimum	0.66	2.43	1.60	0.99	1.46	1.32	0.83	0.69	2.29	1.56	1.03	1.45	1.33	0.89
Mean	0.73	2.54	1.63	1.05	1.49	1.35	0.91	0.77	2.43	1.60	1.11	1.48	1.36	0.99
Median	0.73	2.54	1.64	1.05	1.49	1.35	0.90	0.77	2.43	1.60	1.11	1.48	1.36	0.99
Maximum	0.79	2.65	1.67	1.12	1.52	1.38	1.00	0.84	2.58	1.65	1.19	1.51	1.39	1.10
σ	0.02	0.03	0.01	0.02	0.01	0.01	0.03	0.02	0.04	0.01	0.02	0.01	0.01	0.03
CV (%)	3.04	1.32	0.69	2.34	0.52	0.82	3.46	3.05	1.72	0.81	2.01	0.62	0.74	2.92
IQR	0.03	0.04	0.01	0.04	0.01	0.02	0.04	0.03	0.05	0.02	0.03	0.01	0.01	0.03
γ	0.12	-0.04	-0.19	0.36	-0.21	0.24	0.35	-0.46	0.66	0.24	-0.82	-0.22	-0.20	-0.90
	From July 1st of 2015 to October 1st of 2015							From October 1st of 2015 to January 1st of 2016						
	α_{min}	α_{max}	α_0	α_2	D_0	D_1	D_2	α_{min}	α_{max}	α_0	α_2	D_0	D_1	D_2
Minimum	0.69	2.31	1.55	1.01	1.45	1.32	0.87	0.69	2.35	1.57	1.02	1.46	1.32	0.88
Mean	0.77	2.42	1.60	1.11	1.48	1.36	0.99	0.76	2.46	1.61	1.09	1.48	1.35	0.96
Median	0.77	2.42	1.60	1.11	1.48	1.36	0.99	0.76	2.46	1.61	1.09	1.48	1.35	0.96
Maximum	0.83	2.54	1.62	1.18	1.50	1.39	1.08	0.82	2.55	1.63	1.16	1.51	1.38	1.05
σ	0.02	0.04	0.01	0.03	0.01	0.01	0.03	0.02	0.03	0.01	0.02	0.01	0.01	0.03
CV (%)	3.22	1.56	0.75	2.48	0.68	0.98	3.47	2.99	1.36	0.64	2.17	0.57	0.84	3.10
IQR	0.04	0.05	0.02	0.04	0.01	0.02	0.05	0.03	0.04	0.01	0.03	0.01	0.02	0.04
γ	-0.38	0.07	-0.30	-0.56	-0.21	-0.49	-0.53	-0.14	0.05	-0.15	-0.03	-0.11	0.00	-0.05

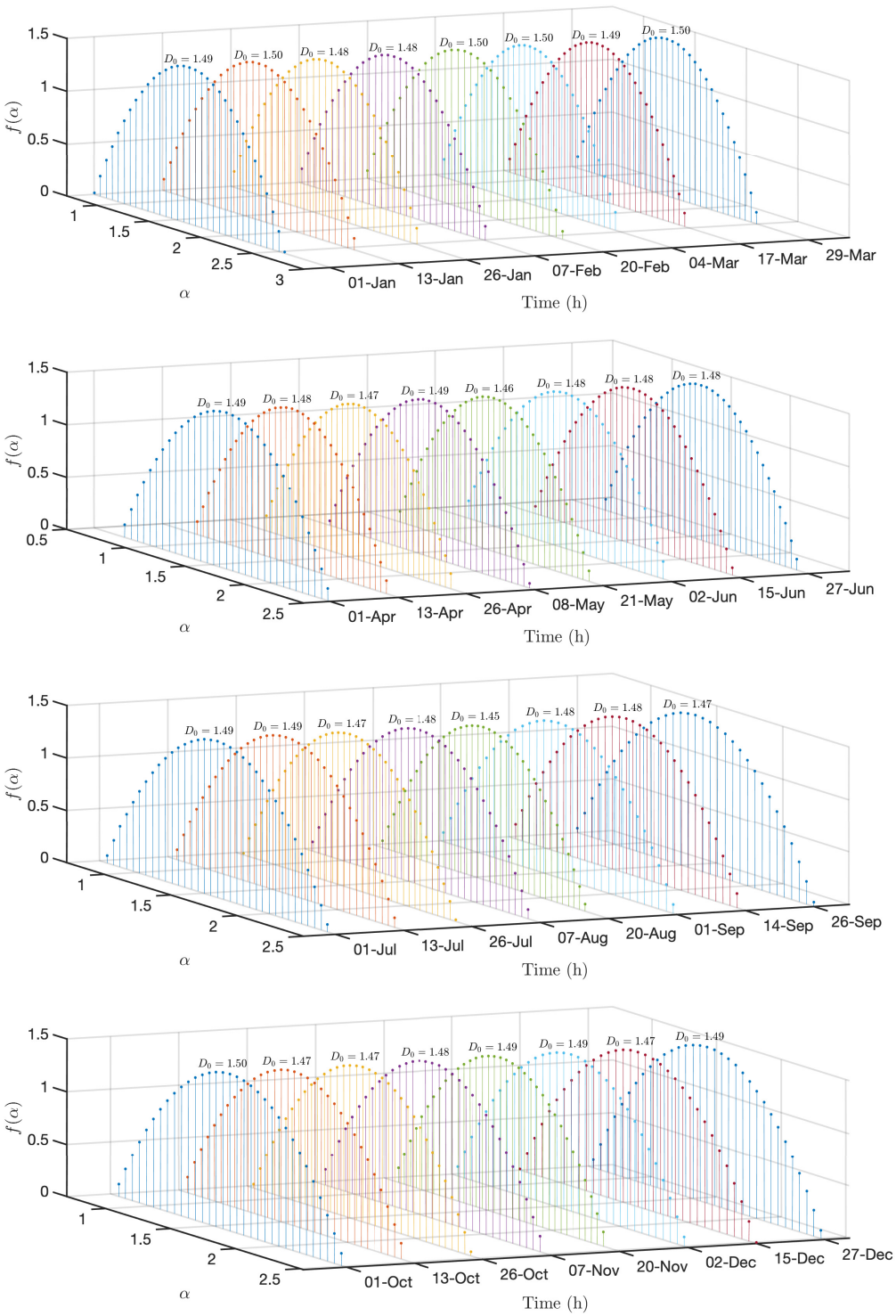

Figure 3-15: Time evolution of the estimated multifractal spectrum for the TRMM satellite mission observations of rainfall intensity in the year 2015 over the tropical region defined between the latitudes 30°S and 30°N.

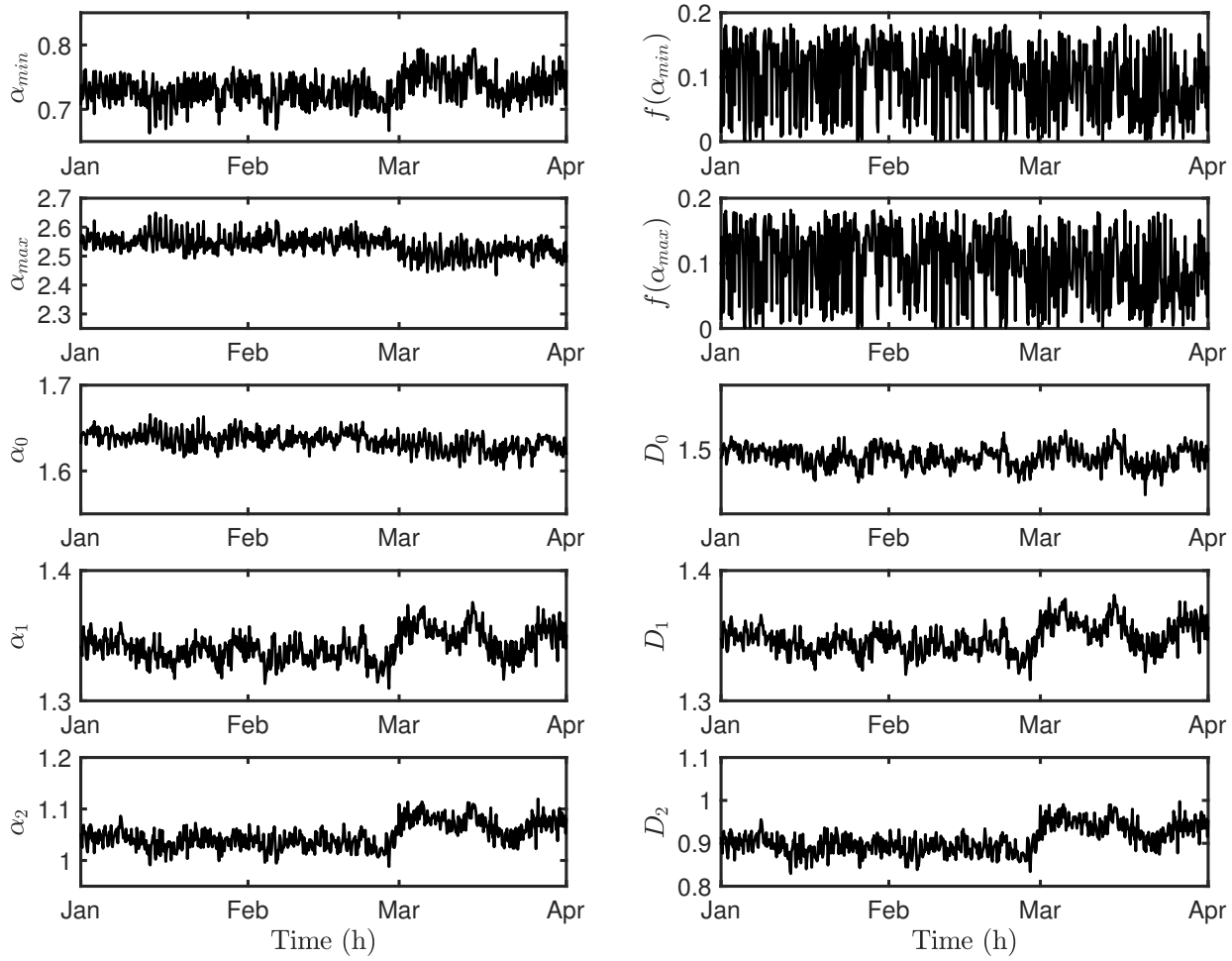

Figure 3-16: Time variation of the multifractal variables: $\alpha_{min} \equiv \min\{\alpha\}$, $\alpha_{max} \equiv \min\{\alpha\}$, α_0, α_1, $f(\alpha_{min})$, $f(\alpha_{max})$, $D_0 = f(\alpha_0)$ (dimension of the support), $D_1 = f(\alpha_1)$ (dimension of the concentrated measure), and $D_2 = f(\alpha_2)$ (correlation dimension). All these variables were obtained from the TRMM satellite mission observations of rainfall intensity (in mm/h) between January 1st to April 1st of 2015 over the tropical region defined between the latitudes 30°S and 30°N..

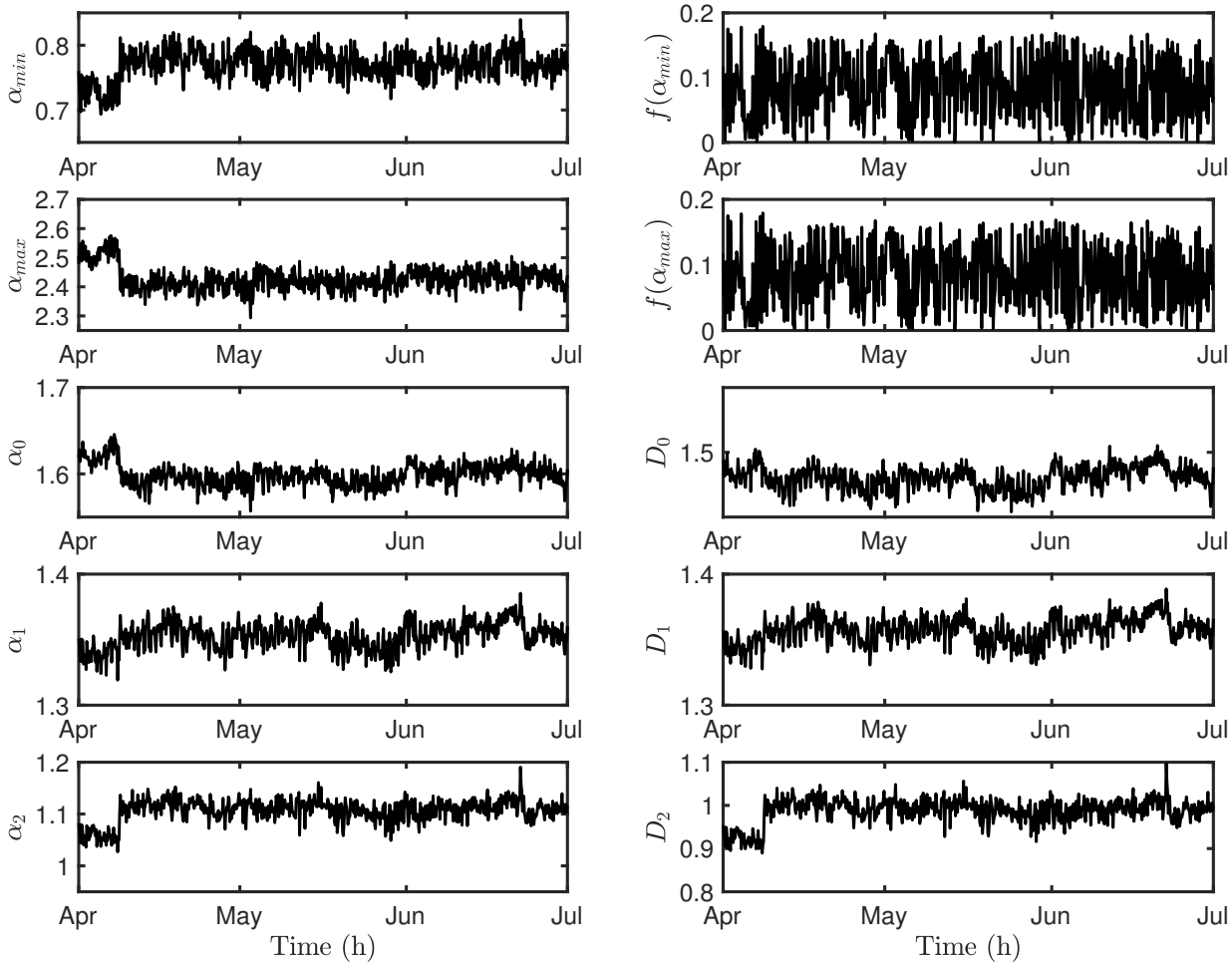

Figure 3-17: Time variation of the multifractal variables: $\alpha_{min} \equiv \min\{\alpha\}$, $\alpha_{max} \equiv \min\{\alpha\}$, α_0, α_1, $f(\alpha_{min})$, $f(\alpha_{max})$, $D_0 = f(\alpha_0)$ (dimension of the support), $D_1 = f(\alpha_1)$ (dimension of the concentrated measure), and $D_2 = f(\alpha_2)$ (correlation dimension). All these variables were obtained from the TRMM satellite mission observations of rainfall intensity between April 1st to July 1st of 2015 over the tropical region defined between the latitudes 30°S and 30°N..

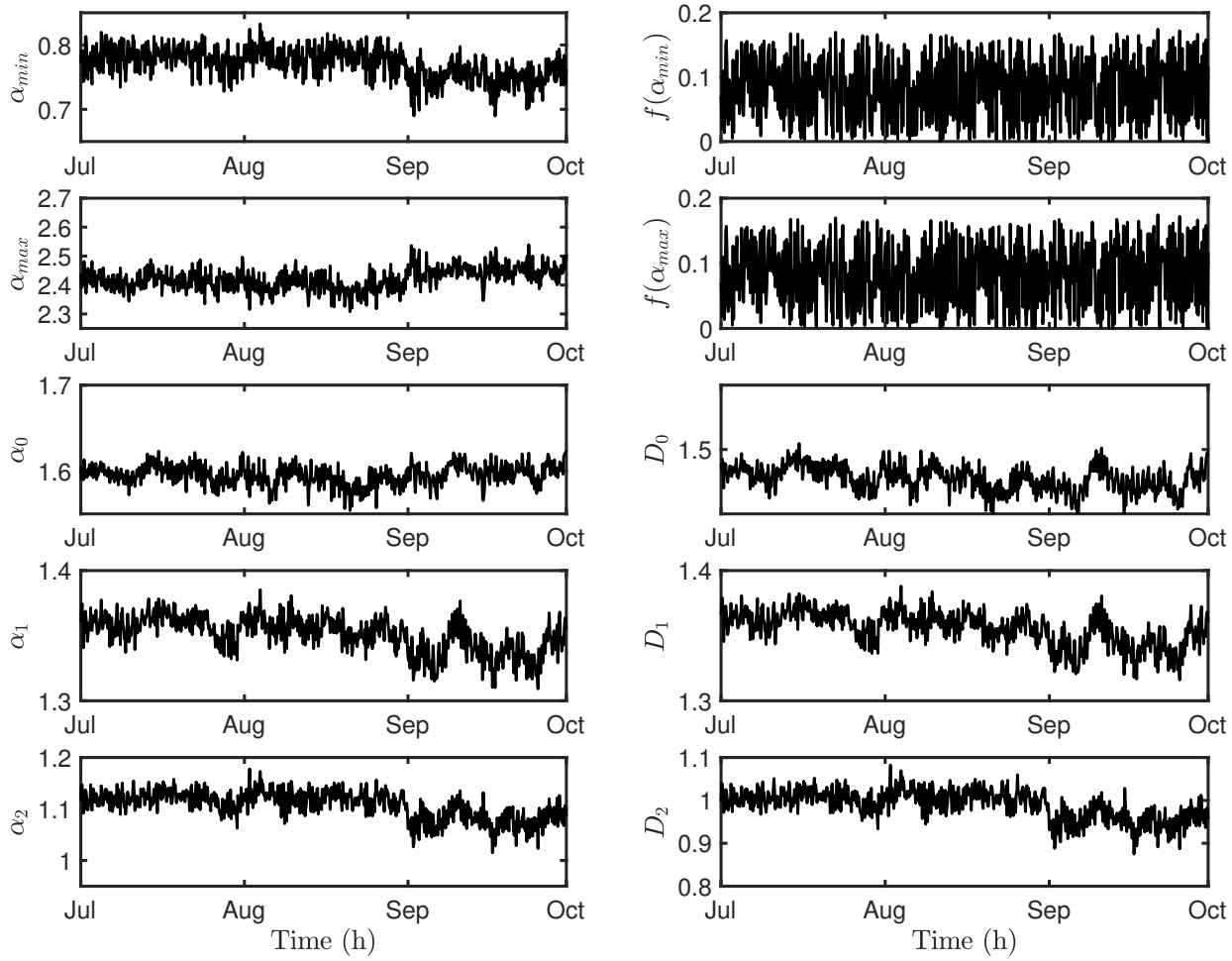

Figure 3-18: Time variation of the multifractal variables: $\alpha_{min} \equiv \min\{\alpha\}$, $\alpha_{max} \equiv \min\{\alpha\}$, α_0, α_1, $f(\alpha_{min})$, $f(\alpha_{max})$, $D_0 = f(\alpha_0)$ (dimension of the support), $D_1 = f(\alpha_1)$ (dimension of the concentrated measure), and $D_2 = f(\alpha_2)$ (correlation dimension). All these variables were obtained from the TRMM satellite mission observations of rainfall intensity between July 1st to October 1st of 2015 over the tropical region defined between the latitudes 30°S and 30°N..

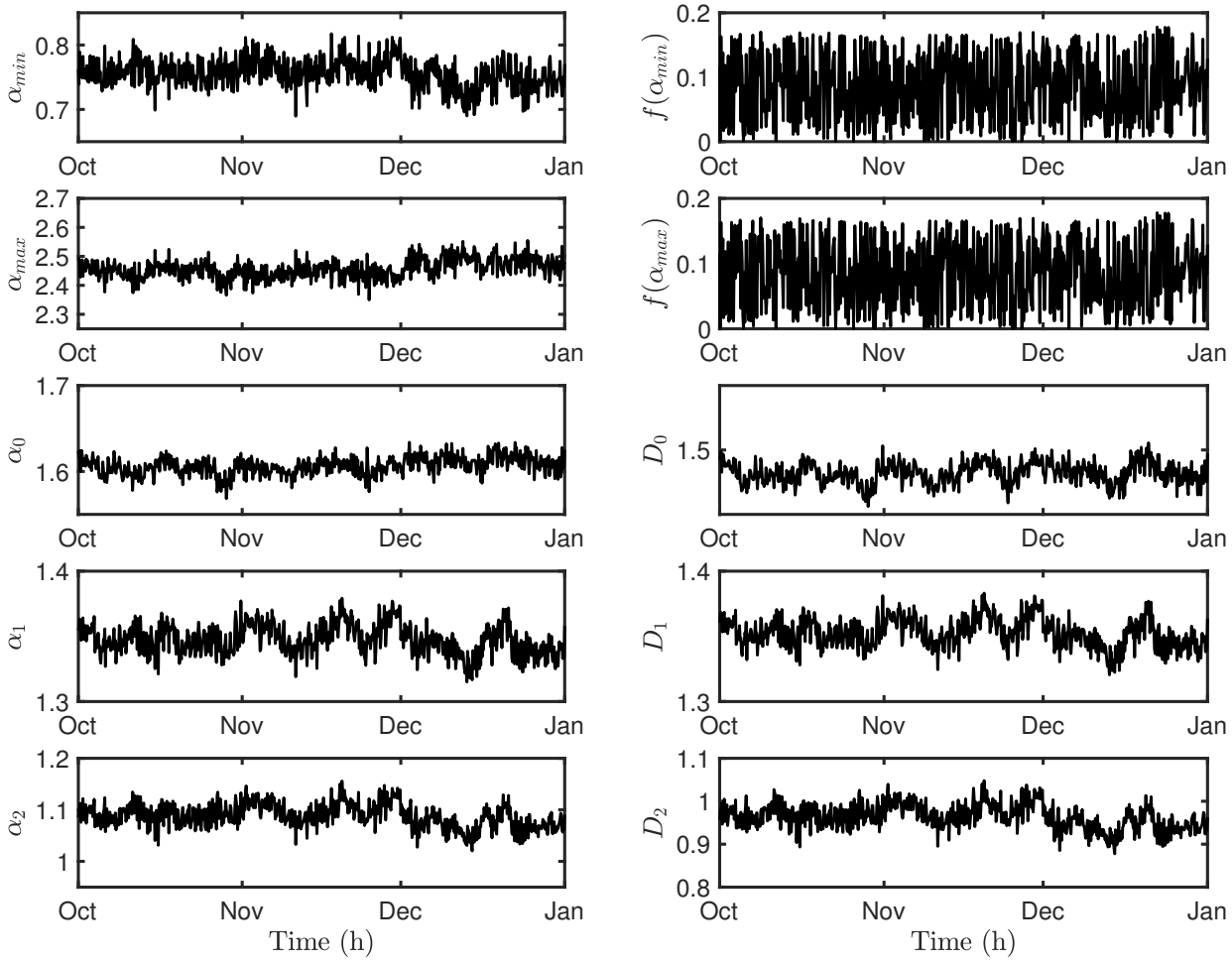

Figure 3-19: Time variation of the multifractal variables: α_{min}, α_{max}, α_0, α_1, $f(\alpha_{min})$, $f(\alpha_{max})$, $D_0 = f(\alpha_0)$ (dimension of the support), $D_1 = f(\alpha_1)$ (dimension of the concentrated measure), and $D_2 = f(\alpha_2)$ (correlation dimension). All these variables were obtained from the TRMM satellite mission observations of rainfall intensity between October 1st of 2015 to January 1st of 2016 over the tropical region defined between the latitudes 30°S and 30°N.

The cumulant-based magnitude coefficients of TRMM–precipitation records also show evidence of non–linearity in the rainfall field, nevertheless, an interesting fact was found in the coefficients C_0 and C_2 of equation 3-11. They also present a non–linear dynamic in the time as multifractal descriptors do. Figure 3-20 show a plot of coefficients C_0 and C_2 as a function of time. The solid blue and black lines represent the four studied seasons. The red line in the plots are indicating the average value of the coefficients during the season. As it can be observed in Figure 3-20, the average value of C_0 seems to change as the seasons pass, whereas C_2 seems to change only once at the mid year. In Figure 3-20, C_0 and C_2 gets the smallest values during the wet season (Gr2 and Gr3) and C_0 gets the highest value in the dry season.

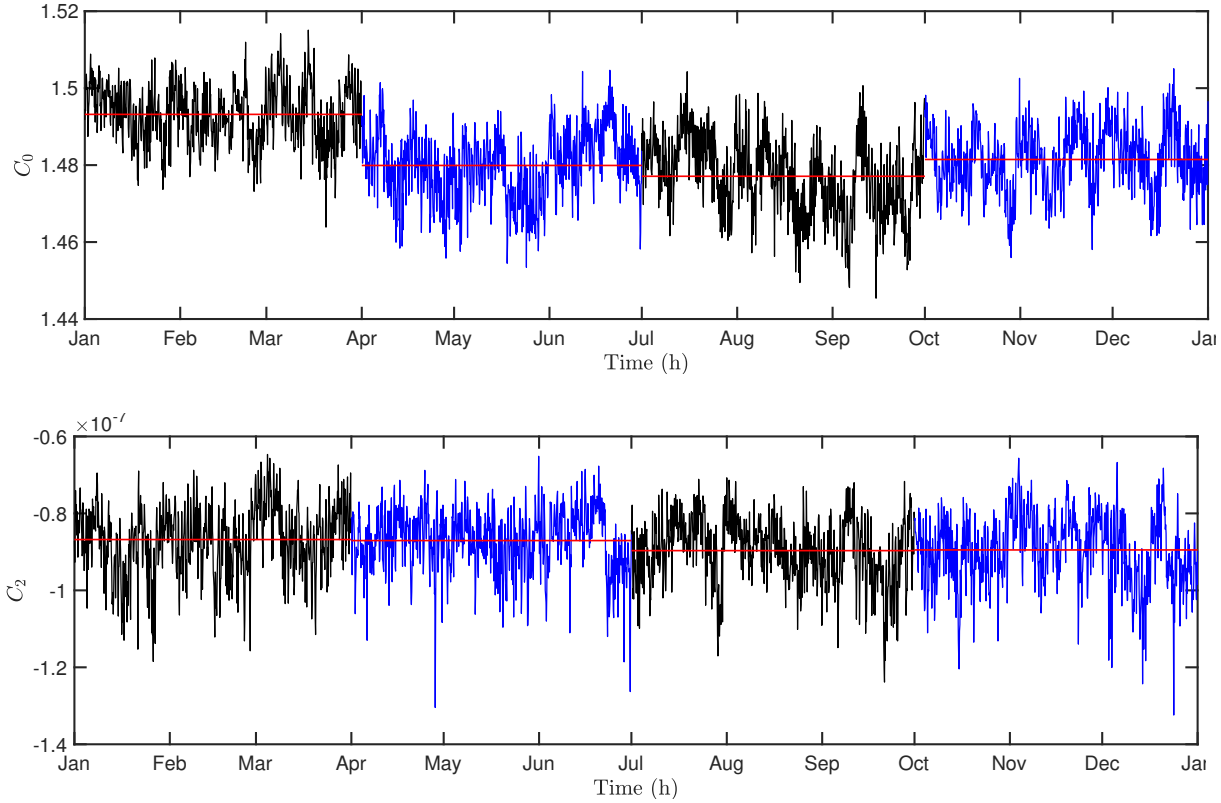

Figure 3-20: Time variation of the cumulant-based magnitude coefficients C_0 and C_2 which were computed from the product 3B42 v7 of TRMM satellite mission in the year 2015. The estimations were obtained over the region defined between the latitudes 30°S and 30°N. The coefficient C_1 was not plotted because it does not present variability in the time of observation, rather a constant value equal to -5.03×10^{-5}.

In Figure 3-21, one can observe the two–point correlation functions of either maximums or averages values of rainfall intensity. Moreover, Figure 3-21 shows two–point correlation functions for different spatial scales; the upper left panel (Figure 3-21 (a)) for the spatial scale $\delta = \Delta x = 0.25° \approx 27.7$ km, the upper right panel (Figure 3-21 (b)) for the spatial scale $\delta = \Delta x = 0.50° \approx 55.5$ km, the lower left panel (Figure 3-21 (c)) for the spatial scale

$\delta = \Delta x = 0.75^\circ \approx 83.2$ km, and the lower right panel (Figure 3-21 (d)) for the spatial scale $\delta = \Delta x = 1.00^\circ \approx 110.9$ km.

In the original spatial resolution of the product 3B42 v7 (i.e. $\delta \approx 27.7$ km), a linear–logarithm decay in the correlation functions is observed. This behavior in the correlation functions indicates there exists a long–range correlation in the rainfall field. Moreover, the relationship between $C(\delta \approx 27.7, \Delta x)$ and $\ln(\Delta x)$ is linear for $\Delta x > \delta$. Since the slope of the relation $C(\delta, \Delta x)$ vs $\ln(\Delta x)$ is bigger than zero, such a result suggests the presence of multifractality. For the other spatial scales (i.e. $27.7 \lessapprox \delta \lessapprox 110.9$ km), the long–range correlation is also held, albeit it can not be good represented by a logarithmic equation when the Δx-value is large enough, so for the scales δ bigger than the original–observational scale there could be a kind of perturbation, possibly it was induced during the data manipulation. Thus, the long–term correlation and the scale independence in the TRMM–precipitation records, suggest not only the existence of multifractality, but also its representation through multiplicative cascade processes.

Regarding the incremental similarity (IS) analysis, evidence of multifractality in TRMM–precipitation records were also found on it. In Figure 3-22 is depicting the empirical PDF of the increment $\Delta_{t,u}$ of TRMM's rainfall intensity (red dots). The increments were taken in a spatial way, first selecting one of the most intense precipitation record and secondly taking the increments $\Delta_{t,u}$ from the spatial point where the most intense rainfall event took place at time t, so u is representing a spatial distance from the core of the storm. Figure 3-22 also shows the fitting to a NIG distribution (black solid line) and its fitting test result (i.e. $H_0 = 1$ for rejection and $H_0 = 0$ for acceptance, where H_0 is the null hypothesis).

Under the aforementioned conditions, the IS analysis reveals some remarkable observations: i) TRMM spatial rainfall patterns are highly intermittent as seen in turbulence processes and the main evidence is the form of the empirical PDF of the rainfall–intensity increments $\Delta_{t,u}$ and its comparison with the results obtained by Barndorff-Nielsen & Schmiegel [2015] and Barndorff-Nielsen et al. [2004]; ii) the NIG distribution seems to represent suitably the statistical law of TRMM rainfall–intensity increments, nevertheless, there exist important differences in the tails of the distribution, whereby the null hypothesis is rejected for long enough u. Furthermore, according to results exhibited in Figure 3-22, there exists a correlation length which possibly determines the validity of the NIG law; and iii) the variance σ^2 increases inasmuch as u is higher, however for long enough values of u, the variance σ^2 is roughly stable. In the distributions exhibited in Figure 3-22 where σ^2s are almost similar (e.g. the distributions for $\Delta_{0,40}$ and $\Delta_{0,50}$ in which $\sigma^2 \approx 1.35$), the IS property, i.e. $\Delta_{t,u}(Y) \overset{\text{dist}}{=} \Delta_{t,v}(X)$, is valid for the time t when strong rainfall events take place. As a final remark, the results indicated above offer evidence of an intrinsic multifractal process in the statistical description of the product 3B42 v7, and seemingly, there is not dependence of the spatial scale for identifying such a multifractality.

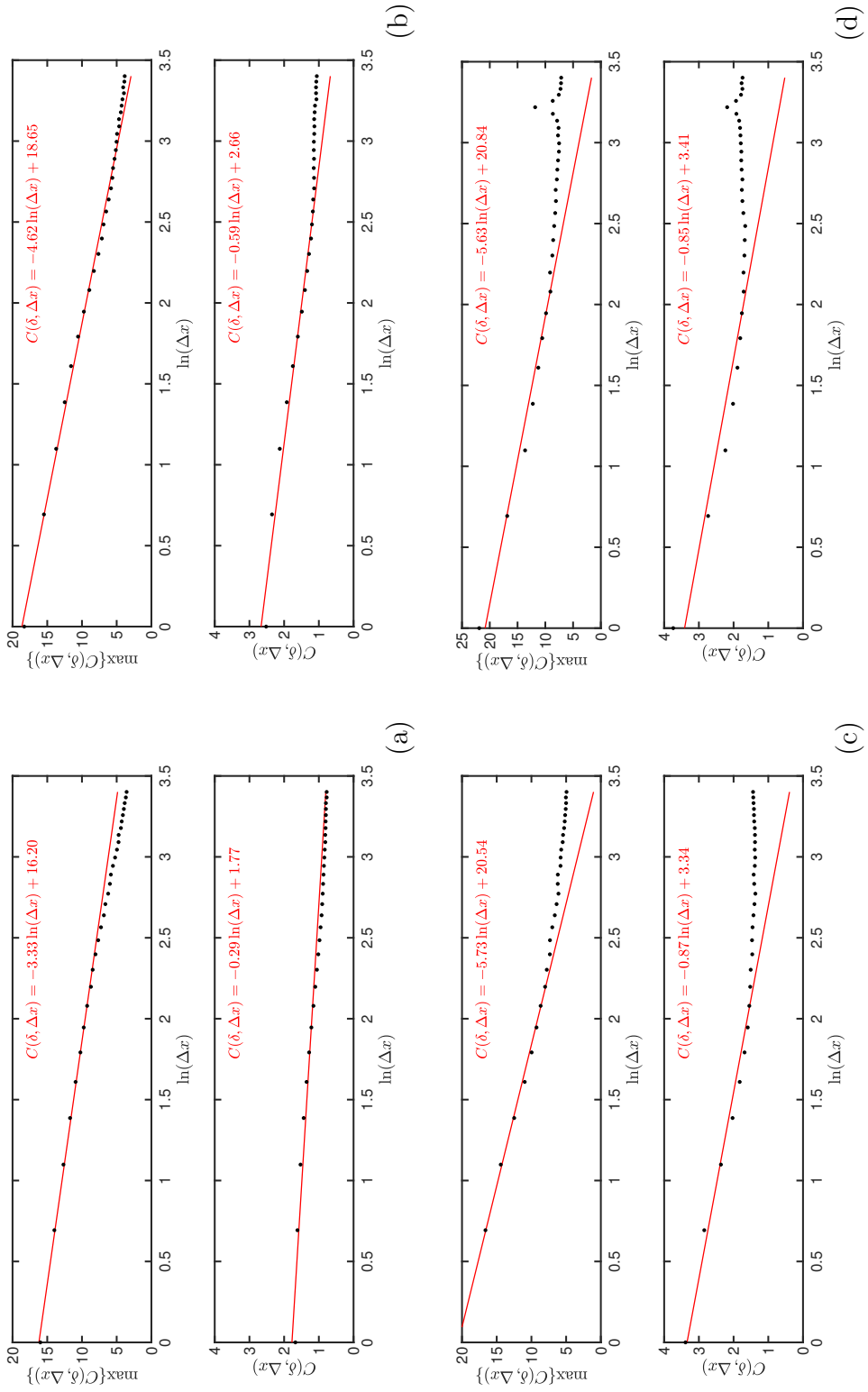

Figure 3-21: Two-point correlation functions of the observed maximum values of the rainfall field ($\max\{C(\delta, \Delta x)\}$ vs $\ln(\Delta x)$) and the observed average values of the rainfall field ($C(\delta, \Delta x)$ vs $\ln(\Delta x)$). The rainfall fields were obtained from TRMM satellite mission observations in the year 2015 and bound in the latitudes 30°S and 30°N. In this plot the two-point correlation analysis was developed for the scales $\delta = \Delta x = 0.25° \approx 27.7$ km (a), $\delta = 2\,\Delta x$ (b), $\delta = 3\,\Delta x$ (c), and $\delta = 4\,\Delta x$ (d).

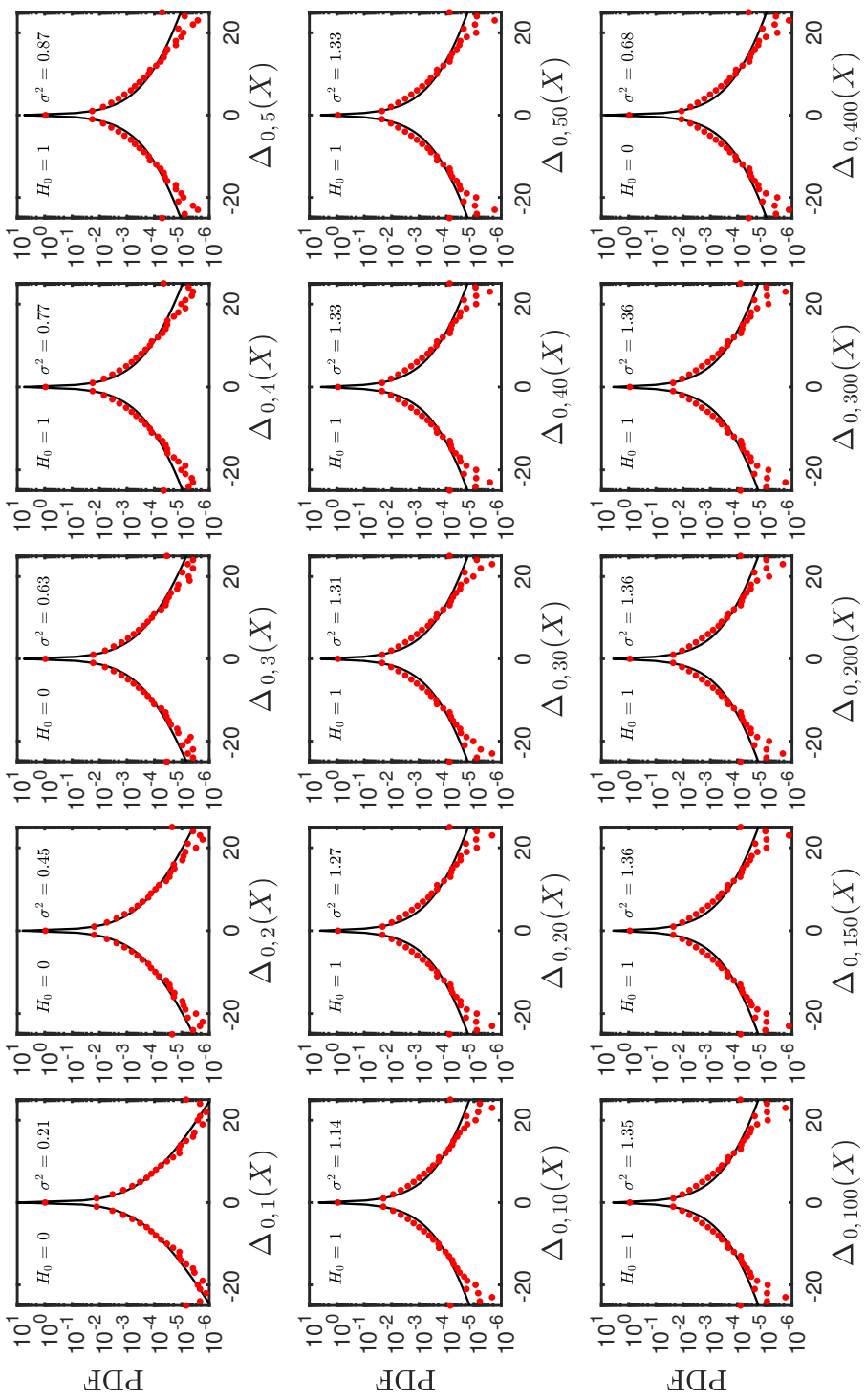

Figure 3-22: Probability density function of the increments $\Delta_{t,u}$ of rainfall intensity. The observations were recorded by the TRMM satellite mission in the year 2015 over the region bound by the latitudes 30°S and 30°N. The spatial increments were derived taking as pivot point the maximum rainfall intensity recorded on June 11th of 2015 and for $u = \{\Delta x, 2\,\Delta x, 3\,\Delta x, 4\,\Delta x, 5\,\Delta x, 10\,\Delta x, 20\,\Delta x, 30\,\Delta x, 40\,\Delta x, 50\,\Delta x, 100\,\Delta x, 150\,\Delta x, 200\,\Delta x, 300\,\Delta x, 400\,\Delta x\}$. In every plot, red dots represent the empirical PDF and the solid black line represents the normal inverse Gaussian distribution fitted to the observations. In each plot is indicated the value of the null hypothesis H_0 (zero for the acceptance of H_0 and one for the rejection of H_0; both values for a 5% of significance level α). The null hypothesis states data come from a normal inverse Gaussian distribution.

The dynamic scaling analysis was developed taking into account either the whole set of TRMM rainfall intensity (see Figure D-5) or the four derived subsets (see Figures D-6 to D-9). In Figure 3-23, one can observe the energy spectrum in the Fourier space for the the whole set of TRMM rainfall–intensity observations. The upper left panel of Figure 3-23 represents the energy spectra of meridionally average values of rainfall intensity during the year 2015 ($P_{\rightarrow}(\mathbf{k},\omega)$) and the upper right panel of Figure 3-23 represents the energy spectra of zonally average values of rainfall intensity during the year 2015 ($P_{\uparrow}(\mathbf{k},\omega)$). Both energy spectrum present a broken symmetry or a space–time anisotropy, i.e. $H_{\text{zonal}} \,/\, H_{\text{meridional}} \approx 2.5$. It is highlighted that the zonal dynamic scaling exponent is near to $\approx 1/3$ which represents a kind of scaling alike to those found in turbulence phenomena [Lovejoy & Schertzer, 2013, Marzan et al., 1996].

In the study of the subsets of TRMM rainfall intensity, for the first term of 2015 (i.e. from January 1st to March 30th), the dynamic scaling analysis shows a significant change in the value of the zonal dynamic scaling exponent H_{zonal} as against that estimated using the whole year data (see Figure D-6). For the first term, $H_{\text{zonal}} = 0.6$ ($H_{\text{zonal}} \approx 3/5$), whose value is also very particular. Lovejoy & Schertzer [2013] studied the vertical stratification of the atmosphere and its spatial anisotropy and they identified a scaling law given by Bolgiano–Obukhov theory about the buoyancy–driven turbulence[10] in which the anisotropy exponent equals to 3/5. The meridional scaling exponent for the first term of 2015 equals to $H_{\text{meridional}} = 0.18$ which is a little higher value than that estimated with the whole dataset of TRMM rainfall intensities, however, its value also represents a tendency to an isotropic space–time.

For the second term of 2015 (i.e. from April 1st to June 30th), either the zonal or meridional dynamic scaling exponents are closer to 1/3. This closeness between the values of the zonal and meridional dynamic scaling exponent could be understood as a more uniform spatial distribution of rainfall events during the second term of 2015 and rainfall events could be driven preferentially by turbulence processes. In the third term of 2015 (i.e. from April 1st to June 30th) the relationship $H_{\text{zonal}} \,/\, H_{\text{meridional}} \approx 2.5$ is also held as it was aforementioned for the analysis of the whole dataset. However, H_{zonal} is not 1/3 as one would expect, but for this particular subset of data, either the zonal or meridional dynamic scaling exponents have a relationship as follows[11]: $H_{\text{meridional}} \approx H_{\text{zonal}}^2$. For the fourth term there also exists a relationship. Such a relationship can be represented as: $H_{\text{zonal}} \approx H_{\text{meridional}}^{0.576} \approx H_{\text{meridional}}^{3/5}$. The fourth term presents changes in the dynamic scaling exponents in contrast to those found in the first three terms. Here, the $H_{\text{meridional}}$ is higher than H_{zonal}, therefore the relationship $H_{\text{meridional}} \propto H_{\text{zonal}}^2$ is not held, but it could be suggested one like this: $H_{\text{meridional}} \propto H_{\text{zonal}}^{\gamma}$, where the exponent γ would be $\gamma \approx \frac{9}{5}$ for the year 2015, $\gamma \approx \frac{10}{5}$ for the first term, $\gamma \approx \frac{6}{5}$ for the second term, $\gamma \approx \frac{10}{5}$ for the third term, and $\gamma \approx \frac{3}{5}$ for the fourth term.

[10] In Bolgiano–Obukhov theory the velocity fluctuations Δv which are separated a distance Δr follow a scaling law given by $\Delta v \approx \chi_{\theta}^{1/5}(g/\theta_0)^{2/5}|\Delta r|^{3/5}$, where χ_{θ} is the potential temperature variance flux, θ_0 is a time-averaged potential temperature and g is the gravity of Earth [Lovejoy & Schertzer, 2013].

[11] The results show that $H_{\text{zonal}} \approx 2/5$ and $H_{\text{meridional}} \approx (2/5)^2$.

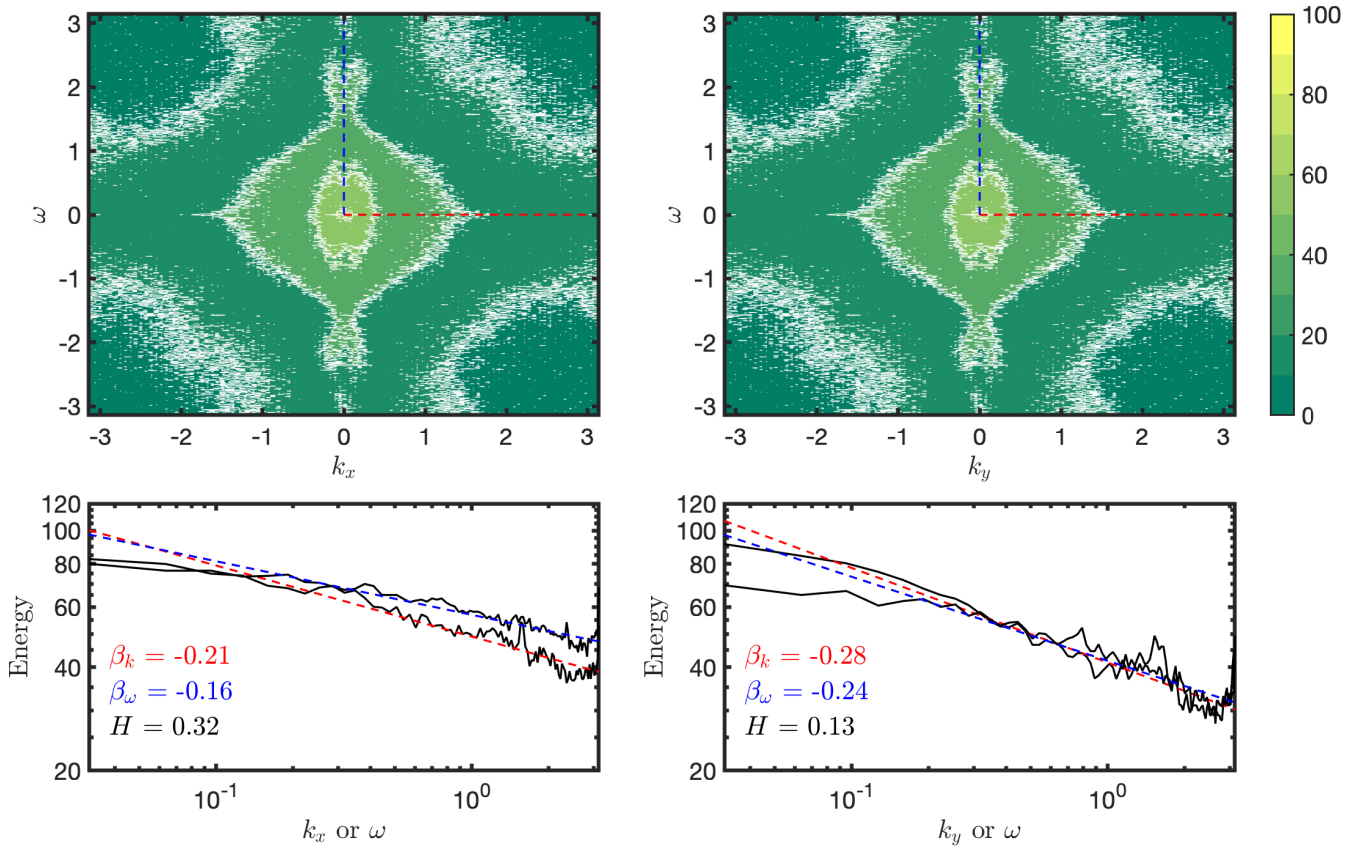

Figure 3-23: Isocorrelation contours in the $2D$ Fourier space for the x–t section (upper left panel) and the y–t section (upper right panel) of the averaged values of rainfall intensity fields measured by the TRMM satellite mission in the year 2015 over the region bound by the latitudes 30°S and 30°N. The lower panels are representing two cuts in the $2D$ Fourier spectra in the wavelength ($k.$) and frequency direction $f.$. In the lower panels are indicated the slopes $\beta_{\omega,k}$ of each cuts in the Fourier spectra and besides the scaling anisotropy exponent H which is computed with the slopes $\beta_{\omega,k}$.

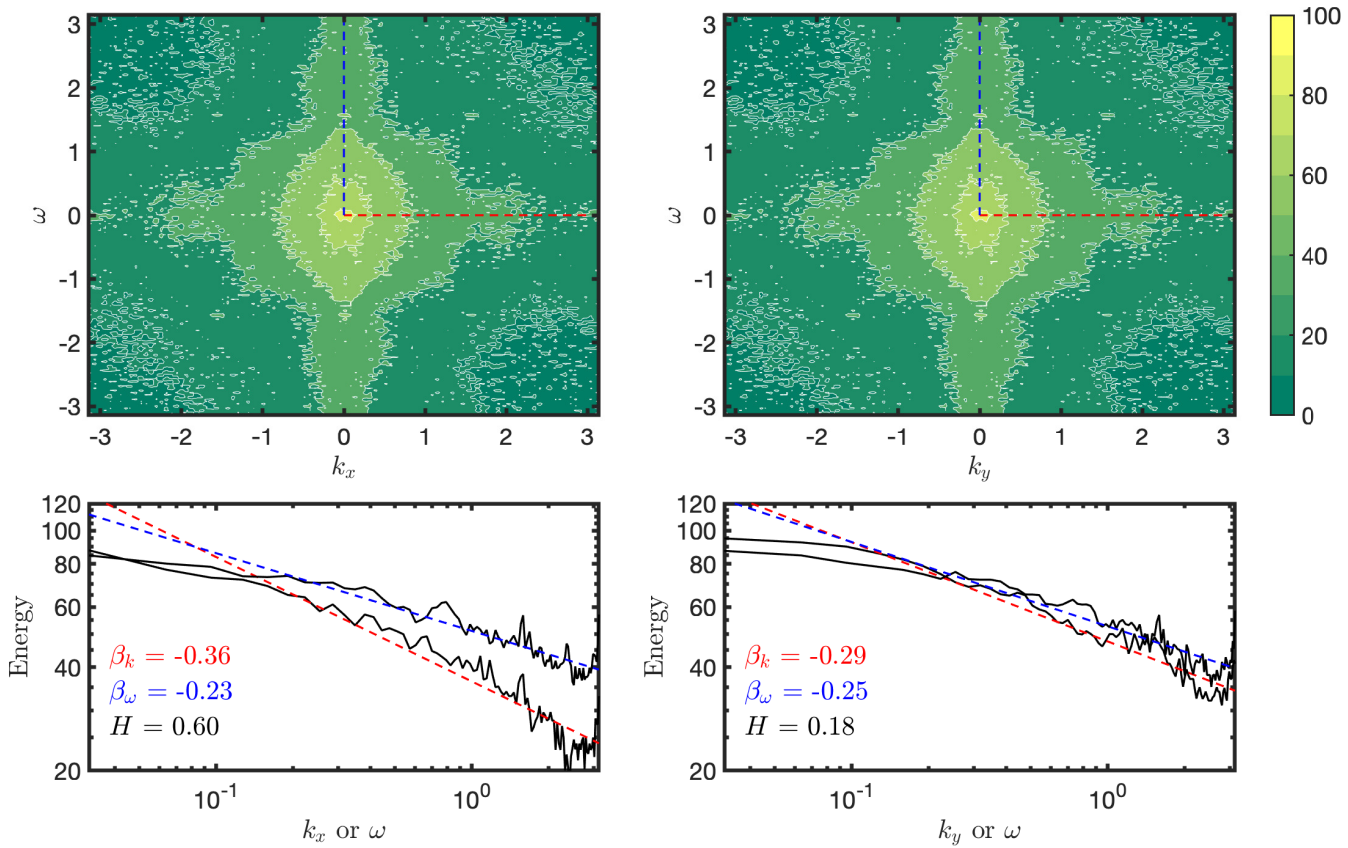

Figure 3-24: Isocorrelation contours in the $2D$ Fourier space for the x–t section (upper left panel) and the y–t section (upper right panel) of the averaged values of rainfall intensity fields measured by the TRMM satellite mission in the first term (January 1st–March 30th) of the year 2015 over the region bound by the latitudes 30°S and 30°N. The lower panels are representing two cuts in the $2D$ Fourier spectra in the wavelength ($k.$) and frequency direction $f.$. In the lower panels are indicated the slopes $\beta_{\omega,k}$ of each cuts in the Fourier spectra and besides the scaling anisotropy exponent H which is computed with the slopes $\beta_{\omega,k}$.

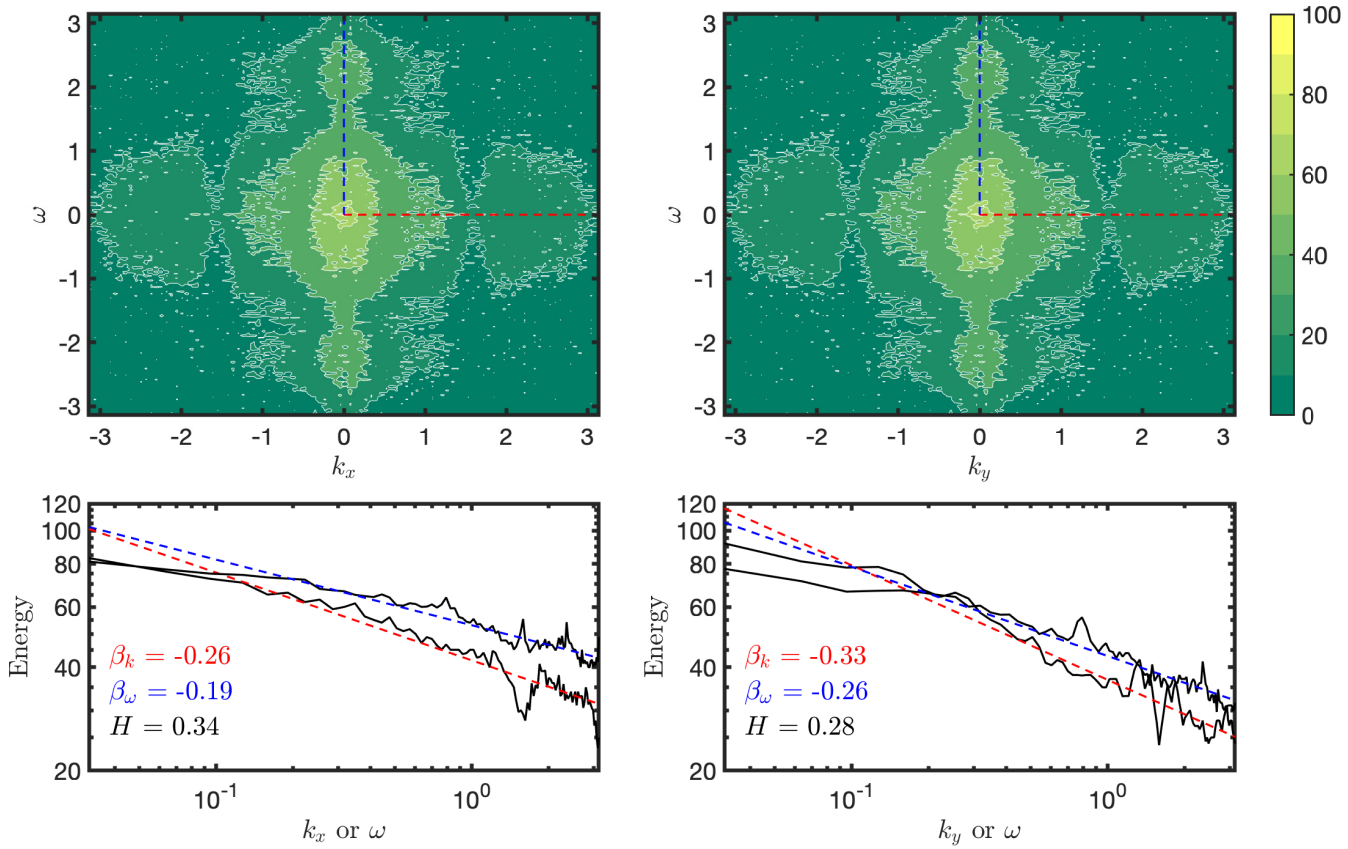

Figure 3-25: Isocorrelation contours in the $2D$ Fourier space for the x–t section (upper left panel) and the y–t section (upper right panel) of the averaged values of rainfall intensity fields measured by the TRMM satellite mission in the second term (April 1st–June 30th) of the year 2015 over the region bound by the latitudes 30°S and 30°N. The lower panels are representing two cuts in the $2D$ Fourier spectra in the wavelength ($k.$) and frequency direction $f.$. In the lower panels are indicated the slopes $\beta_{\omega,k}$ of each cuts in the Fourier spectra and besides the scaling anisotropy exponent H which is computed with the slopes $\beta_{\omega,k}$.

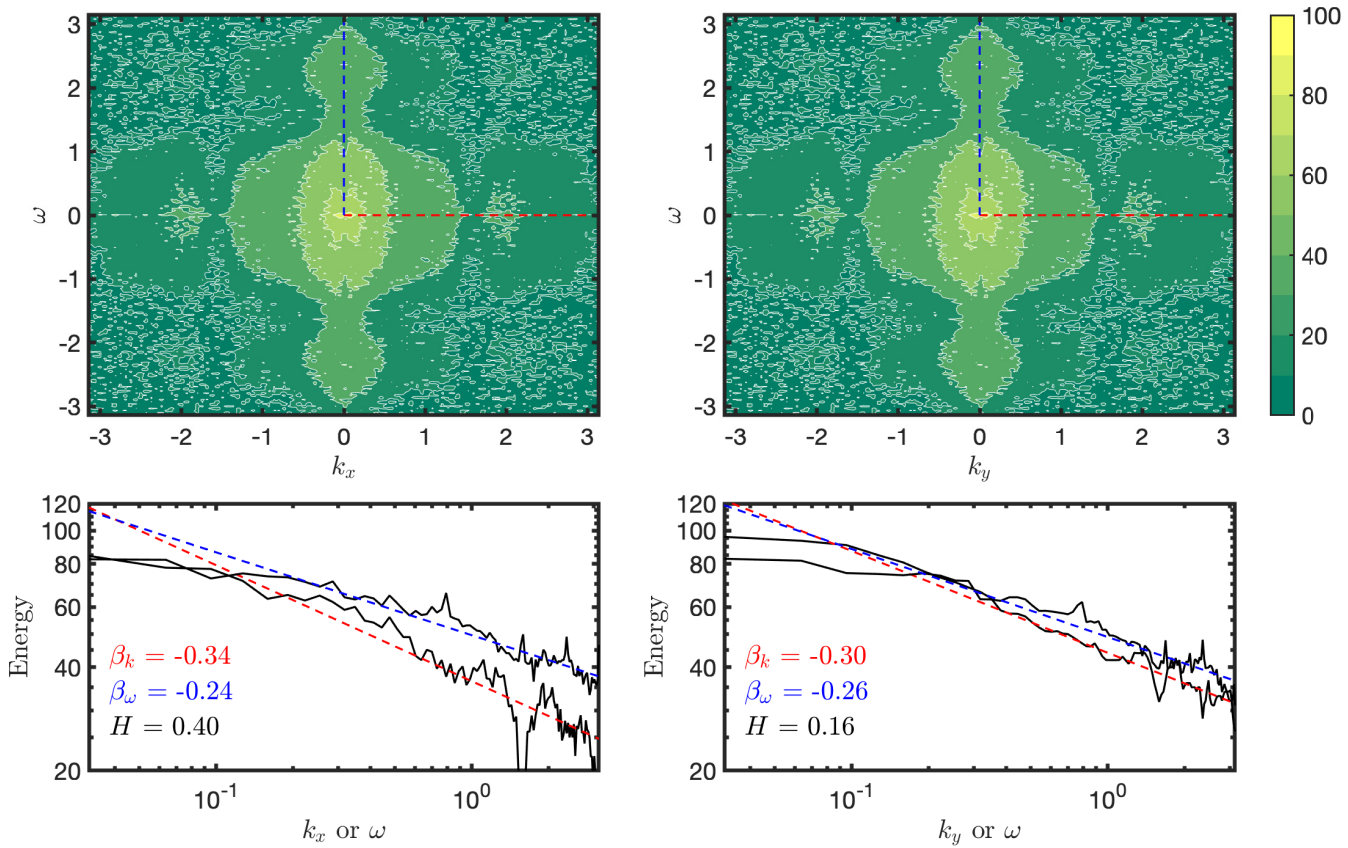

Figure 3-26: Isocorrelation contours in the $2D$ Fourier space for the x–t section (upper left panel) and the y–t section (upper right panel) of the averaged values of rainfall intensity fields measured by the TRMM satellite mission in the third term (July 1st–September 30th) of the year 2015 over the region bound by the latitudes 30°S and 30°N. The lower panels are representing two cuts in the $2D$ Fourier spectra in the wavelength ($k.$) and frequency direction $f.$. In the lower panels are indicated the slopes $\beta_{\omega,k}$ of each cuts in the Fourier spectra and besides the scaling anisotropy exponent H which is computed with the slopes $\beta_{\omega,k}$.

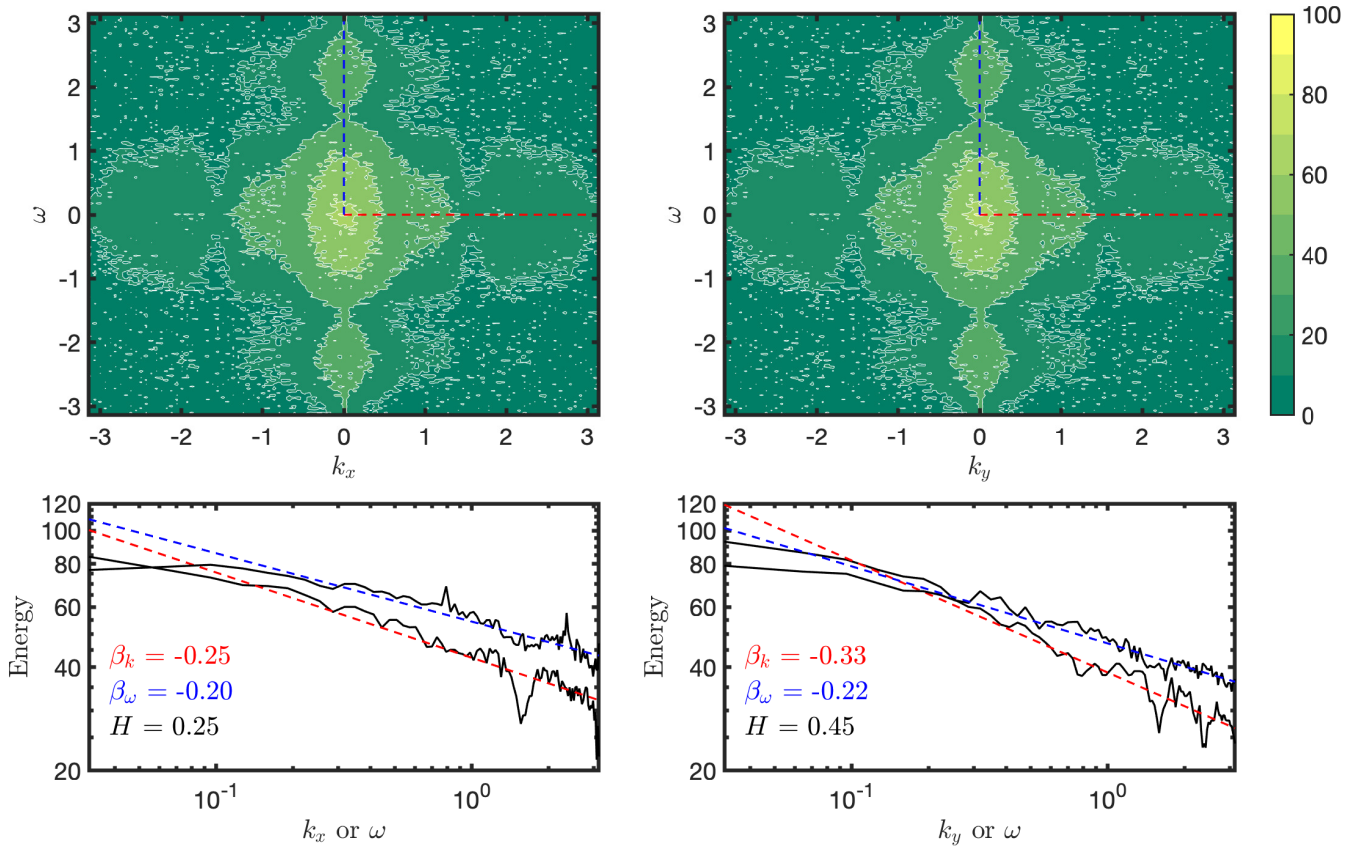

Figure 3-27: Isocorrelation contours in the $2D$ Fourier space for the x–t section (upper left panel) and the y–t section (upper right panel) of the averaged values of rainfall intensity fields measured by the TRMM satellite mission in the fourth term (October 1st–December 30th) of the year 2015 over the region bound by the latitudes 30°S and 30°N. The lower panels are representing two cuts in the $2D$ Fourier spectra in the wavelength (k.) and frequency direction f.. In the lower panels are indicated the slopes $\beta_{\omega,k}$ of each cuts in the Fourier spectra and besides the scaling anisotropy exponent H which is computed with the slopes $\beta_{\omega,k}$.

Clearly, the exponent γ connects with seasonal changes and the activity of rainfall events. Nevertheless, further analysis will be required in order to establish the real dependence of this exponent with the seasonal changes.

3.3. Simulations of Rainfall Fields

In this section, the multifractality will be explored in some numerical models. The selection of models took into account the following characteristics: i) to have a link with physical processes associated to rainfall, ii) to provide a parsimonious structure that allows an easy understanding of physical processes that exist therein, and iii) to have any association with fractal attributes in the model mathematical structure or model outputs. The analysis of models follows the same organization used above for the observational analysis.

3.3.1. Nordstrom and Gupta's Model

The first selected model was developed by Nordstrom & Gupta [2003] whose model was designed under physical arguments to describe the tropical atmospheric convection over the ocean. Model equations were previously presented in section 2.2.3, however, they will be briefly brought back here. In Nordstrom & Gupta's model [2003], the cold–pool depth $h(\mathbf{x}, t)$ is described by an advection–diffusion equation as follows:

$$\partial_t h(\mathbf{x}, t) = \nu_a \, \Delta h(\mathbf{x}, t) - \mathbf{u} \cdot \nabla h(\mathbf{x}, t) \tag{3-33}$$

$$h(\mathbf{x}, 0) = h_0(\mathbf{x}) \tag{3-34}$$

$$h(0, t) = h(L, t) \tag{3-35}$$

where $\mathbf{u}$ is the velocity of the cold pool propagation and ν_a is a diffusion coefficient for the air into the cold pool. Rainfall is here computed as:

$$R(\mathbf{x}, t) = r \, C(\mathbf{x}, t) \tag{3-36}$$

where r is a constant value of rainfall intensity and $C(\mathbf{x}, t)$ is the cloudiness field which depends of a Heaviside function $\Theta(\kappa)$ as follows:

$$\partial_t C(\mathbf{x}, t) = c \, \Theta(\kappa) \tag{3-37}$$

where c is the velocity scale for convection and κ is the triggering energy for the deep convection which is computed as:

$$k(\mathbf{x}, t) = (U \cdot \nabla h - b_1)(b_2 - U \cdot \nabla h) \tag{3-38}$$

where U is the incident wind of the warm air parallel to the surface, ∇h is the gradient of the cold pool, b_1 and b_2 are constants depending on atmospheric state variables as explained in section 2.2.3. For the example simulation which is exhibited in Figure 3-28, the numerical implementation of it required the following parameters and criteria:

1. The cool pool depth $h(\mathbf{x}, t)$ was initialized using an homogeneous distribution of the field settled on 1000 m, then it was perturbed by a low–amplitude noise.

2. The time evolution of equation 3-33 was computed for a two dimensional domain using an explicit finite difference scheme with a double periodic domain of size 256×256 grid cells, each one of size 0.5×0.5 km^2 ($L = 128$ km, $\Delta x = 500$ m).

3. The time resolution is $\Delta t = 5$ seconds, and the total time of simulation is $T = 12$ h.

4. The incident wind velocity vector U is defined fixed to $U = 10\,\hat{i} + 10\,\hat{j}$ m s^{-1} ($\|U\| = 14.14$ m s^{-1}).

5. The cool pool velocity vector $\mathbf{u}$ is assumed to be the same as the incident wind velocity, so $\mathbf{u} = 10\,\hat{i} + 10\,\hat{j}$ m s^{-1} ($\| \mathbf{u} \| = 14.14$ m s^{-1}).

6. The diffusion coefficient ν_a is assumed to be constant and equals to 1×10^4 m^2 s^{-1}. It is highlighted this diffusion coefficient ν_a is different to that used by Nordstrom & Gupta [2003] whose value was 400 m^2 s^{-1}. This last value of the diffusion coefficient do not allow the numerical stability of the model (i.e. $\frac{\nu_a \Delta t}{(\Delta x)^2} \leq \frac{1}{2}$), therefore, the selected diffusion coefficient does allow the numerical stability of the model.

7. The penetration velocity b_2 equals to 5 m s^{-1}.

8. The vertical time scale for convection τ equals to 5 min. This value is lesser than that used by Nordstrom & Gupta [2003] whose value was 30 min.

9. The velocity scale for convection c equals to 0.1 cm s^{-1}. This value is lesser than that used by Nordstrom & Gupta [2003] whose value was 84 m s^{-1}.

10. The frequency scales for rainout r equals to 1 h^{-1} and for heating F equals to 2 h^{-2}.

11. The sample output is the resulting product when the parameter b_1 equal to 0.019 m s^{-1}.

Figure 3-28 show some snapshots of model outputs after 12 h of simulation. Some snapshots are exhibited in Figure 3-28, at the times 0, 4, 8 and 12 h. The left panels show the dynamic of the cool pool depth $h(\mathbf{x}, t)$ for the aforementioned times. The simulated cool pool changes from a random pattern to an organized structure that looks as a sink. The central panels of Figure 3-28 are depicting the cloudiness. As it can be evidenced in equation 3-37, cloudiness is a dimensional quantity depending on the velocity scale for convection and its units are represented in meters. Thus, the central panels of Figure 3-28 are representing the same variable but re-scaled between $[0, 1]$. The right panels of Figure 3-28 are depicting the rainfall field and its quantities are expressed in mm h^{-1}.

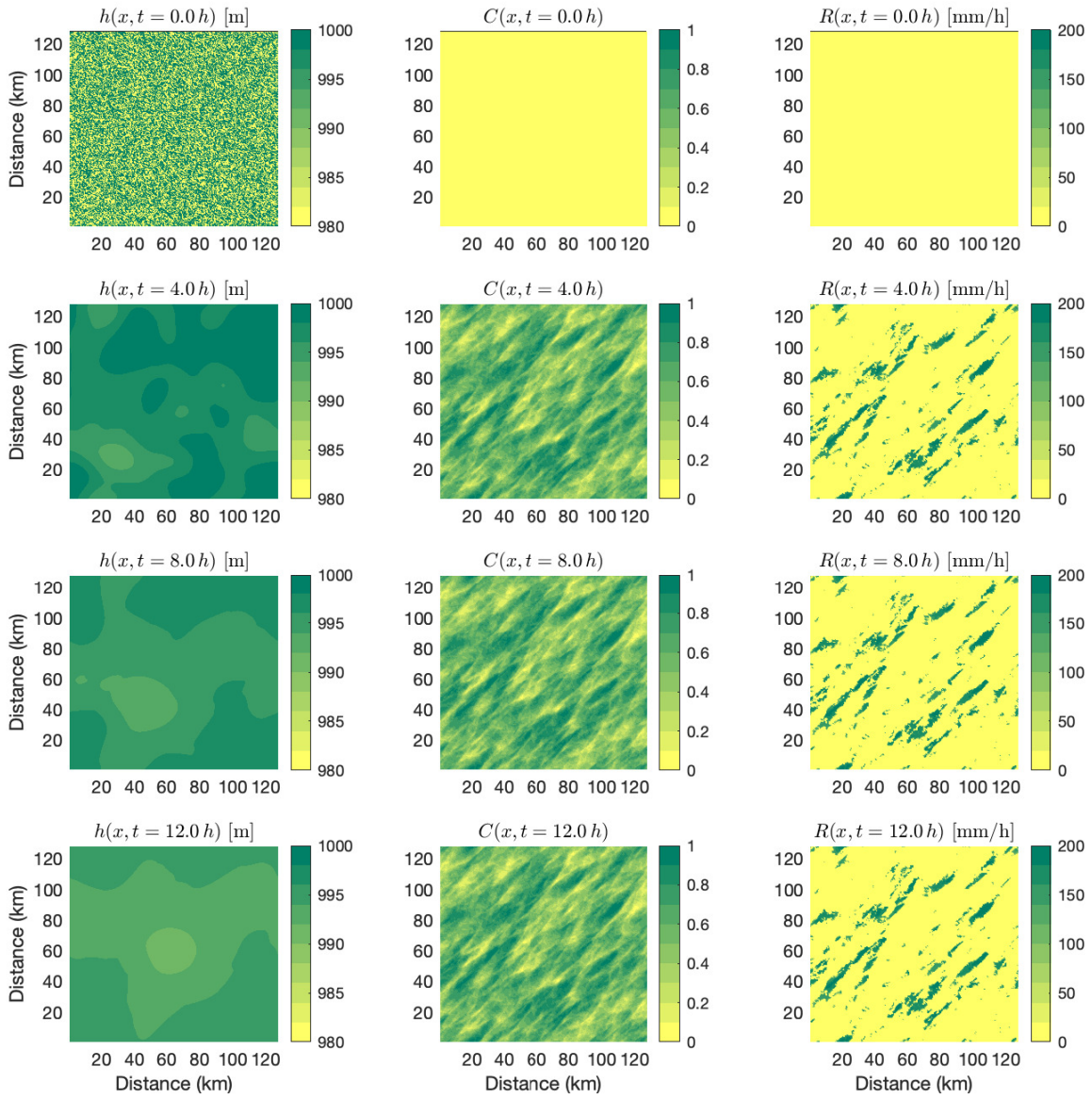

Figure 3-28: Example of simulated rainfall fields via Nordstrom & Gupta's model [2003]. In left panels are shown the depth of the cool pool field ($h(\mathbf{x}, t)$ in mm), the central ones show the cloudiness field ($C(\mathbf{x}, t)$) and the right ones show the rainfall field ($R(\mathbf{x}, t)$ in mm h^{-1}) for the times t indicated on every panel. The model parameters used for these simulations were: $\Delta t = 5$ s, $\Delta x = 500$ m, $\mathbf{u} = 10\,\hat{i} + 10\,\hat{j}$ (m s^{-1}), $a = 1 \times 10^5$ m^2 s^{-1}, $b_1 = 0.019$ m s^{-1}, $b_2 = 5$ m s^{-1}, $U = 10\,\hat{i} + 10\,\hat{j}$ (m s^{-1}), $\tau = 5$ min, $c = 1 \times 10^{-3}$ m s^{-1}, and the time lapse for the simulation was 12 h.

Figure 3-29 shows some statistics of the rainfall field during the simulation time. The spatial average value of the rainfall field $\langle \mathbf{R}(\mathbf{x}, t) \rangle \equiv \overline{R}$ at the time t starts from a zero value to reach a limit value of ≈ 165.8 mm h^{-1}. In the same way, the maximum value of the simulated

rainfall field $\max\{R\}$ starts from a zero value to reach a limit value of ≈ 211.9 mm h^{-1}. The variability of rainfall field σ also grows up from zero to ≈ 16.3 mm h^{-1}. Finally the fractional wet area is settled in 10.3% after long enough simulation time. Clearly, results exhibit three (3) time regions; the first one is a growth region from time 0.14 h (8.6 min) to ≈ 0.79 h (47.4 min), the second one is a transition region from 0.79 h to ≈ 0.92 h (55.3 min), and the last one is a ripening region after time 0.92 h.

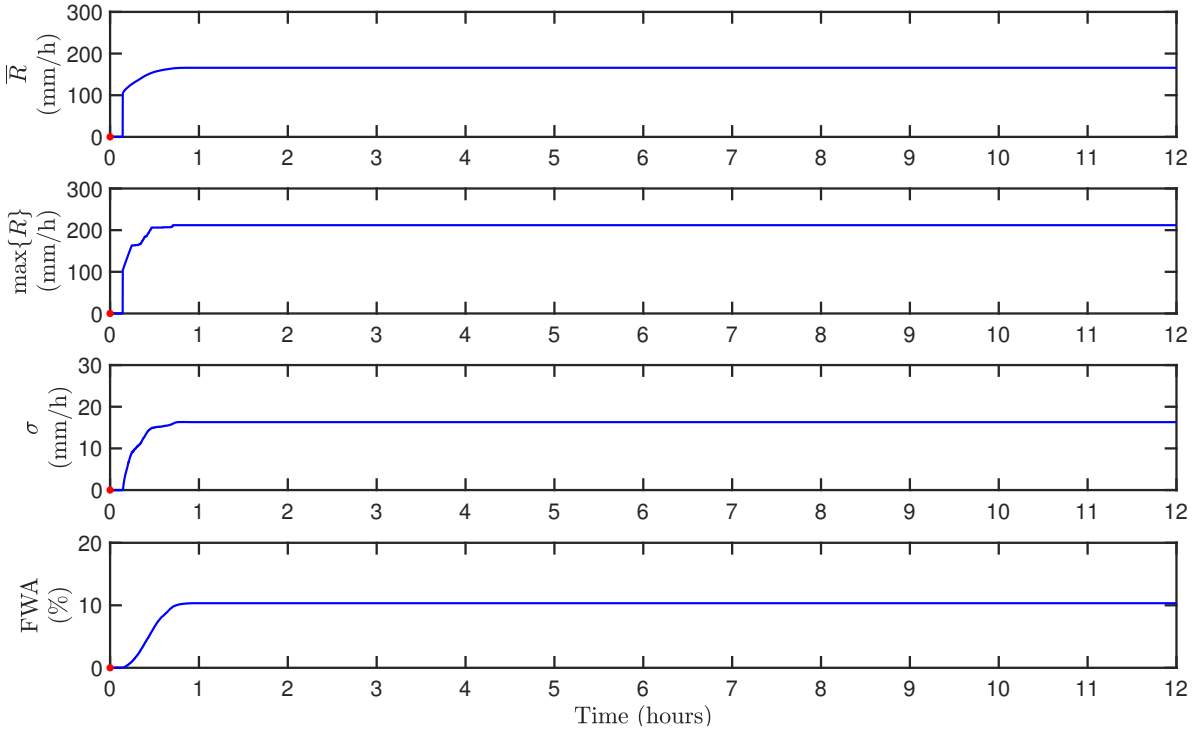

Figure 3-29: Time variation of the mean ($\overline{R}$), maximum ($\max\{R\}$), standard deviation (σ) and fractional wet area of the rainfall intensity fields simulated by the Nordstrom & Gupta's model [2003]. The parameters for getting the simulated field were: The model parameters used for these simulations were: $\Delta t = 5$ s, $\Delta x = 500$ m, $\mathbf{u} = 10\,\hat{i} + 10\,\hat{j}$ (m s^{-1}), $a = 1 \times 10^5$ m^2 s^{-1}, $b_1 = 0.019$ m s^{-1}, $b_2 = 5$ m s^{-1}, $U = 10\,\hat{i} + 10\,\hat{j}$ (m s^{-1}), $\tau = 5$ min, $c = 1 \times 10^{-3}$ m s^{-1}, and the time lapse for the simulation was 12 h.

Some multifractal spectra of simulated rainfall fields are shown in Figure 3-31 and they are organized in a time-axis for noticing how multifractal spectra change over time. The first simulated rainfall field exhibits a shift to the left in the α–axis as against others computed spectra, and also a fractal dimension D_0 lesser in value (i.e. $D_0 \approx 1.51$). This last could consider a spurious multifractality due to the initial random perturbation over the cold pool field. After crossing the so-called transition region, the fractal dimension is settled in $D_0 \approx 1.59$ and no-variability is observed as $t \to \infty$. Another feature to highlight in results is the non-existence of singularity exponents α to characterize the measures derived from the simulated rainfall field. Furthermore, the range of singularity exponents is small that could

represent a tendency of the model to generate patterns of weak multifractality.

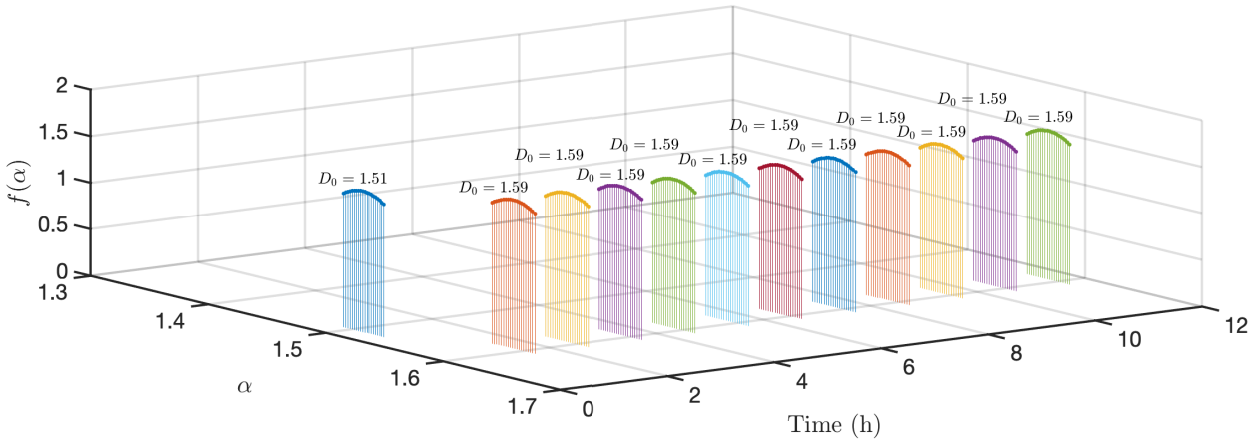

Figure 3-30: Time evolution of the estimated multifractal spectrum for the Nordstrom & Gupta's model simulations [2003] shown in Figure 3-28.

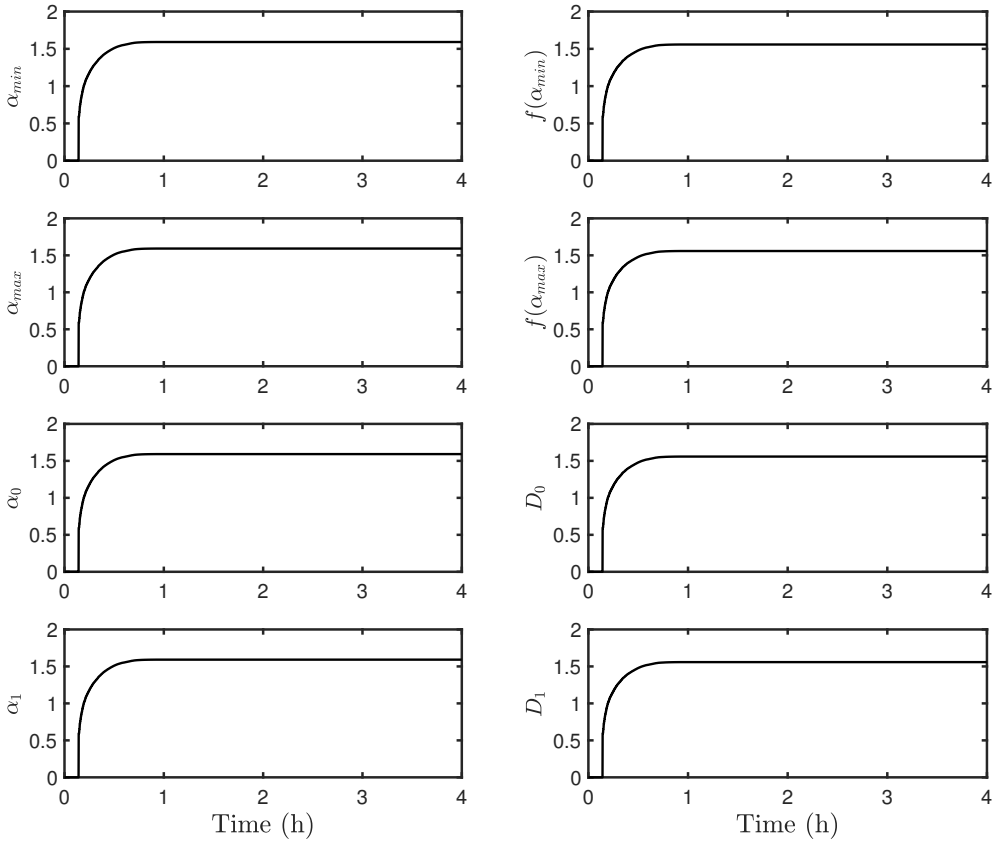

Figure 3-31: Time variation of the multifractal variables: α_{min}, α_{max}, α_0, α_1, $f(\alpha_{min})$, $f(\alpha_{max})$, $D_0 = f(\alpha_0)$, and $D_1 = f(\alpha_1)$. All these variables were obtained for the simulated rainfall fields via Nordstrom & Gupta's model.

Table 3-8: Statistics of the multifractal variables: $\alpha_{min} \equiv \min\{\alpha\}$, $\alpha_{max} \equiv \max\{\alpha\}$, α_0, α_2, $f(\alpha_{min})$, $f(\alpha_{max})$, $D_0 = f(\alpha_0)$, $D_1 = f(\alpha_1) = \alpha_1$, and $D_2 = f(\alpha_2)$. The statistics were obtained for the multifractal spectra of the simulated rainfall fields via Nordstrom & Gupta's model [2003]. In this table σ, CV, IQR, γ represent the standard deviation, the coefficient of variation, the interquartile range and the skewness, respectively.

	α_{min}	α_{max}	α_0	α_1	$f(\alpha_{min})$	$f(\alpha_{max})$	$f(\alpha_0)$	$f(\alpha_1)$
Minimum	0.00	0.00	0.00	0.00	0.00	0.00	0.00	0.00
Mean	1.50	1.50	1.50	1.50	1.47	1.47	1.47	1.47
Median	1.59	1.59	1.59	1.59	1.56	1.56	1.56	1.56
Maximum	1.59	1.59	1.59	1.59	1.56	1.56	1.56	1.56
σ	0.31	0.31	0.31	0.31	0.30	0.30	0.30	0.30
CV (%)	20.78	20.78	20.78	20.78	20.72	20.72	20.72	20.72
IQR	0.00	0.00	0.00	0.00	0.00	0.00	0.00	0.00
γ	-4.16	-4.16	-4.16	-4.16	-4.19	-4.19	-4.19	-4.19

The magnitude cumulant method was applied to the simulated rainfall field via Nordstrom & Gupta's model [2003]. The analysis of results shows a non–linear structure in simulated patterns. In Figure 3-32, the first cumulant depicts a convex function since the beginning of rainfall to reach a value of $C_0 \sim 1.6$. An interesting fact of this result is its similar value to those estimated in either SIATA's radar reflectivity records or TRMM rainfall intensity records, i.e. Nordstrom & Gupta's model mimics the same value of the coefficient $C_0 \equiv D_0$. On the other hand, the behavior of the coefficient C_1 is rather trivial since it is settled in an unique value during the entire simulation time. The C_2–function is also a concave function after the first rainfall event appears, although its growth velocity is higher than that of C_0–function exhibits.

The two–point correlation functions for either the maximums or the averaged correlations of simulated rainfall fields denote a long–range dependence, since there exists a linear relationship between $C(\delta, \Delta x)$ vs $\ln(\Delta x)$ and scale independence as well. Nonetheless, the log–linear slopes of correlation functions in Figure 3-32 tend to be equal to zero (i.e. $m \to 0$ in the representation $C(\delta, \Delta x) = m \ln(\Delta x) + b$); therefore, the non–linear structure of the outputs cannot be characterized as outcomes of a multifractal process. Another aspect to highlight is the deviation of a log–linear description in the relationship between $C(\delta, \Delta x)$ vs Δx if $\delta > 1.5$ km. This means there is a cut–off point (or scales) where a description based on multiplicative cascade processes is valid.

The incremental similarity analysis was also applied to the outputs derived from Nordstrom and Gupta's model [2003]. Clearly, as seen in Figure 3-34, a NIG distribution does not describe the statistical law of the rainfall increments $\Delta_{t,s}$. The lack of intermittency in the simulated patterns or the weak presence of multifractality on them, could explain

these results. On the other hand, incremental similarity is not observed in the obtained results; the variance is not stable as s (in $\Delta_{t,s}$) increases, so this overrides the IS property: $\Delta_{t,u}(Y) \overset{\text{dist}}{=} \Delta_{t,v}(X)$.

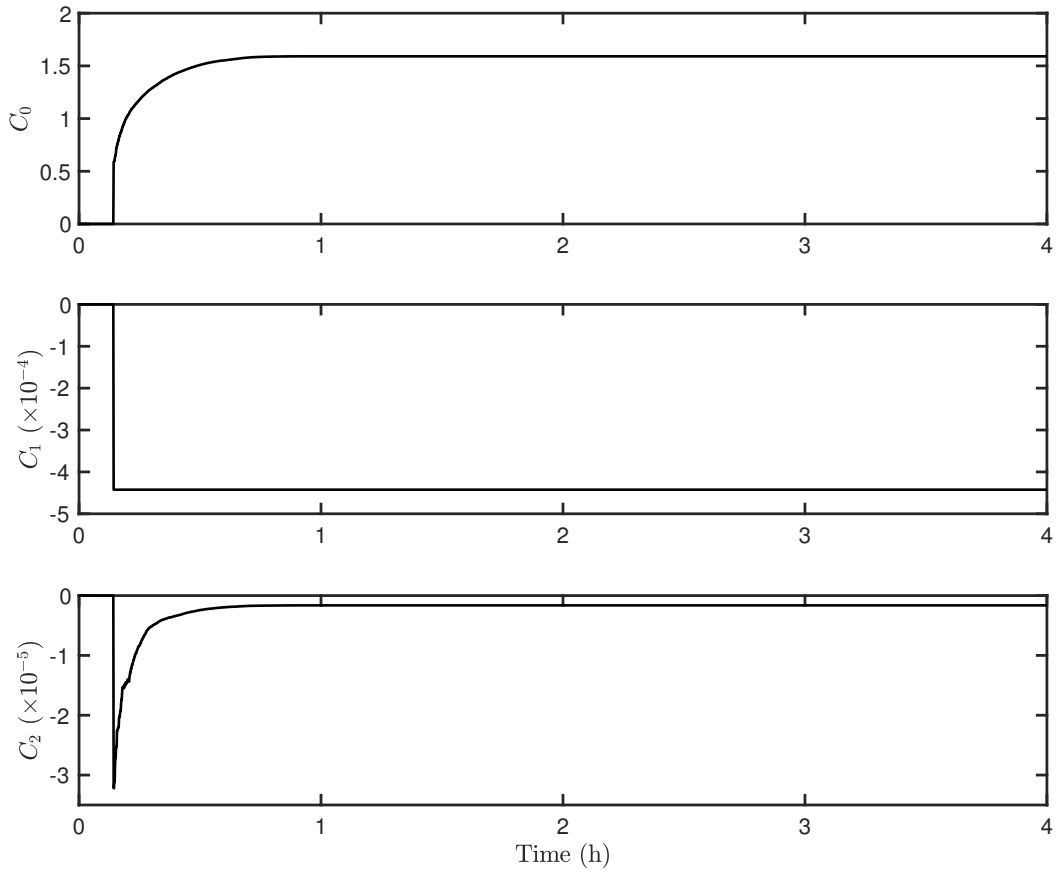

Figure 3-32: Time variation of the first coefficients C_0, C_1, and C_2 of equation 3-11 which were computed from the simulated rainfall fields via Nordstrom & Gupta's model [2003].

Finally, the dynamic scaling analysis does not identified any connection with symmetries observed in turbulence processes. However, the estimated dynamic scaling exponents seem to those observed in diffusive–driven process such as the variable temperature happens (i.e. $H \approx 0.5$ [Lovejoy & Schertzer, 2013]) . Moreover, the proximity of dynamic scaling exponents values, obtained for the x and y direction, suggests a quasi–isotropic space–time field, as observed in normal diffusive–driven process.

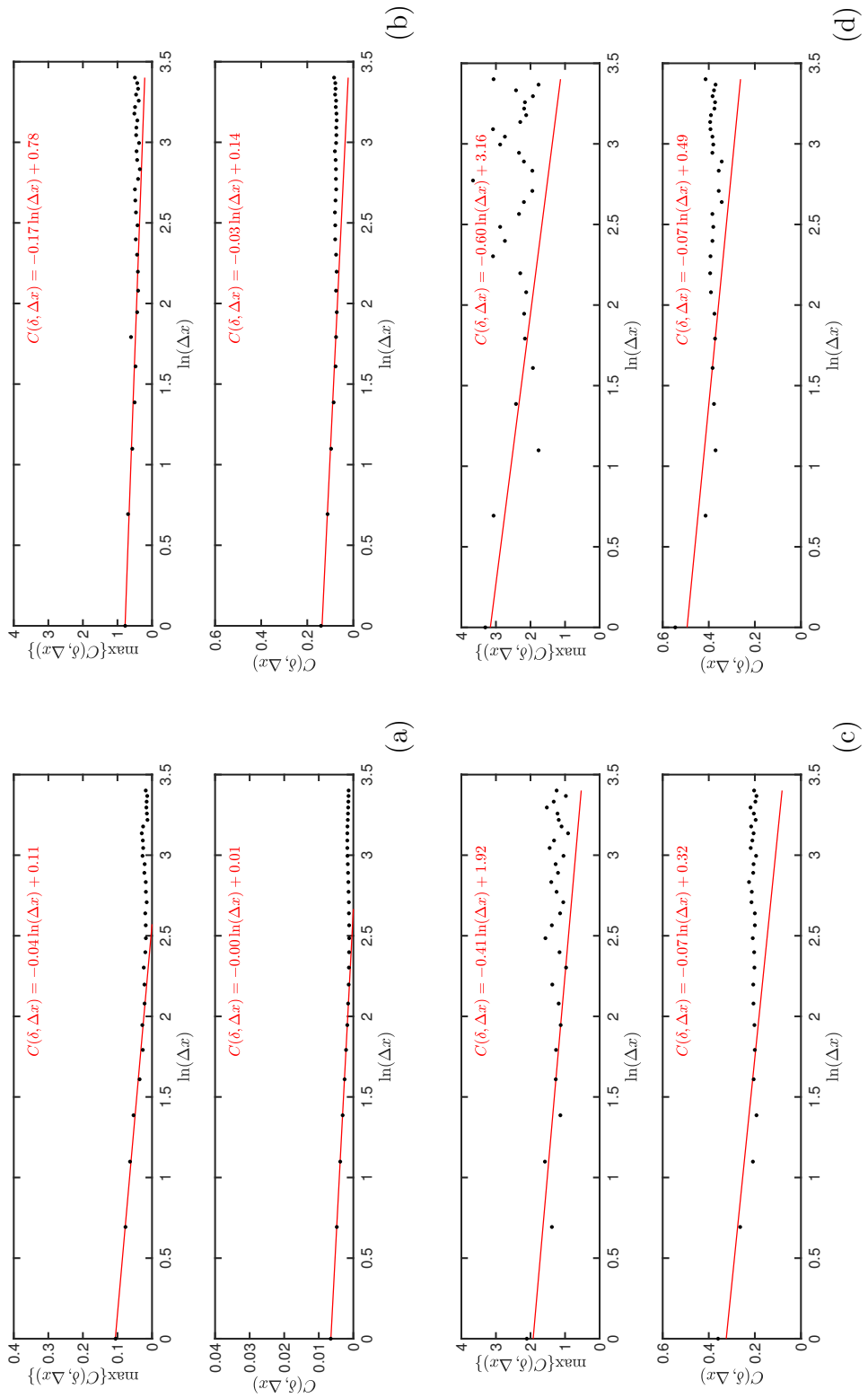

Figure 3-33: Maximum value of the two-point correlation field ($\max\{C(\delta,\Delta x)\}$ vs $\ln(\Delta x)$) and average value of the two-point correlation field ($C(\delta,\Delta x)$ vs $\ln(\Delta x)$) obtained for the simulated rainfall fields via Nordstrom & Gupta's model [2003] which are shown at Figure 3-28. In this plot the two-point correlation analysis is developed for the scales $\delta = \Delta x = 0.5$ km (a), $\delta = 2\,\Delta x$ (b), $\delta = 3\,\Delta x$ (c), and $\delta = 4\,\Delta x$ (d).

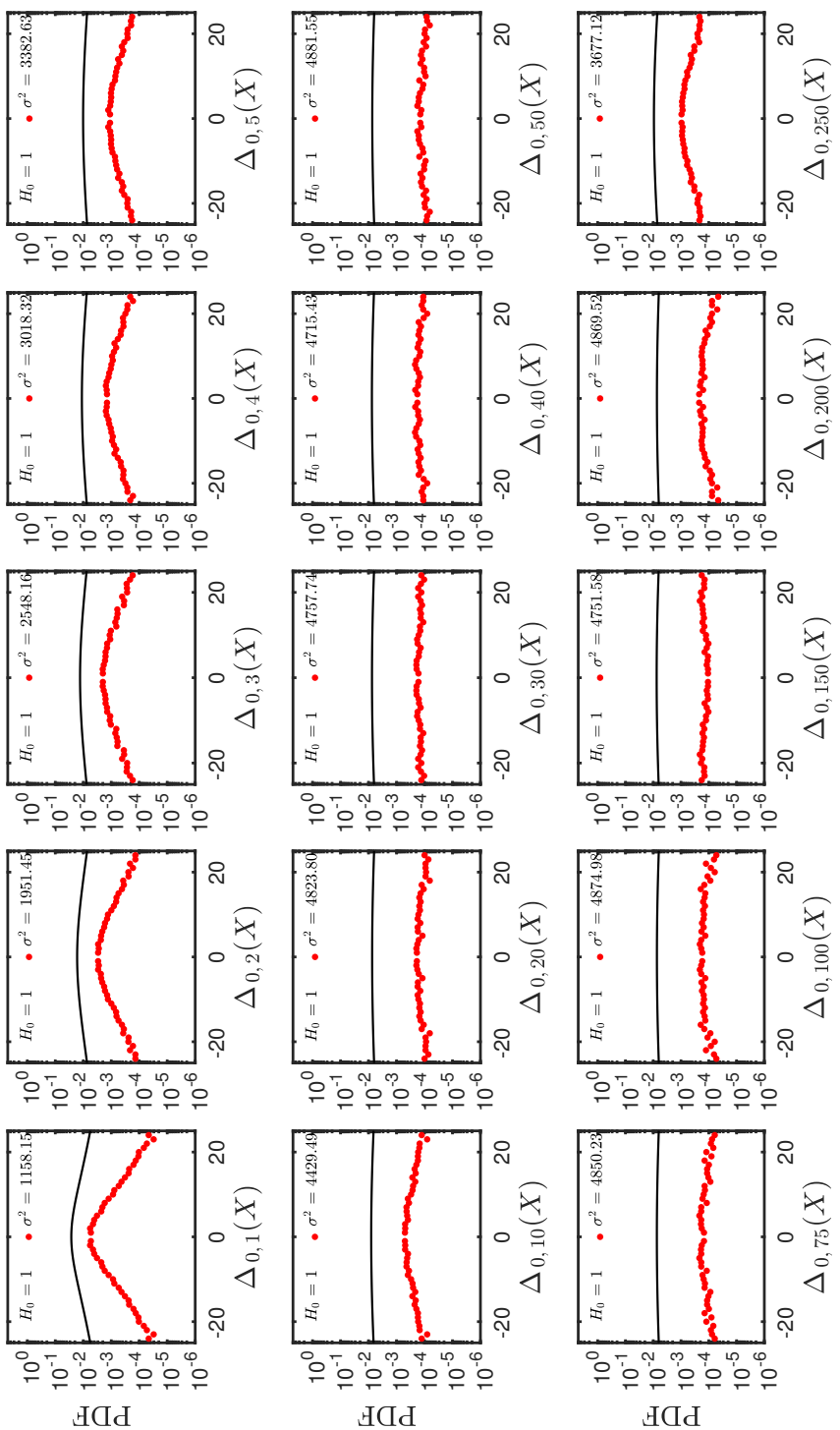

Figure 3-34: Probability density function of the increments $\Delta_{t,u}$ of the simulated rainfall fields via Nordstrom & Gupta's model [2003] which are shown at Figure 3-28. The red dots represent the empirical PDF corresponding to the simulated data and the solid line represents the normal inverse Gaussian distribution fitted to the data set. In each frame is indicated the value of null hypothesis H_0 (zero for the acceptance of H_0 and one for the rejection of H_0; both values for a 5% of significance level α). The null hypothesis states that data come from a normal inverse Gaussian distribution.

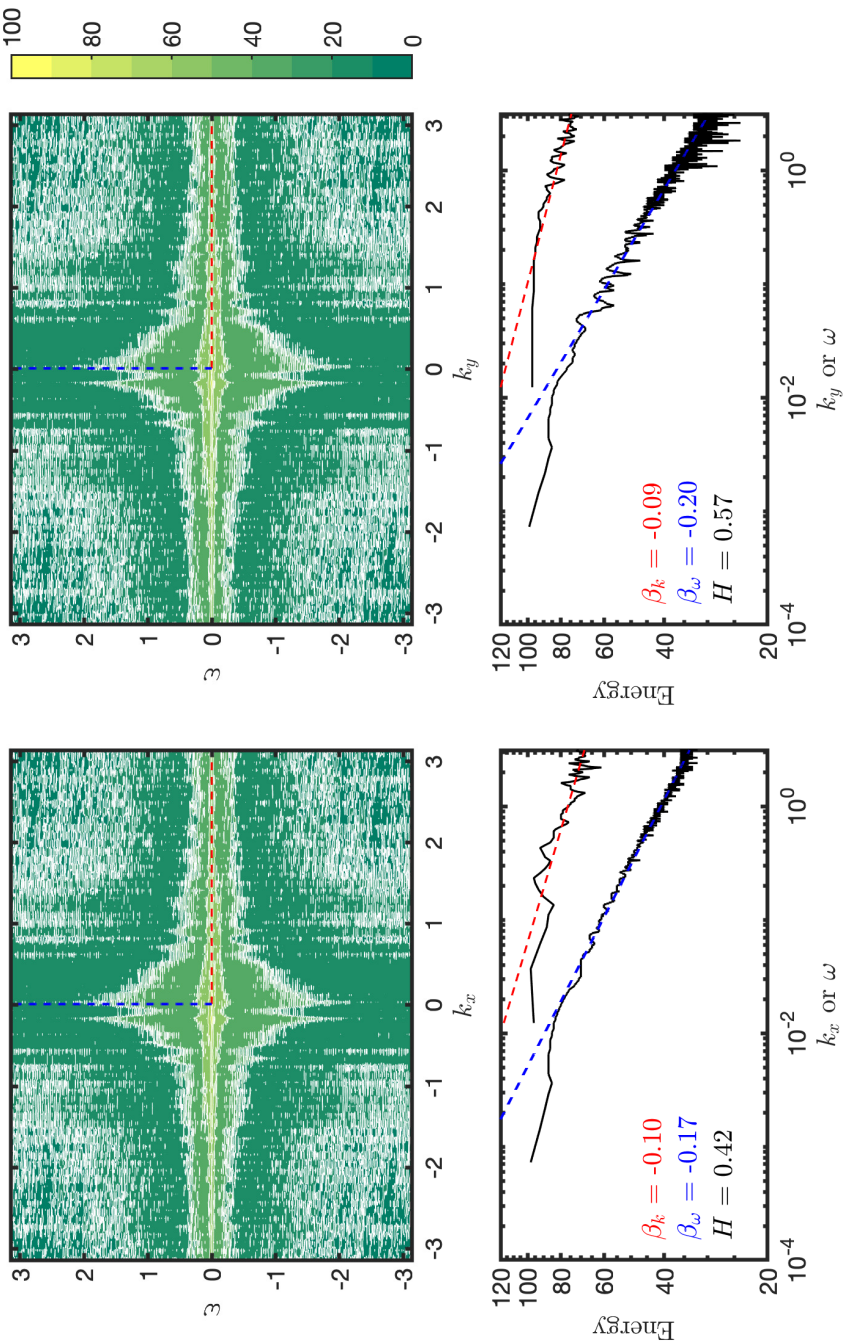

Figure 3-35: Isocorrelation contours in the $2D$ Fourier space for the x–t section (upper left panel) and the y–t section (upper right panel) of the averaged values of simulated rainfall fields via Nordstrom & Gupta's model [2003] and shown in Figure 3-28. The lower panels are representing two cuts in the $2D$ Fourier spectra in the wavelength direction ($k.$) and frequency direction $f.$. In the lower panels are indicated the slopes β of each cuts in the Fourier spectra and besides the scaling exponent H is computed from these values.

3.3.2. Craig and Mack's Model

The second model that was studied in this research was developed by Craig & Mack in the year 2013. This model was also designed under simple physical arguments to describe the oceanic tropical atmospheric convection under the assumption that convection mainly depends on the moisture content at the lower troposphere. A brief description of the model was previously presented in section 2.2.3 and it is suggested to be check by the reader for a better comprehension of the model philosophy. Craig and Mack's model [2013] is assembled over the basis a tropospheric moisture budget where three physical processes exist: i) a moisture sink given by a subsidence drying (SD), ii) a vertical transport mechanism of moisture given by convective moistening (CM), and iii) an horizontal transport mechanism of moisture given by a down–gradient diffusive flux (DGDF). These processes are formally presented as follows:

$$\partial_t I_v(\mathbf{x},t) = -\alpha I_v + \left(\frac{1-\epsilon}{\epsilon}\right) a(t)\,\phi(\mathbf{x},t) + \nu\,\Delta I_v(\mathbf{x},t) = \text{SD} + \text{CM} + \text{DGDF} \tag{3-39}$$

$$I_v(\mathbf{x},0) = I_0(\mathbf{x}) \tag{3-40}$$

$$I_v(0,t) = I_v(L,t) \tag{3-41}$$

where $I_v(\mathbf{x},t)$ represents the moisture content at the time t and spatial location $\mathbf{x}$, α is the rate of drying by subsidence, ϵ is the precipitation efficiency, $a(t)$ is a variable representing a constrain in the total amount of areal precipitation, $\phi(\mathbf{x},t)$ is a variable representing the quantity of rainfall at the time t and location $\mathbf{x}$, and ν represents an eddy diffusivity.

Rainfall is here modeled as a function that depends on the moisture content in a non–linear form. Thus, Craig & Mack [2013] suggest the following expression for computing rainfall:

$$R(\mathbf{x},t) = a(t)\,\left[\exp\left(b\,\frac{I_v(\mathbf{x},t)}{I_v^*}\right) - 1\right] = a(t)\,\phi(\mathbf{x},t) \tag{3-42}$$

where I_V^* represents a saturation integrated moisture and b is a scaling parameter. For the example simulation which is exhibited in Figure 3-36, the numerical implementation of it required the following parameters and criteria:

1. The moisture content $I_v(\mathbf{x},t)$ was initialized using an homogeneous distribution of the field settled on 50 kg m^{-2}, then it was perturbed by a low-amplitude noise.

2. The time evolution of equation 3-39 was computed for a two dimensional domain using an explicit finite difference scheme with a double periodic domain of size 256×256 grid cells, each one of size 40×40 km^2 ($L = 10,240$ km, $\Delta x = 40$ km).

3. The time resolution is $\Delta t = 10$ min, and the total simulation time is $T = 30$ d.

4. The rate (or frequency scale) of drying by subsidence α equals to 5×10^{-6} s^{-1}.

5. The scaling parameter b of equation 3-42 equals to 11.4.

6. The precipitation efficiency ϵ which presents the relationship between $\epsilon = \beta I_v / I_v^*$, was computed for $\beta = 1.1$.

7. The saturation integrated moisture I_v^* was adopted to be 57 kg m^{-2}, as suggested by Craig & Mack [2013], Bretherton et al. [2004, 2005].

8. The eddy diffusivity ν is assumed to be constant and equals to 1×10^5 m^2 s^{-1}.

9. All parameters were selected in order to get a numerical stability of the model (i.e. $\frac{\nu \Delta t}{(\Delta x)^2} \leq \frac{1}{2}$).

Figure 3-36 shows some snapshots for 30 days of simulation time. The snapshots of Figure 3-36 were selected at the times 0.0, 1.25, 2.5, 5.0, 7.5 and 30.0 d, in order to illustrate the time evolution of rainfall patterns. Here, outputs are depicting rainfall fields which in turn are represented in mm h^{-1}. During the progress of simulation, the final simulated pattern is the outcome of a coarsening process in which the size of the convective cells grows and settles in a specific location as time goes by.

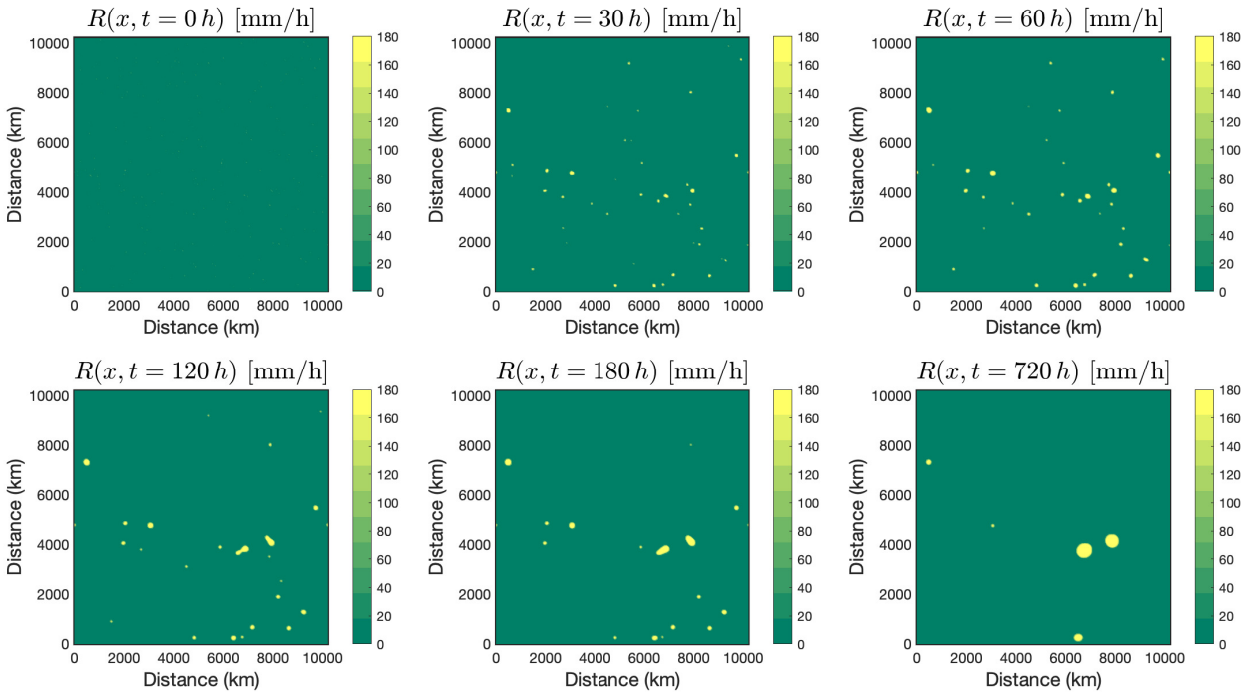

Figure 3-36: Example of simulated rainfall fields via Craig & Mack's model [2013]. In every panel is shown the rainfall field $R(\mathbf{x}, t)$ (in mm h^{-1}) for the times t indicated on the top of each panel. The model parameters used for these simulations were: $\Delta t = 10$ min, $\Delta x = 40$ km, $P_{av} = 8$ kg m^{-2} d^{-1}, $\alpha = 5 \times 10^{-6}$ s^{-1}, $b = 11.4$, $I_v^* = 57$ kg m^{-2}, $\nu = 1 \times 10^5$ m^2 s^{-1} and the time lapse for the simulation was 30 d.

Figure 3-37 shows some statistics of the rainfall field during the simulation time. As one can observe in Figure 3-37, rainfall patterns evolve toward a preferential state of organization over the domain. This can be observed in the mean value of the rainfall field $\langle \mathbf{R}(\mathbf{x}, t) \rangle \equiv \overline{R}$, since it starts from a zero value to reach a limit value of ≈ 130.7 mm h^{-1}. In the same way, the maximum value of the simulated rainfall field $\max\{R(\mathbf{x}, t)\} \equiv \max\{R\}$ starts from a zero value to reach a limit value of ≈ 175.8 mm h^{-1}; albeit, at the times 3.75 h, 4.25 h and 4.75 h, there exist some peaks values of ≈ 255 mm h^{-1} which represent any kind of hysteresis or transition state. Indeed, at the time 4.75 h the slope of $\overline{R}$ changes from a smooth to a steeper form. On the other hand, the spatial variability of the rainfall field σ also grows up from zero to a maximum value of ≈ 75.8 mm h^{-1} at ≈ 3.23 h, then it decreases to a stable value of 65.5 mm h^{-1}.

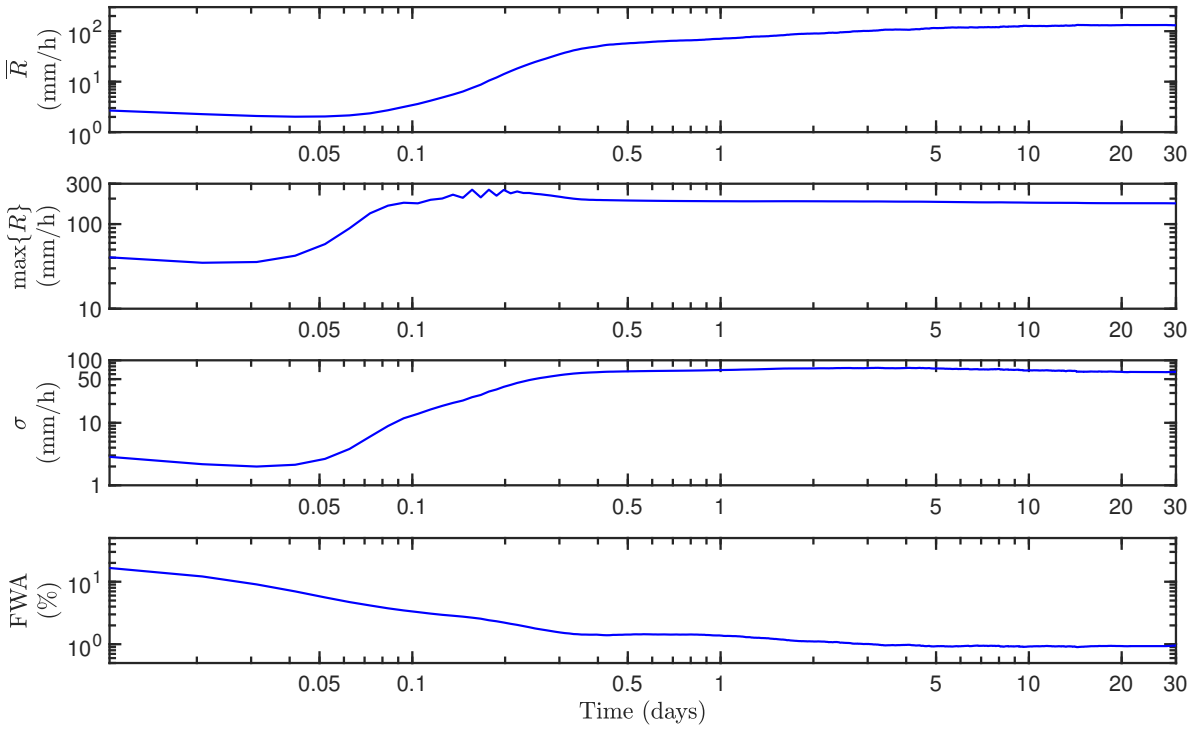

Figure 3-37: Time variation of the mean ($\overline{R}$), maximum ($\max\{R\}$), standard deviation (σ) and fractional wet area of the rainfall intensity fields simulated by the Craig & Mack's model [2013]. The parameters for getting the simulated field were: $\Delta t = 10$ min, $\Delta x = 40$ km, $P_{av} = 8$ kg m^{-2} d^{-1}, $\alpha = 5 \times 10^{-6}$ s^{-1}, $b = 11.4$, $I_v^* = 57$ kg m^{-2}, $\nu = 1 \times 10^5$ m^2 s^{-1} and the simulation time lapse equals 30 d.

In the fractional wet area (FWA), there exists another kind of behavior. Since FWA decreases in a logarithmic way from 22.4% at 0 h to 1.5% at ≈ 7.3 h. After that time, FWA is still decreasing with a very smooth slope to get a value of $\approx 0.9\%$. Based on data, there are four regions describing the model outcomes: i) a initial–phase region starting at 0 h to ≈ 1.0 h ii) a growth region starting at 1.0 h to 9.6 h, iii) a ripening region starting at

9.6 h to 5.0 d, and iv) a steady–state region from time 5.0 d to the end of the simulation time.

Empirical multifractal spectra of simulated rainfall fields via Craig & Mack's model [2013] are shown in Figure 3-38. Similarly to the results shown in the previous section for Nordstrom & Gupta's model [2003] results, the first simulated rainfall field exhibits a shift to the left in the α–axis as against others computed spectra, and also a fractal dimension D_0 lesser in value (i.e. $D_0 \approx 0.82$). Clearly, this behavior shows a spurious multifractality as a result of the low–amplitude noise applied to moisture field at the beginning of the simulation. Inasmuch as the simulation advances and the coarsening process takes place, the fractal dimension D_0 increases as well. After crossing the so-called ripening region [Craig & Mack, 2013], the fractal dimension D_0 is settled in a value of ≈ 1.13 and a weak variability is observed during the rest of the simulation time. After ripening region is passed through, multifractal spectra are characterized by non–singular measures and a weak multifractality begins to appear.

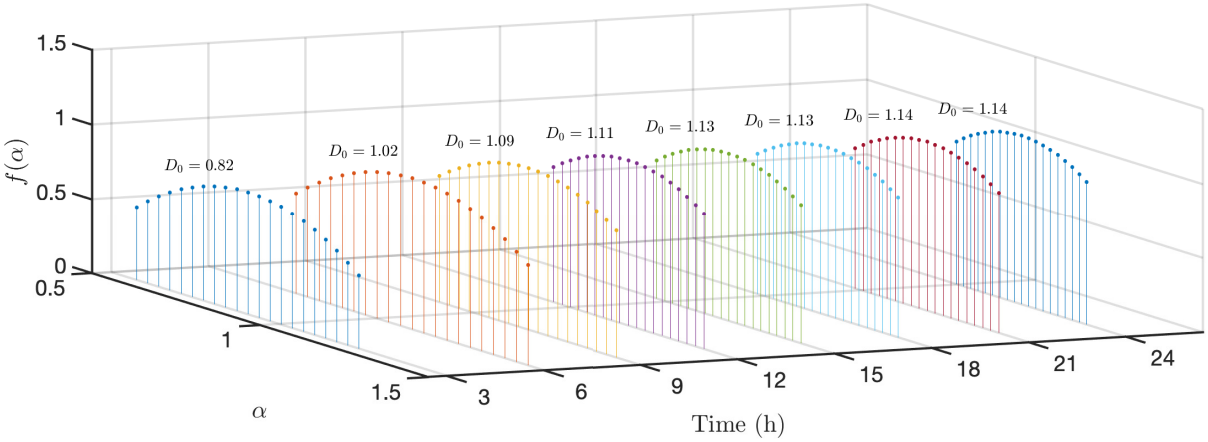

Figure 3-38: Time evolution of empirical multifractal spectra for a Craig & Mack model simulation. These spectra correspond to some of the plots exhibited in Figure 3-36.

Statistics of multifractal variables for simulated rainfall fields, can be observed in Table 3-9. The average value of the singularity exponent α_{min} is ≈ 1.05 which means measures are non–singular most of the time. The spectral width H_α changes over time and its maximum value (≈ 0.67) is obtained at ≈ 6.25 h. After this time, the spectral width decreases significantly to a value ≈ 0.17 which indicates patterns evolve statistically toward a weak multifractality. This last can be also verified by the closeness between the larger (≈ 1.12) and the smaller fractal dimensions (≈ 1.03).

The magnitude cumulant method was also applied to simulated rainfall fields. During the initial–phase of the simulation, either C_0 or C_2 decrease as time progresses. In the so–called growth region, either C_0 or C_2 also decrease as time progresses, but a kind of plateau is formed in C_2 from 4.8 h to $\approx$ 24 h. From day 1 to day 15, C_2 decays in a logarithmic way up to the ending simulation time, whereas C_0 increase slowly to the value ≈ 1.13. It

is to highlight that as C_2 is decreasing as time progresses, the resulting rainfall patterns are moving away from a strong multifractality; indeed, only patterns which were generated during the plateau region in C_2 can be considered as those patterns having a non–spurious multifractality.

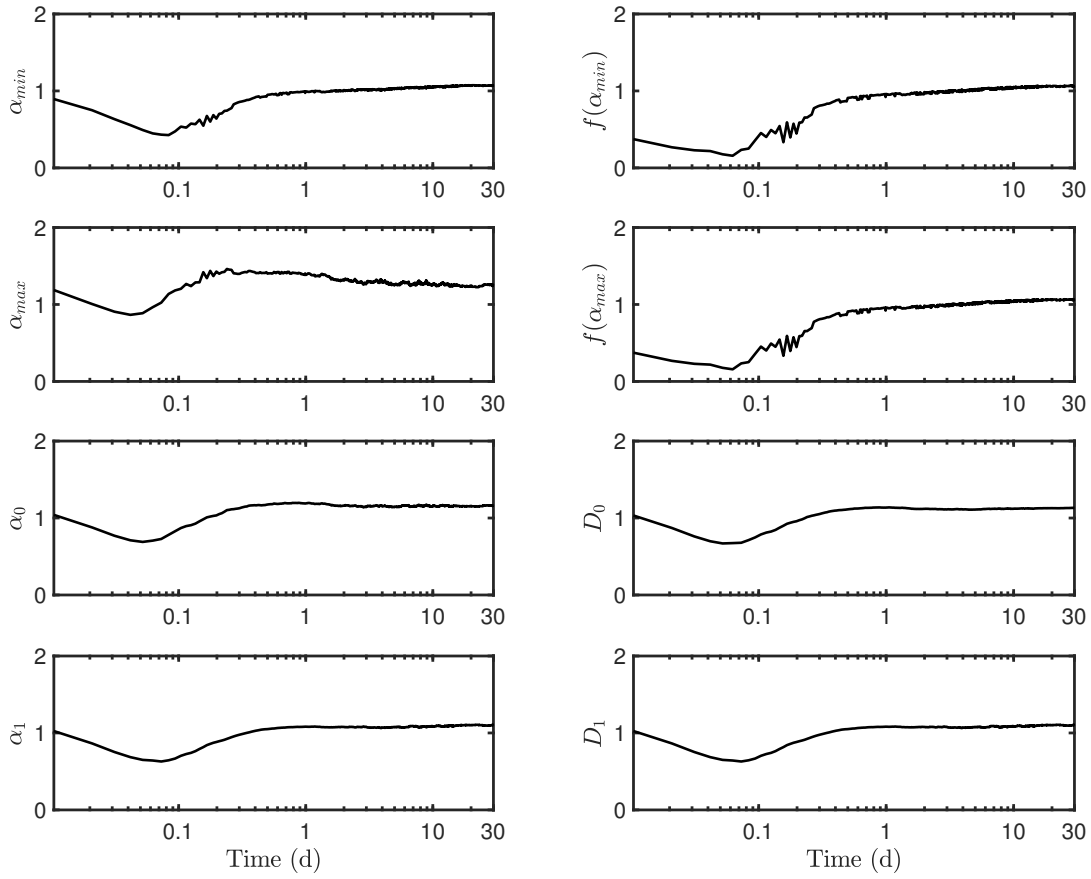

Figure 3-39: Time variation of the multifractal variables: α_{min}, α_{max}, α_0, α_1, $f(\alpha_{min})$, $f(\alpha_{max})$, $D_0 = f(\alpha_0)$, and $D_1 = f(\alpha_1)$. All these variables were obtained for the simulated rainfall fields via Craig & Mack's model [2013).

Figure 3-40 shows two–point correlation functions of either the maximums or averaged quantities of the simulated rainfall fields. In every panel of Figure 3-40, the maximum correlation are depicted in the upper part and the averaged correlations are depicted in the lower part; furthermore, every plot shows a solid red line to identify a logarithmic–linear fitting applied to the first data of the correlation function. As one can evidence in Figure 3-40, these correlation functions are characterized by the existence of a linear relationship between $C(\delta, \Delta x)$ vs $\ln(\Delta x)$ for long–enough values of Δx and for the scales $\delta = \{40, 80, 120, 160\}$ km. These results are representing long–range spatial dependencies; however, the log–linear slopes of the correlation functions in Figure 3-32 tend to be equal to zero, i.e. $m \to 0$ in the representation $C(\delta, \Delta x) = m\ \ln(\Delta x) + b$ and therefore, the non–linear structure of model outputs cannot be described through multiplicative cascade processes.

Table 3-9: Statistics of the multifractal variables: α_{min}, α_{max}, α_0, α_2, $f(\alpha_{min})$, $f(\alpha_{max})$, $D_0 = f(\alpha_0)$, $D_1 = f(\alpha_1) = \alpha_1$, and $D_2 = f(\alpha_2)$. The statistics were obtained for the multifractal spectra of the simulated rainfall fields via Craig & Mack's model [2013]. In this table σ, CV, IQR, γ represent the standard deviation, the coefficient of variation, the interquartile range and the skewness, respectively.

	α_{min}	α_{max}	α_0	α_1	$f(\alpha_{min})$	$f(\alpha_{max})$	D_0	D_1
Minimum	0.43	0.87	0.69	0.63	0.16	0.16	0.67	0.63
Mean	1.05	1.26	1.16	1.09	1.03	1.03	1.12	1.09
Median	1.06	1.26	1.16	1.09	1.05	1.05	1.13	1.09
Maximum	1.07	1.47	1.25	1.22	1.07	1.07	1.24	1.22
σ	0.05	0.04	0.03	0.03	0.07	0.07	0.03	0.03
CV (%)	4.74	3.19	2.24	2.91	6.64	6.64	2.44	2.91
IQR	0.03	0.03	0.01	0.02	0.03	0.03	0.01	0.02
γ	-7.18	0.84	-12.25	-9.41	-7.60	-7.60	-11.93	-9.41

Figure 3-41 exhibits the distribution of rainfall increments $\Delta_{t,s}$ at the time the maximum value of the field was obtained (i.e. at 3.75 h). Moreover, in every panel of Figure 3-41 is depicted the fitting to the NIG distribution. Increments $\Delta_{t,s}$ were computed for an orthogonal basis of point whose distance between the central point and extremes are equal to $s = \{40, 80, \ldots, 10000\}$ km. For all cases where increments were computed, the distributions exhibit a quasi–Gaussian form, but a NIG distribution can not describe suitably the statistical law of increments $\Delta_{t,s}$. It is to highlight that the distributions of simulated data are characterizing an intermittent pattern but not a multifractal one. Once more, the NIG–distribution qualify intermittent structures as multifractal if there exists a good fitting to this distribution. On the other hand, the variance of increments σ^2 is almost stable for $s \geq 120$ km and although there is not a specific statistical distribution that describes the increments $\Delta_{t,s}$, a visual inspection of the distributions allows to assume that $\Delta_{t,u}(Y) \overset{\text{dist}}{=} \Delta_{t,v}(X)$ can be accepted and the incremental similarity hypothesis as well.

As a final analysis, the identification of dynamic scaling exponents was also implemented. In Figure E-2 is observed the space – time diagram which was generated from the spatial average in either zonal (left panel of Figure E-2) or meridional (right panel of Figure E-2) direction. The resulting Fourier spectra are exhibited in Figure 3-42 and both spectra seem to be very alike in symmetry. The lower panels of Figure E-2 show two orthogonal cuts over each spectra. Their slopes were computed and jotted down into each plot. The dynamic scaling exponents H are $\approx 1/5$ for the zonally–averaged data and $\approx 1/7$ for the meridionally–averaged data. These exponents are not related with symmetries observed in turbulence processes neither with pure diffusive–driven process; in fact, such values are unrealistic in statistical analysis of rainfall data.

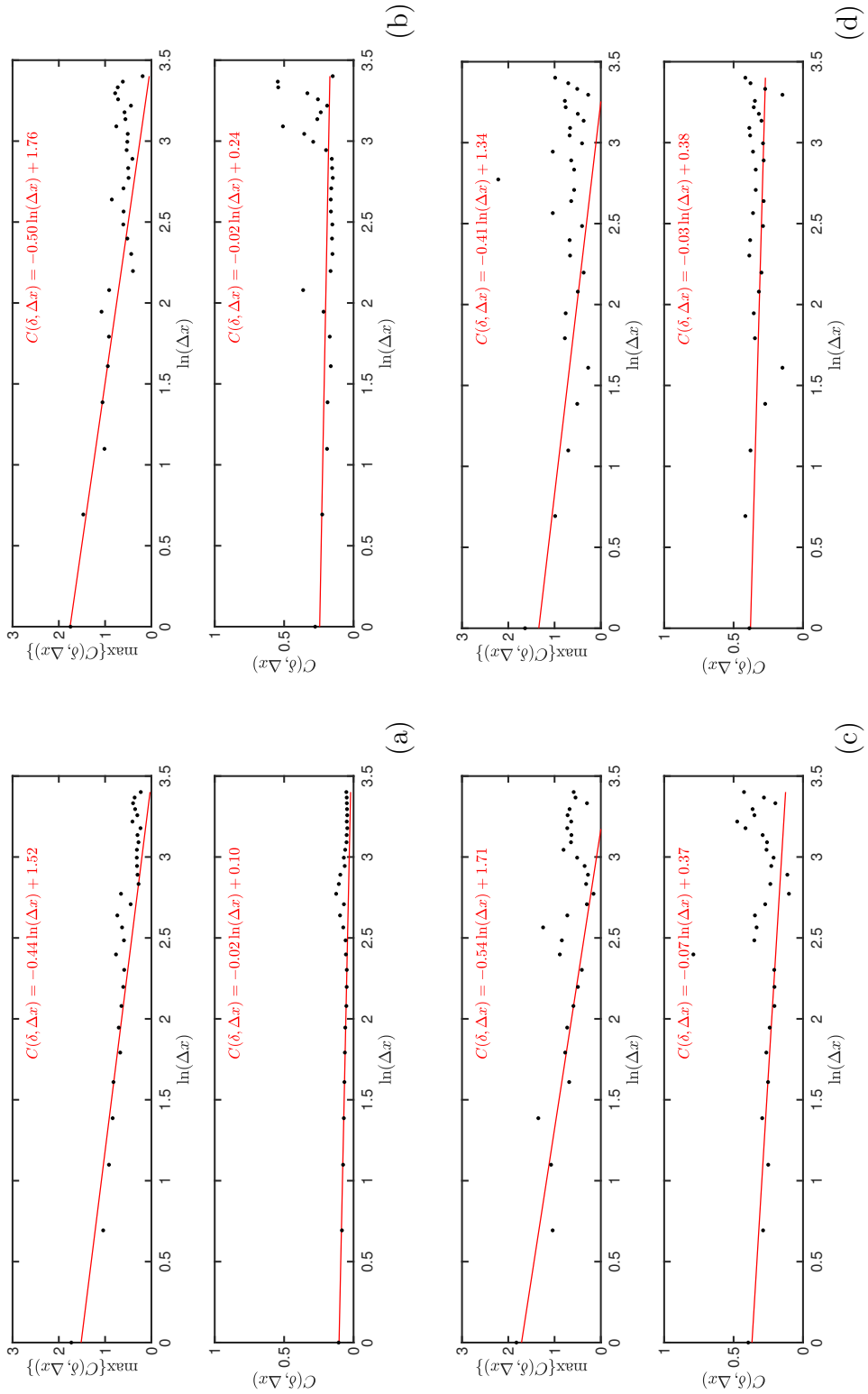

Figure 3-40: Maximum ($\max\{C(\delta, \Delta x)\}$ vs $\ln(\Delta x)$) and average ($C(\delta, \Delta x)$ vs $\ln(\Delta x)$) values of the two–point correlation function obtained for the simulated rainfall fields via Craig & Mack's model [2013]. In this plot the two–point correlation analysis is developed for the scales $\delta = \Delta x = 40$ km (a), $\delta = 2\,\Delta x$ (b), $\delta = 3\,\Delta x$ (c), and $\delta = 4\,\Delta x$ (d).

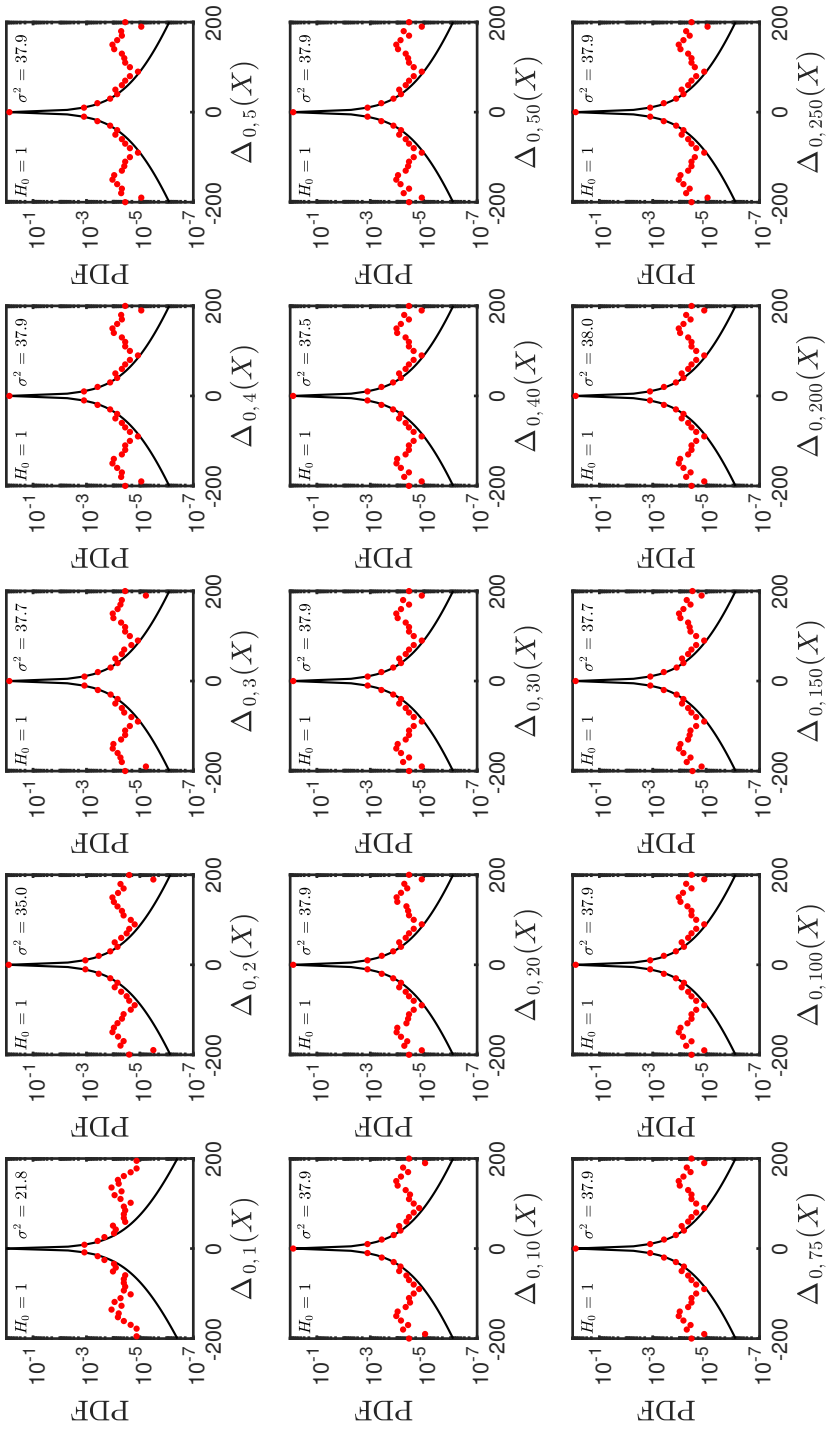

Figure 3-41: Probability density function of increments $\Delta_{t,a}$ of simulated rainfall fields via Craig & Mack model [2013]. The red dots represent the empirical PDF of simulated data and the solid line represents the normal inverse Gaussian distribution fitting. In each frame is indicated the null hypothesis value H_0 (zero for the acceptance of H_0 and one for the rejection of H_0; both values for a 5% of significance level α). The null hypothesis states that data come from a normal inverse Gaussian distribution.

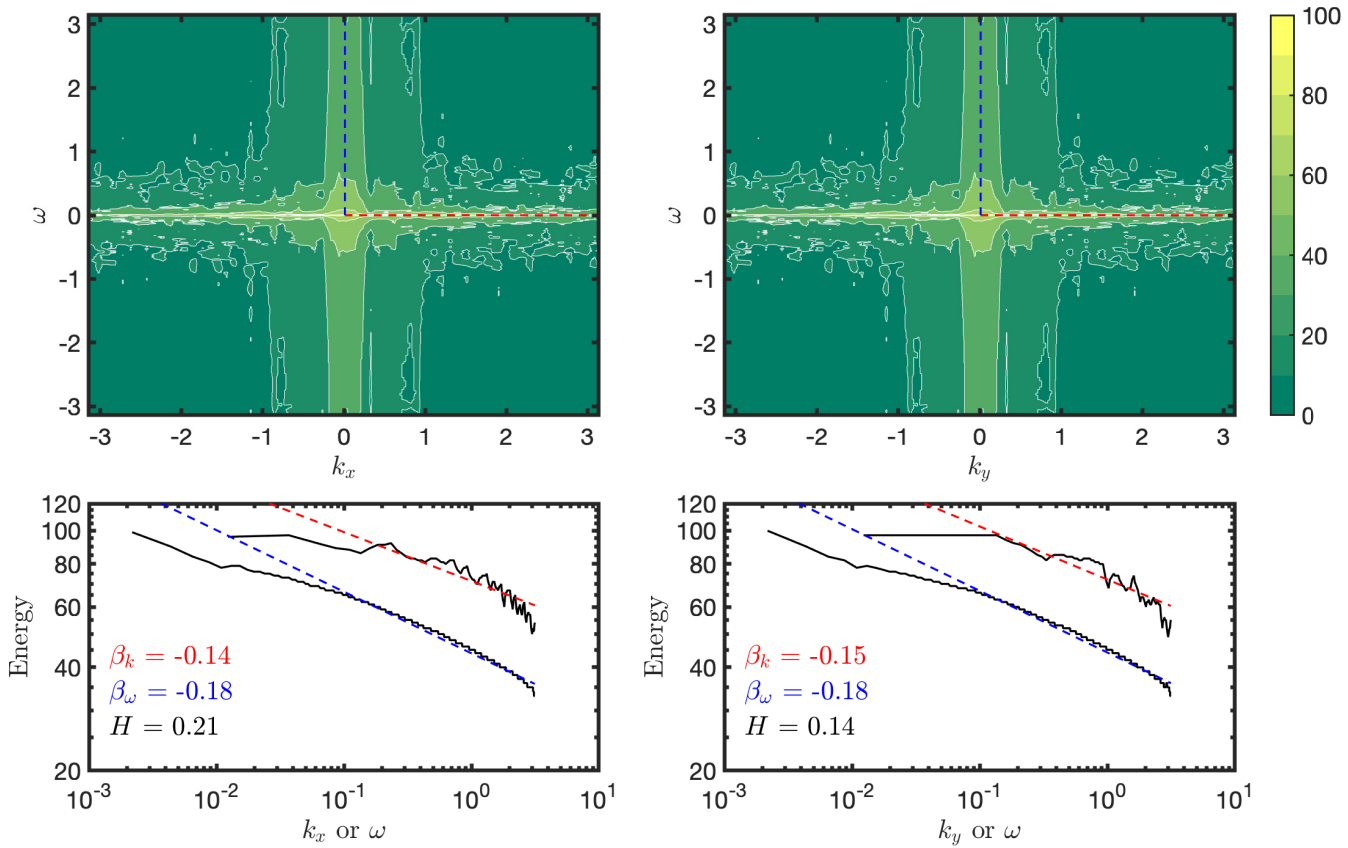

Figure 3-42: Isocorrelation contours in the $2D$ Fourier space for the x–t section (upper left panel) and the y–t section (upper right panel) of the averaged values of simulated rainfall fields via Craig & Mack's model [2013] and shown in Figure 3-36. The lower panels are representing two cuts in the $2D$ Fourier spectra in the wavelength direction ($k.$) and frequency direction $f.$. In the lower panels are indicated the slopes β of each cuts in the Fourier spectra and besides the scaling exponent H is computed from these values.

3.3.3. Hottovy and Stechmann's Model

In the year 2015, Hottovy & Stechmann introduced a stochastic reaction–diffusion equation to describe the water vapor dynamics over tropical oceanic regions (see section 2.2.3). Hottovy & Stechmann's model is formally presented as follows:

$$\partial_t q(\mathbf{x},t) = \left[-\frac{1}{\tau}(q(\mathbf{x},t) - q^*) + F(\mathbf{x},t) \right] + b_0\, \Delta q(\mathbf{x},t) + D_* \dot{W}(\mathbf{x},t) \tag{3-43}$$

$$q(\mathbf{x},0) = q_0(\mathbf{x}) \tag{3-44}$$

$$q(0,t) = q(L,t) \tag{3-45}$$

where $q(\mathbf{x},t)$ is the integrated column water vapor in the location $\mathbf{x} = x_1\,\hat{e}_1 + x_2\,\hat{e}_2$ and at time t, τ is a relaxation time, q^* is a threshold water vapor content for strong convection takes place, $F(\mathbf{x},t)$ is an external force, b_0 is a diffusion coefficient, D_*^2 is a stochastic forcing variance, and $\dot{W}(\mathbf{x},t)$ is an independent white noise random variable.

Hottovy & Stechmann's model [2015] sketches the physical processes of precipitation, evaporation, and turbulent advection–diffusion of water vapor in a tropical atmosphere. Among others considerations of the model, the small scale flux convergence is modeled as an eddy diffusion process $b_0\,\Delta q(\mathbf{x},t)$, the turbulent effect in the water vapor dynamics is modeled under a damping mechanism $-\frac{1}{\tau}[q(\mathbf{x},t) - q_*]$ and a stochastic forcing $D_*\dot{W}(\mathbf{x},t)$, and the precipitation/evaporation effect is modeled by mean of a forcing parameter $F(\mathbf{x},t)$. In this model, precipitation is modeled as a non–linear transformation. Such a transformation represents a phase–transition function as suggested by Peters & Neelin [2006] and Neelin et al. [2009], thus:

$$R(\mathbf{x},t) = f\big(\,[q(\mathbf{x},t) - q_*]\;\sigma(\mathbf{x},t)\big) \tag{3-46}$$

where $\sigma(\mathbf{x},t) = \Theta(q - q_*)$ represents the cloudiness in terms of a Heaviside function. For the example simulation which is exhibited in Figure 3-43, the numerical implementation of Hottovy & Stechmann's model required the following parameters and criteria:

1. The water vapor content $I_v(\mathbf{x},t)$ was initialized using an homogeneous distribution of the field settled on 50 mm, then it was perturbed by a low–amplitude noise.

2. Equation 3-43 was computed for a two dimensional domain using an explicit finite difference scheme with a double periodic domain of size $1,000 \times 1,000$ grid cells, each one of size 5×5 km^2 ($L = 5,000$ km, $\Delta x = 5$ km). However, in Figure 3-43 is only shown a subset of the domain of size 256×256 grid cells ($L_s = 1280$ km, $\Delta x = 5$ km).

3. Time resolution is $\Delta t = 36$ seconds and the total simulation time is $T = 30$ d.

4. The damping coefficient equals to 96 h.

5. The diffusion coefficient equals to 750 km^2 h^{-1} ($\approx 2.1 \times 10^5$ m^2 s^{-1}).

6. The interaction coefficient $b = b_0/\Delta x^2$ equals to 30 h^{-1}.

7. The magnitude of the stochastic forcing equals to 150 mm h^{-1}.
8. The deterministic forcing is consider to be equal to zero.
9. The threshold water vapor content to switch to convection equals to 65 mm.
10. It is highlighted the selected parameters allow the numerical stability of the numerical model (i.e. $\frac{\nu \Delta t}{(\Delta x)^2} \leq \frac{1}{2}$).

Figure 3-43 shows some output plots after 30 days of simulation time. The left panels of Figure 3-43 show the evolution of the water vapor content $q(\mathbf{x}, t)$ at times 0.0, 7.5, 15, and 30 d. For the same times, central panels of Figure 3-43 show the cloudiness value which is scaled between values 0 and 1. The right panels of Figure 3-43 show the resulting spatial pattern of rainfall intensity $R(\mathbf{x}, t)$ for the times indicated above. Unlike other models, this depicts patterns more heterogeneous and roughly similar to those observed in nature.

Figure 3-44 shows time series plots of variables: i) spatially–averaged precipitation ($\overline{R}$), ii) maximum amount of precipitation of the field ($\max\{R\}$), iii) spatial standard deviation of the field (σ) and iv) fractional wet area (FWA) of the rainfall field, are exhibited in Figure 3-44. During the first 20.0 h of the simulation time, spatially–averaged precipitation fluctuates in the range from 0.0 mm h^{-1} to 183 mm h^{-1}. After 20 h of simulation, $\overline{R}(t)$ decays of the form $\overline{R}(t) \sim t^{1/2}$ up to the day 5.0 and then it starts to increase so slightly (slope$\approx 9.5 \times 10^{-2}$ mm h^{-1} d^{-1}) up to the end of simulation. After the day 5.0, the mean value of $\overline{R}$ is ≈ 29.6 mm. A similar behavior to $\overline{R}$ is observed in the maximum amount of precipitation of the field ($\max\{R\}(t)$), since it presents a fluctuating state in the first 20.0 h of simulation and after that time up to the day 5.0, $\max\{R\}(t)$ increases so slightly (slope$\approx$ 0.5 mm h^{-1} d^{-1}).

The standard deviation of the rainfall field σ presents large fluctuations before the first 20.0 h of simulation, then it decays following a potential function of the form $\sigma \sim t^{0.5}$ up to reach a stable value around 20 mm h^{-1}. On the other hand, the fractional wet area (FWA) is almost zero during the first 5 days of simulation. After day 5, FWA continues growing as a random walk with drift (i.e. $\text{FWA}_{t+1} = a + \text{FWA}_t + \epsilon_t$), where ϵ_t is a white noise term. Since there is a constant rise of FWA, one would expect FWA$\rightarrow 1$ if the simulation time is long enough ($t \rightarrow \infty$). However, the model finds a state of high FWA but stable. Based on the data description, there are three regions describing the model outputs: i) a initial–phase region starting from zero to the time 20.0 h ii) a transition region starting at 20.0 h to the fifth day of simulation, and iii) a quasi–steady–state region since day 5.0 to the ending time of simulation.

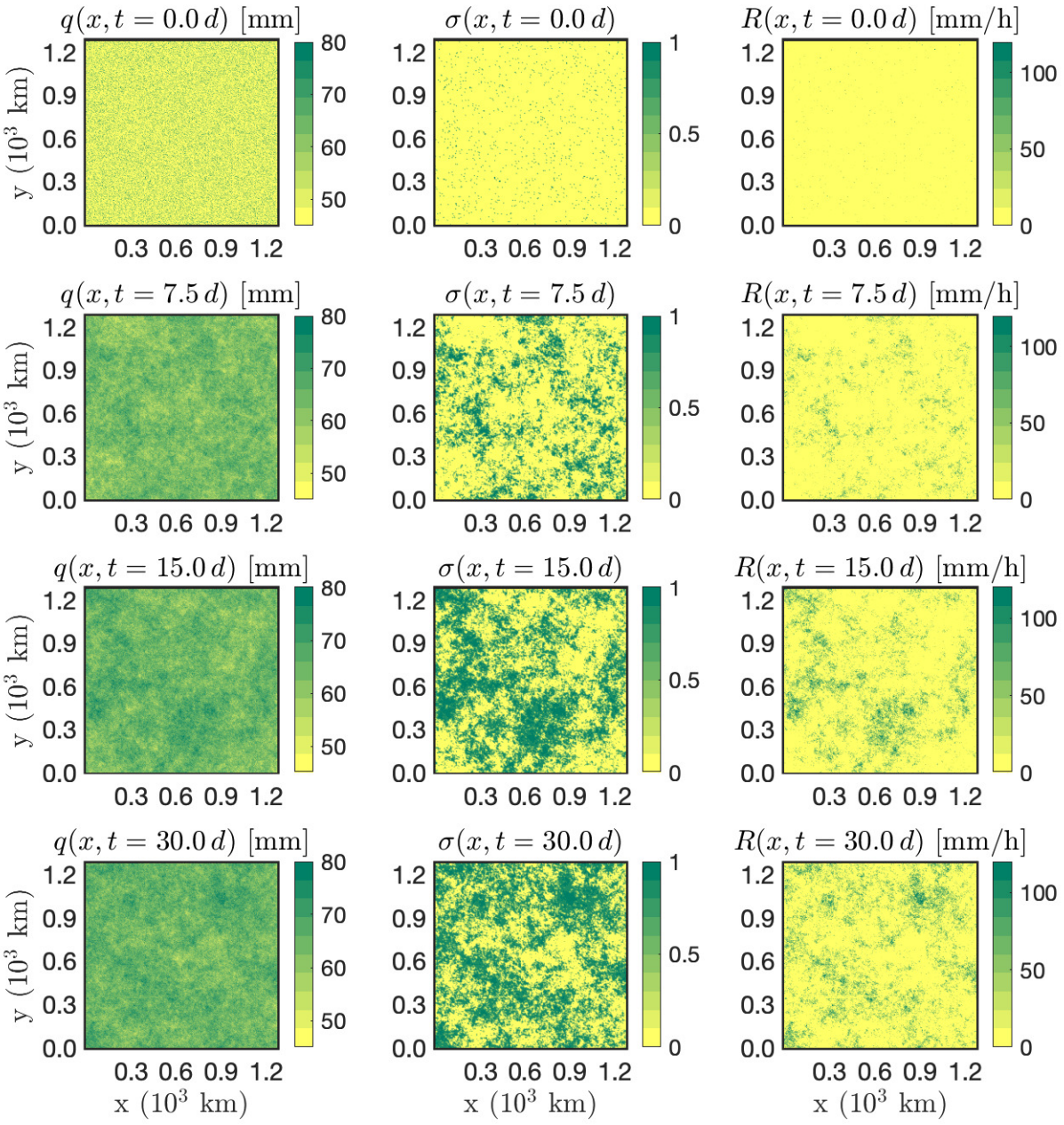

Figure 3-43: Example of simulated rainfall fields via Hottovy & Stechmann's model [2015]. Each row has three panel indicating three outputs of the model. The first panel shows the integrated column water vapor $q(\mathbf{x}, t)$, the second one shows the cloudiness field $\sigma(\mathbf{x}, t)$ and the third one shows the rainfall rate field $r(\mathbf{x}, t)$. For getting these results, the following model parameters were used: $\Delta t = 0.01$ h, $\Delta x = 5$ km, $\tau = 96$ h, and $q_* = 65$ mm, $b_0 = 750$ km^2 h^{-1}, $D_* = 0.15$ mm h^{-1} and the time lapse for the simulation was 30 d.

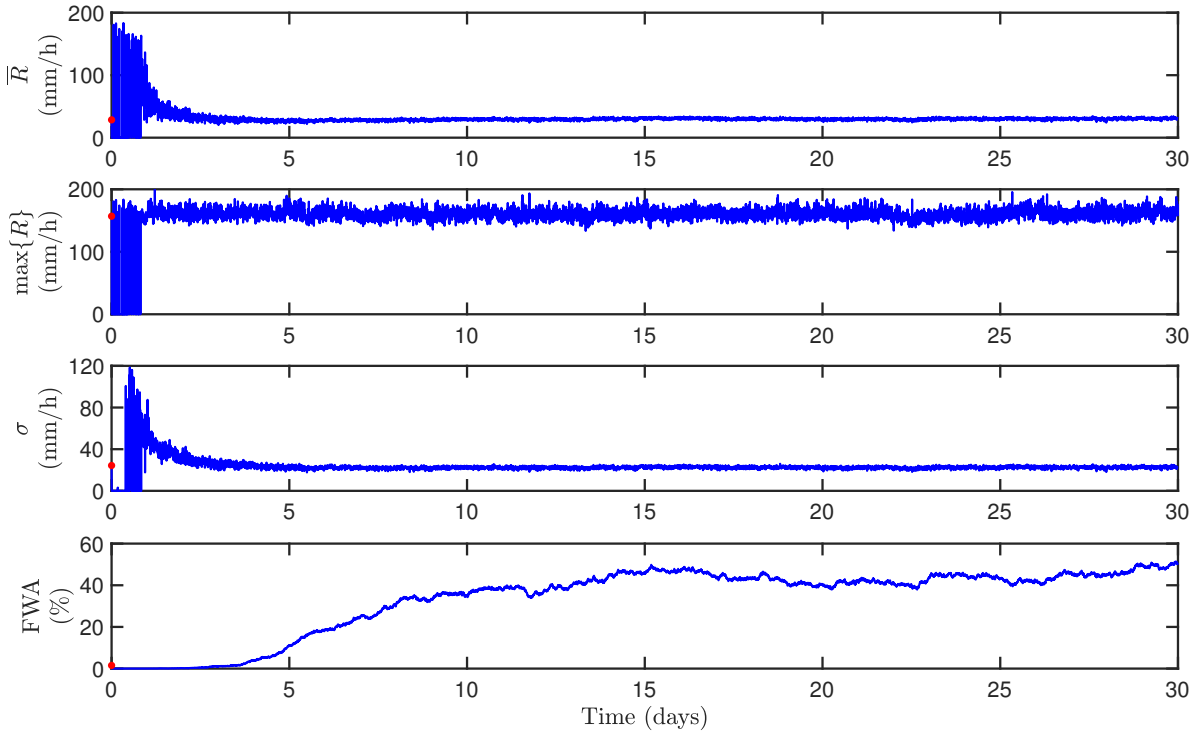

Figure 3-44: Time variation of the mean ($\overline{R}$), maximum (max$\{R\}$), standard deviation (σ) and fractional wet area of the rainfall intensity fields simulated by the Hottovy & Stechmann's model [2015].

Empirical multifractal spectra of simulated rainfall fields are shown in Figure 3-45. As one can observe in Figure 3-45, multifractal spectra change their fractal features over time; for instance, the fractal dimension of the support D_0 increases from $D_0 = 0.38$ to $D_0 = 1.83$. However, the spectral width H_α decreases over time. Albeit there exists a large variability of multifractal properties for empirical spectra, there exists a kind of stability condition in their statistics. Table 3-10 and Figure 3-45 show that the average value of the fractal dimension D_0 is ≈ 1.63, whose value is nearly similar to those found in observational data (i.e. weather radars, satellite records, etc.). On the other hand, the average spectral width H_α is ≈ 0.6, whose value indicates the existence of several scaling exponents and consequently the appearance of multifractality in simulated patterns. It is highlighted that the variability of fractal descriptors is higher in this model outputs as compared to the results obtained by other studied physically–based models. The stochastic forcing could be connected with such a variability of fractal descriptors. Whether the stochastic forcing is reduced to zero, one would expect either a smaller statistical variability or spectra representing weak multifractality.

Figure 3-46 shows time series of some multifractal spectra descriptors from the beginning of simulation up to the end of it at day 30.0. For all descriptors, a sustained growth is observed which is faster for the first 5.0 days of simulation and slower from time 5.0 d to

time 30 d. During the first five days of simulation, the measures of simulated rainfall fields are characterized as singular ones, and only after the fifth day of simulation the singularities barely appear during the rest of simulation.

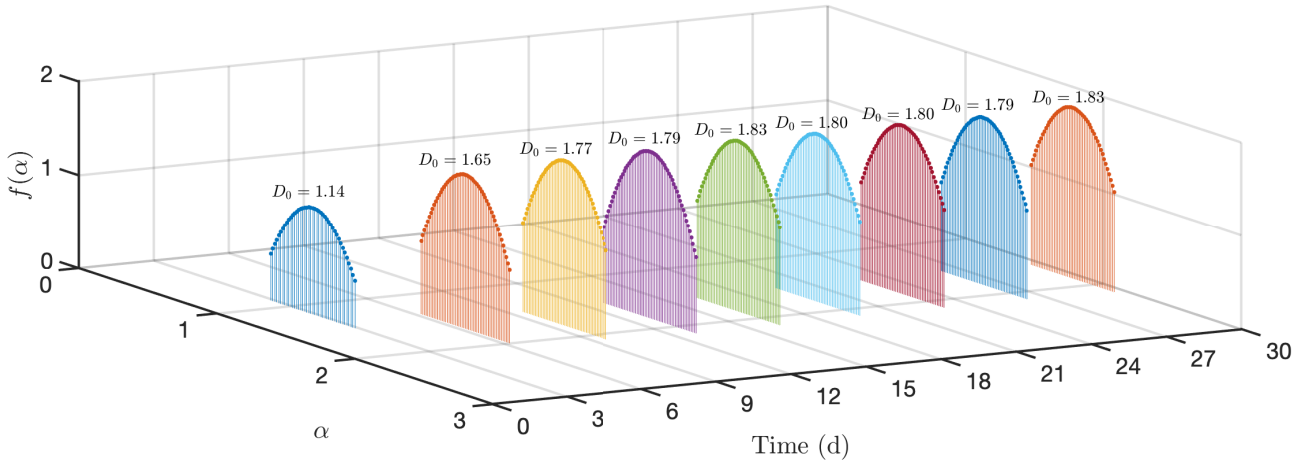

Figure 3-45: Time evolution of multifractal spectra for Hottovy & Stechmann's model simulations [2015]. These results correspond to the data analysis of those shown at Figure 3-43.

Table 3-10: Statistics of the multifractal variables: $\alpha_{min} \equiv \min\{\alpha\}$, $\alpha_{max} \equiv \min\{\alpha\}$, α_0, α_2, $f(\alpha_{min})$, $f(\alpha_{max})$, $D_0 = f(\alpha_0)$, $D_1 = f(\alpha_1) = \alpha_1$, and $D_2 = f(\alpha_2)$. The statistics were obtained for multifractal spectra of simulated rainfall fields via Hottovy & Stechmann's model [2015]. In this table σ, CV, IQR, γ represent the standard deviation, the coefficient of variation, the interquartile range and the skewness, respectively.

	α_{min}	α_{max}	α_0	α_1	$f(\alpha_{min})$	$f(\alpha_{max})$	$f(\alpha_0)$	$f(\alpha_1)$
Minimum	0.00	0.00	0.00	0.00	0.00	0.00	0.00	0.00
Mean	1.37	1.96	1.66	1.60	0.87	0.87	1.63	1.60
Median	1.52	2.13	1.82	1.77	0.99	0.99	1.80	1.77
Maximum	1.58	2.20	1.87	1.81	1.17	1.17	1.84	1.81
σ	0.37	0.43	0.39	0.40	0.29	0.29	0.40	0.40
CV (%)	26.75	21.77	23.71	24.63	33.34	33.34	24.17	24.64
IQR	0.10	0.09	0.10	0.10	0.18	0.18	0.10	0.10
γ	-2.45	-3.07	-2.75	-2.69	-1.81	-1.81	-2.72	-2.69

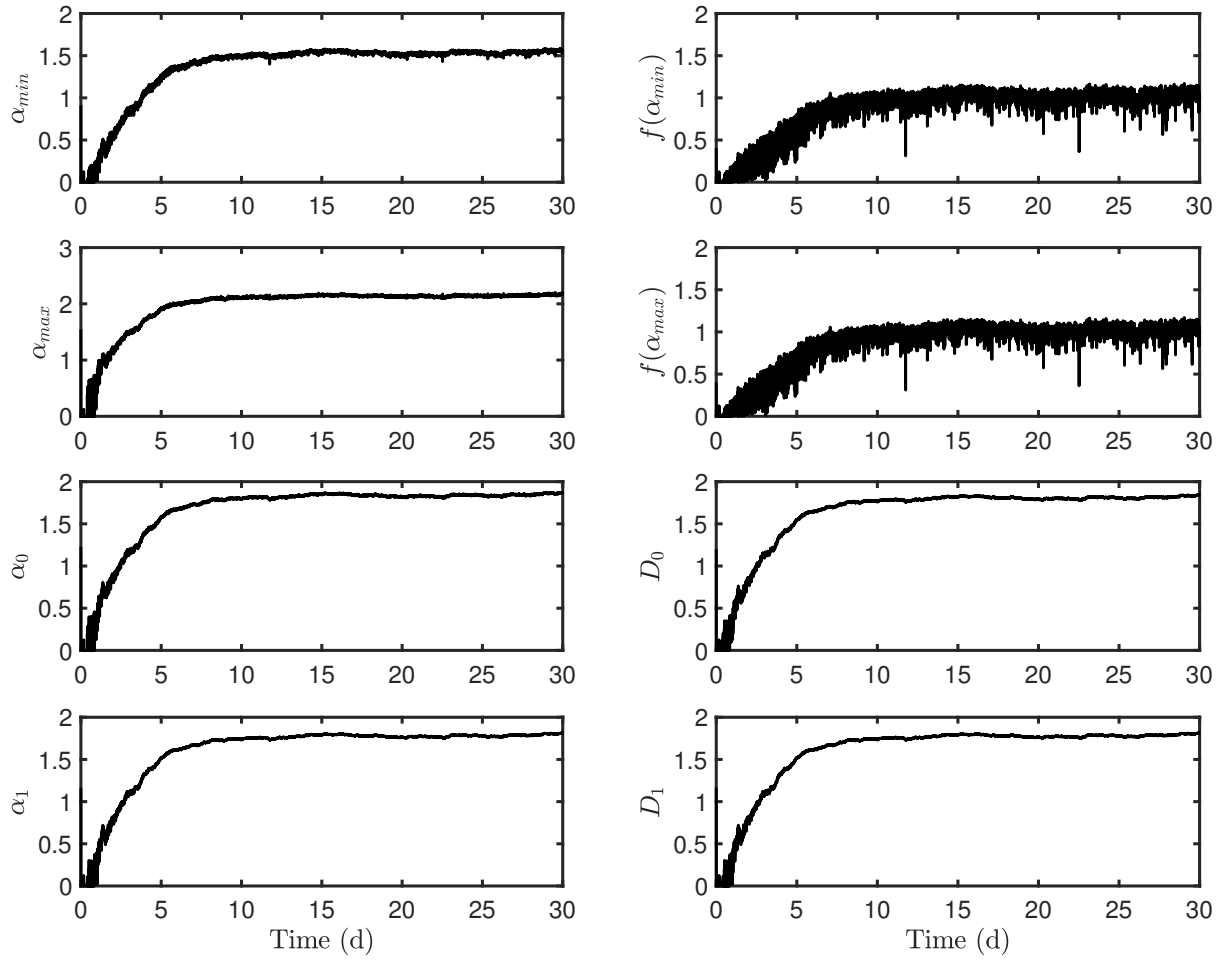

Figure 3-46: Time variation of the multifractal variables: $\alpha_{min} \equiv \min\{\alpha\}$, $\alpha_{max} \equiv \min\{\alpha\}$, α_0, α_1, $f(\alpha_{min})$, $f(\alpha_{max})$, $D_0 = f(\alpha_0)$, and $D_1 = f(\alpha_1)$. All these variables were obtained for the simulated rainfall fields via Hottovy & Stechmann's model [2015].

Figure 3-47 shows the first cumulant–based magnitude coefficients $C_{0,1,2}$. The first 20 h of simulation show a kind of hysteresis in the computed coefficients. Only after the first 20 h, C_0 and C_2 begin to increase monotonically and C_1 gets a stable value. The growth of C_0 is representing a fill of the spatial domain by rainfall, therefore, this implies there is a raise of rainfall events over time.

Figure 3-48 shows two–point correlation functions of either the maximum or averaged correlation quantities of simulated rainfall fields via Hottovy & Stechmann's model [2015]. All correlation functions shown in Figure 3-48 describe a long–range dependence, since the fitting to a logarithmic function of the relationship between $C(\delta, \Delta x)$ and Δx; furthermore, this long–range dependence does not rely on scales, at least for a range no longer than ≤ 20 km.

Albeit there exists a long–range dependence, the slope of the logarithmic fitting is nearly close to zero which means there could not be a representation based multiplicative cascades.

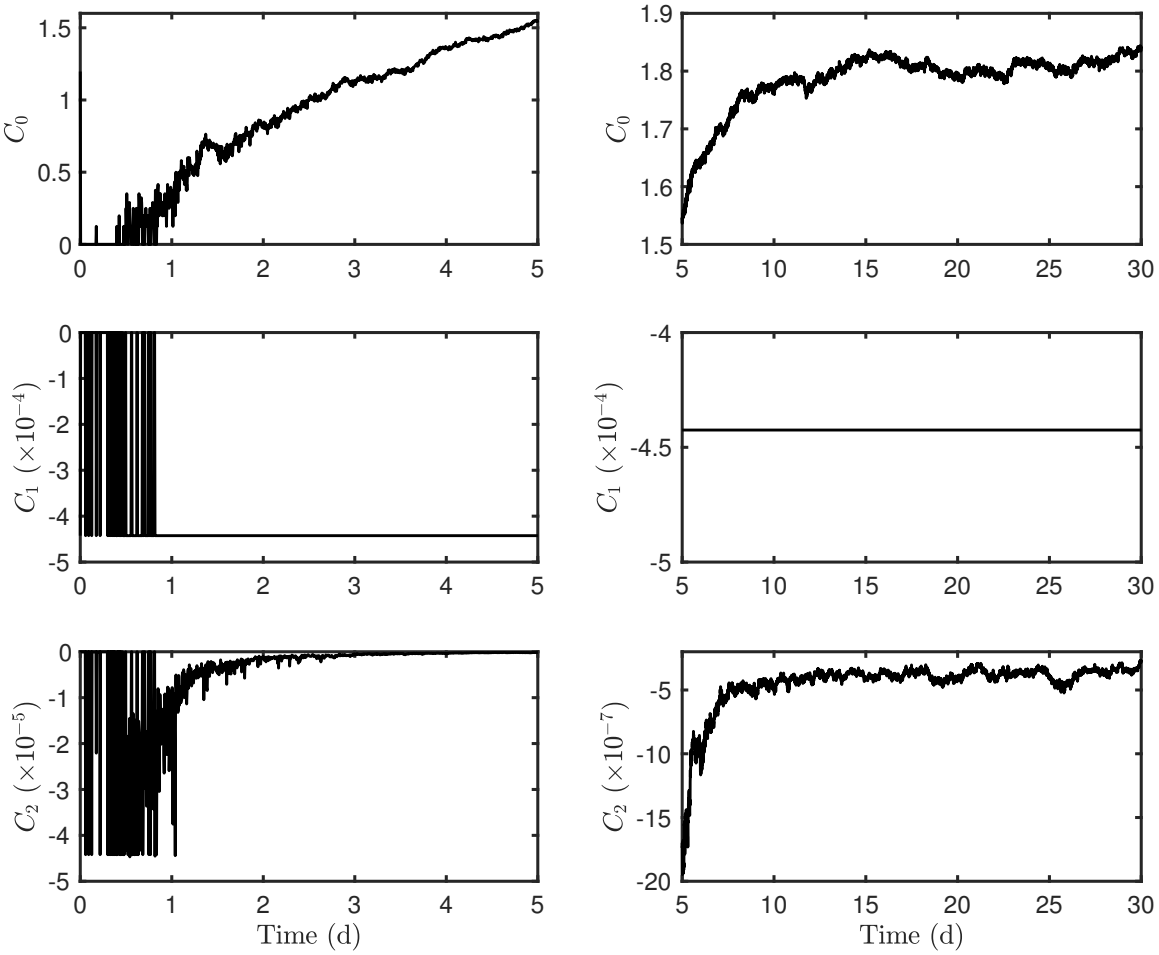

Figure 3-47: Time variation of first cumulant–based magnitude coefficients C_0, C_1, and C_2 for simulated rainfall fields via Hottovy & Stechmann's model [2015]. These results correspond to those data shown at Figure 3-43. In the left panels, the time axis is bound to the first 5 hours of simulation for a better visualization of results. The right panels show the first cumulant–based magnitude coefficients from day 5 to day 30.

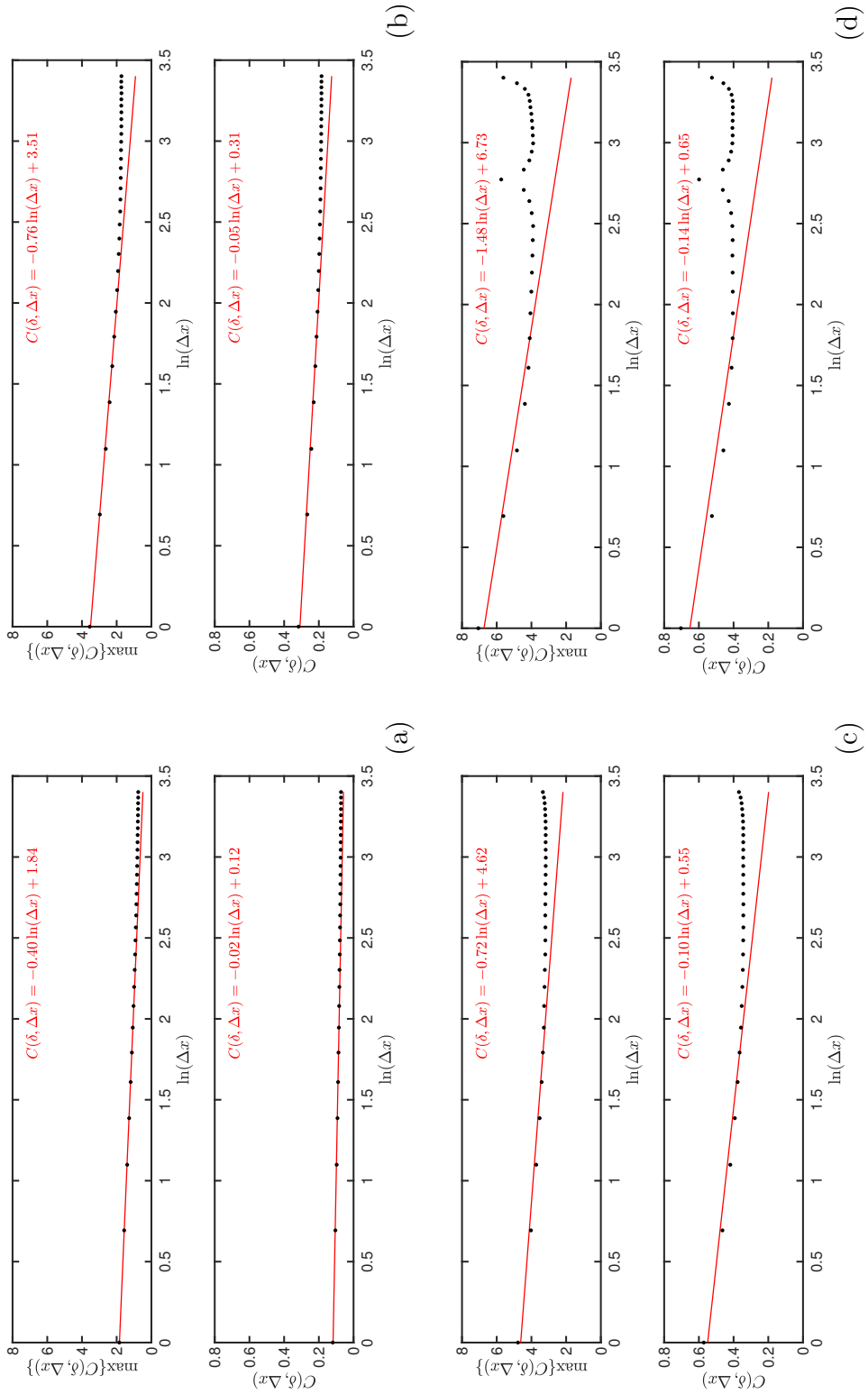

Figure 3-48: Maximum value of two-point correlation field ($\max\{C(\delta, \Delta x)\}$ vs $\ln(\Delta x)$) and average value of two–point correlation field ($C(\delta, \Delta x)$ vs $\ln(\Delta x)$) obtained for simulated rainfall fields via Hottovy & Stechmann's model [2015]. In this plot the two–point correlation functions are build for the scales $\delta = \Delta x = 5$ km (a), $\delta = 2\,\Delta x$ (b), $\delta = 3\,\Delta x$ (c), and $\delta = 4\,\Delta x$ (d).

The incremental similarity analysis reveals some important characteristic of the Hottovy & Stechmann's model [2015] outputs. Figure 3-49 shows distributions of rainfall increments $\Delta_{t,s}$. All the increment $\Delta_{t,s}$ were computed for the rainfall field which was generated at the time $\approx$ 11.75 d ($\approx$ 282 h). The selected field corresponds to the one where higher values of precipitation took place (i.e. $R(x,t) \approx 193$ mm h^{-1}). In Figure 3-49, the variable s represents spatial lags (i.e. $s = \{5, 10, \ldots, 1250\}$ km) in orthogonal directions respect to a reference point. Furthermore, Figure 3-49 includes the fitting of increments $\Delta_{t,s}$ to the NIG–distribution.

As can be seen in Figure 3-49, the empirical distribution of increments $\Delta_{t,s}$ describes a good fitting to the NIG distribution for all selected values of s; however, some slight deviations can be observed at the tails of distributions. The marginal variance of increments $\Delta_{t,s}$ changes inasmuch as s is higher, nonetheless, some fluctuations in variances are given for $s > 30$. Based on the observations of obtained empirical distributions, one could assumes that the incremental similarity hypothesis, i.e.

$$\Delta_{t,u}(Y) \overset{\text{dist}}{=} \Delta_{t,v}(X) \tag{3-47}$$

is valid for selected data, which in turn seem to be independent of the variance σ^2. This propitious result is likely to be connected with the structure of the model. Barndorff-Nielsen & Schmiegel [2015] claimed that there exists a class of random processes known as IS type where incremental similarity property is intrinsically satisfied (e.g. Gaussian processes). The random process known as Ornstein–Uhlenbeck process is a Gaussian process which resembles to the structure of Hottovy & Stechmann's model [2015], therefore, this model could possibly represents an IS–type random process and future research could lead to prove such a hypothesis.

As a final analysis to Hottovy & Stechmann's model outputs, the identification of dynamic scaling exponents was done. The resulting 2D Fourier spectra are exhibited in Figure 3-50 whose symmetries are rather similar for either a zonal or a meridional analysis. The former means there is an isotropic space and it can be verified through the values of dynamic scaling exponents. The computed dynamic scaling exponents are nearly equal ($H \sim 1/4$) and these exponent values are nearly close to those found in random growth models, e.g. Edwards & Wilkinson's model [1982]. One could think that the random term in Hottovy & Stechmann's model plays an important role in the statistical description of multifractality, however, the main framework of the model is able to represent main features of multifractality. Some complementary analysis will be discussed in the next chapter in order to prove the aforementioned statement.

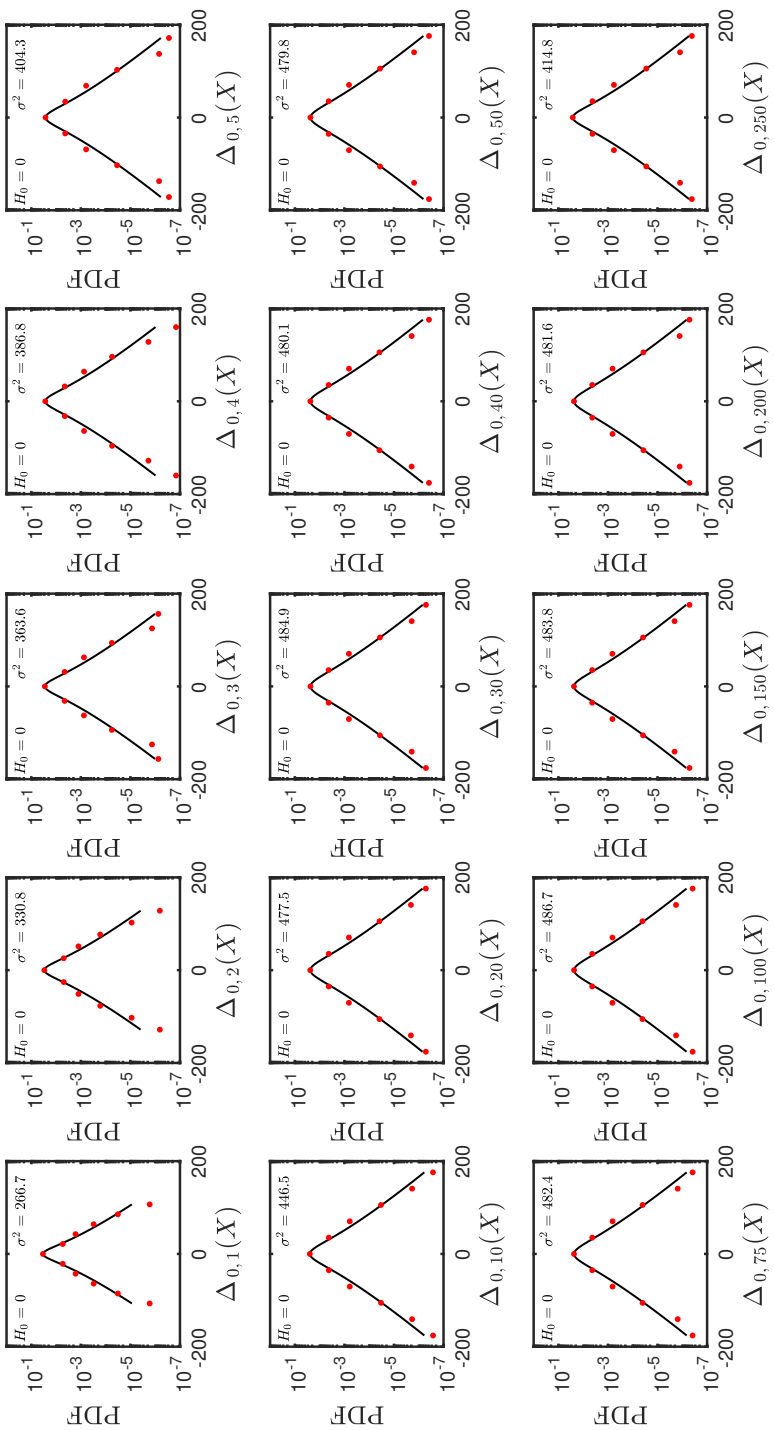

Figure 3-49: Probability density function of increments $\Delta_{t,u}$ of simulated rainfall fields via Hottovy & Stechmann's model [2015]. The red dots represent the empirical PDF corresponding to simulated data and the solid line represents the fitting to the normal inverse Gaussian distribution. In each frame is indicated the null hypothesis value H_0 (zero for the acceptance of H_0 and one for the rejection of H_0; both values for a 5% of significance level α). The null hypothesis states that data come from a normal inverse Gaussian distribution. The field selected for the incremental similarity analysis corresponds to the simulated field at time 11.75 d.

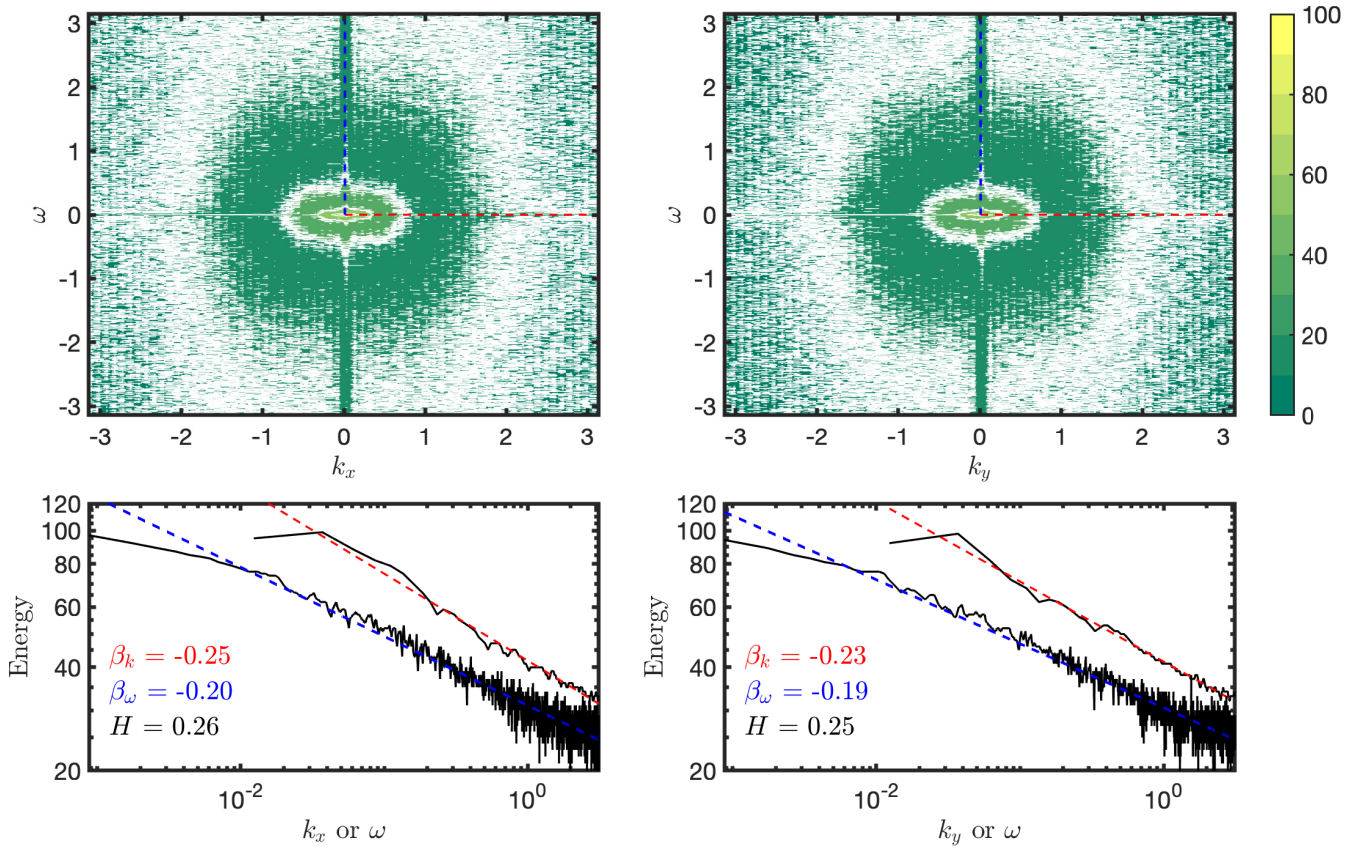

Figure 3-50: Isocorrelation contours in the $2D$ Fourier space for the x–t section (upper left panel) and the y–t section (upper right panel) of the averaged values of simulated rainfall fields via Hottovy & Stechmann model [2015] and shown in Figure 3-43. The lower panels are representing two cuts in the $2D$ Fourier spectra in the wavelength direction ($k.$) and frequency direction $f.$. In the lower panels are indicated the slopes β of each cuts in the Fourier spectra and besides the scaling exponent H is computed from these values.

3.3.4. Raymond and Zeng's Cloud Resolving Model

The last model that were studied in the framework of this research is the single–column and cloud–resolving model introduced by Raymond & Zeng [2005]. This model was designed to study the large–scale tropical precipitation under a simplified physical parametrization of convection dynamics. In this model is assumed that the large–scale tropical dynamics is given by a weak temperature gradient (WTG) approximation which in turn allows to compute the domain–averaged vertical velocity from the domain–averaged heating. Furthermore, the model also provides a tool for computing rainfall as a function of the vertically–averaged saturation deficit as suggested by Peters & Neeling [2006, 2009].

For a WTG environment, the vertical velocity w is defined as a function of the horizontally–averaged potential temperature excess θ', such that:

$$w(z,t) = \frac{\theta'(z,t)}{\tau(d\bar{\theta}/dz)} \tag{3-48}$$

where τ is the relaxation time, $d\bar{\theta}/dz$ represents the vertical gradient of potential temperature, and θ' represents an anomaly of the potential temperature profile $((\bar{\theta}(z,t) - \theta_0(z,t))\, M(z))$ where θ_0 is an external reference potential temperature and $M(z)$ is a masking function defined as:

$$M(z) = \begin{cases} \sin\left(\pi \dfrac{z}{h}\right) & z < h \\ 0 & z \geq h \end{cases} \tag{3-49}$$

where h is the height of the tropopause. The Raymond & Zeng's model [2005] was implemented on a non–rotating and horizontally periodic domain where the governing mass equation to solve is:

$$\partial_t\, \rho + \nabla(\rho\, \mathbf{u}) = -\nu\, \frac{p_0 - p_R}{R\, T_R} \tag{3-50}$$

and the governing momentum equation to solve is:

$$\partial_t\, \rho\, \mathbf{u} + \nabla \cdot (\rho\, \mathbf{u}\, \mathbf{u} - K D - K_h \nabla_h \rho\, \mathbf{u}) + \nabla p + g\rho\hat{k} = \rho(\mathbf{F}_s - \mathbf{E}_m) - \mu(\mathbf{u}_h - \mathbf{u}_{h0}) \tag{3-51}$$

where ρ is the air density, $\mathbf{u}$ is the air velocity vector, the term $-\nu(p_0 - p_R)/(R\, T_R)$ represents a mass source to relax the surface pressure p_0 to $p_R = 1.0 \times 10^3$ hPa, R is the ideal gas constant for the air, T_R is a reference temperature equal to 300 K, ν is a rate for the mass adjustment equals to 1.0×10^{-3} s^{-1}, K is an eddy mixing coefficient, D is a deformation rate tensor given by $(1/2)(\partial_j u_i - \partial_i u_j)$, K_h is a horizontal eddy mixing coefficient for the suppression of high–frequency numerical modes, p is the pressure, g is gravity, $\mathbf{F}_s$ is the force due to surface stresses, $\mathbf{E}_m$ is a relaxation term which forces the mean wind profile $\bar{\mathbf{u}}$ to the reference profile $\mathbf{u}_0$, $\mathbf{u}_h$ is the horizontal velocity, $\mathbf{u}_{h0}$ is the horizontal reference velocity, and μ is an externally specified damping profile which will be turned on only in the stratosphere for damping upward–propagating gravity waves.

The thermodynamic equation for solving is represented as follows:

$$\partial_t \rho\theta_e + \nabla \cdot (\rho\theta_e \mathbf{u} - K\nabla\rho\theta_e - K_h\nabla_h\rho\theta_e) = \rho\,(S_{es} + S_{er} - E_e) \tag{3-52}$$

where θ_e is the equivalent potential temperature, S_{es} is the source of equivalent potential temperature from surface fluxes, S_{er} is the source of equivalent potential temperature from radiation, and E_e is the external sink of equivalent potential temperature due to interaction with the large scale flow.

The equation for total advected water mixing ratio r_t is represented as follows:

$$\partial_t \rho r_t + \nabla \cdot (\rho r_t \mathbf{u} - K\nabla\rho r_t - K_h\nabla_h\rho r_t) = \rho\,(S_{cr} + S_{rs} - E_r) \tag{3-53}$$

where r_t is the water mixing ratio, S_{cr} is the conversion rate of cloud water to precipitation, S_{rs} is the source of total cloud water mixing ratio,and E_r is the external sink of water mixing ratio due to interactions with the large scale flow.

The equation for precipitation mixing ratio r_r is represented as follows:

$$\partial_t \rho r_r + \nabla \cdot (\rho r_t \mathbf{u} - K\nabla\rho(\mathbf{u} - w_t\hat{k})r_r - K_h\nabla_h\rho r_r) = -\rho S_{cr} \tag{3-54}$$

where r_r is the precipitation mixing ratio, and w_t is the hydrometeor terminal velocity equals to 5 m s^{-1}, S_{cr} is the conversion rate of cloud water to precipitation.

For running the model and to get outputs for using in the framework of this research, the modelers, Herman & Raymond [2014], adopted an atmosphere height equal to 20 km with a vertical resolution Δz equals to 250 m, a horizontal resolution Δx equals to 1×10^3 m, a time resolution Δt equals to 0.5 s and a total time for simulation equals to 57 d. Others aspects and considerations about the modeling protocol can be inspected in the following references: Herman & Raymond [2014] and Raymond & Zeng [2005]. Here only a few details were shown above in order to offer an overview of the studied model.

Simulated rainfall fields via Raymond & Zeng's model [2005] can be observed in Figure 3-51. Here, the horizontal plane represents the space–time domain, and the vertical axis indicates the rainfall intensity (or rain rate) expressed in mm h^{-1}. The spatial domain is bound to 191 km and the simulation time lapse is 57 d. Figure 3-52 shows how some statistics of simulated rainfall fields change over time. The spatial average value of the rainfall field $\langle \mathbf{R}(\mathbf{x}, t)\rangle \equiv \overline{R}$ at time t is depicted in the upper panel of Figure 3-52 and its dynamics is qualitatively alike to that observed in rainfall observations. Likewise, the spatial maximum value of the simulated rainfall field $\max\{R\}$ is also alike to rainfall observations (see central upper panel of Figure 3-52). It is highlighted that among simulated rainfall fields, some extreme events are identified every 3 d approximately, e.g. at $t = 3.0$ d $\max\{R\} = 191.1$ mm h^{-1}, at $t = 6.4$ d $\max\{R\} = 108.5$ mm h^{-1}, at $t = 9.0\}$ d $\max\{R\} = 105.1$ mm h^{-1}, and so on.

The spatial variability of the rainfall field over time is represented through the spatially–computed standard deviation σ and it can be observed in the central lower panel of Figure

3-52. σ behaves alike to either $\overline{R}$ or $\max\{R\}$. Its maximum values ($\sigma > 20\%$) were recorded for the times $t_{\sigma>20} = \{3.0, 15.5, 23.7, 25.1, 29.9\}$ in which the precipitation records were $R_{\sigma>20} = \{191.1, 176.5, 144.5, 180.6, 163.3\}$, respectively. The fractional wet area (FWA) is exhibited in the lower panel of Figure 3-52. Based on the observation of this variable, the spatial organization of rainfall is characterized by the development of clusters over time; such a behavior is alike to that found in rainfall records. However, outputs do not show any particular type of space–time organization (e.g. self–aggregation), but a climatic modulation. Simulated rainfall patterns show a slight tendency after $t = 30$ d to reduce the quantity of either rainfall events or quantities of rainfall intensity. One could assume that the first 30 days of simulation represent a wet period and after that time, a dry period is found.

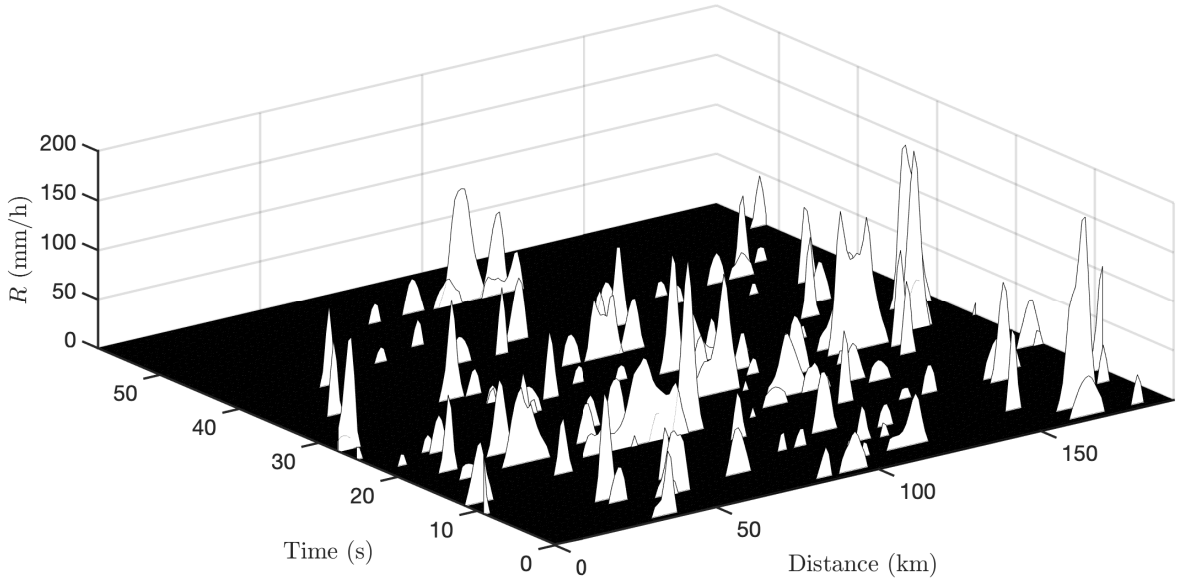

Figure 3-51: Example of simulated rainfall fields $r(\mathbf{x}, t)$ via Raymond & Zeng's model [2014, 2005]. This cloud resolving model was run for a horizontal resolution $\Delta x = 1$ km over a spatial domain of 191 km, and a vertical resolution of $\Delta z = 250$ m over a vertical domain of 20 km. Outputs were recorded every 10^5 s but the model time resolution is $\Delta t = 0.5$ s in order to satisfy the numerical stability criterion. The simulation time lapse was 57 d.

Some multifractal spectra of simulated rainfall fields are shown in Figure 3-53. Spectra were organized in a time-axis for getting an overview of the multifractal dynamics during the first 28 days of simulation. Figure 3-53 shows a irregular dynamics of multifractral spectra over time. Most of these spectra are represented by singular exponents ($\alpha < 1.0$) and low dimensionality $D_0 < 0.5$. Furthermore, some spectra present a low spectral width $H_\alpha = \alpha_{max} - \alpha_{min}$ which characterizes a weak multifractal structures.

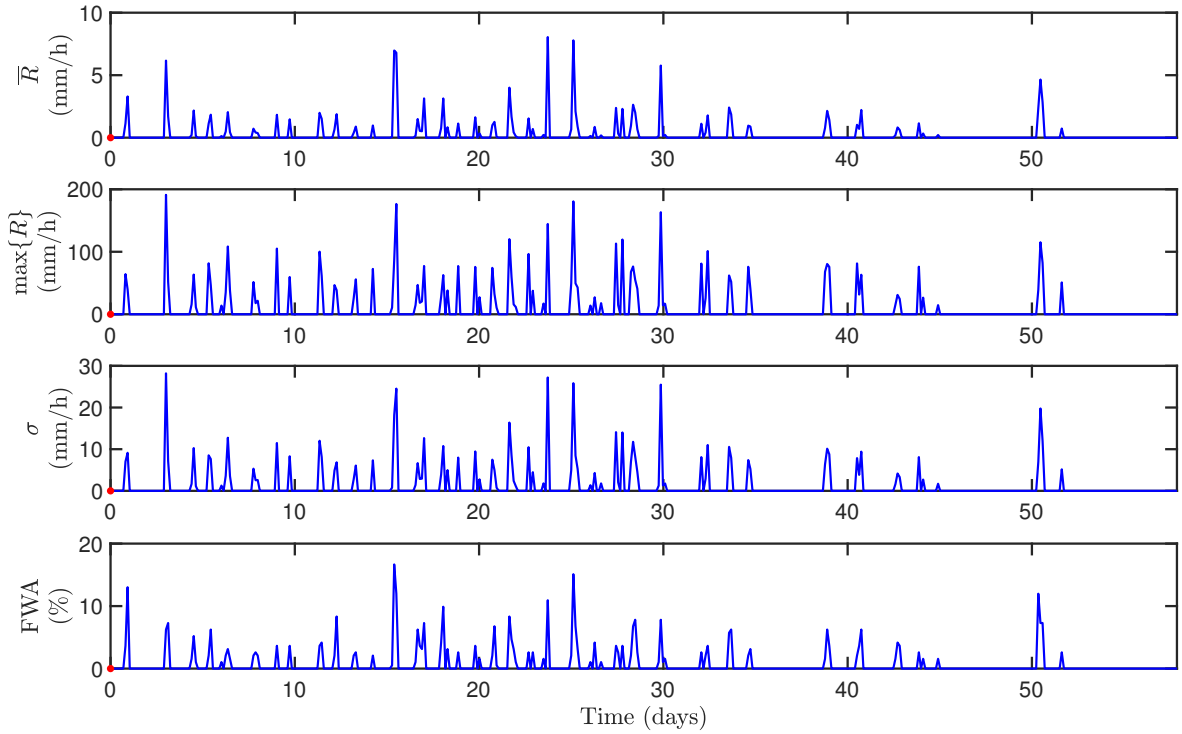

Figure 3-52: Time variation of the mean ($\overline{R}$), maximum (max$\{R\}$), standard deviation (σ) and fractional wet area of the rainfall intensity fields simulated by the Raymond & Zeng's model [2014, 2005].

Figure 3-54 shows the main multifractal descriptors as time series. The statistics of them can be observed in Table 3-11. As one can appreciate, singularity exponents α identify the capability of Raymond & Zeng's model [2005] for generating singular measures during all the simulation time. Furthermore, the model can also generate either weak or strong multifractal structures over time. Weak multifractal structures were identified in the time domain with an average inter-arrival time of 2.8 d, whereas strong multifractal structures were identified in the time domain with an average inter-arrival time of 16.0 h. So, there is a higher frequency of strong multifractal patterns.

Through the model outputs analysis, it is easy to assume that most of simulated rainfall events can be characterized as complex structures alike to those found in rainfall; nonetheless, the velocity for replicating such structures is faster than those observed in nature. Thus, although the model represents a more realistic physics of rainfall processes, there are some drawback for representing realistic statistical properties of rainfall.

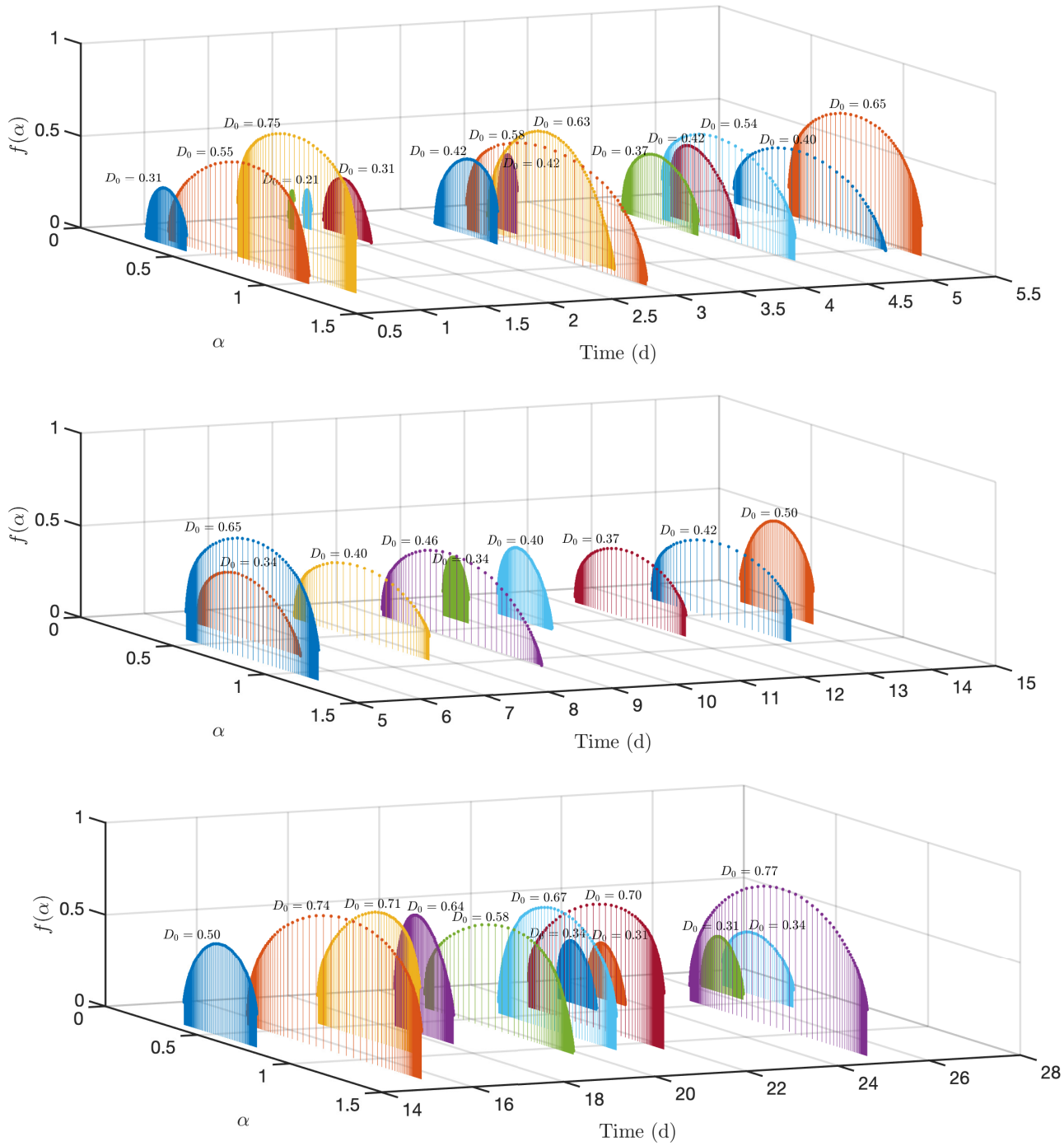

Figure 3-53: Time evolution of multifractal spectra for Raymond & Zeng's model simulations [2014, 2005]. This CRM was run for a horizontal resolution $\Delta x = 1$ km over a spatial domain of 191 km, a vertical resolution $\Delta z = 250$ m and a time resolution $\Delta t = 0.5$ s.

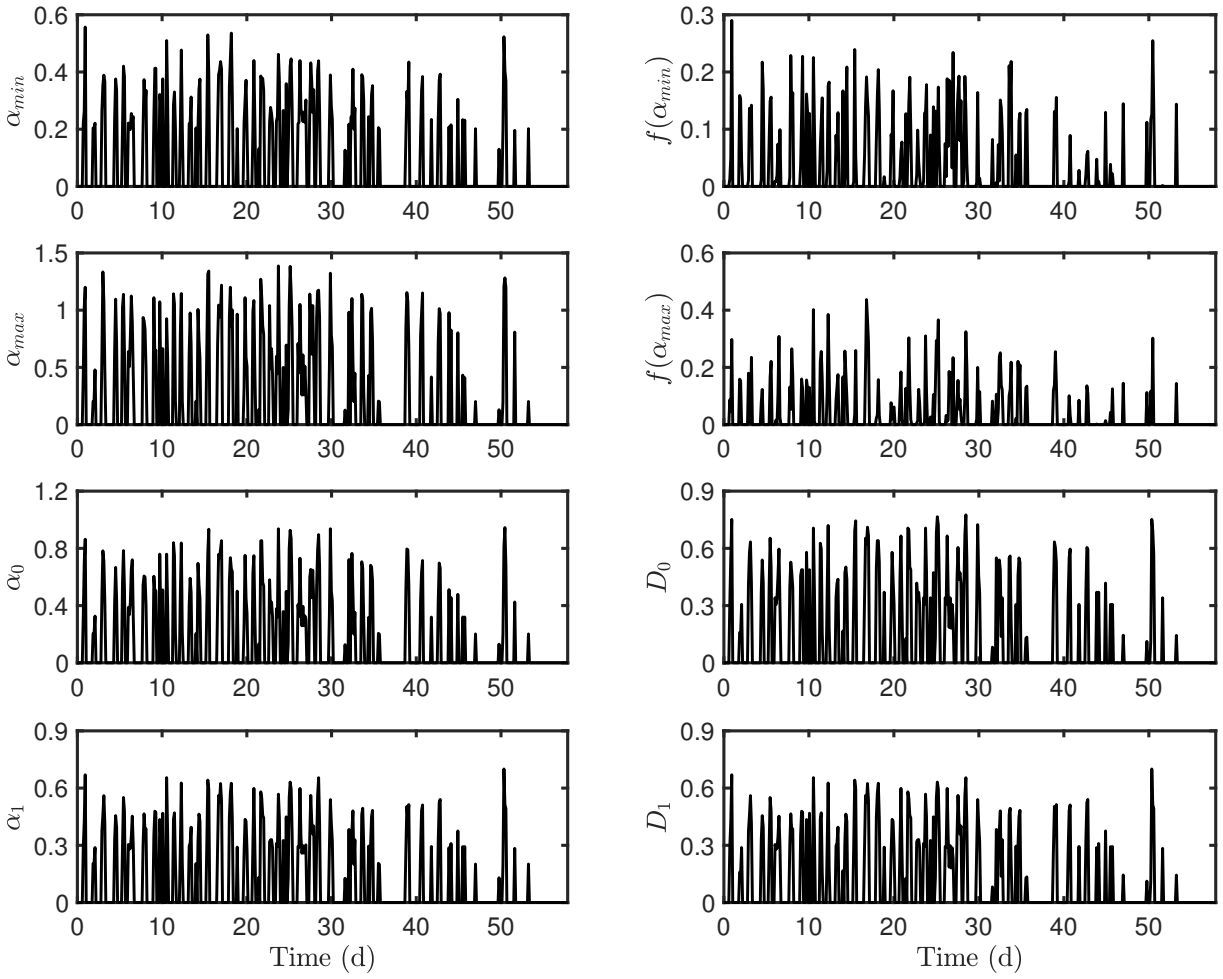

Figure 3-54: Time variation of multifractal variables: $\alpha_{min} \equiv \min\{\alpha\}$, $\alpha_{max} \equiv \min\{\alpha\}$, α_0, α_1, $f(\alpha_{min})$, $f(\alpha_{max})$, $D_0 = f(\alpha_0)$, and $D_1 = f(\alpha_1)$. All these variables were obtained for simulated rainfall fields via Raymond & Zeng's model [2014, 2005].

The cumulant–based magnitude coefficients were estimated for simulated rainfall fields. Figure 3-55 shows the first three coefficients. Every time there is a positive value of the coefficient C_0, a multifractal structure is identified. Another way to identify such structures is based on the criteria of the spectral width. For instance, if $H_\alpha > \overline{H_\alpha}$, where $\overline{H_\alpha}$ is the average spectral width, only multifractal structures will be selected. The magnitude coefficient C_0 makes such a classification intrinsically. Values of C_0 are exhibited as a time series in the first panel of Figure 3-55. Here $\overline{H_\alpha} \approx 0.5$ and the average value of C_0 for these multifractal structures is ≈ 0.4. Finally, the fact that $C_2 \neq 0$ also represents a non-linear structure of simulated patterns.

Table 3-11: Statistics of multifractal variables: $\alpha_{min} \equiv \min\{\alpha\}$, $\alpha_{max} \equiv \min\{\alpha\}$, α_0, α_2, $f(\alpha_{min})$, $f(\alpha_{max})$, $D_0 = f(\alpha_0)$, $D_1 = f(\alpha_1) = \alpha_1$, and $D_2 = f(\alpha_2)$. The statistics were obtained for the multifractal spectra of the simulated rainfall fields. These field were obtained by Herman & Raymond [2014] via Raymond & Zeng's model. In this table σ, CV, IQR, γ represent the standard deviation, the coefficient of variation, the interquartile range and the skewness, respectively.

	α_{min}	α_{max}	α_0	α_1	$f(\alpha_{min})$	$f(\alpha_{max})$	$f(\alpha_0)$	$f(\alpha_1)$
Minimum	0.13	0.13	0.13	0.13	0.00	0.00	0.08	0.08
Mean	0.30	0.77	0.53	0.39	0.10	0.12	0.44	0.38
Median	0.27	0.78	0.50	0.38	0.11	0.12	0.44	0.38
Maximum	0.56	1.39	0.94	0.70	0.29	0.44	0.78	0.70
σ	0.09	0.33	0.21	0.13	0.07	0.10	0.17	0.14
CV (%)	31.70	43.34	39.81	33.33	67.33	84.92	38.56	36.41
IQR	0.15	0.54	0.34	0.19	0.11	0.15	0.24	0.19
γ	0.53	-0.21	0.08	0.28	0.18	0.80	-0.06	0.05

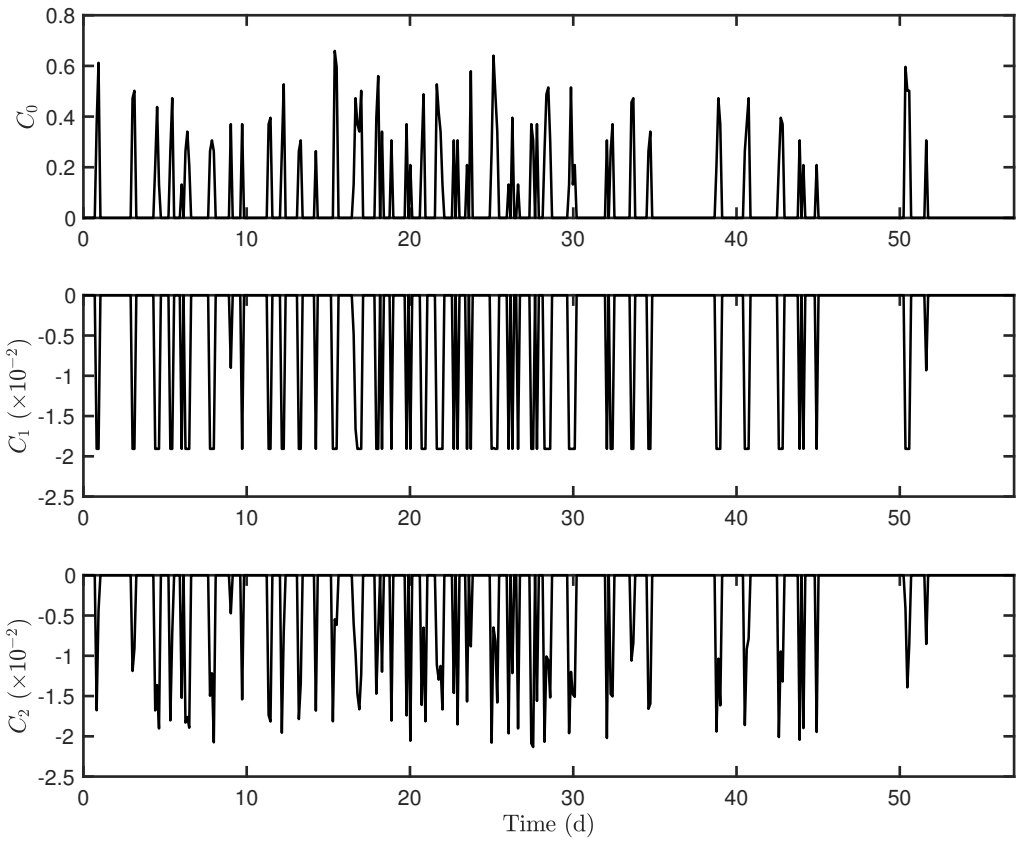

Figure 3-55: Time variation of the first cumulant–based magnitude coefficients C_0, C_1, and C_2 for simulated rainfall fields with Raymond & Zeng's model [2014, 2005].

Figure 3-56 shows two–point correlation functions for either maximums or averaged two–point correlations. Figure 3-56 is divided in four sub-plots, each one is representing a scale for simulated rainfall fields. The selected scales for the analysis were $\delta = \{1, 2, 3, 4\}$ km. The upper panel of every sub-plot depicts the correlation function for maximums correlations and the lower panel depicts the correlation function for averaged correlations. Correlation functions which are exhibited in Figure 3-56, are highly different in comparison to other model outputs or observations shown in the above sections. Here correlation functions show a slightly increasing function which changes in a logarithmic way inasmuch as the lag Δx is larger. This kind of behavior in the correlation function determines the existence of a long–range dependence but not alike to those been the result of multifractal cascades.

Correlation functions of Figure 3-56 were fitted to a logarithmic function of the form $C(\delta, \Delta x) = m\ \ln(\Delta x) + b)$. The logarithmic fit is depicted in Figure 3-56 through a solid red line. For the scale $\delta = 1.0$ km, the logarithmic fit is $C(1, \Delta x) = 0.01\ \ln(\Delta x) + 0.29$ for maximum correlations and $C(1, \Delta x) = 0.03\ \ln(\Delta x) + 0.10$ for average correlations. The long–range dependence is evidenced in computed correlation functions. For the scale $\delta = 1.0$ km, the log–linear behavior of the correlation function is quiet a lot evident; however, for larger scales, the log–linear fitting can not suitably describe the correlation function for large values of Δx. There is a fluctuating and random behavior of the correlation function for $\Delta x \geq 4.0$ km. Moreover, there is not any kind of dependence among the scales δ. This represents there are not feasible multiplicative processes for describing Raymond & Zeng's model outputs.

The incremental similarity analysis was also developed for Raymond & Zeng's model outputs. Figure 3-57 exhibits PDFs for increments $\Delta_{t,u}$ at $t = 0$ and $s = \{1,\ 2,\ 3, \dots\}$ km (see red dots in the plots of Figure 3-57) and the statistical fitting to a NIG distribution (see solid black line in the plots of Figure 3-57). As one can observe in Figure 3-57, empirical PDFs depict an irregular form very different to that of the NIG distribution depicts. The higher probability density is found in $\Delta_{t,u} = 0$ but in the vicinity of $\Delta_{t,u} = 0$, the density is almost zero. Based on the form of these PDFs, the lack of intermittency is roughly evident and therefore the lack of multifractality as well. On the other hand, the variability of increments $\Delta_{t,u}$, expressed through the variance σ^2, increases as well as the parameter s does. Nonetheless, for long enough s–values there is a small oscillation in σ^2 around $\sigma^2 \approx 35$ mm^2 h^{-2}. Apparently, the IS hypothesis is not held for these data. For instance, in the lower panels of Figure 3-57 can be identified two PDF whose $\sigma^2 \approx 35.64$. If both distributions are compared there exists differences in their values and geometry; therefore, $\Delta_{t,u}(X) \overset{\text{dist}}{=} \Delta_{t,v}(X)$ is not true.

The final analysis of data is related to the estimation of the dynamic scaling exponent for the model outputs. The left panel of Figure 3-58 exhibits the space–time plot for simulated rainfall fields, the right panels show its power spectrum and two orthogonal profiles identified by dash red and blue lines. As one can observe, there is not connection with symmetries observed in turbulence processes, but a space–time hyper–asymmetry (i.e. $H > 1$). The lack of time correlation (see the dash blue line in Figure 3-58) seems to be an straightforward explanation for this hyper–asymmetry.

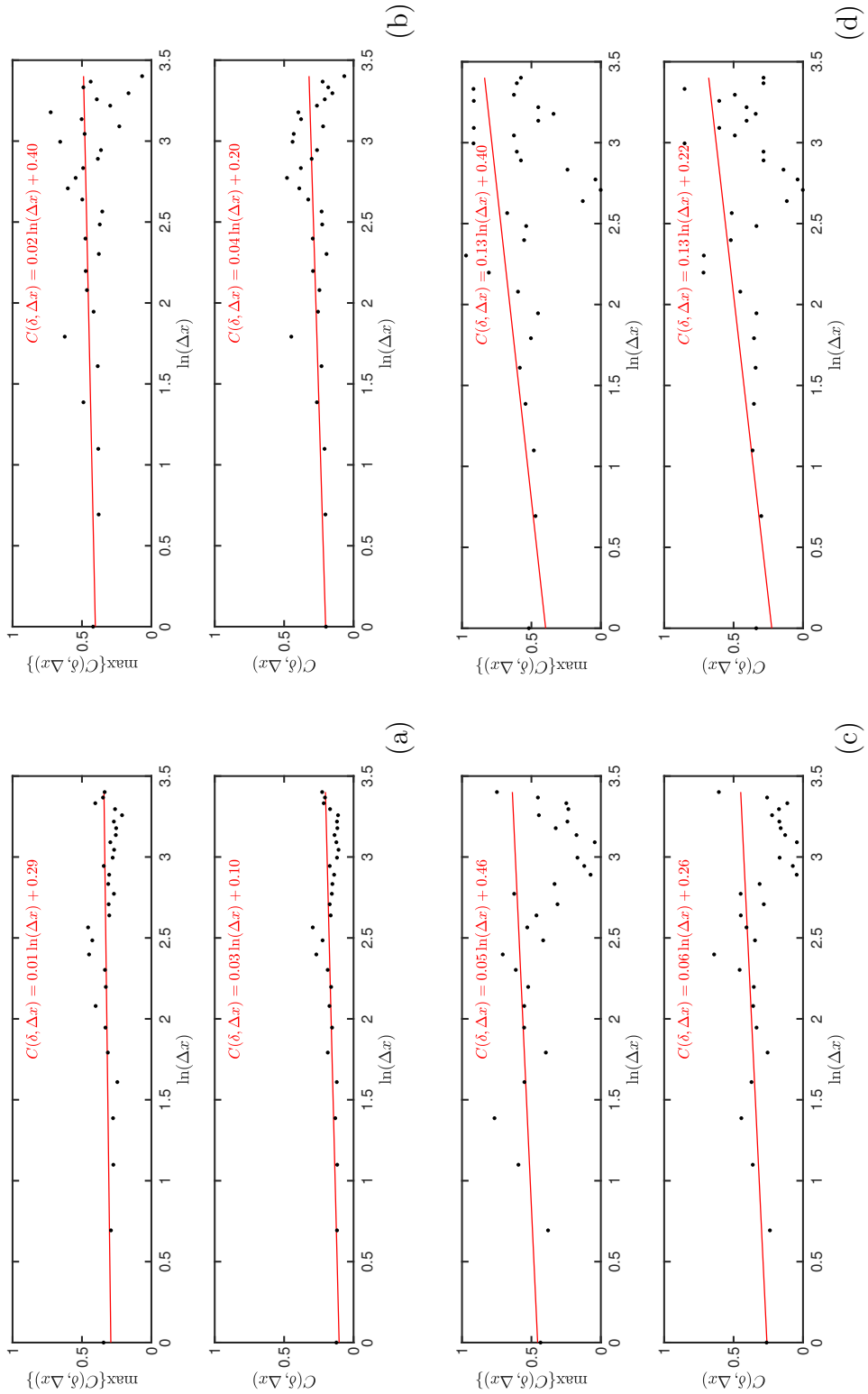

Figure 3-56: Two-point correlation functions for maximum correlations ($\max\{C(\delta, \Delta x)\}$) and average correlations ($C(\delta, \Delta x)$) of simulated rainfall fields with Raymond & Zeng's model [2005]. In this plot the two–point correlation functions are build for the scales $\delta = \Delta x = 1$ km (a), $\delta = 2\,\Delta x$ (b), $\delta = 3\,\Delta x$ (c), and $\delta = 4\,\Delta x$ (d).

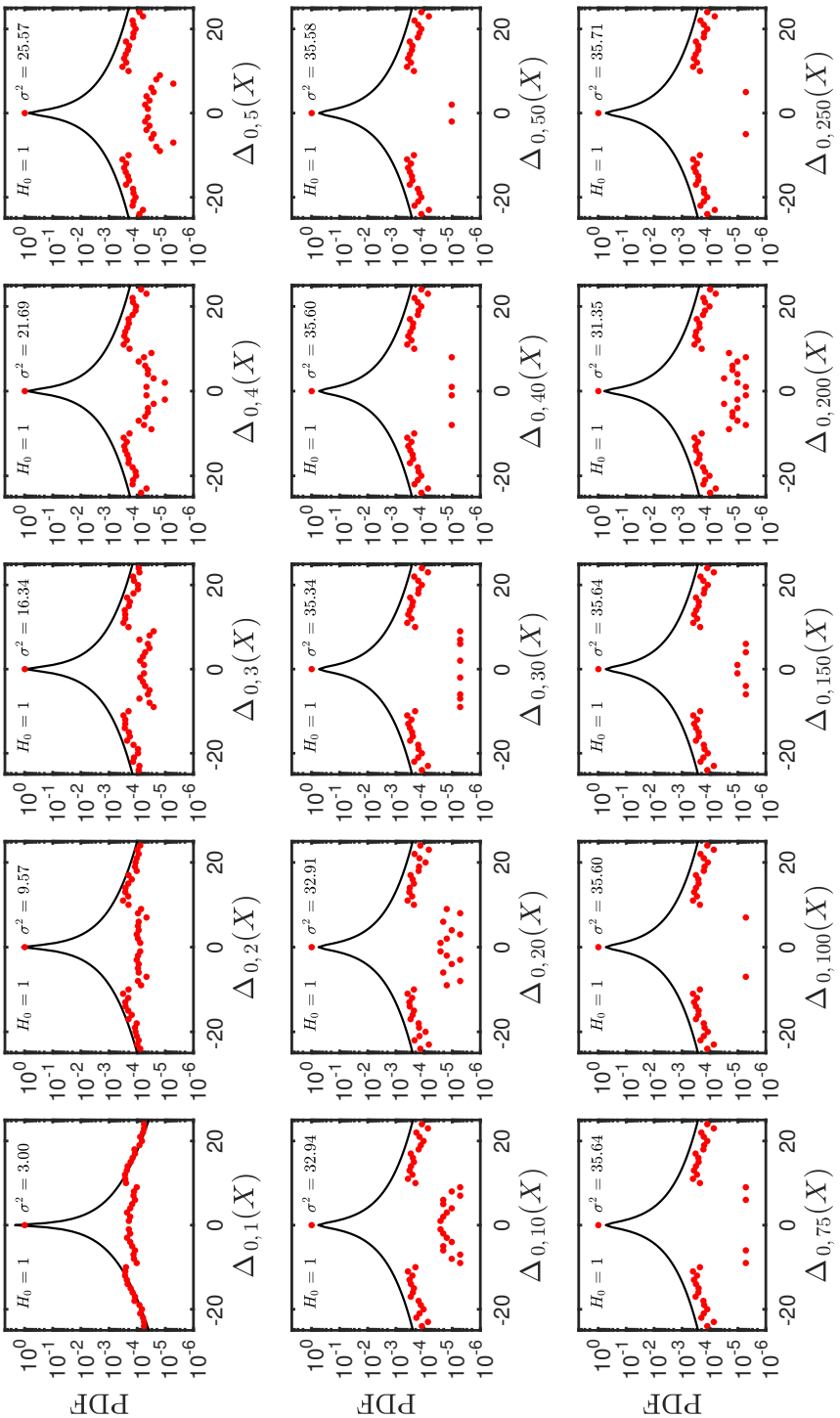

Figure 3-57: Probability density function of increments $\Delta_{t,u}$ for simulated rainfall fields with Raymond & Zeng's model. The red dots depicts the empirical PDF corresponding to simulated data and the solid line represents the curve fitting to the normal inverse Gaussian distribution. Each frame shows the value of the null hypothesis H_0 (zero for acceptance of H_0 and one for rejection of H_0; both values for a 5% of significance level α). The null hypothesis states that data come from a normal inverse Gaussian distribution.

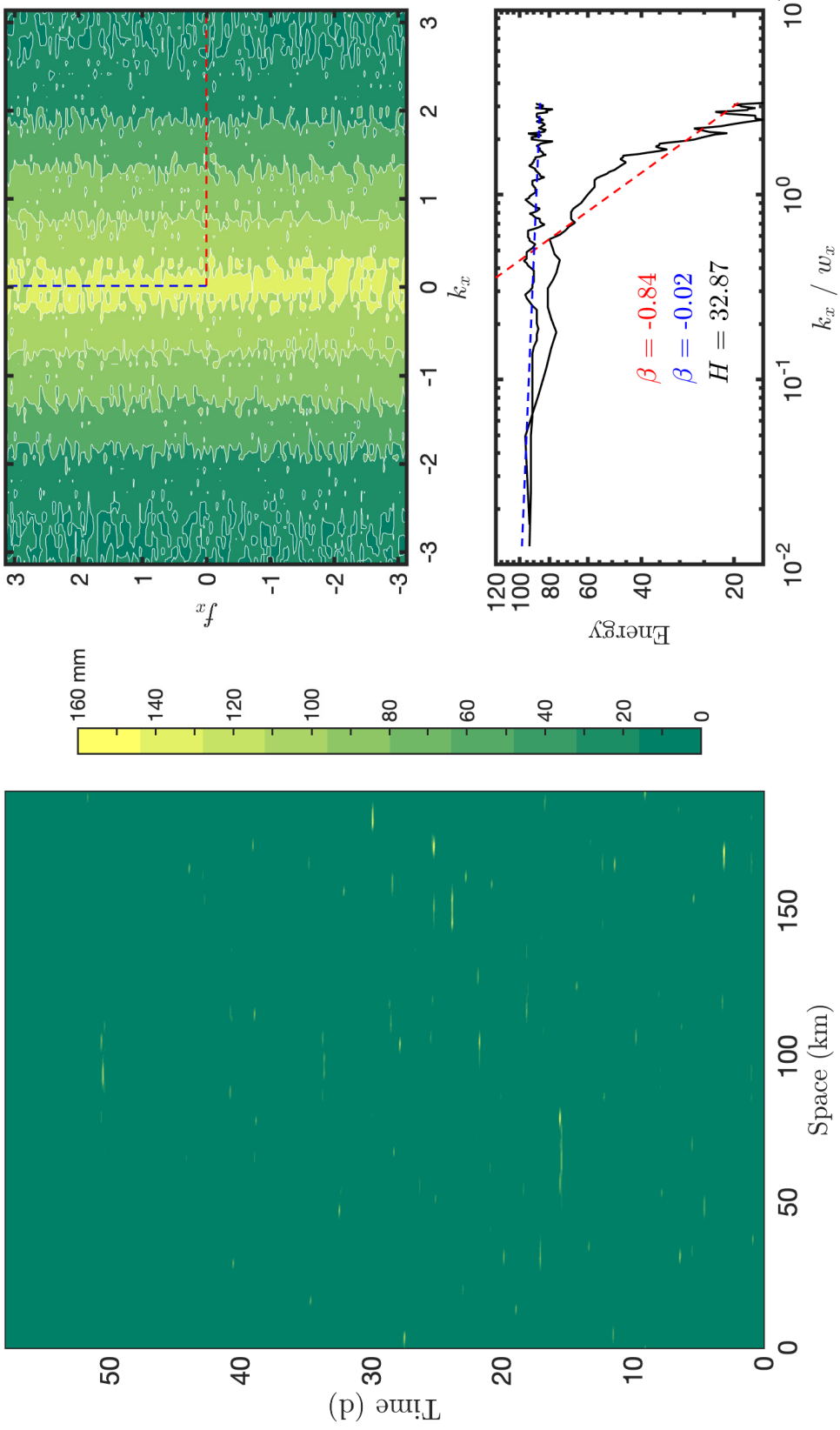

Figure 3-58: Space–time diagrams and isocorrelation contours for simulated rainfall fields with Raymond & Zeng's model. The left panel shows a space–time plot of simulated rainfall fields. The upper right panels shows the isocorrelation contours in the $2D$ Fourier space . The bottom right panel shows two cuts of the $2D$ Fourier spectrum in the wavelength direction ($k_.$) and in the frequency direction $f_.$. Moreover, in this panel are indicated the slopes β of each cuts and the computed scaling exponent H.

3.3.5. Summing Up

Throughout this chapter several statistical analyses have been developed to identify evidence of rainfall multifractality. The first studied data correspond to high–resolution rainfall data which were recorded at Bogotá[12]. Among geometrical characteristics of these data, they are similar to those observed in turbulence phenomena. High–resolution rainfall records depict intermittent patterns whose statistical description classifies them as singular measures ($\alpha < 1$), moreover, such a intermittency changes substantially between spatial observation points. As one can observe in the summary Table 3-12, the average values for the computed dimension D_0, the spectral width H_α and the singular exponent α_0 equals to 0.74, 0.68 and 0.81, correspondingly. The IS hypothesis seems to work for the studied data and the NIG distribution characterizes the statistical distribution of increments $\Delta_{t,u}$. Based on the statistical examination of high–resolution rainfall records, their non–linear structure and their multifractal descriptors alike to those found in synthetic (or theoretical) multifractal objects, punctual rainfall records can be classified as multifractal geophysical patterns.

Reflectivity fields from SIATA's weather radar at Medellín were also studied here. These high–resolution space–time data are characterized for having multifractal spectra with wide spectral widths, i.e. $H_\alpha > 1.0$. Most of the scaling exponents in those spectra can categorize measures of the reflectivity fields as non–singular, since $\alpha > 1$; therefore, reflectivity fields can be understood as non–intermittent fields. The average multifractal spectrum is center at $\alpha_0 = 1.69$ (with dimension $D_0 = 1.65$). Since the non–intermittent behavior of reflectivity fields, the NIG distribution cannot well describe the statistical law of their increments $\Delta_{t,u}$. On the other hand, the computed dynamic scaling exponent H shows there is a space–time anisotropy in reflectivity fields records. The estimated dynamic scaling exponent H for the reflectivity fields is $\approx 1/2$. Lovejoy & Schertzer [2013] suggested a value of $H \approx 1/3$ for passive scalar in a turbulent environment; therefore, if rainfall behaves as a passive scalar, $H \approx 0.5$ does not suggest a space–time anisotropy in the sense of turbulence but does in the sense of critical phenomena where non–conserved fields have a dynamic scaling exponent $H \approx 0.5$ [Sornette, 2004, Goldenfeld, 1992]. Based on the statistical description of reflectivity fields records, they could be considered as those geophysical patterns with weak multifractality.

Based on the multifractal analysis of TRMM–rainfall records, the resulting average multifractal spectrum is described for having a fractal dimension $D_0 \approx 3/2$, a singularity scaling exponent $\alpha_0 \approx 1.61$ and a spectral width $H_\alpha \approx 1.71$. The aforementioned characteristics confirm TRMM-rainfall records are partially made–up by non–singular measures. Nonetheless, TRMM–rainfall fields are intermittent and their increments $\Delta_{t,u}$ follow a NIG distribution law. Furthermore, the incremental similarity hypothesis is valid for TRMM–rainfall increments $\Delta_{t,u}$. On the other hand, the long–range dependence exhibited in two–point correlation functions suggests TRMM–rainfall records could be described through multiplicative

[12]Researches done by Peñaranda [2008, 2011], Bernal [2008], Santos [2011] about the statistical description of punctual rainfall data studied these data. However, the statistical tools were different to those used in this research. Thus, the results obtained from this research are supplementary to previous studies.

processes as suggested by Roux et al. [2009] and Arneodo et al. [1998]. Albeit there is a space–time anisotropy, differences between zonal and meridional dynamic scaling exponent values suggest a spatial anisotropy in the rainfall field. The zonal dynamic scaling exponent shows a resemblance to that obtained for passive scalar in turbulence phenomena whose value is $H \approx 1/3$. The statistical examination of TRMM–rainfall records suggests these kind of data are multifractal geophysical patterns because all statistical descriptors behaves alike to those found in theoretical multifractal objects.

Among the selected physically–based and parsimonious models, three of them were studied to identify multifractal properties in model outputs and to verify how possible is multifractal properties emerge from physically–based models. The first model was introduced by [Nordstrom & Gupta, 2003]. It describes tropical atmospheric convective processes through the phenomenology of cool pools over oceans. For the sample simulation, parameters were selected so that the numeral stability of the mathematical model was guaranteed and estimated physical quantities were realistic as much as possible. Taking into account the aforementioned criteria, there were changes in some parameter values; for instance, parameters $\nu_a = 10^4$ m^2 s^{-1} and $b_1 = 1.9 \times 10^{-2}$ m s^{-1} changed respect to those values selected by Nordstrom & Gupta [2003] in their research. The model was run for a time resolution of 5 seconds and spatial resolution of 500 m. This research found output fields are statistically described by a weak multifractality since quantities of computed multifractal attributes are dissimilar to those found in theoretical multifractal objects (e.g. small spectral width). Although simulated spatial patterns look either irregular or heterogeneous, their are not intermittent. These observations can be also verified by observing how empirical probability density functions behave different to those where the incremental similarity property is satisfied. On the other hand, the zonal and meridional dynamic scaling exponents show there exists a spatial anisotropy as rainfall fields records show. Albeit, there is not a full description of multifractal properties of rainfall fields by means of Nordstrom & Gupta's model [2003], there exists a clear approximation about how multifractal properties emerge from physically–based models.

The second studied model was introduced by Craig & Mack [2013]. This model describes how interactions of water vapor in the lower troposphere lead to the development of tropical oceanic convection. Among model attributes, it is highlighted its capability for depicting structures through an intrinsic process of spatial organization. The model was run for the selected space–time scales and parameters that Craig & Mack reported in their work in the year 2013. The average empirical multifractal spectra found in simulated patterns is characterized for having an averaged spectral width $H_\alpha \approx 0.21$, an average fractal dimension $D_0 \approx 1.12$, and a singularity exponent $\alpha \approx 1.16$. Because of the geometry of multifractal spectra, generated measures by the model can be classified as non–singular; furthermore, such measures are not intermittent. The IS analysis shows the NIG distribution is not able to describe the statistics of increments $\Delta_{t,u}$ which confirms the lack of intermittency of model outputs. Albeit the model cannot produce intermittent patterns as those found in multifractal processes, the output fields exhibit a weak long–range dependence and a space–time anisotropy as multifractal fields do. In fact, the space–time anisotropy is alike to that founded in critical phenomena whose systems are described by conserved fields [Sornette,

2004]. Clearly, the model outputs describe a coarsening process of the atmospheric moisture over time, therefore, measures or quantities are smoothed as time goes by. Such a process represents a mechanism of concentration, as well as an intuitive idea about how multifractal patterns emerge.

The third studied model was designed by Hottovy & Stechmann [2015] with a akin philosophy to that given by Craig & Mack's model [2013]. Hottovy & Stechmann's model [2015] also describes the dynamics of water vapor in the tropical troposphere over ocean and how they lead to the development of convection. The linear model suggested by Hottovy & Stechmann [2015] is also known as a stochastic reaction–diffusion equation for representing the space–time dynamics of integrated–column water vapor. For this model, the small scale flux convergence of integrated–column water vapor is modeled as an eddy diffusion ($b_0\Delta q(\mathbf{x},t)$), the turbulent effect is modeled by a damping mechanism ($\tau^{-1}(q(\mathbf{x},t)-q^*)$) and a stochastic forcing ($D_*\dot{W}(\mathbf{x},t)$); rainfall and evaporation are modeled by a source term $F(\mathbf{x},t)$. For running its computational model, parameters were chosen exactly as suggested by Hottovy & Stechmann [2015] for their simulations. For the sample run, time and space resolutions were 36 seconds and 5 km, respectively. As against others physically–based models that were studied here, Hottovy & Stechmann's model [2015] is able to depicts outputs more complex and closer to those found in rainfall observations; however, some statistics are less realist to those found in other models (e.g. FWA estimations are prone to be higher to those estimated in rainfall observations). The average multifractal spectrum is characterized by having a fractal dimension $D_0 \approx 1.63$, a spectral width $H_\alpha \approx 0.59$ and a singularity exponent $\alpha_0 \approx 1.66$. These quantities are roughly similar to D_0 and α_0 found in reflectivity fields. The model outputs are intermittent and the empirical probability distribution functions of increments $\Delta_{t,u}$ confirms such an observation. The NIG distribution describes quite well the estimated increments $\Delta_{t,u}$; moreover, the incremental similarity hypothesis is valid for the model outputs. Since the resemblance between zonal and meridional dynamic scaling exponents, one could presume simulated fields are homogeneous and isotropic. The magnitude of these dynamic scaling exponents are rather similar to those provided by critical phenomena of conserved fields.

So far, parsimonious physically–based model can partially mimic some attributes of theoretical multifractal patterns, therefore one would expect non–parsimonious ones were able to make up supplementary aspects that parsimonious models have neglected in their foundations. A fourth non–parsimonious model was also studied in the framework of this research. This model is classified as a cloud resolving model (CRM) and it was introduced by Raymond & Zeng [2005] for the description of large–scale tropical atmospheric convection. This model has a physical conceptualization where the large–scale tropical dynamics is driven by a weak temperature gradient [Herman & Raymond, 2014, Raymond et al., 2009, Raymond & Zeng, 2005]. Despite Raymond & Zeng's model [2005] describes a more realistic physics of tropical convective processes, its simulated rainfall patterns do not have the same geometrical features of those found in observational evidence, therefore, this model is not able to emulate the rainfall multifractality that one would expect to obtain.

Table 3-12: Summary results of the rainfall–fields data analysis for punctual observations, TRMM records, Reflectivity fields, and model outputs. The first column of this table shows the data source used for the data analysis. In order to simplify the lecture of data the names of models were abbreviated, thus NG correspond to Nordstrom & Gupta's model [2003], CM to Craig & Mack's model [2013], HS to Hottovy & Stechmann's model [2015], and RZ to Raymond & Zeng's model [2005].

Source of Data	Data Type	Time Resolution	Space Resolution	H_α	α_0	D_0	D_1	C_2	Fit to NIG Distribution	$C(\delta_0, 1)$	H_x (zonal)	H_y (meridional)
EAAB	Punctual	30 min	-	0.68	0.81	0.74	0.67	-1.66E-07	Yes	0.64	-	-
SIATA	Spatial	5 min	250 m	1.07	1.69	1.65	1.61	-3.70E-08	Not	0.30	0.51	0.57
TRMM	Spatial	3 h	111 km	1.71	1.61	1.48	1.36	-8.83E-08	Yes	1.77	0.32	0.13
NG model [2003]	Spatial	5 s	500 m	0.00	1.50	1.47	1.47	-1.63E-06	Not	0.01	0.42	0.57
CM model [2013]	Spatial	10 min	40 km	0.21	1.16	1.12	1.09	-1.08E-05	Not	0.10	0.21	0.14
HS model [2015]	Spatial	36 s	5 km	0.59	1.66	1.63	1.60	-4.97E-07	Yes	0.12	0.26	0.25
RZ model [2005]	Spatial	0.5 s	1 km	0.47	0.53	0.44	0.38	-2.58E-03	Not	0.10	32.87	-

4. Conceptual Integration

This chapter provides some bricks in the construction of a theory about the physics of rainfall multifractality. Three main subjects will be discussed in this chapter. The first one regards how Yanai et al.'s theory [1973] about the description of tropical atmospheric dynamics provides a physical mechanism about the formation of clustered spatial distribution of cumulus clouds and therefore, a feasible mechanism for obtaining multifractal patterns of rainfall fields. The second subject regards how critical–phenomena theory could explain scaling properties of rainfall but not multifractal scaling ones. The third and last subject regards how multifractality could be evoked as a diffusion–driven instability in reaction–diffusion models for atmospheric water vapor dynamics.

4.1. Thermodynamics Foundations of Multifractality

Multifractal theory deals with uneven distributions of physical or other quantities on a geometrical support [Feder, 1988]. Example of quintessential multifractal structures are the distribution of energy dissipation in turbulent flows, the spatial distribution of gold in the world, the spatial distribution of impurities on surfaces, the distribution of money among people, and so on. These examples have something in common: *quantities are concentrated on their geometrical domain.* Since rainfall is regularly clustered on the spatial domain[1], multifractal theory provides a suitable tool for describing rainfall patterns.

Tropical active cumulus clouds also cover a small fractional area[2]; therefore, either clouds or rainfall have a geometrical similarity. So far, the work made by Bjerknes [1938] suggests the role of clouds in the large–scale tropical atmospheric dynamics is heating the atmosphere and such a heating process is optimized if a restriction is imposed on the geometry of clouds. If the tropical region is considered as a large horizontal domain containing several individual cumulus clouds, the areal–averaged dry static energy[3] $\bar{s}$ is given by the weighted sum of the dry static energy over the cloudy area (s_c) and the dry static energy over the non–cloudy area (s_{nc}), so that:

$$\bar{s} = \mathrm{FCA}\, s_c + (1 - \mathrm{FCA})\, s_{nc} \tag{4-1}$$

[1] The data analysis exhibited on section 3.2 shows the rainfall fractional area is around 6 to 11 %.

[2] In the tropics the cloud fractional area is around 2 to 3 % [Sarachik & Cane, 2010].

[3] The dry static energy is defined as $s = c_p\, T + g\, z$, where c_p is the specific heat for an ideal air–gas at constant pressure, T is the temperature of an air parcel, g is gravity and z is the height at which the air parcel is located. In other words, the dry static energy is the sum of enthalpy and potential energy [Yanai et al., 1973].

where FCA is the fractional cloud area. An equivalent form for equation 4-1 is:

$$\bar{s} = s_{nc} + \text{FCA}(s_c - s_{nc}) = s_c + (1 - \text{FCA})(s_{nc} - s_c) \tag{4-2}$$

Similarly, for the quantities large–scale vertical velocity $\bar{w}$ and areal–averaged moisture flux $\bar{M} = \rho\bar{w}$, they can be computed as the weighted sum of their quantities measured in cloud and non–cloud areas, as follows:

$$\bar{w} = w_{nc} + \text{FCA}(w_c - w_{nc}) = w_c + (1 - \text{FCA})(w_{nc} - w_c) \tag{4-3}$$

$$\bar{M} = M_{nc} + \text{FCA}(M_c - M_{nc}) = M_c + (1 - \text{FCA})(M_{nc} - M_c) \tag{4-4}$$

Assuming a condition for the synoptic–scale tropical region where there exists a uniform temperature over the whole horizontal spatial domain with an actual lapse rate given by $\Gamma = -\partial_z T$, then, the local changes of temperature due to the vertical motion in the cloudy and non–cloudy areas are represented as follows [Randall, 2006, Bjerknes, 1938]:

$$\partial_t T_c = w_c \left((\partial_z T)_s - \partial_z T\right) \equiv w_c \left(\Gamma - \Gamma_s\right) \tag{4-5}$$

$$\partial_t T_{nc} = w_{nc} \left((\partial_z T)_a - \partial_z T\right) \equiv w_{nc} \left(\Gamma - \Gamma_a\right) \tag{4-6}$$

where $\partial_t T_c$ and $\partial_t T_{nc}$ are representing the local changes of temperature over cloudy and non–cloudy areas, respectively; w_c and w_{nc} are representing the vertical velocity components over cloudy and non–cloudy areas, respectively; $-(\partial_z T)_s \equiv \Gamma_s$ represents the saturated–adiabatic lapse rate (SALR) and $-(\partial_z T)_a \equiv \Gamma_a$ represents the dry–adiabatic lapse rate (DALR).

If the actual lapse rate Γ is smaller than the DALR (i.e. $\Gamma - \Gamma_a < 0$) and smaller than the SALR (i.e. $\Gamma - \Gamma_s < 0$), an absolutely stable atmosphere will be obtained. In this case, to heat the atmosphere will be necessary a net synoptic downward motion to compensate the lack of buoyancy of parcels. Now, the converse will happens for an absolutely unstable atmosphere. In this case, the actual lapse rate Γ is greater than the DALR (i.e. $\Gamma - \Gamma_a < 0$) and greater than the SALR (i.e. $\Gamma - \Gamma_s < 0$), for heating the atmosphere will be necessary a net synoptic upward motion of air. Finally, if the actual lapse rate Γ is smaller than the DALR (i.e. $\Gamma - \Gamma_a < 0$) and greater than the SALR (i.e. $\Gamma - \Gamma_s > 0$), saturated parcels are unstable but unsaturated parcels are not. This conditions is referred as convective conditional instability [Wallace & Hobbs, 2006]. So, in the case of a convective conditional instability of the synoptic tropical atmosphere, a local change of temperature due to vertical motion will be always positive if the vertical velocity into the cloudy area w_c is upward (i.e. positive respect to the common reference framework) and the vertical velocity into the non–cloudy area w_{nc} is downward. Now, if one takes the difference between equations 4-5 and 4-6, such that:

$$\partial_t \left(T_c - T_{nc}\right) = w_c \left(\Gamma - \Gamma_s\right) - w_{nc} \left(\Gamma - \Gamma_a\right) \tag{4-7}$$

Now, replacing equation 4-3 on 4-7, one finds that:

$$\begin{aligned}
\partial_t \left(T_c - T_{nc}\right) &= \left[\bar{w} - (1 - \text{FCA})(w_{nc} - w_c)\right] \left(\Gamma - \Gamma_s\right) - \left[\bar{w} - \text{FCA}(w_c - w_{nc})\right] \left(\Gamma - \Gamma_a\right) \\
&= \left[\bar{w} + (1 - \text{FCA}) \left(w_c - w_{nc}\right)\right] \left(\Gamma_a - \Gamma_s\right) + \left(w_c - w_{nc}\right) \left(\Gamma - \Gamma_a\right) \qquad (4\text{-}8) \\
&= \bar{w} \left(\Gamma_a - \Gamma_s\right) + \left(w_c - w_{nc}\right) \left[\left(\Gamma - \Gamma_s\right) - \text{FCA} \left(\Gamma_a - \Gamma_s\right)\right] \qquad (4\text{-}9)
\end{aligned}$$

Supposing an scenery where the FCA$\rightarrow 1$ and there is not net mass flux ($\bar{M} = 0$ and $\bar{w} = 0$), then, the local change of temperature is given by:

$$\partial_t \left(T_c - T_{nc}\right) = \left(w_c - w_{nc}\right)\left(\Gamma - \Gamma_a\right) \tag{4-10}$$

Now, for an scenery where the FCA$\rightarrow 0$ and there is not net mass flux ($\bar{M} = 0$ and $\bar{w} = 0$), then, the local change of temperature is given by:

$$\partial_t \left(T_c - T_{nc}\right) = \left(w_c - w_{nc}\right)\left(\Gamma - \Gamma_s\right) \tag{4-11}$$

For an absolutely stable atmosphere, where $\Gamma \leq \Gamma_s < \Gamma_a$, the lack of clouds implies a cooling of the atmosphere. The former is proved if one considers that $w_c = 0$, $w_{nc} < 0$, $\Gamma - \Gamma_a < 0$ and $\Gamma - \Gamma_s < 0$. On the other side, an absolutely unstable atmosphere brings up an overheating of the atmosphere. This atmospheric condition implies $w_c - w_{nc} > 0$, $\Gamma - \Gamma_a > 0$, $\Gamma - \Gamma_s > 0$, and therefore, $\partial_t \left(T_c - T_{nc}\right) > 0$. However, for a convective conditional instability of the atmosphere, where $\Gamma - \Gamma_a < 0$, $\Gamma - \Gamma_s > 0$, $w_c > 0$ and $w_{nc} < 0$, the heating of the atmosphere will only be given when the FCA$\rightarrow 0$; therefore, the spatial extension of clouds plays an important role in the dynamics, heating of the atmosphere and the spatial configuration of rainfall.

Some remarks to highlight about the aforementioned physical arguments are as follows:

- The saturated rising motion is held by positive buoyancy which in turn is induced by condensation processes[4], nonetheless, the updraft motion is mainly due to the upward wind velocity over the base of cloudy areas.

- For a convective conditional instability, a natural subsidence motion is created to compensate the instability which in turn is proportional to the downward velocity over the non–cloudy area (w_{nc}); therefore, the interactions between downdraft and updraft wind motions determines the strength of convection and how fast the atmosphere is heated.

- According to equation 4-11, the difference of temperatures between the cloudy and non–cloudy areas will be larger if the fractional cloud area vanishes over the domain (i.e. FCA$\rightarrow 0$), such a condition benefits the convective instability and the atmospheric heating. Moreover, the no net synoptic vertical mass flux implies there is not net large–scale moisture convergence and therefore,

  $$\text{FCA} \sim 1 - \frac{M_c}{M_c - M_{nc}} \tag{4-12}$$

  Equation 4-12 suggests that for higher upward moisture fluxes over the cloudy area, this area will be smaller. In other words, if the cumulus clouds work as conduits for upward moisture fluxes and they are long and narrow, there will be a larger flux heat and moisture toward the atmosphere.

[4]During the condensation of water vapor latent heat is released into the atmosphere. Such a process does not allow the temperature to drop off rapidly with height during the ascent of the parcel, but it does allow to hold a positive buoyancy [Randall, 2006].

- Yanai et al. [1973] made some synoptic observations to quantify the heat and moisture budget in the tropical atmosphere. Their observations suggest that the distribution of clouds in the tropical atmosphere is mainly made up by deep and shallow clouds. The heating of the atmosphere is mainly promoted by cloud mass fluxes (i.e. $M_c\,\partial_z\bar{s}$) but not by the cooling effect due to evaporation (i.e. $-L\,e$). Evaporation is a process that happens preferentially by the low–level detrainment of liquid water whereas the atmospheric drying happens by cloud mass fluxes; therefore, shallow clouds have a function of moistening lower levels of the atmosphere, whereas deep clouds have a function of drying the atmosphere with the help of the precipitation [Sarachik & Cane, 2010].
- So far, there is not a direct bonding between the physics that explains how the atmosphere is heated and how rainfall patterns are clustered and multifractal. The former physical theory introduced a mechanism that explains which is the preferential geometry of the most active clouds in the atmosphere. Such a mechanisms suggests that the atmospheric heating will be improved if the geometry of clouds is long and narrow. Now, for a larger vertical extension of clouds, it is likely to find higher rainfall intensities. So, the differences between cloud geometries characterize a competence mechanism between processes for drying and moistening the atmosphere. Such a competence mechanism could be explained through a multifractal dynamics as that observed and studied in rainfall patterns.

In order to build a bonding between the physical theory of the tropical atmospheric dynamics and the theory of rainfall multifractality, it is important to recall the work done by Over & Gupta [1994, 1996] about the description of rainfall patterns via random multiplicative cascades. Over & Gupta [1994] suggest that the spatial distribution of rainy and non–rainy areas is determined by a scaling parameter of rainfall field. This parameter is defined as the rate of growth of the fraction of non–rainy areas. The larger value of the rate of growth of the fractional non–rainy areas becomes, the faster the rate of non–cloud areas will be obtained in the rainfall pattern. Over & Gupta [1994] found a relationship between the mean rainfall intensity and the parameter p as follows:

$$p = p_* \left[1 - \left(\frac{\bar{R}}{R_*}\right)^k\right] \tag{4-13}$$

where p is the rate of growth of the fractional non–rainy areas, $\bar{R}$ represents the spatial average rain rate, R_* and k are empirical parameters depending on time, and p_* is a scaling parameter (approximated to 0.75 as suggested by Over & Gupta [1994]). Supporting the theory of random cascades, Over & Gupta [1994] compute the parameter p, as follows:

$$p = 1 - b^{-m/d} \tag{4-14}$$

where b is the branching number of a random cascade, d is the embedding dimension of the random cascade, and the exponent m is obtained under the following relationships [Over & Gupta, 1994]:

$$m \sim \frac{\log \mathrm{FWA}(\lambda)}{\log \lambda} \sim d - \tau_0 \sim d - D_0 \tag{4-15}$$

where τ_0 is the mass exponent[5] evaluated for the order of the moment equals to zero, λ represents the spatial scale and D_0 represents the dimension of the support. Taking as an example TRMM–rainfall observations reported in the previous chapter, the average fractional wet area should be close to 2.28% for an average dimension of the support $\overline{D_0} \approx 1.48$; therefore, the average parameter values for modeling tropical rainfall patterns via random multiplicative cascades are $m \approx 0.52$, $b = 4$ and $p \approx 0.30$. Under the aforementioned considerations, the value of the parameter $p \approx 0.30$ is clearly in the range that Over & Gupta's research [1994, 1995, 1996] found through the data analysis of GATE[6] experimental records.

Now, assuming the fractional cloud area (FCA) and the fractional wet area[7] (FWA) are approximated interchangeable for the long–term and large–domain analysis, FCA could be approximated as follows:

$$\mathrm{FCA}(\lambda) \sim (1-p)^{-d \log \lambda / \log b} \tag{4-16}$$

Thus, if the parameters d, λ and b in equation 4-16 are fixed for modeling tropical active clouds fields through random multiplicative cascades, p represents not only a long–term statistic of the rainfall field but also a physical quantity representing the large–scale moisture convergence; therefore, another approximation for the parameter p would be given by:

$$p \approx 1 - \left(1 - \frac{M_c}{M_c - M_{nc}}\right)^{-\log b / (d \log \lambda)} \tag{4-17}$$

The former approximation establishes a bonding between the theories of random multiplicative cascades and that one related to the large–scale physics of tropical rainfall. Clearly, equation 4-17 shows a dependency between the parameter p and the moisture convergence over cloudy and non–cloudy areas. If the moisture convergence over cloudy areas is much greater than over non–cloudy areas, the parameter p will be in the range of observations (i.e. $0.2 \leq p \leq 0.5$). For instance, for $b = 4$, $d = 2$ and $\lambda \to 0$:

$$\frac{M_c}{M_c - M_{nc}} \sim 1 \qquad \text{if} \quad p \geq 0.2 \tag{4-18}$$

These results show us that parameter p offers a physical restriction given by the atmospheric moisture dynamics and for modeling purpose, such a dynamics should be taken into account. Further studies could be oriented to identify functional forms between the scaling parameters of the rainfall field (i.e. p, $\bar{R}$, R_*, p_*, k, FWA, FCA) and the moisture convergence over cloudy and non–cloudy area (i.e. M_c, M_{nc}, $\bar{M}$), since these studies could confirm under empirical bases the physics of some concepts here explained.

[5] The mass exponent $\tau(q) = \lim_{\lambda \to 0} - \log M_\lambda(q) / \log \lambda$ is computed as the logarithmic relationship between the marginal spatial moment $M_\lambda(q)$ of order q and the spatial scale λ. For $q = 0$, the mass exponent $\tau(0)$ is also known in the fractal theory as the dimension of the support D_0.

[6] Global Atmospheric Research Program (GARP) – Atlantic Tropical Experiment (GATE).

[7] The fractional wet area corresponds to the spatial region where precipitation took place and was recorded.

4.2. A View of Rainfall as a Critical Phenomenon

The empirical work has determined the existence of multifractal scaling properties of the rainfall field [Lovejoy & Schertzer, 2013, Peñaranda, 2008, Gómez & Poveda, 2008, Lovejoy & Schertzer, 1995, Over & Gupta, 1994, Lovejoy, 1982] but a physical explanation of such scaling properties has not been provided. Among the ideas found in the study of atmospheric convection, Peters & Neelin [2006, 2009] introduced a new concept for understanding some statistical properties of the atmospheric precipitation. They suggest rainfall should be understood as a quasi–critical phenomenon.

First of all, critical phenomena were first evoked in the study of phase ordering dynamics. The statistical physics partakes in the construction of models allowing understanding of such phase ordering dynamics with applications in the theory of ferromagnetism [e.g. Ising, 1925]. As a result of thermodynamics interactions, critical states emerge and they in turn give rise to scaling laws[8]. If results of several experiments can be encoded in a single equation along with their scaling exponents, one obtains a *static scaling law*. For instance, in magnetic systems the growth of magnetization $M(t,h)$ is formally expressed as:

$$M(t,h) = \begin{cases} 0 & \text{for} \quad t > 0 \\ \pm\, A\, t^{\beta} & \text{for} \quad t < 0 \end{cases} \tag{4-19}$$

where $M(t,h)$ is the magnetization and represents an order parameter of the magnetic system, $t = (T - T_c)/T_c$ is a tuning parameter which represents a relative deviation of the temperature T in respect to a critical temperature state T_c, h represents the effect of an external magnetic field, A and β are parameters of the system. After analyzing several experiments, Widom [1965] proved that for magnetic systems, the growth of magnetization can be also represented through scaling functions, thus:

$$M(t,h) = \begin{cases} t^{\beta}\, f_M^{+}\left(\dfrac{h}{t^{\Delta}}\right) & \text{for} \quad t > 0 \\ (-t)^{\beta}\, f_M^{-}\left(\dfrac{h}{(-t)^{\Delta}}\right) & \text{for} \quad t < 0 \end{cases} \tag{4-20}$$

where $f_M^{+}(\cdot)$ and $f_M^{-}(\cdot)$ are scaling functions, and β and Δ are assumed to be universal scaling exponents. In the context of atmospheric precipitation over the tropical ocean, Peters & Neelin [2006] suggest precipitation is an order parameter and its growth (or strength) depends on the atmospheric water vapor content w. Formally, this model is represented as follows:

$$\langle P \rangle(w_*, \lambda) \approx \begin{cases} 0 & \text{for} \quad w_* < 0 \\ A\, w_*^{\beta} & \text{for} \quad w_* > 0 \end{cases} \tag{4-21}$$

where $\langle P \rangle(w_*, \lambda)$ is the order parameter which represents a spatially–averaged precipitation over ocean, $w_* = (w - w_c)/w_c$ is a tuning parameter where w_c is a critical value of the

[8] For example, there exists the Rushbrooke's scaling law [1963] whose critical exponents (α, β, γ) satisfy the following inequality: $\alpha + 2\,\beta + \gamma \geq 2$.

atmospheric water vapor content w depending on the sea surface temperature (SST), A and β are parameters that depend on the spatial location over the tropical ocean.

The former model is complemented by including a definition for the susceptibility function[9] as the variance of the order parameter $\langle P \rangle(w_*, \lambda)$, such that:

$$\chi(w_*, \lambda) = \lambda^d \sigma_p^2(w_*, \lambda) = \lambda^d \left[\langle P^2(w_*, \lambda) \rangle - \langle P(w_*, \lambda) \rangle^2 \right] \tag{4-22}$$

where $\chi(w_*, \lambda)$ is the susceptibility function, d is the spatial dimension where precipitation takes place, λ represents the spatial scale, and $\sigma_p^2(w_*, \lambda)$ is a measure of rainfall fluctuations over the spatial domain. Based on the structure of Peter & Neeling's model [2006], this model suggests a static scaling law for the description of atmospheric precipitation as Widom [1965] introduced for describing magnetic systems. Therefore, Peter & Neeling's model [2006] could be re-defined through scaling functions as follows:

$$\langle P \rangle(w_*, \lambda) = \begin{cases} (-w_*)^{\beta} \, f_P^- \left(\dfrac{\lambda^d}{(-w_*)^{\Delta}} \right) & \text{for} \quad w_* < 0 \\ \\ w_*^{\beta} \, f_P^+ \left(\dfrac{\lambda^d}{w_*^{\Delta}} \right) & \text{for} \quad w_* > 0 \end{cases} \tag{4-23}$$

$$\chi(w_*, \lambda) \sim \begin{cases} (-w_*)^{\gamma} \, g_P^- \left(\dfrac{\lambda^d}{(-w_*)^{\Delta}} \right) & \text{for} \quad w_* < 0 \\ \\ w_*^{\gamma} \, g_P^+ \left(\dfrac{\lambda^d}{w_*^{\Delta}} \right) & \text{for} \quad w_* > 0 \end{cases} \tag{4-24}$$

where $f_P^+(\cdot)$, $f_P^-(\cdot)$, $g_P^+(\cdot)$ and $g_P^-(\cdot)$ would be scaling functions, $0 < \beta < 1$, Δ and $\gamma < 0$ would be scaling exponents of the atmospheric precipitation model. So far, there are not theoretical or empirical evidence about how those exponents are related. Furthermore, there is no findings that proves the existence of scaling functions in Peter & Neeling's model [2006]. On the other hand, one could evidence in the structure of Peter & Neeling's model [2006] that a static scaling law for the description of atmospheric precipitation is not realistic in the sense that time does not interact with the spatial dynamics of rainfall. In chapter 3 was shown that rainfall fields exhibit dynamic scaling, therefore, rainfall should be studied and understood in the space–time domain and its scaling properties too.

An important fact to highlight about Peter & Neeling's model [2006] is observed in its susceptibility function $\chi(w_*, \lambda)$. This function is represented by the spatial variance of precipitation $\sigma_p^2(w_*, \lambda)$ and this formulation suggests there could be a kind of diffusive process to describe the dynamics of atmospheric precipitation, such that:

$$\chi(w_*, \lambda) = \sigma_p^2(w_*, \lambda) \sim \langle P^2(w_*, \lambda) \rangle \sim \nu \, t^{\alpha} \qquad \text{for} \quad 0 \leq t \leq 1 \tag{4-25}$$

where ν is a diffusion coefficient, t is a relative time in respect to the time at which the phase transition takes place, $\nu \, t^{\alpha}$ is an asymptotic law introduced by Bouchaud & Georges

[9] This function means how susceptible is the system to attain a phase transition.

[1990] for describing the evolution of Brownian particles in disordered environments through an anomalous diffusion. If $\alpha = 1$ corresponds to a normal diffusive process[10], if $0 < \alpha < 1$ corresponds to sub-diffusion, and if $\alpha > 1$ correspond to super-diffusion [Masoliver, 2017]. Some systems that are represented under an anomalous–diffusion process describe a fractal structure [Gmachowski, 2015, Kolb, 1999, Aharony, 1984, Witten & Sander, 1981] as rainfall does. The fractal dimension D of a 2D–anomalous–diffusion process is related to the exponent α as follows $\alpha \sim 2/D$ [Gmachowski, 2015].

Recalling the definition of the Hausdorff–Besicovitch dimension D of a fractal set S; it is stated as the critical dimension for which the measure M_d changes from zero to infinity [Feder, 1988], thus:

$$M_d = \sum \gamma(d)\,\lambda^d = \gamma(d)\,N(\lambda)\,\lambda^d \xrightarrow[\lambda\to 0]{} \begin{cases} 0 & \text{for} \quad d > D \\ \infty & \text{for} \quad d < D \end{cases} \tag{4-26}$$

where λ represents the scale of the elements that cover the set S, $\gamma(d)$ is a geometrical factor, and $N(\lambda)$ is the total number of non–empty boxes that cover the set S. If the measure is changed by the statistical moment of the second order of the moment (see equation A-5), such that:

$$M_d = \frac{1}{N(\lambda)} \sum_{n=1}^{N(\lambda)} \left[P(w_*, \lambda)\right]^2 \sim \chi(w_*, \lambda) \xrightarrow[\lambda\to 0]{} \nu\, t^{\alpha} \qquad \text{for} \quad \alpha = d/(d - D) \tag{4-27}$$

Thus, the measure should converge to an asymptotic law given by $\nu\, t^{\alpha}$, where ν is a diffusion coefficient for representing the dynamics of the tropical atmospheric precipitation system, $\alpha > 1$ is the anomalous exponent that allows the description of atmospheric precipitation dynamics, $0 \leq D \leq d$ is the fractal dimension of the diffusive process which can be estimated as follows:

$$D(w_*, t) = d\,[1 - \zeta] \qquad \text{with} \quad \zeta = \frac{\log t}{\log \chi(w_*, \lambda) - \log \nu} \ll 1 \tag{4-28}$$

To obtain a coherent relationship between the fractal dimension D and the anomalous diffusion exponent α in equation 4-27, it was necessary to introduce a new definition of such a relationship that is quite different from the original one suggested by Gmachowski [2015]. Thus far, Peter & Neeling's model [2006] suggests the existence of static scaling exponents which in principle could possess a fractal nature. In the event such exponents have a fractal character, the physics of the model could suggest the existence of a kind of anomalous diffusive process which would be able to explain how rainfall is segregated either by time or space. Equation 4-27 suggests there should be a super–diffusion process during the development of strong atmospheric precipitation, therefore α should be always positive and greater than 1. Nonetheless, it is unclear how such an exponent could be estimated under physical criteria.

[10] Einstein [1905] showed that if $X(t)$ represents the position of a particle in a liquid and it can be described as a Gaussian process, its variance grows linearly with time, i.e. $\langle \Delta X(t)^2 \rangle = \nu t$, where $\Delta(X) = X(t + \Delta t) - X(t)$ and ν is the diffusion coefficient of the liquid.

In the theory of critical phenomena some physical quantities depend on divergences and relationships between scaling exponents[11], but such quantities for atmospheric precipitation have not been identified so far.

4.3. Multifractality as a Diffusion–Driven Instability

Under the perspective of critical phenomena theory, scaling properties describe thermodynamic quantities of system and they appear near to critical states of the system inasmuch as a tuning parameter is pushed to them. Some examples of critical phenomena take the relative deviation of temperature in respect to a critical value as a tuning parameter in order to describe a phase ordering dynamics. A thermodynamic definition of temperature for systems at equilibrium is stated as the inverse rate of change of entropy with respect to energy i.e. $T^{-1} = \partial S/\partial E$. if this rate of change is large, temperature is small and the system is characterized for having a few excited states and looks organized. Conversely, if this rate of change is small, temperature is large and the systems is characterized for having many excited states and looks disorganized.

Thus far, a suitable tuning parameter for the description of atmospheric precipitation processes have not been stated clearly. Peters & Neelin [2006] suggested the vertically–averaged saturation deficit (i.e. $w_* = (w - w_c)/w_c$) as a tuning parameter for the description of atmospheric precipitation processes. In this tuning parameter, the vertically–average water vapor content (w) is the physical quantity that modules the dynamics of convection and the saturated water vapor content (w_c) represents a critical state of the system. It is highlighted that the saturated water vapor content (w_c) depends on temperature, thus, w_c will rise as temperature increases. On the other side, one could intuit that if the vertically–averaged saturation deficit is large at constant temperature, the air could be unsaturated, therefore, condensation of water vapor is not possible, and neither is convection. Conversely, if the vertically–averaged saturation deficit is small at constant temperature, the air is saturated enough to condensate water vapor and therefore, there exists a favorable environment for convection. However, one cannot state as a fact that this favorable environment is a sufficient condition for obtaining a multifractal scaling properties in the rainfall field. So, there should be more physical attributes or dynamical interactions that explain how such scaling properties are attained.

Under the basis of critical phenomena theory, there is not a complete physical definition of all elements that explain how multifractal properties of rainfall emerge. However, the following arguments and results could suggest there could be another perspective to identify a physical explanation of the multifractal scaling. In section 3.3, some models have been studied and some techniques were applied for exploring multifractal properties. Among these models, those known by their begetters Craig & Mack [2013] and Hottovy & Stechmann [2015] are characterized for possessing multifractal attributes in their outputs. These model will be analyzed in this section to get an insight into the complexities of their dynamical systems.

[11] e.g. for the specific heat, $c_V \sim t^{\alpha}$, $t \to 0$ [Goldenfeld, 1992].

First of all, recalling Craig & Mack's model [2013] equations:

$$\partial_t I_v(\mathbf{x},t) = -\alpha I_v(\mathbf{x},t) + \left(\frac{1-\epsilon}{\epsilon}\right) a(t)\,\phi(\mathbf{x},t) + \nu\,\Delta I_v(\mathbf{x},t) \tag{4-29}$$

$$I_v(\mathbf{x},0) = I_0(\mathbf{x}) \tag{4-30}$$

$$I_v(0,t) = I_v(L,t) \tag{4-31}$$

where

$$\phi(\mathbf{x},t) = \exp\left(b\,\frac{I_v(\mathbf{x},t)}{I_v^*}\right) - 1 \tag{4-32}$$

and the constraint $a(t)$ is originally defined as:

$$a(t) = \frac{P_{av}}{\frac{1}{A}\int\left(\exp\left(b\,\frac{I_v(\mathbf{x},t)}{I_v^*}\right)-1\right)dA} \tag{4-33}$$

where $P_{av} \approx 8$ kg m^{-2} day^{-1} is an areal–averaged precipitation value [Craig & Mack, 2013]. The model that represents equation 4-29 can be defined as a reaction–diffusion model where the first two terms at the right of equation 4-29 are the reactive component and the third one is the diffusive component. A non-dimensional form of equation 4-29 can be represented as follows:

$$\partial_{\check{t}}\, r_v(\mathbf{x},\check{t}) = -\tau\,\alpha\left(r_v(\check{\mathbf{x}},\check{t}) + \left(\frac{1-\epsilon}{\epsilon}\right)\check{a}(\check{\mathbf{x}},\check{t})\,\phi(\check{\mathbf{x}},\check{t})\right) + \left(\frac{\nu\,\tau}{\lambda^2}\right)\Delta r_v(\check{\mathbf{x}},\check{t}) \tag{4-34}$$

$$= -r_v(\check{\mathbf{x}},\check{t}) + \left(\frac{1-r_v(\check{\mathbf{x}},\check{t})}{r_v(\check{\mathbf{x}},\check{t})}\right)\check{a}(\check{\mathbf{x}},\check{t})\,\phi(\check{\mathbf{x}},\check{t}) + \Delta r_v(\check{\mathbf{x}},\check{t}) \tag{4-35}$$

$$r_v(\check{\mathbf{x}},0) = r_0(\mathbf{x}) \tag{4-36}$$

$$r_v(0,t) = r_v(\check{L},t) \tag{4-37}$$

$$\phi(\check{\mathbf{x}},\check{t})) = \exp\left(b\,r_v(\check{\mathbf{x}},\check{t})\right) - 1 \tag{4-38}$$

$$\check{a}(\check{\mathbf{x}},\check{t})^{-1} = \frac{1}{A}\int\left(\exp\left(b\,r_v(\check{\mathbf{x}},\check{t})\right)-1\right)dA \tag{4-39}$$

where $r_v = I_v(\mathbf{x},t)/I_v^*$. Equation 4-34 supposes there exists a natural time scale τ and a natural length scale λ in the systems in order to represent the non-dimensional form of equation 4-29, such that $t \to \tau\check{t}$ and $\mathbf{x} \to \lambda\check{\mathbf{x}}$. These natural scales can be represented as follows:

$$\tau = \frac{1}{\alpha} \tag{4-40}$$

$$\lambda = \sqrt{\frac{\nu}{\alpha}} \tag{4-41}$$

Having taken into account the last results, the non–dimensional reaction–diffusion equation of the Craig & Mack's model [2013] is as follows:

$$\partial_t\, r_v = -\, r_v + a\left(\frac{1-r_v}{r_v}\right)\left(\mathrm{e}^{b\, r_v}-1\right) + \Delta r_v \tag{4-42}$$

$$= -\, r_v + \left(\frac{1-r_v}{r_v}\right)\frac{\left(\mathrm{e}^{b\, r_v}-1\right)}{\left\langle \mathrm{e}^{b\, r_v}-1\right\rangle} + \Delta r_v \tag{4-43}$$

$$\asymp -\, r_v + \left(\frac{1-r_v}{r_v}\right)\frac{\left(\mathrm{e}^{b\, r_v}-1\right)}{\left(\mathrm{e}^{b\, \sup\{r_v\}}-1\right)} + \Delta r_v \tag{4-44}$$

$$\approx -\, \nabla\left(\frac{r_v^2}{2} - \log r_v + r_v - \nabla r_v\right) \tag{4-45}$$

If the non–linear terms of equation 4-45 are neglected, a linear non–dimensional reaction–diffusion equation of Craig & Mack's model [2013] is obtained, thus:

$$\partial_t\, r_v = -\nabla\left(r_v - \nabla r_v\right) \tag{4-46}$$

The linear non–dimensional reaction–diffusion equation of the Craig & Mack's model [2013] can be represented in Fourier space as follows. The variable $r_v(\mathbf{x}, t)$ and its derivatives can be written as:

$$r_v(\mathbf{x}, t) = \int A_{\mathbf{k}}(t)\, e^{-i\,\mathbf{k}\,\mathbf{x}}\, d\,\mathbf{k} \tag{4-47}$$

$$\partial_t\, r_v(\mathbf{x}, t) = \int \dot{A}_{\mathbf{k}}(t)\, e^{-i\,\mathbf{k}\,\mathbf{x}}\, d\,\mathbf{k} \tag{4-48}$$

$$\nabla^n r_v(\mathbf{x}, t) = \int A_{\mathbf{k}}(t)\, (i^n)\, |\mathbf{k}|^n\, e^{-i\,\mathbf{k}\,\mathbf{x}}\, d\,\mathbf{k} \tag{4-49}$$

Therefore, the dynamical system equation for the evolution of each Fourier component is as follows:

$$\dot{A}_{\mathbf{k}} = \left(-i\,|\mathbf{k}| + |\mathbf{k}|^2\right) A_{\mathbf{k}} \tag{4-50}$$

whose general solution of the dynamic equation for every wave vector is given by:

$$A_{\mathbf{k}}(t) = A_{\mathbf{k}}(0)\, e^{\left(-i\,|\mathbf{k}|+|\mathbf{k}|^2\right)t} \tag{4-51}$$

where the initial conditions for every wavenumber is given by:

$$A_{\mathbf{k}}(0) = \frac{1}{2\pi}\int r_v(\mathbf{x}, 0)\, e^{i\,\mathbf{k}\,\mathbf{x}}\, d\,\mathbf{x} \tag{4-52}$$

Figure 4-1 shows the phase portrait of the dynamical system represented by equation 4-50. The flow of this system goes to the right where $\dot{A}_{\mathbf{k}} > 0$ and to the left where $\dot{A}_{\mathbf{k}} < 0$. For an

arbitrary initial condition $A_{\mathbf{k}}(0)$, instabilities[12] with wavenumber $|\mathbf{k}| > 1$ grow exponentially and those ones with wavenumber $|\mathbf{k}| < 1$ decay exponentially. Therefore, there will be a rapid evolution of large–wavenumber features and a long–time evolution of small–wavenumber features. Those features whose wavenumbers are in the vicinity of $|\mathbf{k}| = 1/2$ are characterized for having less instability. Based on the qualitative characteristic of the model, it depicts a growth (or coarsening) mechanism of features in the direction of a local equilibrium state at $|\mathbf{k}| = 0$. Furthermore, the characteristic time scale is $1/\dot{A}_{\mathbf{k}}(0) \to \infty$ which means the coarsening process is developed indefinitely.

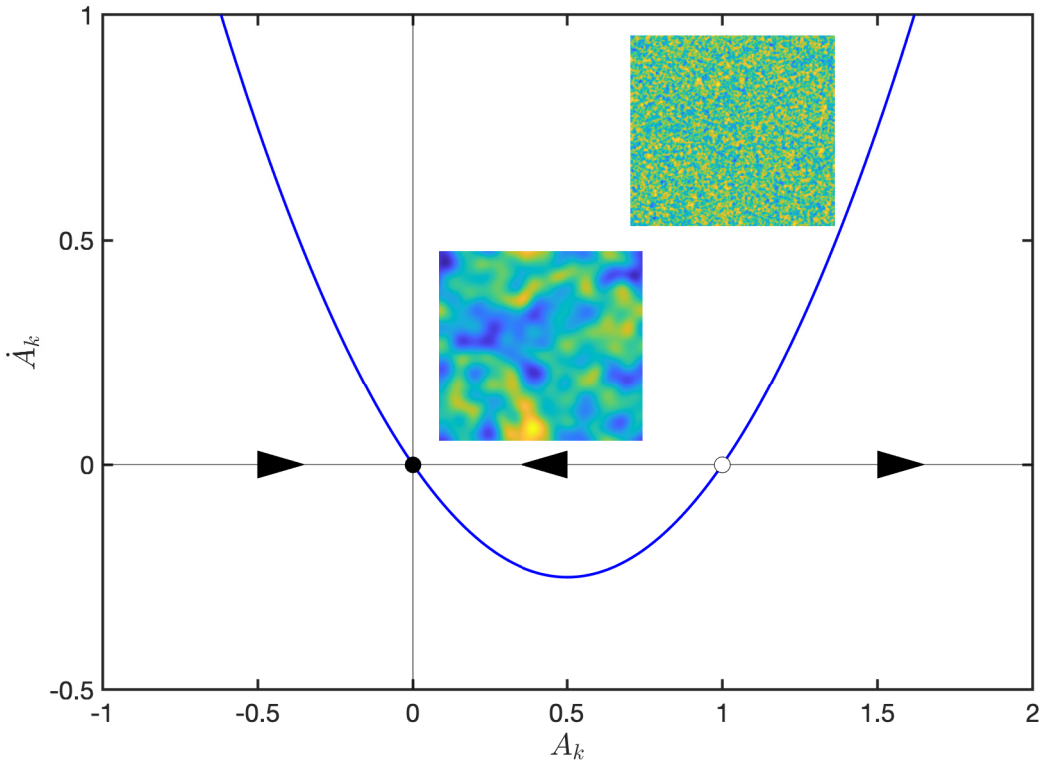

Figure 4-1: Phase portrait in Fourier space of the linear non–dimensional Craig & Mack's model. The solid black dot is showing the location of a stable fixed point and the open circle is showing the location of a unstable fixed point. The solid arrows are indicating the flow of the dynamical system. For the linear non–dimensional Craig & Mack's model there exists a stable fixed point at $A_{\mathbf{k}} = 0$, therefore, the flow of the wavenumber vector field is representing a growth mechanism of features into the field.

In order to get a multifractal structure, a dynamic equation for the evolution of each Fourier component should be completely different to the original model suggested by Craig & Mack [2013]. Multifractal patterns are described by the existence of features made up by several wavenumbers, but with preference to some specific ones. Under the concept of potential function (i.e. $\dot{A}_{\mathbf{k}} = -\partial_{A_{\mathbf{k}}} V_{\mathbf{k}}$), dynamical systems are studied in order to characterize fixed

[12]Instabilities are also known as perturbutations of the field in respect to an equilibrium condition.

points. For instance, the spinoidal decomposition in a diffusive system is well represented by the Cahn–Hilliard equation [Ursell, 2007]. Its potential function $V_{\mathbf{k}} = (-|\mathbf{k}|^3/3 + |\mathbf{k}|^5/5)\, A_{\mathbf{k}}$ exhibits a preferential wavenumber vector at $|\mathbf{k}| = 1$ which is identified as an equilibrium condition (or a well). The converse happens in Craig & Mack's model [2013]. In this model, the potential function is given by $V_{\mathbf{k}} = (|\mathbf{k}|^2/2 - |\mathbf{k}|^3/3)\, A_{\mathbf{k}}$ and the well is stated at the wavenumber vector $|\mathbf{k}| = 0$. So, the features in the spinoidal decomposition will evolve to features with wavenumber $|\mathbf{k}| = 1$, while in Craig & Mack's model, some features will evolve to features with wavenumber $|\mathbf{k}| = 0$.

Thus, if multifractality emerges from a diffusive mechanism, the dynamics of the Fourier components would be likely well represented in a more complex fashion. In a similar way, the Hottovy & Stechmann's model [2015] will be studied under the theory of linear stability. Taking only the deterministic component of equation 3-43, the deterministic Hottovy & Stechmann's model would be as follows:

$$\partial_t\, q(\mathbf{x},t) = \left[-\frac{1}{\tau_q}(q(\mathbf{x},t) - q^*) + F(\mathbf{x},t) \right] + b_0\, \Delta q(\mathbf{x},t) \tag{4-53}$$

$$q(\mathbf{x},0) = q_0(\mathbf{x}) \tag{4-54}$$

$$q(0,t) = q(L,t) \tag{4-55}$$

Equation 4-53 is also known as a reaction–diffusion equation in which the reactive component is defined by the first two terms at the right of equation 4-53 and the diffusive component by its third term. A non-dimensional deterministic equation of Hottovy & Stechmann's model [2015] could be represented as follows:

$$\partial_{\check{t}}\, r_v(\check{\mathbf{x}},\check{t}) = \left[-\frac{\tau}{\tau_q}(r_v(\check{\mathbf{x}},\check{t}) - 1) + \frac{\tau F(\check{\mathbf{x}},\check{t})}{q^*} \right] + \frac{\tau\, b_0}{\lambda^2}\, \Delta r_v(\check{\mathbf{x}},\check{t}) \tag{4-56}$$

$$= -\, r_v(\check{\mathbf{x}},\check{t}) + \phi(\check{\mathbf{x}},\check{t}) + \Delta r_v(\check{\mathbf{x}},\check{t}) \tag{4-57}$$

$$r_v(\check{\mathbf{x}},0) = r_0(\check{\mathbf{x}}) \tag{4-58}$$

$$r_v(0,\check{t}) = r_v(\check{L},\check{t}) \tag{4-59}$$

where $r_v = q(\mathbf{x},t)/q^*$ and $\phi(\check{\mathbf{x}},\check{t}) = 1 + \tau\, F(\check{\mathbf{x}},\check{t})/q^*$. The natural scales of the model for either time or space are:

$$\tau = \tau_q \tag{4-60}$$

$$\lambda = \sqrt{\tau_q\, b_0} \tag{4-61}$$

Assuming the forcing term $\phi(\check{\mathbf{x}},\check{t}) \equiv \phi$ is constant in the whole spatial domain, the model would be expressed as follows:

$$\partial_{\check{t}}\, r_v(\check{\mathbf{x}},\check{t}) = \nabla \left[-\frac{r_v(\check{\mathbf{x}},\check{t})^2}{2} + \phi\, r_v(\check{\mathbf{x}},\check{t}) + \nabla r_v(\check{\mathbf{x}},\check{t}) \right] \tag{4-62}$$

If the non–linear term at the right of equation 4-62 are neglected, a linear non–dimensional form of Hottovy & Stechmann's model would be represented as follows:

$$\partial_{\check{t}}\, r_v = \nabla\left[\phi\, r_v + \nabla r_v\right] \tag{4-63}$$

The variable $r_v \equiv r_v(\check{\mathbf{x}}, \check{t})$ and its derivatives can be represented in the Fourier space as follows:

$$r_v(\mathbf{x}, t) = \int A_{\mathbf{k}}(t)\, e^{-i\,\mathbf{k}\,\mathbf{x}}\, d\,\mathbf{k} \tag{4-64}$$

$$\partial_t\, r_v(\mathbf{x}, t) = \int \dot{A}_{\mathbf{k}}(t)\, e^{-i\,\mathbf{k}\,\mathbf{x}}\, d\,\mathbf{k} \tag{4-65}$$

$$\nabla^n r_v(\mathbf{x}, t) = \int A_{\mathbf{k}}(t)\, (i^n)\, |\mathbf{k}|^n\, e^{-i\,\mathbf{k}\,\mathbf{x}}\, d\,\mathbf{k} \tag{4-66}$$

Thus, the dynamical system equation for the evolution of each Fourier component is as follows:

$$\dot{A}_{\mathbf{k}} = \left(i\,\phi\,|\mathbf{k}| - |\mathbf{k}|^2\right) A_{\mathbf{k}} \tag{4-67}$$

whose general solution of the dynamic equation for every wave vector is given by:

$$A_{\mathbf{k}}(t) = A_{\mathbf{k}}(0)\, e^{\left(i\,\phi\,|\mathbf{k}| - |\mathbf{k}|^2\right)t} \tag{4-68}$$

where the initial conditions for every wavenumber are given by:

$$A_{\mathbf{k}}(0) = \frac{1}{2\pi} \int r_v(\mathbf{x}, 0)\, e^{i\,\mathbf{k}\,\mathbf{x}}\, d\,\mathbf{x} \tag{4-69}$$

At first glance, equation 4-67 seems to be alike to equation 4-50, however there exist some essential changes. If parameter $\phi \leq 0$, instabilities with wavenumber $|\mathbf{k}| > 0$ are exponentially damped, whereas, if parameter $\phi > 0$, instabilities with wavenumber $|\mathbf{k}| > \phi$ are exponentially damped and instabilities with wavenumber $0 < |\mathbf{k}| < \phi$ grow exponentially. Those instabilities with wavenumbers in the vicinity of $|\mathbf{k}| = \phi/2$ grow faster as shown in the phase portrait of Figure 4-2. Hottovy & Stechmann's model [2015] have a mathematical structure similar to those model used for describing the spinoidal decomposition in diffusive systems. There exists a rapid evolution of features with wavenumber $|\mathbf{k}| < \phi$ and a long–time evolution of large–wavenumber features. For this system, the characteristic time scale is $1/\dot{A}_{\mathbf{k}}(\phi) = (2\,\phi - 1)^{-1}$ which also depends on the parameter ϕ. The larger the parameter ϕ becomes, the smaller the characteristic time scale will be.

Qualitatively, the linear non-dimensional Hottovy & Stechmann's model describes a *concentration mechanism* where features concentrates toward a local equilibrium state with a certain wavenumber (see Figure 4-2). Another important fact about the model is observed through the analysis of parameter ϕ. No matter which value the parameter ϕ takes, there will always be fixed points, therefore, there exists a transcritical bifurcation given by the

change of value in the parameter ϕ. For $\phi \leq 0$ there exists a stable fixed point that describes how features evolve to those ones with wavenumber $|\mathbf{k}| = 0$. If $\phi > 0$, there will be a stable fixed point that represents how features evolve to those ones with wavenumber $|\mathbf{k}| = \phi$.

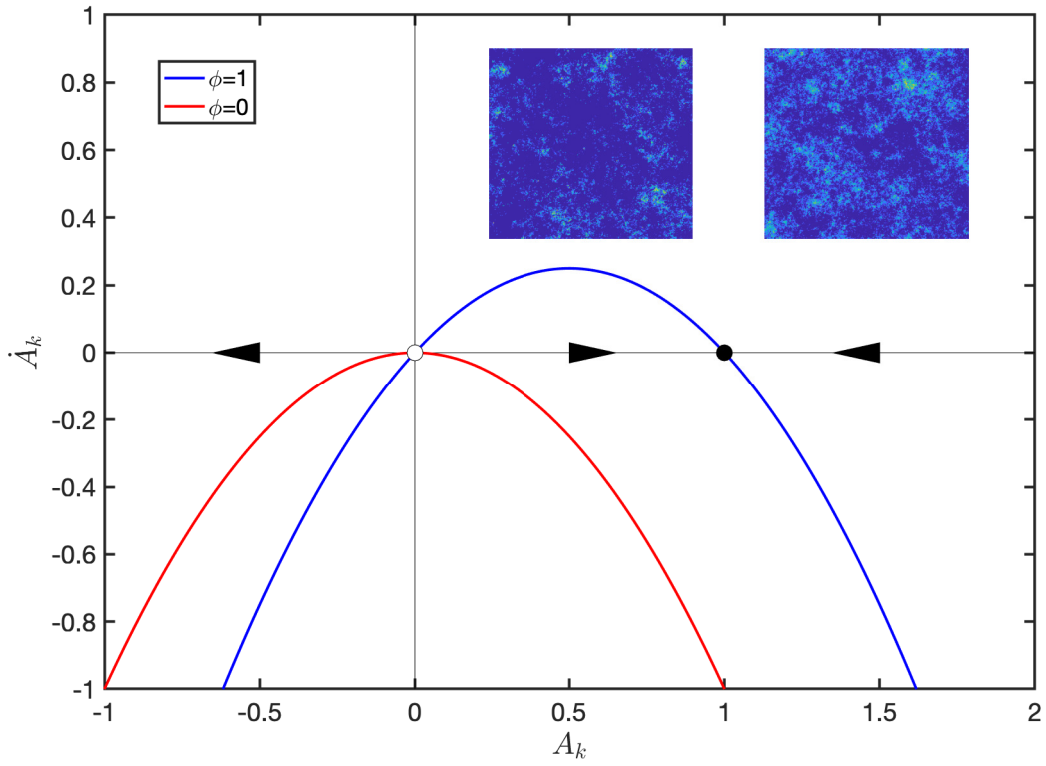

Figure 4-2: Phase portrait in Fourier space of the linear non–dimensional Hottovy & Stechmann's model. The solid black dot is showing the location of a stable fixed point and the open circle is showing the location of a unstable fixed point. The solid arrows are indicating the flow of the dynamical system. For the linear non–dimensional Hottovy & Stechmann's model there exists a fixed point at $A_k = 1$, therefore, the flow of the wavenumber vector field is representing a concentration mechanism of features into the field.

Albeit, Hottovy & Stechmann's model [2015] is able to generate outputs with characteristics akin to rainfall observations (see section 3.3.3), the model outputs are not completely characterized as multifractrals patterns. So, there should be more elements for obtaining a complete description of rainfall multifractality. Sornette [2004] suggests that some out–of–equilibrium systems whose fundamental properties are: highly non–linear behavior, power–law distributions of events and fractal patterns, among others, possess a large number of metastable states whose dynamics take the system from one to another of such metastable states. Neither Craig & Mack's model nor Hottovy & Stechmann's model are constituted by a large number of metastable fixed points, however multifractality can be envisioned in some of their results. Therefore, in order to maintain a model with a suitable statistical description of outputs, its mathematical structure should not only provide a large number of

metastable states, instead it needs a persistent mechanism for disturbing the placement of the system from its fixed points, i.e. there should be a rigidity threshold of all fixed points of the system. In Hottovy & Stechmann's model [2015] the disturbing mechanism is led by the random term whose physics is to represent the atmospheric turbulence effect.

In the theory of universal multifractals, there is a model for representing either an anomalous diffusion process or multifractal fields. This one was introduced by Marzan et al. [1996] who suggested that multifractal rainfall fields should be understood through a causal process in either space or time (i.e. the past influences the future). Marzan et al.'s model [1996] is formally described by a non–homogeneous fractional differential equation as follows:

$$\left(\partial_t^{\xi_1} + (i^2\,\Delta)^{\xi_2}\right)\Gamma_\lambda(\mathbf{x}) = \gamma_\lambda(\mathbf{x}) \tag{4-70}$$

where $\Gamma_\lambda = g_\lambda(\mathbf{x},t) * \gamma_\lambda(\mathbf{x},t)$ is a multifractal field generator that is expressed as the convolution between the impulse–response function $g_\lambda(\mathbf{x},t)$ and a random function $\gamma_\lambda(\mathbf{x},t)$; ξ_1 and ξ_2 are scaling exponents that are related through the dynamical scaling exponent H. Equation 4-70 represents an anomalous diffusion equation for the multifractal field generator instead of a quantifiable physical variable, therefore, the difference between this model and other diffusive models is straightforward. It is highlighted that equation 4-70 includes dynamic scaling properties to represent the space–time asymmetry observed in rainfall; furthermore, the well-known multiplicative process used for describing rainfall measures is changed in this model by an additive process stated by the logarithm of such measures and thus constitutes a mechanism of development of random cascades through a diffusion process.

Other alternatives for representing either diffusive processes or multifractal scaling properties do exists Cortis et al. [e.g. 2014]. However, there are several paradigms for solving in these models: i) the physical meaning of either deterministic or random parameters, and ii) a complete assessment of the turbulence effect in the development of rainfall patterns. In the light of models that were studied in this research, future works could be led to explore a coupling between independent physical processes; one associated to the thermodynamic component and a second one for representing the turbulence effect and its symmetries. Thus far, this research reveals that a diffusive mechanism is the key for explaining how rainfall patterns are formed and therefore, how multifractal scaling properties emerge. This key should be deeply studied to find more pieces in the puzzle of atmospheric science.

5. Conclusions

5.1. Summary of Results and Conclusions

The path followed by this research is to set a physical basis of multifractal properties of space–time rainfall fields. Several researches, including this one, confirms the space–time structure of rainfall is indeed multifractal, however, a conclusive answer of how it emerges under physical basis is still in construction. This research provides some new ideas for solving the aforementioned query and they depart from data analysis to the analytical study of models. Albeit, there are several advances reported in the study of rainfall multifractality, the main one is that rainfall multifractality is not a symmetry property shifted from atmospheric turbulence processes, but an intrinsic quality of diffusive systems.

At first, multifractality was studied under theoretical basis and then identified in observed natural patterns [Mandelbrot, 1989, Feder, 1988, Mandelbrot, 1982]. Rainfall has been seen as an analogy of turbulence either because it is plunged and developed into a turbulent atmosphere, or because its geometrical description is highly complex. As a consequence of this analogy, rainfall multifractality was explored in deterministic and stochastic models that were able to describe complex patterns as turbulence does and to represent statistical scaling properties. A plethora of rainfall models have emerged over the years whose complexity changes according to its mathematical basis, however all have a preference for possessing a parsimonious structure based on rational hypotheses.

Despite the fact that multifractal models for describing rainfall are always improving its prediction, they have disconnected their mathematical formulations from a physical meaning. The converse also happens, i.e. there exists a set of physically-based models that are not able to describe the whole statistical structure of complex rainfall patterns. Moreover, often these models can represent well static scenarios which are derived from a physical realization and they suppose that either space or time are related linearly or even further there is not any linkage between them. Facing the problem of describing rainfall requires not only highly complex mathematical tools as fractal theory and modern mathematics provide, but also a theoretical integration that helps to link the gaps between physics and the statistics of rainfall. The aforementioned problem is quite complex, therefore, this research was enclosed to identify a physical mechanism that explains how multifractal properties emerge in space–time rainfall fields.

Previously to the study of physical mechanisms that explain how multifractality emerges in space–time patterns, a multifractal quantification was necessary to carry out in data of any kind. In this research, a data analysis protocol for exploring non–linear properties in either

time or space–time data was implemented; furthermore, several kinds of data were test under this data–exploration protocol to confirm that multifractality exists in either observations or model outputs. Among the variety of statistical tools reported on scientific literature, five methods were selected: i) multifractal spectra via method of moments, ii) cumulant–based magnitude coefficients, iii) two–point correlation functions, iv) incremental similarity analysis, and v) dynamic scaling exponents. Some technical details about these methods can be reviewed in section 3.1.

The first data sets that were explored are punctual high–resolution rainfall observations recorded by the EAAB at Bogotá. Empirical multifractal spectra obtained from these data are described by several singular scaling exponents ($0.4 \leq \alpha < 1.0$). The average multifractal spectrum is centered at $\alpha = 0.84$, its fractal dimension of the support is set on $D_0 \approx 0.74$ and its spectral width is $H_\alpha = 0.68$. The two–point correlation functions that were estimated for punctual rainfall observations exhibit a power law decay inasmuch as the scale increases; therefore, the former means there is not a long–range dependence as one could find in patterns built via random multiplicative cascade. Evidence about the intermittent nature of rainfall observations was found in the PDFs analysis of increments $\Delta_{t,u}$. The good fitting of PDFs to the NIG–distribution suggests rainfall is as intermittent as those patterns observed in turbulence [e.g. Barndorff-Nielsen & Schmiegel, 2015, Barndorff-Nielsen et al., 2004]. This research suggests that a proof of multifractality would be defined if data satisfy two criteria: i) a good fit of the empirical PDF of increments $\Delta_{t,u}$ to the Normal–Inverse Gaussian distribution and ii) if for a specific value of the variance, the equivalence relation denominated *incremental similarity* is satisfied. These criteria were adopted and used for the subsequent analysis of spatial data.

Weather radar reflectivity records also exhibit multifractal scaling. The selected data for this research were bound in time, so multifractal properties of the reflectivity field are those given during the development of a typical storm at the radar location. Spatial patterns of this type are characterized for having less number of singular scaling exponents in comparison to punctual patterns, therefore, multifractal spectra that describe these fields is shifted to the right where non–singular measures are characterized. The average multifractal spectrum is centered at $\alpha_0 = 1.69$, its dimension of the support is $D_0 = 1.65$ and its spectral width is $H_\alpha \approx 1.0$. Over time, multifractal descriptors change likewise to spatial statistics of the field; however there are not sudden changes in the dynamics of fractal dimensions but they are rather smoothed in nature. Reflectivity patterns exhibit two–point correlation functions that show the existence of a long–range dependence. Thus, the data statistical structure could be represented by a multiplicative process as suggested by Arneodo et al. [1998] and Roux et al. [2009].

On the other hand, there is not a good fitting of empirical PDFs of increments $\Delta_{t,u}$ to the NIG distribution. This proves that reflectivity fields are not as intermittent as those found in turbulence. In the light of the statistical analysis, this research concludes that these kinds of data could be classified as patterns of weak multifractality. However, one event of strong precipitation does not constitute as a sufficient statistical sample for setting a typical quality

of these kinds of data. In order to confirm the weak multifractality of the reflectivity field, a similar data analysis should be extended to other data sets and to verify if there exist similarities to the results reported by this research. Another aspect found in reflectivity fields is that they exhibit a space–time dynamic scaling which is represented by its scaling exponent $H \approx 1/2$.

Satellite rainfall fields from TRMM exhibit multifractal scaling. The average multifractal spectrum is centered at $\alpha = 1.61$, its dimension of the support is $D_0 = 1.48$ and its spectral width is $H_\alpha \approx 1.7$. The dimension D_0 seems to be akin with the seasonal behavior of rainfall. During the dry season, D_0 tends to be higher than in the wet season; then D_0 represents an index of the atmospheric humidity content. The two–point correlation functions computed from these data exhibit a linear relationship between the correlation $C(\delta, \Delta x)$ and $\ln(\Delta x)$ (long–range dependence). This suggests there could be a multiplicative cascade process that is able to describe these spatial patterns. On the other side, satellite rainfall patterns are characterized as having higher intermittency and such a description was confirmed by the good fitting of PDFs of increments $\Delta_{t,u}$ to the NIG distribution. Moreover, the dynamic scaling exponent that were estimated from satellite data suggests there exists a higher connectivity with symmetries found in turbulence (i.e. $H \approx 1/3$), specially during the development of wet seasons. This allows one to presume that symmetries of atmospheric turbulence act over the rainfall field only when turbulence is highly active, in such a way that rainfall seems to play the role of a passive scalar in the atmospheric environment.

From the perspective of physically–based models, this research studied some of them: Nordstrom & Gupta's model [2003], Craig & Mack's model [2013], Hottovy & Stechmann's model [2015], and Raymond & Zeng's model [2005]. Model outputs were evaluated under the aforementioned multifractal techniques in order to characterize their capability for representing multifractal properties. Nordstrom & Gupta's model [2003] is capable of representing multifractal fields, however, this research found the model exhibits a tendency for producing multifractal structures with few scaling exponents. The fact that model outputs have a multifractal structure with few scaling exponents, it means that the intermittency of those output fields is weak. The former is confirmed by the PDF of increments $\Delta_{t,u}$ whose fitting to the NIG distribution is not satisfied. Model output fields also exhibit dynamic scaling and its dynamic scaling exponent is near to $H \approx 1/2$. Such a value is not akin to that found in turbulence but rather in space–time scalar variables (e.g. temperature).

Craig & Mack's model [2013] describes a mechanism for the organization of tropical convection through interactions between atmospheric drying by subsidence and atmospheric moistening by vertical and horizontal transport of humidity. This model also exhibits multifractality with few scaling exponents. The averaged spectrum is centered at $\alpha_0 = 1.16$, its dimension of the support is $D_0 = 1.12$ and its spectral width is $H_\alpha \approx 0.2$. Albeit the model tries to emulate multifractal features, there are not realistic values on its multifractal descriptor, since they are not alike to those observed in rainfall records. It is highlighted that multifractal descriptors change in time, and such changes depends on the evolution of a coarsening process by the atmospheric moisture over the spatial domain. On the other hand,

the model roughly exhibits intermittency, so once again it is confirmed that the model cannot emulate multifractal patterns comparable to those observed in rainfall. Finally, model outputs exhibit either spatial anisotropy or dynamic scaling. However, the estimated dynamic scaling exponent is not akin to that found in turbulence nor with pure diffusive–driven processes.

Hottovy & Stechmann's model [2015] exhibits multifractal scaling in their outputs which is rather similar to that found in rainfall records. The average multifractal spectrum is centered at $\alpha = 1.66$, its fractal dimension of the support is $D_0 = 1.63$ and its spectral width is $H_\alpha \approx 0.6$. Output statistics and multifractal descriptors also exhibit a dynamic over time which it is presumed to be modulated by an intrinsic concentration mechanism. Unlike other physically–based models, Hottovy & Stechmann's model exhibits intermittency and the good fitting of PDFs of increments $\Delta_{t,u}$ to the NIG distribution ascertain this last statement. In addition to the previous arguments, this model exhibits dynamic scaling whose exponent H is approximated to 1/4. This value of the dynamic scaling exponent has been found in patterns generated by random growth models (e.g. Edwards & Wilkinson's model [1982]).

Complementary, the cloud resolving model introduced by Raymond & Zeng [2005] was also studied in the light of multifractal exploration techniques. This model possesses a roughly complex physical parametrization which allows one to analyze the space–time structure of the tropical atmosphere. Model outputs exhibit multifractal scaling, however, there exists a high variability of multifractal descriptors in the 50 days of simulation. This model cannot emulate the intermittency of high–frequency measures, furthermore, the estimated dynamic scaling exponent H seems to be unrealistic. In spite of the model possesses a physical basis more complex than those known by its parsimonious attributes, the output statistics do not seem to be appropriate; therefore, this model is not suitable for describing rainfall multifractality.

In light of the work made by Bjerknes [1938] explaining the role of clouds in the atmospheric heating, an interesting fact is derived from its conceptual basis: the convective instability is more efficient if clouds are concentrated in the spatial domain. Among necessary conditions for obtaining a positive local change of the atmospheric temperature, if there exists a scenery of conditional instability, there should be a upward vertical velocity over the cloudy areas (upwelling) and a downward vertical velocity over non–cloudy areas (subsidence). According to equation 4-11, the difference of temperatures between the cloudy and non–cloudy areas will be larger if the fractional cloud area vanishes over the domain (i.e. FCA$\rightarrow$ 0), such a condition benefits the convective instability and the atmospheric heating. Although there is not a direct bonding between the physics that explains how the atmosphere is heated and how rainfall patterns are clustered and multifractal. Bjerknes's physical theory introduced a mechanism that explains which is the preferential geometry of atmospheric clouds.

In order to build a bonding between the physical theory of the tropical atmospheric dynamics and the theory of rainfall multifractality, the work done by Over & Gupta [1994, 1996] about the description of rainfall patterns via random multiplicative cascades can be intertwined

with Bjerknes's physical theory. Assuming the fractional cloud area (FCA) and the fractional wet area (FWA) are approximated interchangeable for the long–term and large–domain analysis, FCA could be approximated as follows:

$$\mathrm{FCA}(\lambda) \sim (1-p)^{-d \log \lambda / \log b} \tag{5-1}$$

Thus, if parameters d, λ and b are fixed for modeling tropical rainfall through random multiplicative cascades, p represents not only a long–term statistic of the rainfall field but also a physical quantity representing the large–scale moisture convergence; therefore, another approximation for the parameter p would be given by:

$$p \approx 1 - \left(1 - \frac{M_c}{M_c - M_{nc}}\right)^{-\log b / (d \log \lambda)} \tag{5-2}$$

Here, parameter p offers a physical restriction given by the atmospheric moisture dynamics and for modeling purpose, such a dynamics should be taken into account.

On the other side, Peters & Neelin [2006] have suggested that one can understand the atmospheric precipitation under the theory of critical phenomena. This theory has set the origin of scaling through manifestations of the system when criticality states have been reached. The conceptual formulation of Peters & Neelin [2006] underscore the existence of static scaling exponents when limit states of the vertically–integrated water vapor content are reached. A static scaling law for the description of atmospheric precipitation is not realistic in the sense that time should not interact with the spatial dynamics of the field. The aforementioned argument would be a contradiction in the light of findings by this and other researches. An important fact to highlight about Peter & Neeling's model [2006] is observed in its susceptibility function $\chi(w_*, \lambda)$. This function is represented by the spatial variance of precipitation $\sigma_p^2(w_*, \lambda)$ and this formulation suggests there could be a anomalous diffusive process to describe the dynamics of atmospheric precipitation. If so, this research suggests a modification to the Peter & Neeling's model [2006], in order to include a time indexation. Thus, the fractal dimension of the anomalous diffusive process can be estimated in time t through the following expression:

$$D(w_*, t) = d\,[1 - \zeta] \qquad \text{with} \quad \zeta = \frac{\log t}{\log \chi(w_*, \lambda) - \log \nu} \ll 1 \tag{5-3}$$

where $\chi(w_*, \lambda)$ is the susceptibility function, d is the spatial dimension where precipitation takes place, λ represents the spatial scale, and ν is the diffusivity ν of the atmospheric water vapor field. Albeit the model introduced by Peters & Neelin [2006] suggests an explanation for the development of scaling exponents, these ones are not connected to the multifractal theory and therefore, the physics of rainfall multifractality from critical phenomena theory is under construction. However, the conceptual framework of Peters & Neelins model [2006] has set the foundations of a new understanding of atmospheric precipitation, and it also has spread ideas for building models based on the concept of criticality.

Supported on the bases of either the mathematical structure or the physics that represent the models introduced by Craig & Mack [2013] and Hottovy & Stechmann [2015], this research makes an effort for identifying the fundamental mechanism for giving rise to the simulated patterns and its connection with the physics of rainfall multifractality. By means of a linear stability analysis in the Fourier space, the linear non-dimensional non-stochastic Hottovy & Stechmann's model shows that a mechanism of concentration for atmospheric vapor is obtained by instabilities in diffusive environments. In Hottovy & Stechmann's model, the dynamic equation for the evolution of each Fourier component is given by:

$$\dot{A}_{\mathbf{k}} = \left(i\,\phi\,|\mathbf{k}| - |\mathbf{k}|^2\right) A_{\mathbf{k}} \tag{5-4}$$

This equations depicts a flow of the dynamical system toward features whose wavenumber vector is $|\mathbf{k}| = 1$. So, instabilities with wavenumber $|\mathbf{k}| > 1$ and those with wavenumber $0 < |\mathbf{k}| < 1$ are exponentially damped to attain a stability condition of the dynamical system. The former analysis suggests that a multifractal structure of the rainfall field could emerge by a physical mechanism known as diffusion–driven instabilities. However, for a complete multifractal statistical structure of the rainfall field, a persistent perturbation mechanism should exist in the diffusive environment. Turbulence plays an important role in the configuration of such a mechanism and therefore, future directions will be addressed to understand the connectivity between turbulence and diffusive processes.

5.2. Open problems and Future Directions

The path for finding answers to the fundamental question of this research has many derivations and a wide number of open problems. A few of them will be indicated below in order to identify future directions for new researches:

The prediction of the scaling properties of the models should be validated on theoretical ground, so further work to complement the linear analysis used in the analysis of the physically–based models is needed to understand the interaction between scales. For instance, a review of the scientific literature suggests researching a multiscale expansion for the analysis of differential equations [Geiser, 2016]. The exploration of this technique in the context of this research could be worthwhile if from its application one gains a better understanding of the interaction among scales and how they could give rise to multifractality.

Physical interactions between turbulence and atmospheric precipitation processes that lead to the formation of multifractal fields is an unclear subject. The main assumption about how turbulence takes action in the scaling properties of the rainfall field is to make rainfall a passive scalar into a turbulent environment and the symmetries of turbulence are transferred to the rainfall field. Actually, Bedrossian et al. [2019] claim that the mechanism responsible for power laws in passive scalars is the transfer of scalar mass from low to high Fourier modes. However, in the light of this research's results one could assume that there should not be a unique directionality in the transfer of scalar mass as seen in Fourier space. Another assumption is seen in that turbulence could play the role of intensifying the natural scaling

properties of the rainfall field, so if the inertial frame of reference of rainfall models were changed by a rotating one, the role of turbulence could possibly be elucidated from results.

In the field of engineering applications, the implementation of physically–based models for the description of rainfall dynamics can be initialized in future works. It is envisioned that the physically–based models of rainfall can help to identify space–time attributes to be considered in the analysis of hydrological systems, the design of drinking and waste water systems, and the assessment of climate change. To explore these applications on models, the scale for modeling purposes implies a high computational effort. So, future works could be oriented to implement structured algorithms and computational applications in which one of the studied physically–based model of rainfall be the foundation for making decision in engineering and scientific endeavors.

Bibliography

A. Aharony. Percolation, fractals, and anomalous diffusion. *Journal of Statistical Physics*, 34(5):931–939, 1984. doi: 10.1007/BF01009449.

S. Allen and J. Cahn. A microscopic theory for antiphase boundary motion and its application to antiphase domain coarsening. *Acta Metallurgica*, 27(6):1085–1095, 1979. doi: https://doi.org/10.1016/0001-6160(79)90196-2.

American Meteorological Society. Radiative-Convective Equilibrium, 2019a.

American Meteorological Society. Subcloud Layer, 2019b.

F. Anselmet, Y. Gagne, E. Hopfinger, and R. Antonia. High-order velocity structure functions in turbulent shear flows. *Journal of Fluid Mechanics*, 140:63–89, 1984. doi: DOI:10.1017/S0022112084000513.

A. Arneodo, E. Bacry, S. Manneville, and J. Muzy. Analysis of random cascades using space-scale correlation functions. *Physical Review Letters*, 80(4):708–711, 1998.

E. Bacry, J. Muzy, and A. Arnéodo. Singularity spectrum of fractal signals from wavelet analysis: exact results. *Journal of Statistical Physics*, 70(3-4):635–674, 1993.

O. Barndorff-Nielsen and J. Schmiegel. Incremental similarity and turbulence. *arXiv e-prints*, 2015.

O. Barndorff-Nielsen, P. Blæsild, and J. Schmiegel. A parsimonious and universal description of turbulent velocity increments. *The European Physical Journal B - Condensed Matter and Complex Systems*, 41(3):345–363, 2004. doi: 10.1140/epjb/e2004-00328-1.

M. Barnsley. *Fractals Everywhere*. Morgan Kaufmann Publishers, 1993.

J. Bedrossian, A. Blumenthal, and S. Punshon-Smith. The batchelor spectrum of passive scalar turbulence in stochastic fluid mechanics. *arXiv e-prints*, 2019.

H. Bendjoudi, P. Hubert, D. Schertzer, and S. Lovejoy. Interprétation multifractale des courbes intensité-durée-fréquence des précipitations. *Comptes Rendus de l'Académie des Sciences - Series IIA - Earth and Planetary Science*, 325(5):323–326, 1997. doi: http://dx.doi.org/10.1016/S1251-8050(97)81379-1.

F. Bernal. Desarrollo de modelos conceptuales y computacionales para simular estocásticamente la dinámica espacio-temporal de la precipitación en Bogotá. Master's thesis, Universidad Nacional de Colombia, 2008.

J. Bjerknes. Saturated-adiabatic ascent of air through dry-adiabatically descending environment. *Quarterly Journal of the Royal Meteorological Society*, 64:325–330, 1938.

D. Blanchard. Mesoscale convective patterns of the southern high plains. *Bulletin of the American Meteorological Society*, 71(7):994–1005, 1990. doi: 10.1175/1520-0477(1990)071⟨0994:MCPOTS⟩2.0.CO;2.

J. Bouchaud and A. Georges. Anomalous diffusion in disordered media: Statistical mechanisms, models and physical applications. *Physics Reports*, 195(4):127–293, 1990. doi: https://doi.org/10.1016/0370-1573(90)90099-N.

A. Bray. Theory of phase-ordering kinetics. *Advances in Physics*, 43:357–459, 1994. doi: 10.1080/00018739400101505.

C. Bretherton, M. Peters, and L. Back. Relationships between water vapor path and precipitation over the tropical oceans. *Journal of Climate*, 17(7):1517–1528, 2004.

C. Bretherton, P. Blossey, and M. Khairoutdinov. An energy-balance analysis of deep convective self-aggregation above uniform SST. *Journal of the Atmospheric Sciences*, 62(12):4273–4292, 2005.

A. Cortis, C. Puente, and B. Sivakumar. Encoding hydrologic information via a fractal geometric approach and its extensions. *Stochastic Environmental Research and Risk Assessment*, 24(5):625–632, 2010. doi: 10.1007/s00477-009-0349-4.

A. Cortis, C. Puente, H. Huang, M. Maskey, B. Sivakumar, and N. Obregón. A physical interpretation of the deterministic fractal–multifractal method as a realization of a generalized multiplicative cascade. *Stochastic Environmental Research and Risk Assessment*, 28(6):1421–1429, 2014. doi: 10.1007/s00477-013-0822-y.

D. Cox and V. Isham. A simple spatial-temporal model of rainfall. *Proceedings of the Royal Society of London. A. Mathematical and Physical Sciences*, 415(1849):317–328, 1988.

G. Craig and J. Mack. A coarsening model for self-organization of tropical convection. *Journal of Geophysical Research D: Atmospheres*, 118(16):8761–8769, 2013.

C. De-Michele and P. Bernardara. Spectral analysis and modeling of space-time rainfall fields. *Atmospheric Research*, 77(1):124–136, 2005. doi: https://doi.org/10.1016/j.atmosres.2004.10.031.

J. Delour, J. Muzy, and A. Arnéodo. Intermittency of 1D velocity spatial profiles in turbulence: a magnitude cumulant analysis. *The European Physical Journal B*, 23(2):243–248, 2001.

R. Dickman, M. Muñoz, A. Vespignani, and S. Zapperi. Paths to self-organized criticality. *Brazilian Journal of Physics*, 30:27–41, 2000. doi: 10.1590/S0103-97332000000100004.

S. Edwards and D. Wilkinson. The surface statistics of a granular aggregate. *Proceedings of the Royal Society of London. Series A, Mathematical and Physical Sciences*, 381(1780): 17–31, 1982.

A. Einstein. Über die von der molekularkinetischen theorie der wärme geforderte bewegung von in ruhenden flüssigkeiten suspendierten teilchen. *Annalen der Physik*, 322(8):549–560, 1905. doi: 10.1002/andp.19053220806.

C. Evertsz and B. Mandelbrot. *Multifractal measures*, pages 849–881. Springer, Chaos and Fractals: New Frontiers in Science edition, 1992.

K. Falconer. *Fractal Geometry: Mathematical Foundations and Applications*. John Wiley & Sons, Inc., 1990. ISBN 0471922870.

F. Family and T. Vicsek. Scaling of the active zone in the Eden process on percolation networks and the ballistic deposition model. *Journal of Physics A: Mathematical and General*, 18(2):L75–L81, 1985. doi: 10.1088/0305-4470/18/2/005.

J. Feder. *Fractals*. Plenum Press, 1988.

E. Foufoula-Georgiou. *On scaling theories of space–time rainfall: some recent results and open problems*, volume 7, pages 25—72. World Scientific, 1998.

U. Frisch. *Turbulence: the legacy of A. N. Kolmogorov*. Cambridge University Press, 1995.

U. Frisch and G. Parisi. On the singularity structure of fully developed turbulence. *Turbulence and predictability in geophysical fluid dynamics and climate dynamics*, 88, 1985.

K. Gabriel and J. Neumann. A Markov chain model for daily rainfall occurrence at Tel Aviv. *Quarterly Journal of the Royal Meteorological Society*, 88(375):90–95, 1962. doi: 10.1002/qj.49708837511.

J. Geiser. *Multicomponent and multiscale systems: theory, methods, and applications in engineering*. Springer, 2016.

L. Gmachowski. Fractal model of anomalous diffusion. *European Biophysics Journal*, 44(8): 613–621, 12 2015. doi: 10.1007/s00249-015-1054-5.

Goddard Earth Sciences Data and Information Services Center. README document for the tropical rainfall measurement mission (TRMM) version 7. Technical Report 610.2, NASA Goddard Space Flight Center, 2017.

N. Goldenfeld. *Lectures on phase transitions and renormalization group*. Number 85 in Frontiers in Physics. Addison-Wesley Publishing, 1992.

J. Gómez and G. Poveda. Estimación del espectro multifractal para series de precipitación horaria en los Andes Tropicales de Colombia. *Revista de la Academia Colombiana de ciencias exactas, físicas y naturales*, 32(125):483–502, 2008.

F. Guichard and F. Couvreux. A short review of numerical cloud–resolving models. *Tellus A: Dynamic Meteorology and Oceanography*, 69(1), 2017. doi: 10.1080/16000870.2017.1373578.

V. Gupta and E. Waymire. A stochastic kinematic study of subsynoptic space–time rainfall. *Water Resources Research*, 15(3):637–644, 1979. doi: 10.1029/WR015i003p00637.

V. Gupta and E. Waymire. A statistical analysis of mesoscale rainfall as a random cascade. *Journal of American Meteorological Society*, 32:251–267, 1993.

H. Hardy and R. Beier. *Fractals in Reservoir Engineering*. World Scientific, 1994. ISBN 9789810220693.

M. Hassan, M. Hassan, and N. Pavel. Dynamic scaling, data-collapse and self-similarity in Barabási-Albert networks. *Journal of Physics A: Mathematical and Theoretical*, 44(17), 2011. doi: 10.1088/1751-8113/44/17/175101.

M. Herman and D. Raymond. WTG cloud modeling with spectral decomposition of heating. *Journal of Advances in Modeling Earth Systems*, 6(4):1121–1140, 2014. doi: 10.1002/2014MS000359.

C. Holloway and D. Neelin. Moisture vertical structure, column water vapor, and tropical deep convection. *Journal of the Atmospheric Sciences*, 66(6):1665–1683, 2009.

C. Holloway and J. Neelin. Temporal relations of column water vapor and tropical precipitation. *Journal of the Atmospheric Sciences*, 67(4):1091–1105, 2010.

S. Hottovy and S. Stechmann. A spatiotemporal stochastic model for tropical precipitation and water vapor dynamics. *Journal of the Atmospheric Sciences*, 72(12):4721–4738, 2015.

H. Huang, C. Puente, and A. Cortis. Geometric harnessing of precipitation records: reexamining four storms from Iowa City. *Stochastic Environmental Research and Risk Assessment*, 27(4):955–968, 2013.

P. Hubert, Y. Tessier, S. Lovejoy, D. Schertzer, F. Schmitt, P. Ladoy, J. Carbonnel, S. Violette, and I. Desurosne. Multifractals and extreme rainfall events. *Geophysical Research Letters*, 20(10):931–934, 1993. doi: 10.1029/93GL01245.

G. Huffman, R. Adler, D. Bolvin, G. Gu, E. Nelkin, K. Bowman, Y. Hong, E. Stocker, and D. Wolff. The TRMM multi-satellite precipitation analysis: quasi–global, multi–year, combined–sensor precipitation estimates at fine scale. *Journal of Hydrometeorology*, 8(1):38–55, 2007.

Intergovernmental Panel on Climate Change. *Climate Change 2013: The Physical Science Basis. Fifth Assessment Report of the Intergovernmental Panel on Climate Change (AR5).* Cambridge University Press, 2013.

E. Ising. Beitrag zur theorie des ferromagnetismus. *Zeitschrift für Physik*, 31(1):253–258, 1925. doi: 10.1007/BF02980577.

B. Kang and J. Ramírez. A coupled stochastic space–time intermittent random cascade model for rainfall downscaling. *Water Resources Research*, 46(10), 2010. doi: 10.1029/2008WR007692.

M. Khairoutdinov and K. Emanuel. Aggregated convection and the regulation of tropical climate. In *29th Conference on Hurricanes and Tropical Meteorology*, 2010.

M. Khairoutdinov and D. Randall. Cloud resolving modeling of the ARM summer 1997 IOP: model formulation, results, uncertainties, and sensitivities. *Journal of the Atmospheric Sciences*, 60(4):607–625, 2003.

M. Kolb. Shape and selfsimilarity of diffusion limited aggregation clusters. In A. Pekalski and K. Sznajd-Weron, editors, *Anomalous Diffusion From Basics to Applications*, pages 253–261. Springer, 1999.

A. Kolmogorov. The local structure of turbulence in incompressible viscous fluid for very large reynolds' numbers. *Akademiia Nauk SSSR Doklady*, 30:301–305, 1941.

D. Koutsoyiannis, A. Paschalis, and N. Theodoratos. Two-dimensional Hurst–Kolmogorov process and its application to rainfall fields. *Journal of Hydrology*, 398(1):91–100, 2011. doi: doi.org/10.1016/j.jhydrol.2010.12.012.

X. Li and S. Gao. *Precipitation modeling and quantitative analysis*. Springer Atmospheric Science. Springer, 2012. ISBN 9789400723818. doi: 10.1007/978-94-007-2381-8.

R. Lopes and N. Betrouni. Fractal and multifractal analysis: a review. *Medical Image Analysis*, 13(4):634–649, 2009.

S. Lovejoy. Area–perimeter relation for rain and cloud areas. *Science*, 216(4542):185–187, 1982.

S. Lovejoy and D. Schertzer. Multifractals, universality classes and satellite and radar measurements of cloud and rain fields. *Journal of Geophysical Research: Atmospheres*, 95 (D3):2021–2034, 1990. doi: 10.1029/JD095iD03p02021.

S. Lovejoy and D. Schertzer. *Multifractals and rain*, pages 61–103. Cambridge University Press, Cambridge, UK, 1995.

S. Lovejoy and D. Schertzer. *The weather and climate: emergent laws and multifractal cascades*. Cambridge University Press, 2013. ISBN 9781107018983.

B. Mandelbrot. *The fractal geometry of nature*. W. H. Freeman, 1982. ISBN 9780716711865.

B. Mandelbrot. Multifractal measures, especially for the geophysicist. *Pure and Applied Geophysics*, 131:5–42, 1989. doi: 10.1007/BF00874478.

B. Mapes, T. Warner, M. Xu, and A. Negri. Diurnal patterns of rainfall in northwestern South America. part I: Observations and context. *Monthly Weather Review*, 131(5):799–812, 2003. doi: 10.1175/1520-0493(2003)131⟨0799:DPORIN⟩2.0.CO;2.

D. Marzan, D. Schertzer, and S. Lovejoy. Causal space–time multifractal processes: predictability and forecasting of rain fields. *Journal of Geophysical Research*, 101:D21(26): 333–346, 1996.

M. Maskey, C. Puente, B. Sivakumar, and A. Cortis. Encoding daily rainfall records via adaptations of the fractal multifractal method. *Stochastic Environmental Research and Risk Assessment*, 30(7):1917–1931, 2016. doi: 10.1007/s00477-015-1201-7.

M. Maskey, C. Puente, and B. Sivakumar. Deterministic simulation of highly intermittent hydrologic time series. *Stochastic Environmental Research and Risk Assessment*, 31(10): 2719–2732, 2017. doi: 10.1007/s00477-016-1343-2.

J. Masoliver. *Random Processes*. World Scientific, 2017.

C. Meneveau and K. Sreenivasan. Simple multifractal cascade model for fully developed turbulence. *Physical Review Letters*, 59(13), 1987.

C. Meneveau and K. Sreenivasan. The multifractal nature of turbulent energy dissipation. *Journal of Fluid Mechanics*, 224(429-484):180, 1991.

Ó. Mesa. *¿Adónde va caer este globo?* Universidad Nacional de Colombia, Medellín, 2007.

Ó. Mesa. Fractales y caos en ingeniería con aplicaciones. Universidad Nacional de Colombia, 2016.

Ó. Mesa and V. Peñaranda. Complejidad de la estructura espacio-temporal de la precipitación. *Revista de la Academia Colombiana de Ciencias Exactas, Físicas y Naturales*, 39 (152):304–320, 2015. doi: 10.18257/raccefyn.196.

Ó. Mesa, G. Poveda, and L. Carvajal. *Introducción al clima de Colombia*. Universidad Nacional de Colombia, Medellín, 1997.

C. Muller. Impact of convective organization on the response of tropical precipitation extremes to warming. *Journal of Climate*, 26(14):5028–5043, 2013. doi: 10.1175/JCLI-D-12-00655.1.

C. Muller and I. Held. detailed investigation of the self-aggregation of convection in cloud-resolving simulations. *Journal of the Atmospheric Sciences*, 69(8):2551–2565, 2012. doi: 10.1175/JAS-D-11-0257.1.

C. Muller, L. Back, P. O'Gorman, and K. Emanuel. A model for the relationship between tropical precipitation and column water vapor. *Geophysical Research Letters*, 36(16), 2009. doi: 10.1029/2009GL039667.

K. Nagel and E. Raschke. Self-organizing criticality in cloud formation? *Physica A: Statistical Mechanics and its Applications*, 182(4):519–531, 1992. doi: http://dx.doi.org/10.1016/0378-4371(92)90018-L.

National Research Council. *Opportunities in the Hydrologic Sciences*. National Academy Press, 1991.

J. Neelin, O. Peters, and K. Hales. The transition to strong convection. *Journal of the Atmospheric Sciences*, 66(8):2367–2384, 2009.

K. Nordstrom and V. Gupta. Scaling statistics in a critical, nonlinear physical model of tropical oceanic rainfall. *Nonlinear Processes in Geophysics*, 10(6):531–543, 2003.

T. Over. *Modelling space-time mesoscale rainfal using random cascades*. PhD thesis, University of Colorado, 1995.

T. Over and V. Gupta. Statistical analysis of mesoscale rainfall: dependence of a random cascade generator on large–scale forcing. *Journal of Hydrology*, 33:1526–1542, 1994.

T. Over and V. Gupta. A space–time theory of mesoscale rainfall using random cascades. *Journal of Geophysical Research*, 101:26:319–331, 1996.

A. Parodi and K. Emanuel. a theory for buoyancy and velocity scales in deep moist convection. *Journal of the Atmospheric Sciences*, 66(11):3449–3463, 2009. doi: 10.1175/2009JAS3103.1.

A. Parodi, E. Foufoula-Georgiou, and K. Emanuel. Signature of microphysics on spatial rainfall statistics. *Journal of Geophysical Research: Atmospheres*, 116(D14), 2011. doi: 10.1029/2010JD015124.

A. Paschalis, P. Molnar, S. Fatichi, and P. Burlando. A stochastic model for high-resolution space-time precipitation simulation. *Water Resources Research*, 49(12):8400–8417, 2013. doi: 10.1002/2013WR014437.

V. Peñaranda. Representación geométrica de registros de precipitación puntual en Bogotácon el modelo Fractal–Multifractal. Master's thesis, Universidad Nacional de Colombia, Bogotá, 2008.

V. Peñaranda. Rainfall complex pattern trend via multifractal analysis. In P. Nachtnebel and K. Kovar, editors, *HydroEco'2011 Volume of Abstracts*. University of Natural Resources and Applied Life Sciences, Vienna (BOKU), International Commission on Groundwater (ICGW), of the International Association of Hydrological Sciences (IAHS), 2011.

S. Perica and E. Foufoula-Georgiou. Linkage of scaling and thermodynamic parameters of rainfall: Results from midlatitude mesoscale convective systems. *Journal of Geophysical Research*, 101:D3:7431–7448, 1996.

O. Peters and J. Neelin. Critical phenomena in atmospheric precipitation. *Nature Physics*, 2:393–396, 2006.

O. Peters and J. Neelin. Atmospheric convection as a continuous phase transition: further evidence. *International Journal of Modern Physics B*, 23(28-29):5453–5465, 2009.

G. Poveda and Ó. Mesa. Feedbacks between hydrological processes in tropical South America and large-scale ocean-atmospheric phenomena. *Journal of Climate*, 10(10):2690–2702, 1997.

C. Puente. A new approach to hydrologic modeling: derived distribution revisited. *Journal of Hydrology*, 187:65–80, 1995.

C. Puente and C. Obregon. A deterministic geometric representation of temporal rainfall: results for a storm in Boston. *Journal of Water Resources Research*, 32:2825–2839, 1996.

C. Puente and B. Sivakumar. Modeling geophysical complexity: a case for geometric determinism. *Hydrology and Earth System Sciences*, 11(2):721–724, 2007. doi: 10.5194/hess-11-721-2007.

C. Puente, O. Robayo, M. Díaz, and B. Sivakumar. A fractal-multifractal approach to groundwater contamination. 1. Modeling conservative tracers at the Borden site. *Stochastic Environmental Research and Risk Assessment*, 15(5):357–371, 2001. doi: 10.1007/PL00009791.

D. Randall. Why are cumulus updrafts narrow? Class Material, 2006.

D. Raymond and X. Zeng. Modelling tropical atmospheric convection in the context of the weak temperature gradient approximation. *Quarterly Journal of the Royal Meteorological Society*, 131(608):1301–1320, 2005. doi: 10.1256/qj.03.97.

D. Raymond, S. Sessions, A. Sobel, and Z. Fuchs. The mechanics of gross moist stability. *Journal of Advances in Modeling Earth Systems*, 1(3), 2009. doi: 10.3894/JAMES.2009.1.9.

I. Rodríguez-Iturbe. Exploring complexity in the structure of rainfall. *Advances in Water Resources*, 14(4):162–167, 1991.

I. Rodríguez-Iturbe, V. Gupta, and E. Waymire. Scale considerations in the modeling of temporal rainfall. *Water Resources Research*, 20(11):1611–1619, 1984.

I. Rodríguez-Iturbe, B. de Power, and J. Valdés. Rectangular pulses point process models for rainfall: analysis of empirical data. *Journal of Geophysical Research: Atmosphere*, 92 (D8):9645–9656, 1987.

S. Roux, A. Arnéodo, and N. Decoster. A wavelet-based method for multifractal image analysis. III. Applications to high-resolution satellite images of cloud structure. *The European Physical Journal B - Condensed Matter and Complex Systems*, 15(4):765–786, 2000. doi: 10.1007/s100510051180.

S. Roux, V. Venugopal, K. Fienberg, A. Arneodo, and E. Foufoula-Georgiou. Evidence for inherent nonlinearity in temporal rainfall. *Advances in Water Resources*, 32(1):41–48, 2009. doi: http://dx.doi.org/10.1016/j.advwatres.2008.09.007.

G. Rushbrooke. On the thermodynamics of the critical region for the Ising problem. *The Journal of Chemical Physics*, 39(3):842–843, 1963. doi: 10.1063/1.1734338.

A. Santos. Implementación de un modelo de autómata celular para el pronóstico de la precipitación espacial. Caso de estudio ciudad de Bogotá (Colombia). Master's thesis, Universidad Nacional de Colombia, Bogotá, 2011.

E. Sarachik and M. Cane. *The El Niño-Southern Oscillation Phenomenon*. Cambridge University Press, Cambridge, UK, 2010. ISBN 9780521847865.

D. Schertzer and S. Lovejoy. Physical modeling and analysis of rain and clouds by anisotropic scaling multiplicative processe. *Geophysical Research*, 92(D8):9693—9714, 1987a.

D. Schertzer and S. Lovejoy. Singularités, anisotropes, divergence des moments en turbulence: invariance de'échelle généralisée et processus multiplicatifs. *Annales des sciences mathématiques du Québec*, 11(1):139–181, 1987b.

Z. She, E. Aurell, and U. Frisch. The inviscid burgers equation with initial data of brownian type. *Communications in Mathematical Physics*, 148(3):623–641, 1992. doi: 10.1007/BF02096551.

J. Smith and A. Karr. Parameter estimation for a model of space-time rainfall. *Water Resources Research*, 21(8):1251–1257, 1985. doi: 10.1029/WR021i008p01251.

S. Soong and Y. Ogura. response of tradewind cumuli to large-scale processes. *Journal of the Atmospheric Sciences*, 37(9):2035–2050, 1980. doi: 10.1175/1520-0469(1980)037⟨2035:ROTCTL⟩2.0.CO;2.

S. Soong and W. Tao. Response of deep tropical cumulus clouds to mesoscale processes. *Journal of the Atmospheric Sciences*, 37(9):2016–2034, 1980.

D. Sornette. *Critical Phenomena in Natural Sciences, Chaos, Fractals, Self-organization and Disorder: Concepts and Tools*. Springer Series in Synergetics, 2004.

S. Strogatz. *Nonlinear dynamics and chaos: with applications to physics, biology, chemistry, and engineering*. Perseus Books Publishing, 1994.

C. Sui, K. Lau, W. Tao, and J. Simpson. The tropical water and energy cycles in a cumulus ensemble model. Part I: Equilibrium Climate. *Journal of the Atmospheric Sciences*, 51 (5):711–728, 1994. doi: 10.1175/1520-0469(1994)051⟨0711:TTWAEC⟩2.0.CO;2.

Y. Tessier, S. Lovejoy, P. Hubert, D. Schertzer, and S. Pecknold. Multifractal analysis and modeling of rainfall and river flows and scaling, causal transfer functions. *Journal of Geophysical Research: Atmospheres*, 101(D21):26427–26440, 1996. doi: 10.1029/96JD01799.

H. Touchette. The large deviation approach to statistical mechanics. *Physics Reports*, 478 (1):1–69, 2009. doi: https://doi.org/10.1016/j.physrep.2009.05.002.

Tropical Rainfall Measuring Mission. TRMM (TMPA) Rainfall Estimate L3 3 hour 0.25 degree x 0.25 degree V7, 2011.

A. Turing. The chemical basis of morphogenesis. *Philosophical Transactions of the Royal Society of London. Series B, Biological Sciences*, 237(641):37–72, 1952.

T. Ursell. Cahn–hilliard kinetics and spinodal decomposition in a diffuse system. Technical notes, 2007.

D. Veneziano and P. Furcolo. Multifractality of rainfall and scaling of intensity-duration-frequency curves. *Water Resources Research*, 38(12):42–1–42–12, 2002. doi: 10.1029/2001WR000372.

D. Veneziano, A. Langousis, and P. Furcolo. Multifractality and rainfall extremes: A review. *Water Resources Research*, 42(6), 2006. doi: 10.1029/2005WR004716.

V. Venugopal, E. Foufoula-Georgiou, and V. Sapozhnikov. Evidence of dynamic scaling in space–time rainfall. *Journal of Geophysical Research: Atmospheres*, 104(D24):31599–31610, 1999. doi: 10.1029/1999JD900437.

T. Vicsek and F. Family. Dynamic scaling for aggregation of clusters. *Physical Review Letters*, 52(19):1669–1672, 1984. doi: 10.1103/PhysRevLett.52.1669.

S. Vieira. Modelación de la precipitación convectiva en el Océano Pacífico colombiano. Master's thesis, Universidad Nacional de Colombia, Medellín, 2006.

J. Wallace and P. Hobbs. *Atmospheric science: an introductory survey*. Elsevier, 2006.

E. Waymire and V. Gupta. The mathematical structure of rainfall representations: 3. Some applications of the point process theory to rainfall processes. *Water Resources Research*, 17(5):1287–1294, 1981a. doi: 10.1029/WR017i005p01287.

E. Waymire and V. Gupta. The mathematical structure of rainfall representations: 1. A review of the stochastic rainfall models. *Water Resources Research*, 17(5):1261–1272, 1981b. doi: 10.1029/WR017i005p01261.

E. Waymire and V. Gupta. The mathematical structure of rainfall representations: 2. A review of the theory of point processes. *Water Resources Research*, 17(5):1273–1285, 1981c. doi: 10.1029/WR017i005p01273.

E. Waymire, V. Gupta, and I. Rodríguez-Iturbe. A spectral theory of rainfall intensity at the meso-β scale. *Water Resources Research*, 20(10):1453–1465, 1984. doi: 10.1029/WR020i010p01453.

B. Widom. Equation of state in the neighborhood of the critical point. *The Journal of Chemical Physics*, 43(11):3898–3905, 1965. doi: 10.1063/1.1696618.

D. Wilks. Multisite generalization of a daily stochastic precipitation generation model. *Journal of Hydrology*, 210(1):178–191, 1998. doi: https://doi.org/10.1016/S0022-1694(98)00186-3.

A. Wing and K. Emanuel. Physical mechanisms controlling self-aggregation of convection in idealized numerical modeling simulations. *Journal of Advances in Modeling Earth Systems*, 6(1):59–74, 2014. doi: 10.1002/2013MS000269.

T. Witten and L. Sander. Diffusion-limited aggregation, a kinetic critical phenomenon. *Physical Review Letters*, 47(19):1400–1403, 1981. doi: 10.1103/PhysRevLett.47.1400.

M. Yanai, S. Esbensen, and J. Chu. Determination of bulk properties of tropical cloud clusters from large-scale heat and moisture budgets. *Journal of the Atmospheric Sciences*, 30(4):611–627, 1973. doi: 10.1175/1520-0469(1973)030⟨0611:DOBPOT⟩2.0.CO;2.

K. Zybin and V. Sirota. Multifractal structure of fully developed turbulence. *Physical Review E*, 88(4), 2013.

A. Basics on Multifractal Spectrum

Mathematically, rainfall intensities can be defined as multifractal measures μ defined in $\mathbb{R}^d$ that have a singularity order α. Empirical rainfall measures are obtained through the division between the magnitude N_i of a $i-$th rainfall pulse and the total rainfall amount N developed during an specific recorded time:

$$\mu_i = \frac{N_i}{N}; \qquad \boldsymbol{\mathcal{M}} = \{\mu_i\}_{i=0}^{N-1}; \qquad M(x) = \sum_{i}^{x} \mu_i \tag{A-1}$$

where $M(x)$ is the accumulated measure function. So, rainfall intensities can then be re-defined as probability measures of a given aggregated state if:

$$p_i = \lim_{N\to\infty} \frac{N_i}{N} \tag{A-2}$$

Multifractal measures defined in $\mathbb{R}^d$ have a fractal dimension $f(\alpha)$ represented as follows

$$f(\alpha) = \{x \in \mathbf{R} : \mu(B_\delta(x)) \sim \delta^\alpha\} \quad \text{as} \quad \delta \to 0 \tag{A-3}$$

where $B_\delta(x)$ is a closed ball of radius $\delta > 0$ located at x, and the singularity order α is defined as:

$$\alpha = \lim_{\delta\to 0} \frac{\log \mu(B_\delta(x))}{\log \delta} \tag{A-4}$$

The singularity exponent α (also called "Hólder exponent") and the associated dimension $f(\alpha)$ define a distribution known as "singularity spectrum" or "multifractal spectrum". The multifractal formalism, applied to rainfall datasets, is simply a statistical description that provides global information on the self-similarity properties of rainfall patterns. For its practical implementation is necessary to calculate the statistical moments, defined by:

$$M_q(\delta) = \frac{1}{N(\delta)} \sum_{n=1}^{N(\delta)} \mu_n^q \tag{A-5}$$

where q is the order of the moment, $N(\delta)$ is the total number of non-empty boxes and $\mu_n \equiv T(x, \delta)$ is also called multi-resolution coefficient which capture the fluctuations in the time series at the scale δ.

B. High–Resolution Punctual Rainfall Records Analysis

B.1. Rainfall Time Series Plots

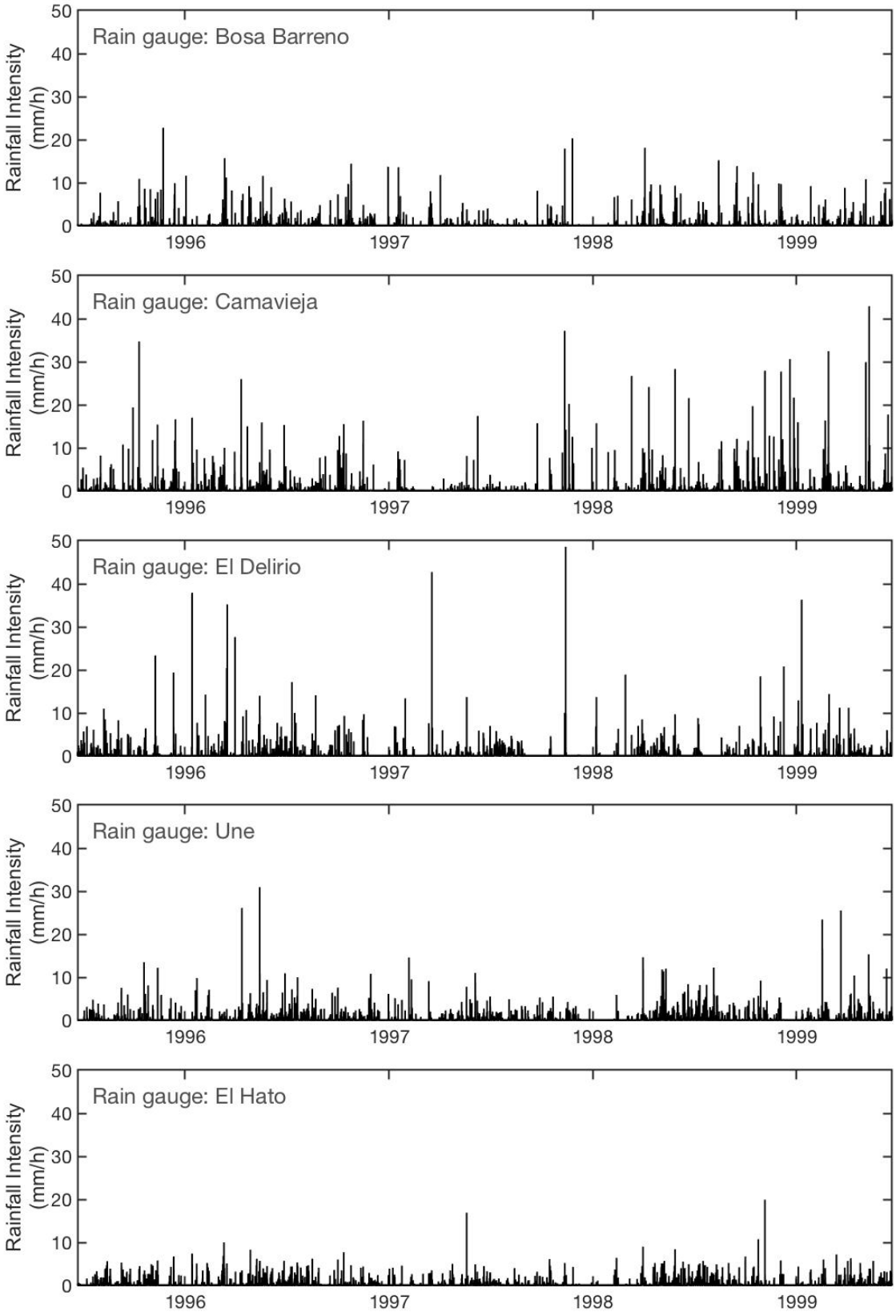

Figure B-1: Plots of the rainfall time series indicated at table 3-1.

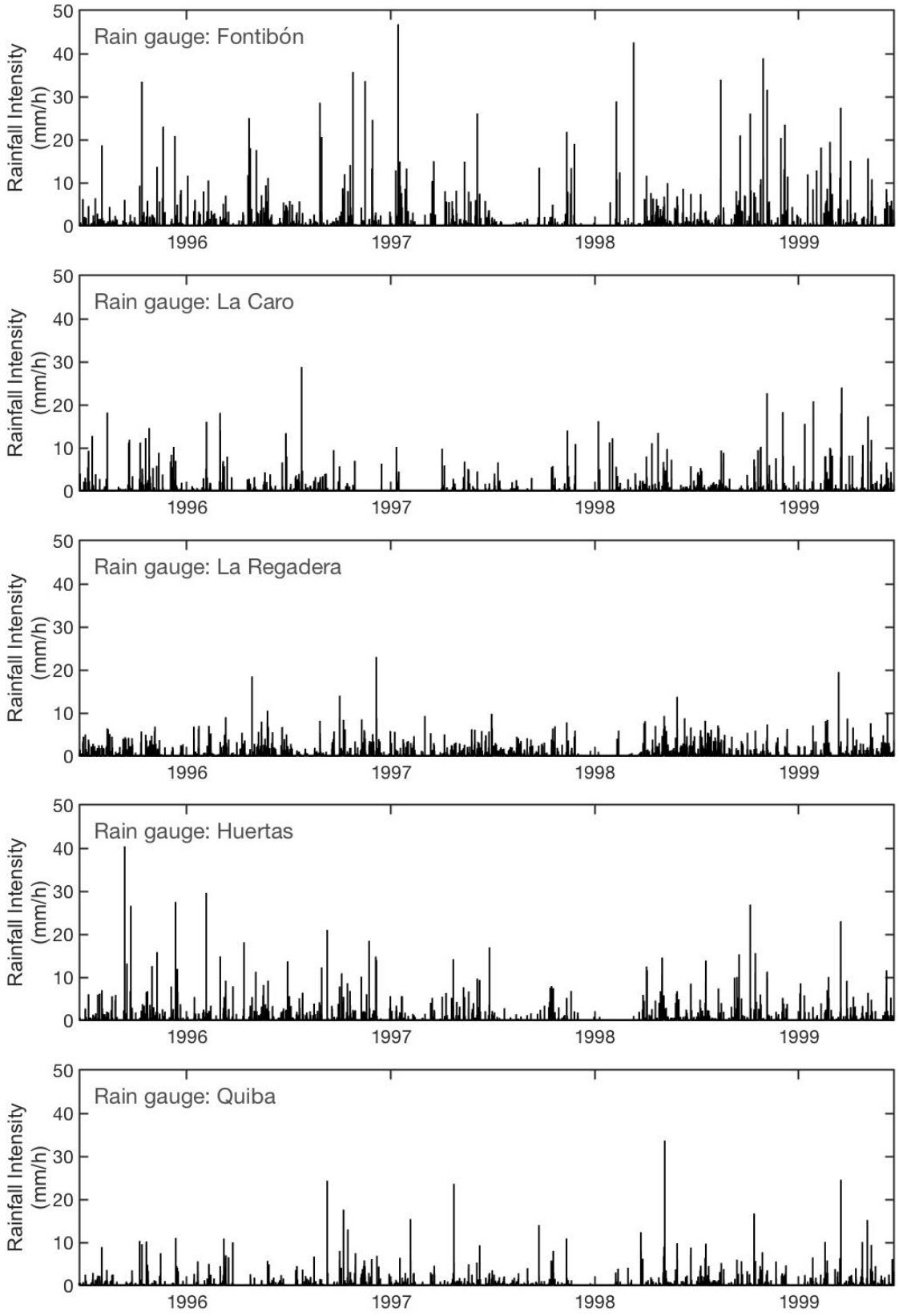

Figure B-2: Plots of the rainfall time series indicated at table 3-1

.

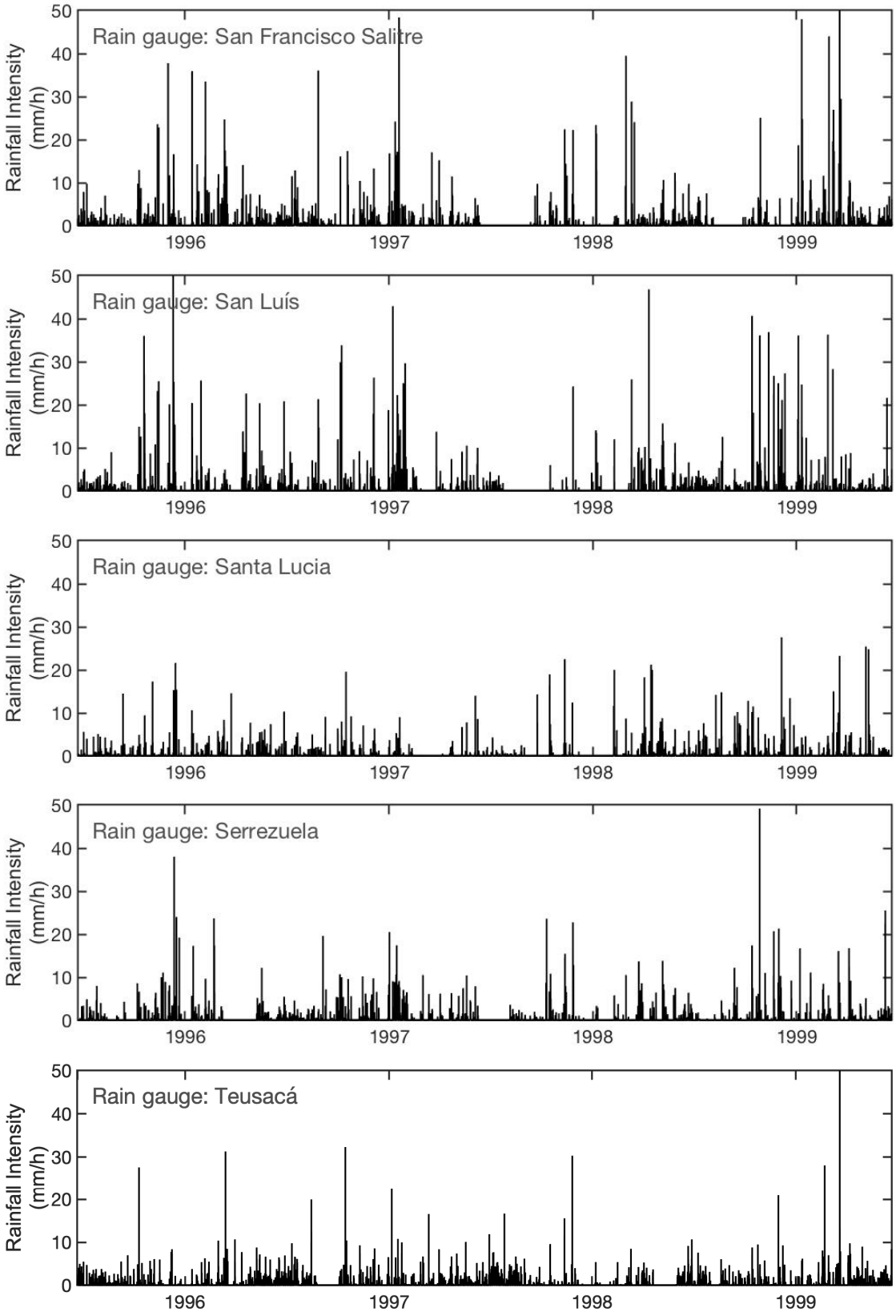

Figure B-3: Plots of the rainfall time series indicated at table 3-1

.

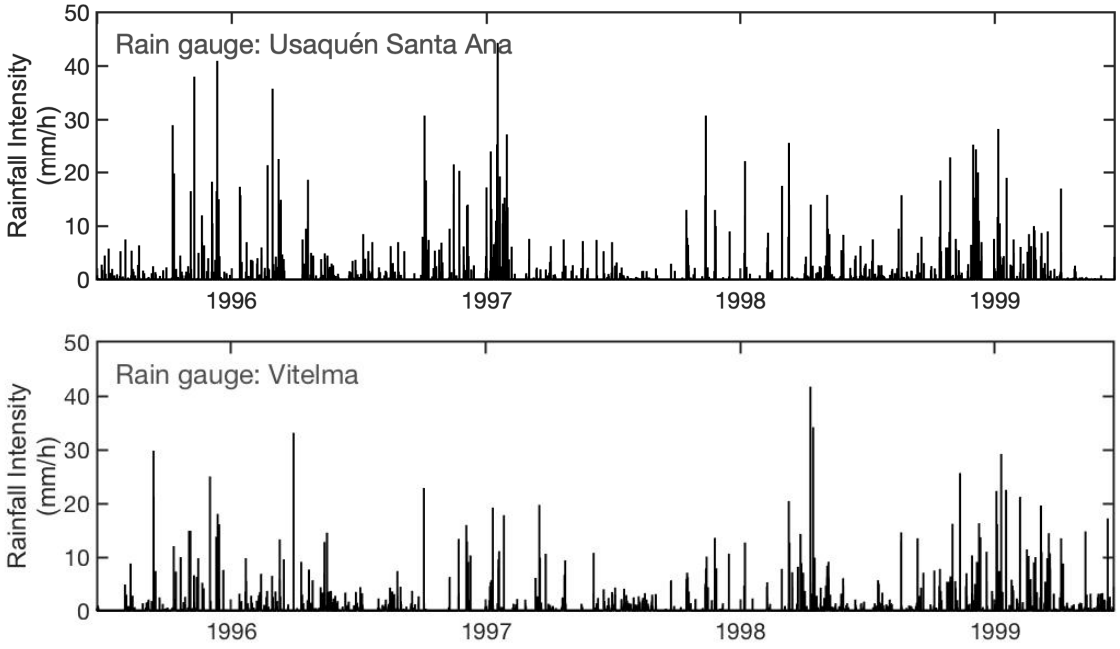

Figure B-4: Plots of the rainfall time series indicated at table 3-1

.

B.2. Multifractal Analysis Statistics

Table B-1: Distance among the rain–gauges identified at Table 3-1. These values are expressed in kilometers.

	RG 1	RG 2	RG 3	RG 4	RG 5	RG 6	RG 7	RG 8	RG 9	RG 10	RG 11	RG 12	RG 13	RG 14	RG 15	RG 16	RG 17
RG 1	0.00	10.54	15.78	25.10	6.88	32.33	23.64	7.24	9.80	16.65	16.43	8.26	25.24	25.31	28.97	19.59	13.26
RG 2	10.54	0.00	9.57	28.41	6.98	26.43	25.47	17.66	14.11	7.44	5.93	6.92	17.28	14.79	25.65	9.90	6.28
RG 3	15.78	9.57	0.00	22.24	15.73	34.45	18.51	21.18	12.36	5.06	10.84	7.58	24.38	16.38	16.15	15.94	3.30
RG 4	25.10	28.41	22.24	0.00	30.56	54.81	4.31	23.51	15.51	27.26	32.35	21.62	45.53	38.59	17.02	37.44	23.92
RG 5	6.88	6.98	15.73	30.56	0.00	25.52	28.43	13.73	15.08	14.41	11.77	9.97	18.47	20.35	31.16	13.65	12.51
RG 6	32.33	26.43	34.45	54.81	25.52	0.00	51.89	38.55	39.92	29.82	23.67	33.20	10.46	23.02	49.99	18.75	31.72
RG 7	23.64	25.47	18.51	4.31	28.43	51.89	0.00	23.32	13.84	23.57	28.95	18.94	42.32	34.73	13.02	34.08	20.50
RG 8	7.24	17.66	21.18	23.51	13.73	38.55	23.32	0.00	10.96	23.10	23.58	13.77	32.19	32.45	31.61	26.83	19.29
RG 9	9.80	14.11	12.36	15.51	15.08	39.92	13.84	10.96	0.00	16.06	19.25	7.30	31.32	27.22	20.66	23.91	11.93
RG 10	16.65	7.44	5.06	27.26	14.41	29.82	23.57	23.10	16.06	0.00	6.19	9.56	19.57	11.49	20.24	11.12	4.15
RG 11	16.43	5.93	10.84	32.35	11.77	23.67	28.95	23.58	19.25	6.19	0.00	11.97	13.54	8.89	26.43	5.14	8.45
RG 12	8.26	6.92	7.58	21.62	9.97	33.20	18.94	13.77	7.30	9.56	11.97	0.00	24.20	20.17	21.42	16.62	5.56
RG 13	25.24	17.28	24.38	45.53	18.47	10.46	42.32	32.19	31.32	19.57	13.54	24.20	0.00	12.91	39.63	8.46	21.88
RG 14	25.31	14.79	16.38	38.59	20.35	23.02	34.73	32.45	27.22	11.49	8.89	20.17	12.91	0.00	28.97	7.71	15.42
RG 15	28.97	25.65	16.15	17.02	31.16	49.99	13.02	31.61	20.66	20.24	26.43	21.42	39.63	28.97	0.00	31.24	19.38
RG 16	19.59	9.90	15.94	37.44	13.65	18.75	34.08	26.83	23.91	11.12	5.14	16.62	8.46	7.71	31.24	0.00	13.58
RG 17	13.26	6.28	3.30	23.92	12.51	31.72	20.50	19.29	11.93	4.15	8.45	5.56	21.88	15.42	19.38	13.58	0.00

Table B-2: Spatial gradient of D_0 values (dimension of the geometrical support) which were estimated among the rain–gauges identified at Table 3-1. These values are expressed in 10^{-3} km^{-1}.

	RG 1	RG 2	RG 3	RG 4	RG 5	RG 6	RG 7	RG 8	RG 9	RG 10	RG 11	RG 12	RG 13	RG 14	RG 15	RG 16	RG 17
RG 1	0.00	-0.85	-1.64	-1.76	2.86	0.31	-2.31	3.56	-0.42	-1.43	0.81	-3.59	-0.18	-3.45	-1.65	-0.52	-1.42
RG 2	0.85	0.00	-1.77	-1.24	4.11	0.72	-1.79	1.97	0.34	-1.99	3.74	-2.99	0.26	-5.29	-1.51	-0.13	-1.57
RG 3	1.64	1.77	0.00	-0.82	2.90	1.05	-1.55	2.44	1.76	0.42	3.61	-0.49	0.88	-3.75	-1.35	0.99	2.16
RG 4	1.76	1.24	0.82	0.00	2.09	0.99	-2.43	2.97	2.57	0.74	1.77	0.67	0.87	-1.12	-0.21	0.90	1.06
RG 5	-2.86	-4.11	-2.90	-2.09	0.00	-0.38	-2.61	0.44	-1.58	-3.02	-0.55	-4.95	-1.31	-5.26	-2.16	-2.19	-3.08
RG 6	-0.31	-0.72	-1.05	-0.99	0.38	0.00	-1.25	0.41	-0.36	-1.14	0.13	-1.20	-1.39	-4.23	-1.16	-1.08	-0.91
RG 7	2.31	1.79	1.55	2.43	2.61	1.25	0.00	3.44	3.64	1.31	2.34	1.31	1.18	-0.94	0.52	1.30	1.74
RG 8	-3.56	-1.97	-2.44	-2.97	-0.44	-0.41	-3.44	0.00	-2.73	-2.15	-0.53	-4.03	-0.94	-3.48	-2.32	-1.34	-2.31
RG 9	0.42	-0.34	-1.76	-2.57	1.58	0.36	-3.64	2.73	0.00	-1.22	0.90	-3.50	-0.01	-3.05	-2.11	-0.25	-1.23
RG 10	1.43	1.99	-0.42	-0.74	3.02	1.14	-1.31	2.15	1.22	0.00	5.98	-0.61	0.99	-5.52	-1.18	1.22	1.20
RG 11	-0.81	-3.74	-3.61	-1.77	0.55	-0.13	-2.34	0.53	-0.90	-5.98	0.00	-3.58	-1.31	-11.31	-2.31	-4.56	-3.79
RG 12	3.59	2.99	0.49	-0.67	4.95	1.20	-1.31	4.03	3.50	0.61	3.58	0.00	1.04	-2.86	-0.84	1.17	1.95
RG 13	0.18	-0.26	-0.88	-0.87	1.31	1.39	-1.18	0.94	0.01	-0.99	1.31	-1.04	0.00	-6.41	-1.09	-0.68	-0.66
RG 14	3.45	5.29	3.75	1.12	5.26	4.23	0.94	3.48	3.05	5.52	11.31	2.86	6.41	0.00	1.37	9.99	4.44
RG 15	1.65	1.51	1.35	0.21	2.16	1.16	-0.52	2.32	2.11	1.18	2.31	0.84	1.09	-1.37	0.00	1.20	1.49
RG 16	0.52	0.13	-0.99	-0.90	2.19	1.08	-1.30	1.34	0.25	-1.22	4.56	-1.17	0.68	-9.99	-1.20	0.00	-0.63
RG 17	1.42	1.57	-2.16	-1.06	3.08	0.91	-1.74	2.31	1.23	-1.20	3.79	-1.95	0.66	-4.44	-1.49	0.63	0.00

Table B-3: Spatial gradient of D_1 (dimension of the concentrated measure) values which were estimated among the rain–gauges identified at Table 3-1. These values are expressed in 10^{-3} km^{-1}.

	RG 1	RG 2	RG 3	RG 4	RG 5	RG 6	RG 7	RG 8	RG 9	RG 10	RG 11	RG 12	RG 13	RG 14	RG 15	RG 16	RG 17
RG 1	0.00	-0.20	-1.43	-2.34	4.17	0.63	-2.79	3.43	-0.94	-0.64	1.32	-1.45	0.41	-3.60	-2.07	0.18	-0.61
RG 2	0.20	0.00	-2.15	-1.99	4.41	0.85	-2.50	1.52	-0.51	-1.15	4.01	-1.42	0.72	-6.02	-2.26	0.58	-0.95
RG 3	1.43	2.15	0.00	-1.62	3.26	1.25	-2.34	2.24	1.08	2.37	4.09	1.41	1.35	-4.19	-2.31	1.65	4.41
RG 4	2.34	1.99	1.62	0.00	2.86	1.44	-1.68	3.55	3.19	1.76	2.48	2.16	1.51	-0.84	-0.08	1.66	2.11
RG 5	-4.17	-4.41	-3.26	-2.86	0.00	-0.32	-3.32	-0.28	-2.51	-2.73	-0.59	-4.07	-0.99	-5.89	-2.84	-1.83	-2.94
RG 6	-0.63	-0.85	-1.25	-1.44	0.32	0.00	-1.66	0.11	-0.74	-1.04	0.05	-0.97	-0.97	-4.85	-1.61	-0.90	-0.90
RG 7	2.79	2.50	2.34	1.68	3.32	1.66	0.00	3.89	4.09	2.34	3.02	2.85	1.80	-0.73	0.45	2.04	2.82
RG 8	-3.43	-1.52	-2.24	-3.55	0.28	-0.11	-3.89	0.00	-3.11	-1.53	-0.13	-2.67	-0.45	-3.57	-2.68	-0.79	-1.70
RG 9	0.94	0.51	-1.08	-3.19	2.51	0.74	-4.09	3.11	0.00	-0.09	1.61	-0.37	0.62	-3.01	-2.46	0.54	0.10
RG 10	0.64	1.15	-2.37	-1.76	2.73	1.04	-2.34	1.53	0.09	0.00	5.22	-0.14	1.07	-7.01	-2.44	1.28	0.61
RG 11	-1.32	-4.01	-4.09	-2.48	0.59	-0.05	-3.02	0.13	-1.61	-5.22	0.00	-2.81	-0.84	-12.70	-3.09	-3.51	-3.52
RG 12	1.45	1.42	-1.41	-2.16	4.07	0.97	-2.85	2.67	0.37	0.14	2.81	0.00	0.92	-3.93	-2.24	0.94	0.69
RG 13	-0.41	-0.72	-1.35	-1.51	0.99	0.97	-1.80	0.45	-0.62	-1.07	0.84	-0.92	0.00	-7.86	-1.77	-0.79	-0.84
RG 14	3.60	6.02	4.19	0.84	5.89	4.85	0.73	3.57	3.01	7.01	12.70	3.93	7.86	0.00	1.08	12.29	5.39
RG 15	2.07	2.26	2.31	0.08	2.84	1.61	-0.45	2.68	2.46	2.44	3.09	2.24	1.77	-1.08	0.00	2.03	2.68
RG 16	-0.18	-0.58	-1.65	-1.66	1.83	0.90	-2.04	0.79	-0.54	-1.28	3.51	-0.94	0.79	-12.29	-2.03	0.00	-0.86
RG 17	0.61	0.95	-4.41	-2.11	2.94	0.90	-2.82	1.70	-0.10	-0.61	3.52	-0.69	0.84	-5.39	-2.68	0.86	0.00

Table B-4: Spatial gradient of D_2 (correlation dimension) values which were estimated among the rain–gauges identified at Table 3-1. These values are expressed in 10^{-3} km^{-1}.

	RG 1	RG 2	RG 3	RG 4	RG 5	RG 6	RG 7	RG 8	RG 9	RG 10	RG 11	RG 12	RG 13	RG 14	RG 15	RG 16	RG 17
RG 1	0.00	2.04	2.72	-3.36	10.10	0.91	-3.05	7.70	1.43	4.31	3.59	0.89	1.15	-1.64	-1.90	1.34	0.82
RG 2	-2.04	0.00	2.24	-3.72	6.87	0.30	-3.68	1.94	-0.53	6.75	6.33	-2.05	0.43	-4.27	-2.98	0.48	-1.69
RG 3	-2.72	-2.24	0.00	-5.72	1.69	-0.39	-6.22	0.61	-2.34	5.69	1.48	-4.70	-0.57	-5.17	-6.06	-1.05	-9.71
RG 4	3.36	3.72	5.72	0.00	5.03	2.07	2.81	5.96	6.33	5.72	4.43	4.24	2.49	1.10	1.72	2.95	3.98
RG 5	-10.10	-6.87	-1.69	-5.03	0.00	-1.57	-4.98	-1.00	-3.68	0.16	-0.89	-6.23	-2.19	-5.46	-3.99	-3.16	-4.68
RG 6	-0.91	-0.30	0.39	-2.07	1.57	0.00	-1.96	0.68	-0.39	1.42	1.25	-0.67	-0.05	-3.09	-1.69	-0.17	-0.59
RG 7	3.05	3.68	6.22	-2.81	4.98	1.96	0.00	5.49	6.22	6.10	4.53	4.20	2.39	0.88	1.31	2.89	4.05
RG 8	-7.70	-1.94	-0.61	-5.96	1.00	-0.68	-5.49	0.00	-3.81	0.69	0.14	-3.52	-0.83	-3.00	-3.50	-1.10	-2.33
RG 9	-1.43	0.53	2.34	-6.33	3.68	0.39	-6.22	3.81	0.00	3.60	2.34	-0.91	0.48	-2.04	-3.34	0.51	-0.26
RG 10	-4.31	-6.75	-5.69	-5.72	-0.16	-1.42	-6.10	-0.69	-3.60	0.00	-2.06	-6.73	-2.18	-9.86	-6.26	-4.09	-14.68
RG 11	-3.59	-6.33	-1.48	-4.43	0.89	-1.25	-4.53	-0.14	-2.34	2.06	0.00	-4.32	-2.22	-11.32	-4.31	-6.37	-5.69
RG 12	-0.89	2.05	4.70	-4.24	6.23	0.67	-4.20	3.52	0.91	6.73	4.32	0.00	0.89	-2.43	-2.91	1.14	0.64
RG 13	-1.15	-0.43	0.57	-2.49	2.19	0.05	-2.39	0.83	-0.48	2.18	2.22	-0.89	0.00	-5.47	-2.12	-0.32	-0.83
RG 14	1.64	4.27	5.17	-1.10	5.46	3.09	-0.88	3.00	2.04	9.86	11.32	2.43	5.47	0.00	-0.46	8.80	3.41
RG 15	1.90	2.98	6.06	-1.72	3.99	1.69	-1.31	3.50	3.34	6.26	4.31	2.91	2.12	0.46	0.00	2.60	3.40
RG 16	-1.34	-0.48	1.05	-2.95	3.16	0.17	-2.89	1.10	-0.51	4.09	6.37	-1.14	0.32	-8.80	-2.60	0.00	-1.13
RG 17	-0.82	1.69	9.71	-3.98	4.68	0.59	-4.05	2.33	0.26	14.68	5.69	-0.64	0.83	-3.41	-3.40	1.13	0.00

B.3. 2-Point Correlation Functions

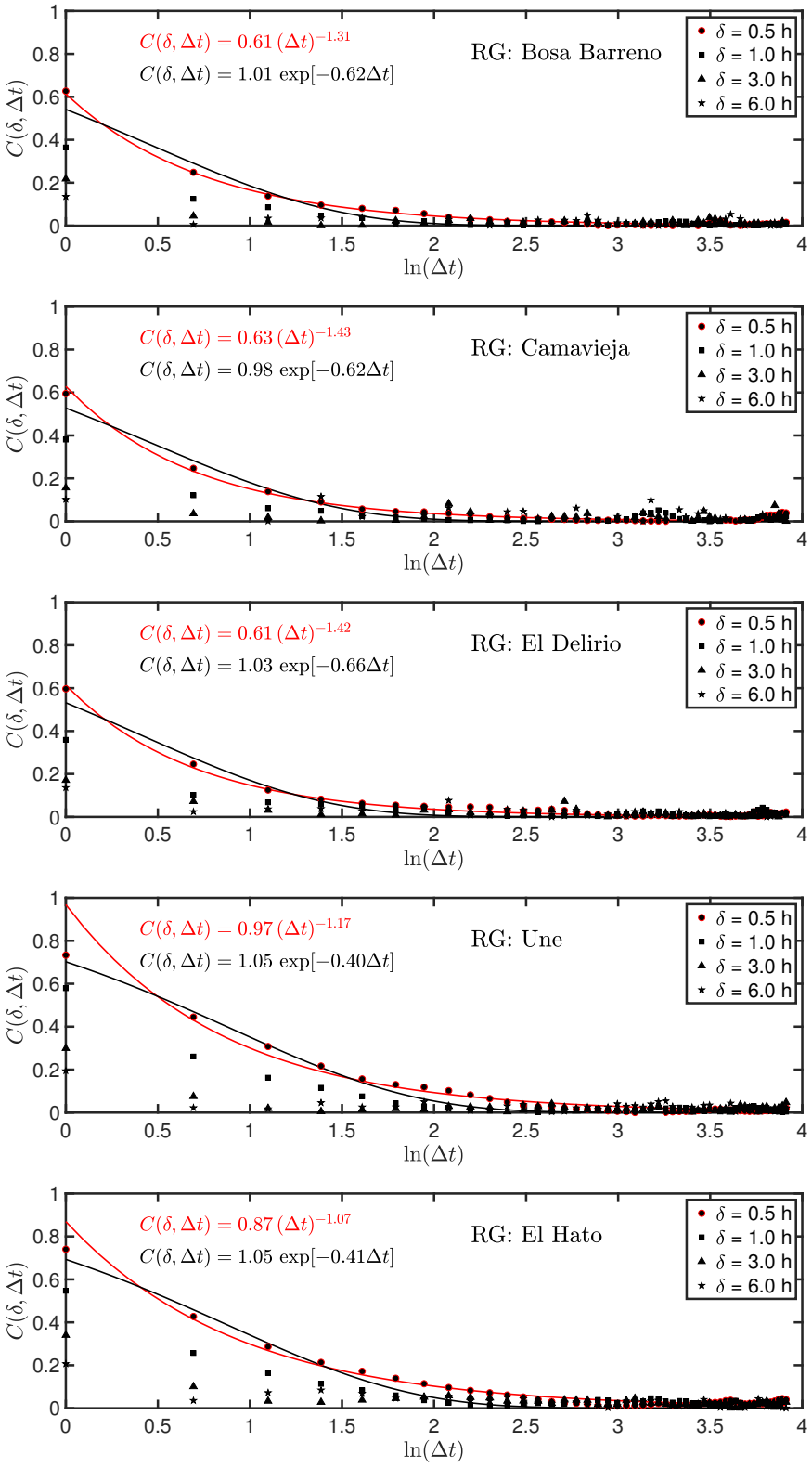

Figure B-5: Two-point correlation plot ($C(\delta,\Delta t)$ vs $\ln(\Delta t)$) for the rainfall time series indicated at table 3-1 and $\delta = \{0.5, 1.0, 3.0, 6.0\}$ h. Every frame in the plot exhibits a regression fit for the potential and exponential models.

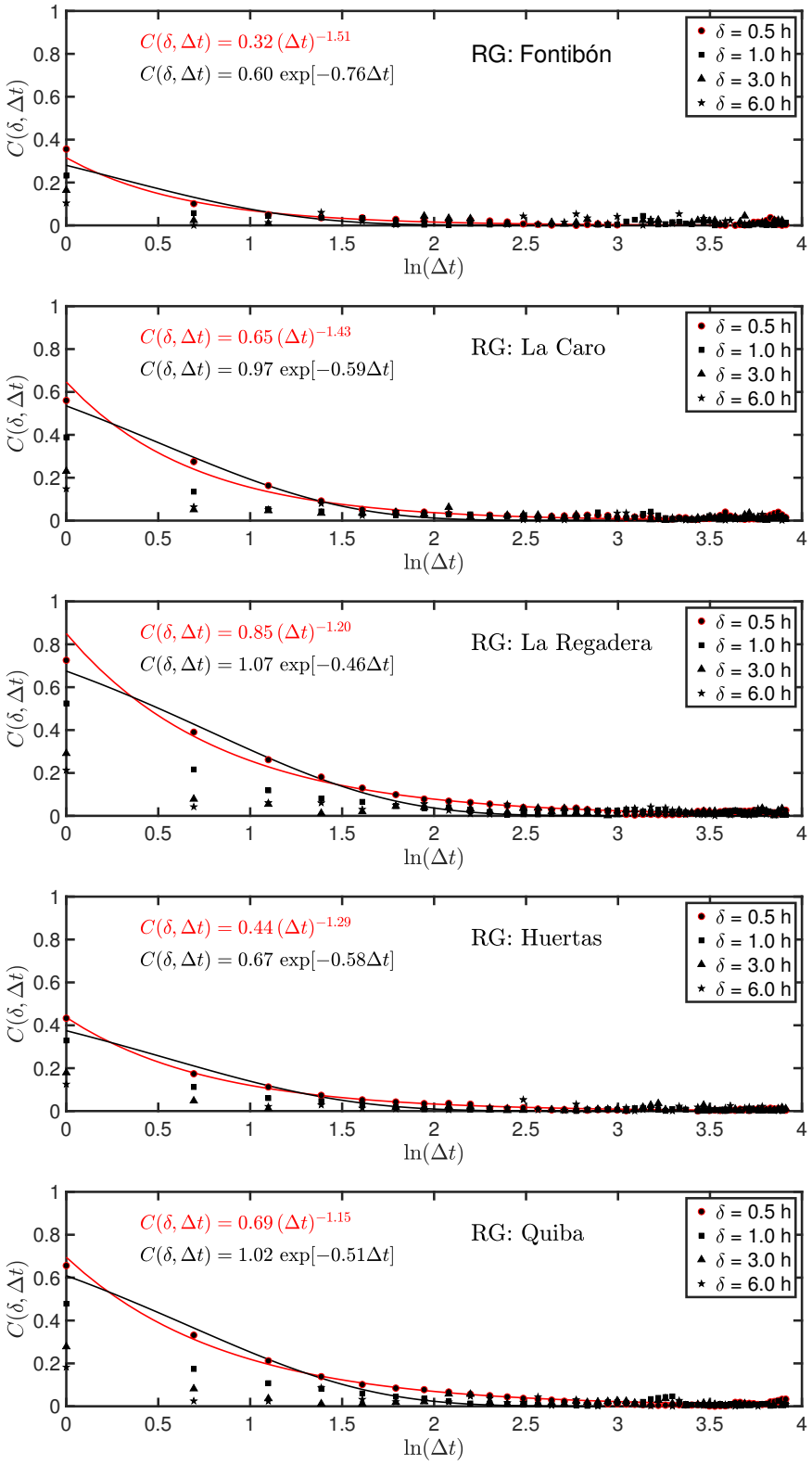

Figure B-6: Two-point correlation plot ($C(\delta,\Delta t)$ vs $\ln(\Delta t)$) for the rainfall time series indicated at table 3-1 and $\delta = \{0.5, 1.0, 3.0, 6.0\}$ h. Every frame in the plot exhibits a regression fit for the potential and exponential models.

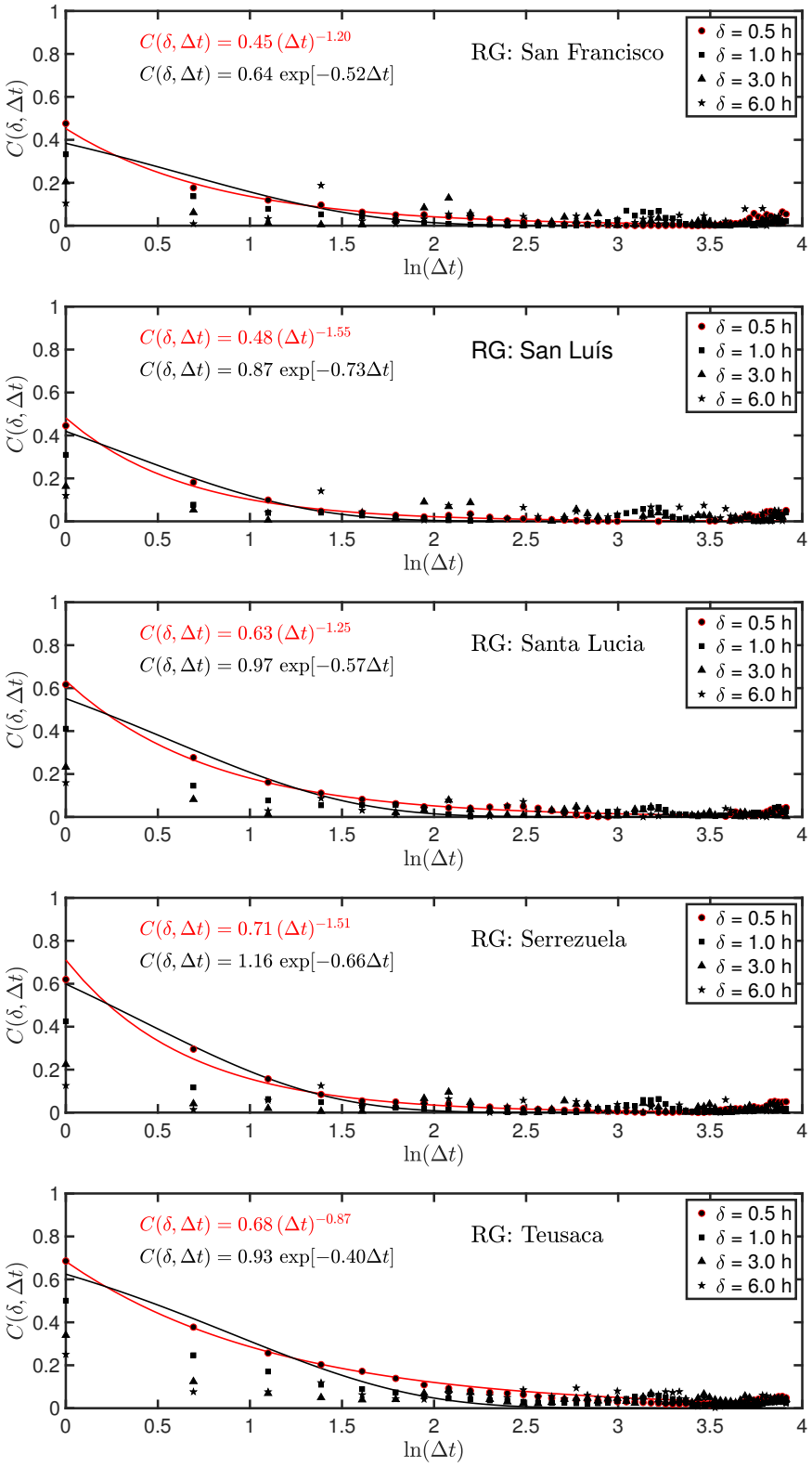

Figure B-7: Two-point correlation plot ($C(\delta,\Delta t)$ vs $\ln(\Delta t)$) for the rainfall time series indicated at table 3-1 and $\delta = \{0.5, 1.0, 3.0, 6.0\}$ h. Every frame in the plot exhibits a regression fit for the potential and exponential models.

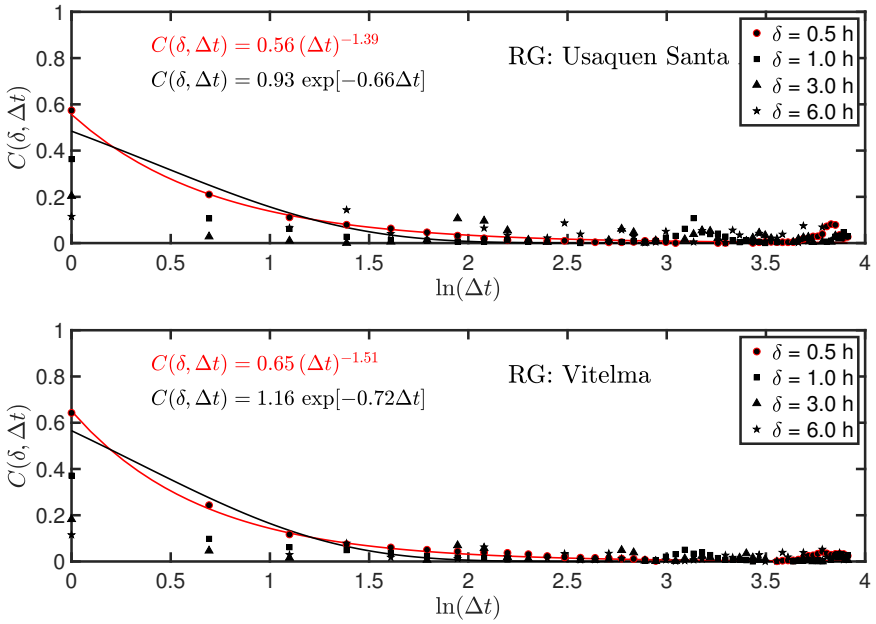

Figure B-8: Two-point correlation plot ($C(\delta, \Delta t)$ vs $\ln(\Delta t)$) for the rainfall time series indicated at table 3-1 and $\delta = \{0.5, 1.0, 3.0, 6.0\}$ h. Every frame in the plot exhibits a regression fit for the potential and exponential models.

B.4. Incremental Similarity Analysis – PDFs

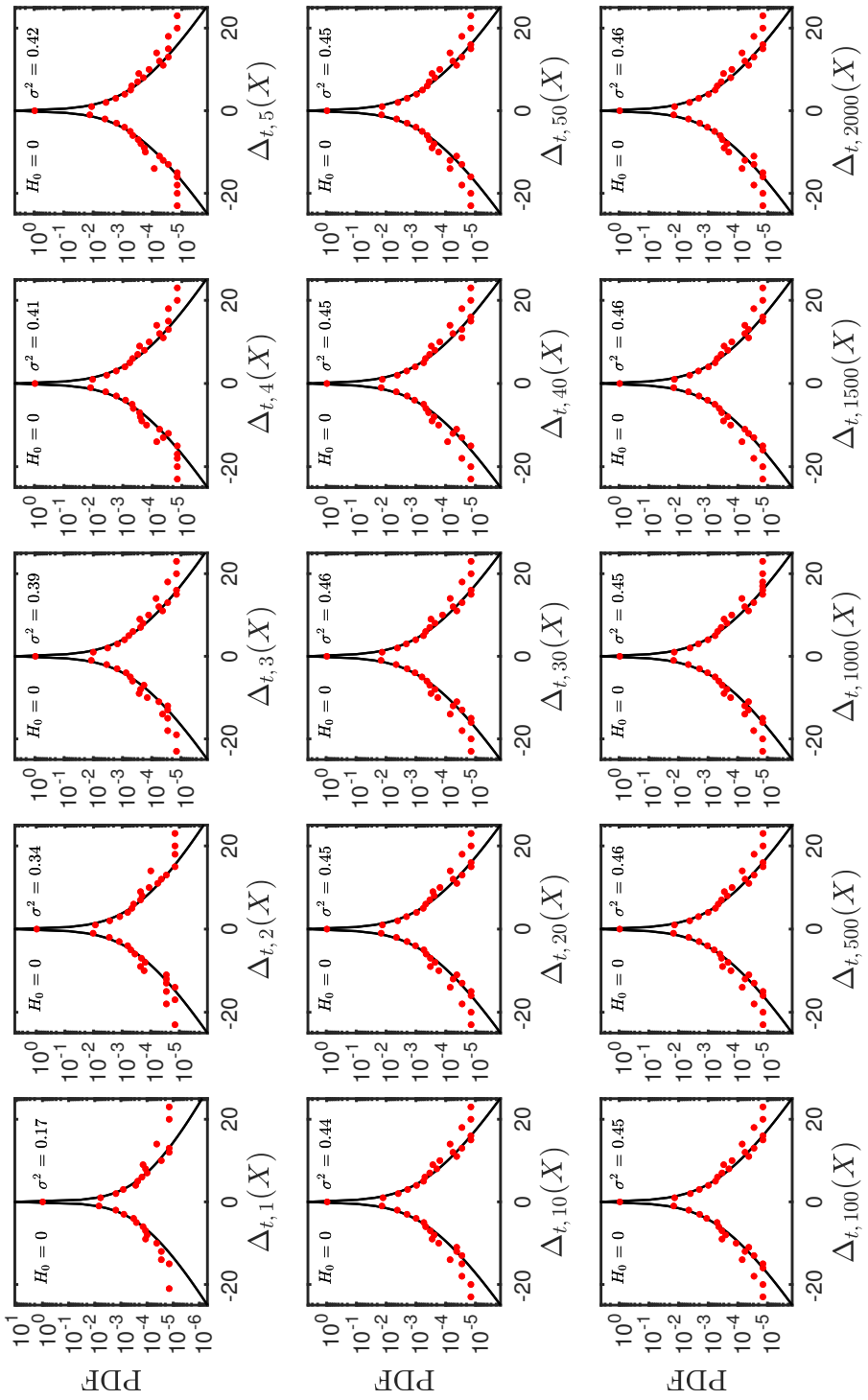

Figure B-9: Probability density function of the increments $\Delta_{t,u}$ of the rainfall time series recorded at gauge Bosa Barreno (RG1) for $u = \{1, 2, 3, 4, 5, 10, 20, 30, 40, 50, 100, 500, 1000, 1500, 2000\}$. The red dots represents the empirical PDF corresponding to the observations from the raingauge and the solid line represents the normal inverse Gaussian distribution for fitted to the rainfall data set. In each frame is indicated the value of null hypothesis H_0 (zero for the acceptance of H_0 and one for the rejection of H_0; both values for a 5% of significance level α). The null hypothesis states the data come from a normal inverse Gaussian distribution.

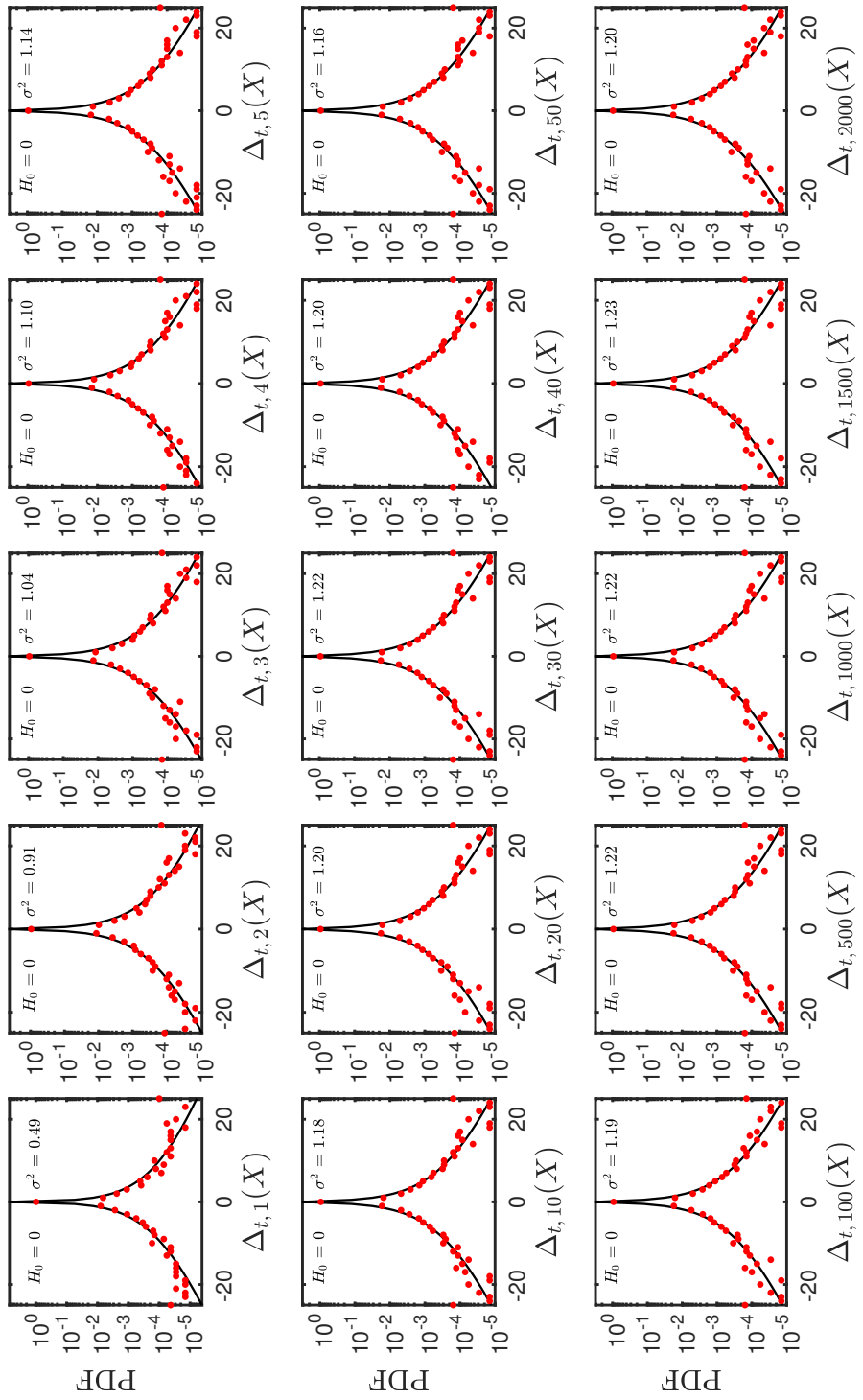

Figure B-10: Probability density function of the increments $\Delta_{t,u}$ of the rainfall time series recorded at gauge Camavieja (RG2) for $u = \{1, 2, 3, 4, 5, 10, 20, 30, 40, 50, 100, 500, 1000, 1500, 2000\}$. The red dots represents the empirical PDF corresponding to the observations from the raingauge and the solid line represents the normal inverse Gaussian distribution for fitted to the rainfall data set. In each frame is indicated the value of null hypothesis H_0 (zero for the acceptance of H_0 and one for the rejection of H_0; both values for a 5% of significance level α). The null hypothesis states the data come from a normal inverse Gaussian distribution.

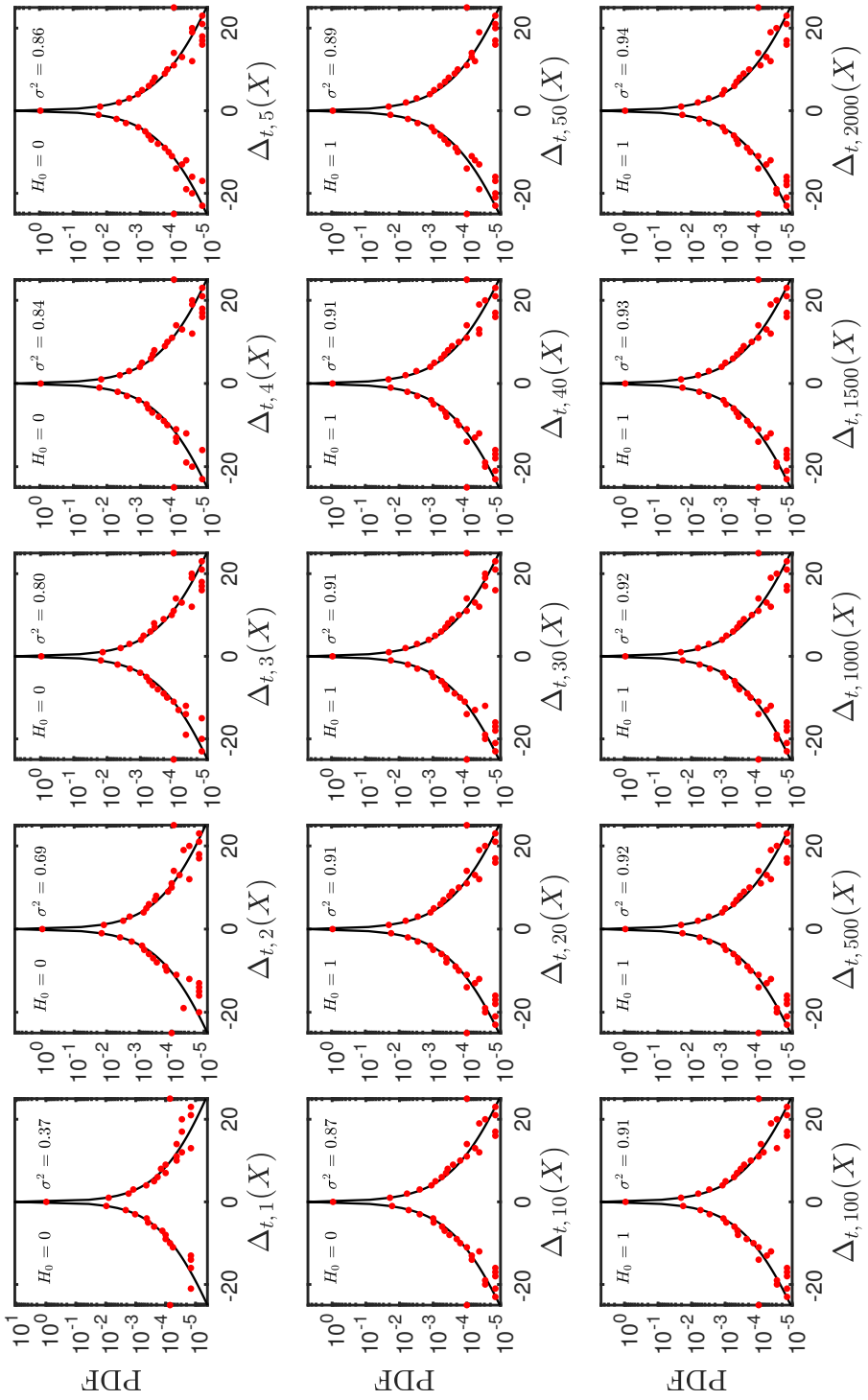

Figure B-11: Probability density function of the increments $\Delta_{t,u}$ of the rainfall time series recorded at gauge El Delirio (RG3) for $u = \{1, 2, 3, 4, 5, 10, 20, 30, 40, 50, 100, 500, 1000, 1500, 2000\}$. The red dots represents the empirical PDF corresponding to the observations from the raingauge and the solid line represents the normal inverse Gaussian distribution for fitted to the rainfall data set. In each frame is indicated the value of null hypothesis H_0 (zero for the acceptance of H_0 and one for the rejection of H_0; both values for a 5% of significance level α). The null hypothesis states the data come from a normal inverse Gaussian distribution.

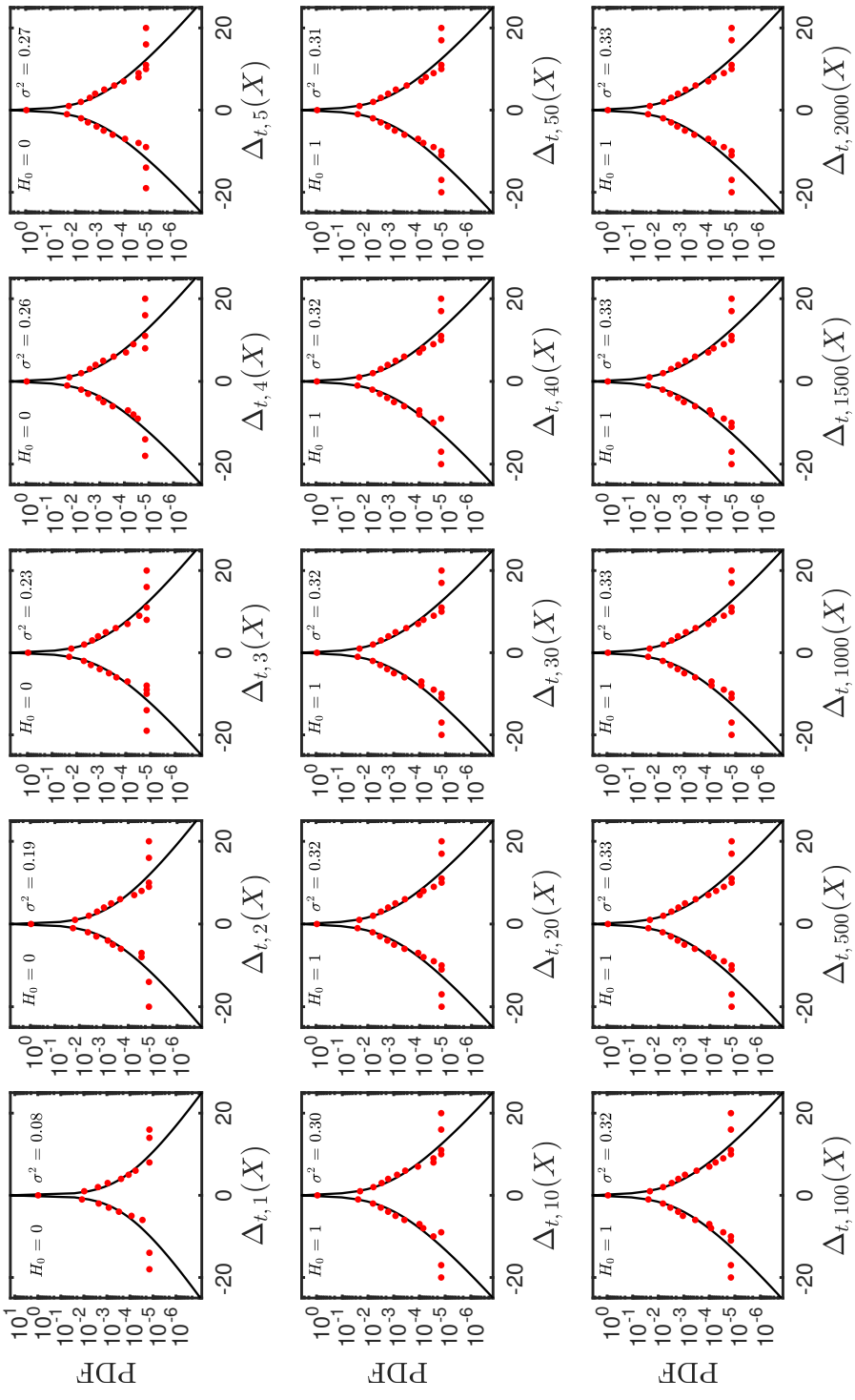

Figure B-12: Probability density function of the increments $\Delta_{t,u}$ of the rainfall time series recorded at gauge El Hato (RG4) for $u = \{1, 2, 3, 4, 5, 10, 20, 30, 40, 50, 100, 500, 1000, 1500, 2000\}$. The red dots represents the empirical PDF corresponding to the observations from the raingauge and the solid line represents the normal inverse Gaussian distribution for fitted to the rainfall data set. In each frame is indicated the value of null hypothesis H_0 (zero for the acceptance of H_0 and one for the rejection of H_0; both values for a 5% of significance level α). The null hypothesis states the data come from a normal inverse Gaussian distribution.

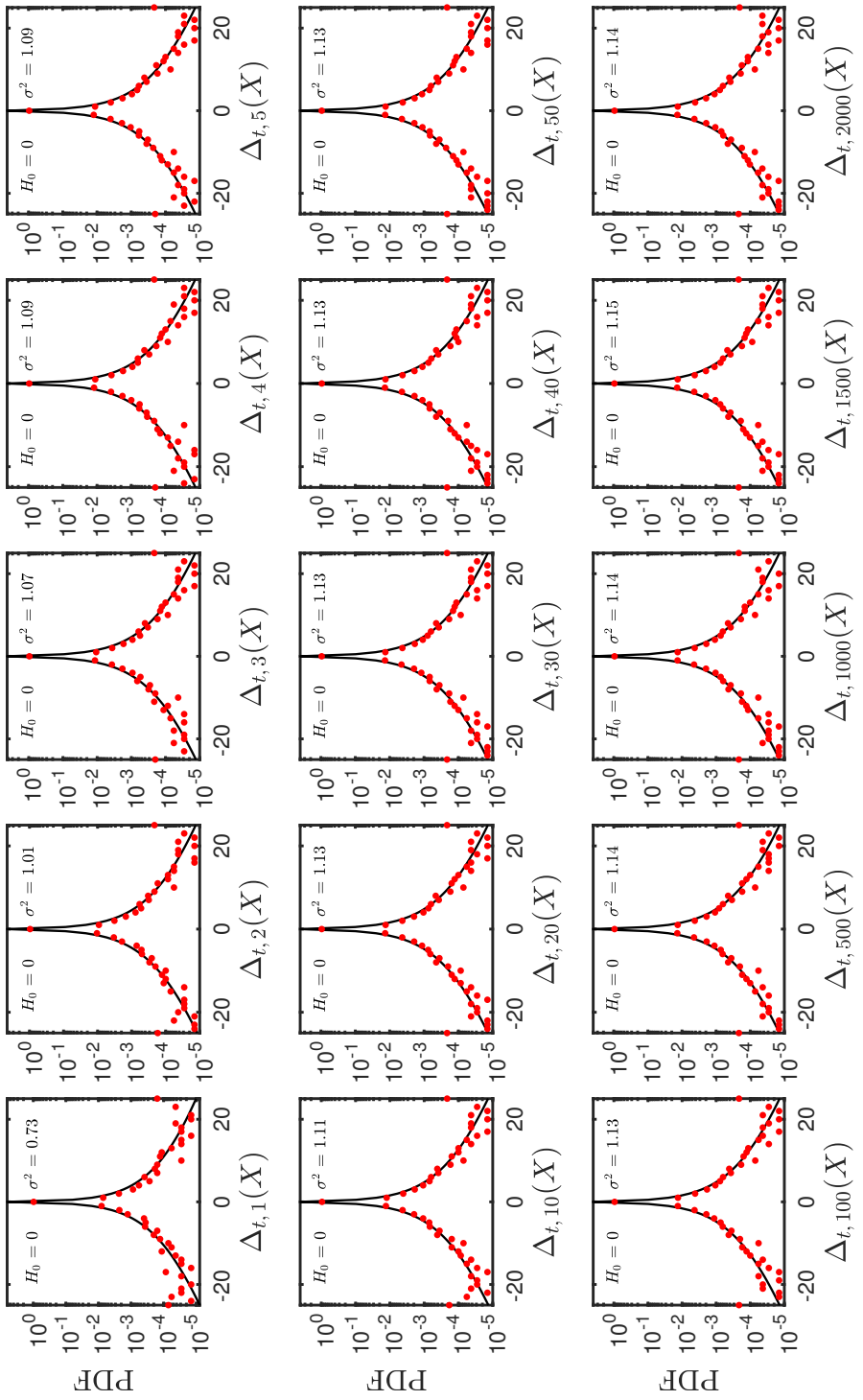

Figure B-13: Probability density function of the increments $\Delta_{t,u}$ of the rainfall time series recorded at gauge Fontibón (RG5) for $u = \{1, 2, 3, 4, 5, 10, 20, 30, 40, 50, 100, 500, 1000, 1500, 2000\}$. The red dots represents the empirical PDF corresponding to the observations from the raingauge and the solid line represents the normal inverse Gaussian distribution for fitted to the rainfall data set. In each frame is indicated the value of null hypothesis H_0 (zero for the acceptance of H_0 and one for the rejection of H_0; both values for a 5% of significance level α). The null hypothesis states the data come from a normal inverse Gaussian distribution.

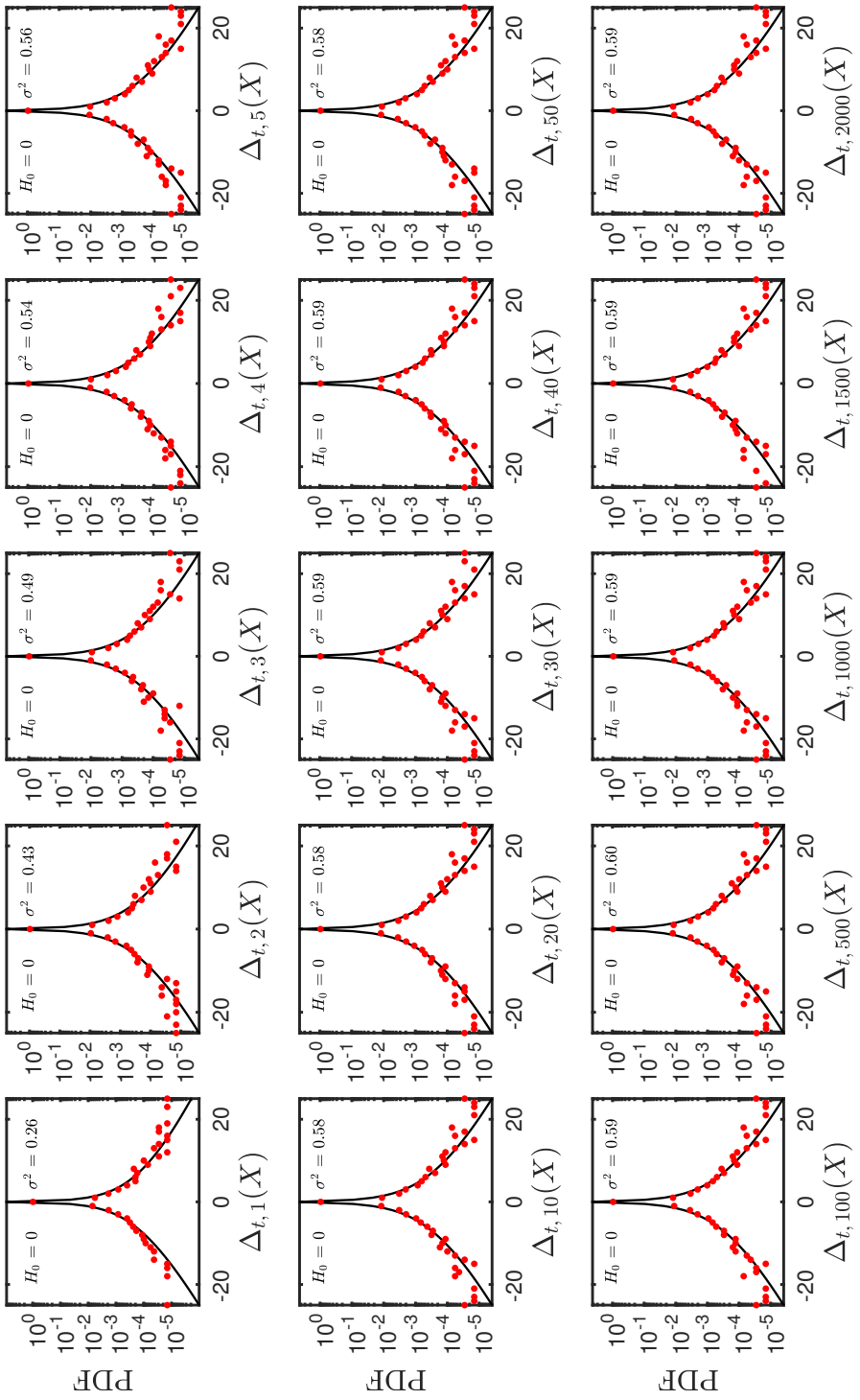

Figure B-14: Probability density function of the increments $\Delta_{t,u}$ of the rainfall time series recorded at gauge La Caro (RG6) for $u = \{1, 2, 3, 4, 5, 10, 20, 30, 40, 50, 100, 500, 1000, 1500, 2000\}$. The red dots represents the empirical PDF corresponding to the observations from the raingauge and the solid line represents the normal inverse Gaussian distribution for fitted to the rainfall data set. In each frame is indicated the value of null hypothesis H_0 (zero for the acceptance of H_0 and one for the rejection of H_0; both values for a 5% of significance level α). The null hypothesis states the data come from a normal inverse Gaussian distribution.

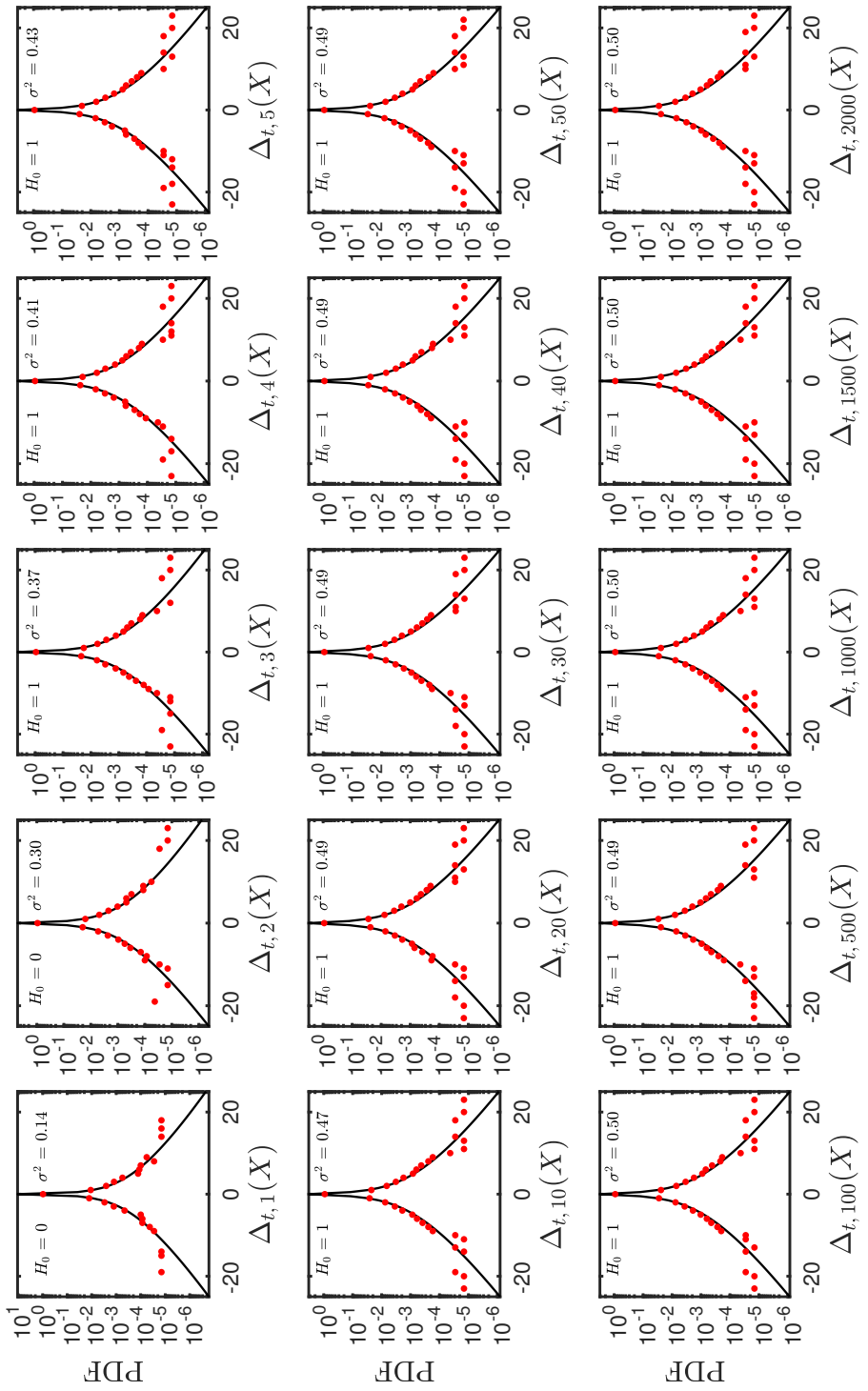

Figure B-15: Probability density function of the increments $\Delta_{t,u}$ of the rainfall time series recorded at gauge La Regadera (RG7) for $u = \{1, 2, 3, 4, 5, 10, 20, 30, 40, 50, 100, 500, 1000, 1500, 2000\}$. The red dots represents the empirical PDF corresponding to the observations from the raingauge and the solid line represents the normal inverse Gaussian distribution for fitted to the rainfall data set. In each frame is indicated the value of null hypothesis H_0 (zero for the acceptance of H_0 and one for the rejection of H_0; both values for a 5% of significance level α). The null hypothesis states the data come from a normal inverse Gaussian distribution.

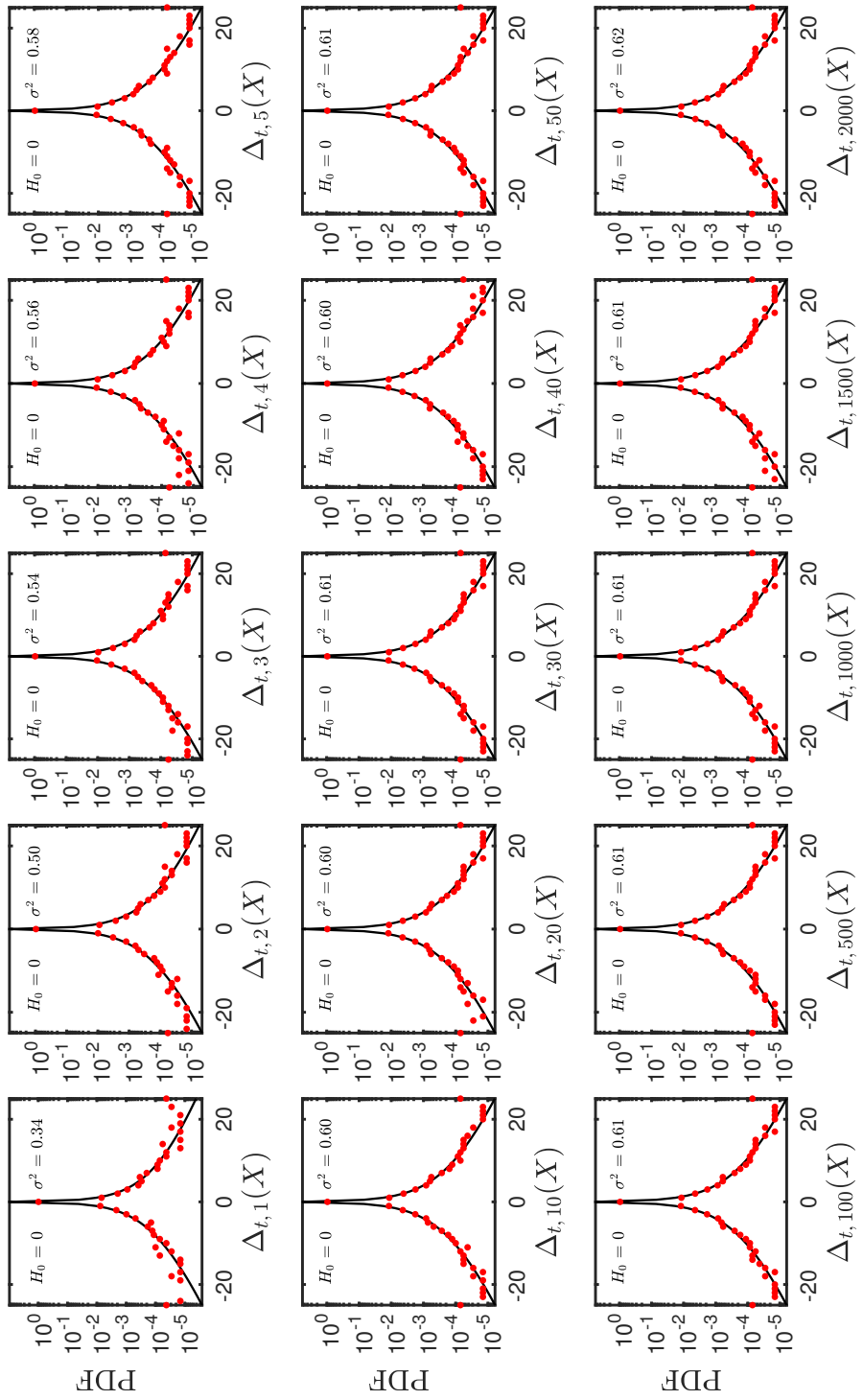

Figure B-16: Probability density function of the increments $\Delta_{t,u}$ of the rainfall time series recorded at gauge Las Huertas (RG8) for $u = \{1, 2, 3, 4, 5, 10, 20, 30, 40, 50, 100, 500, 1000, 1500, 2000\}$. The red dots represents the empirical PDF corresponding to the observations from the raingauge and the solid line represents the normal inverse Gaussian distribution for fitted to the rainfall data set. In each frame is indicated the value of null hypothesis H_0 (zero for the acceptance of H_0 and one for the rejection of H_0; both values for a 5% of significance level α). The null hypothesis states the data come from a normal inverse Gaussian distribution.

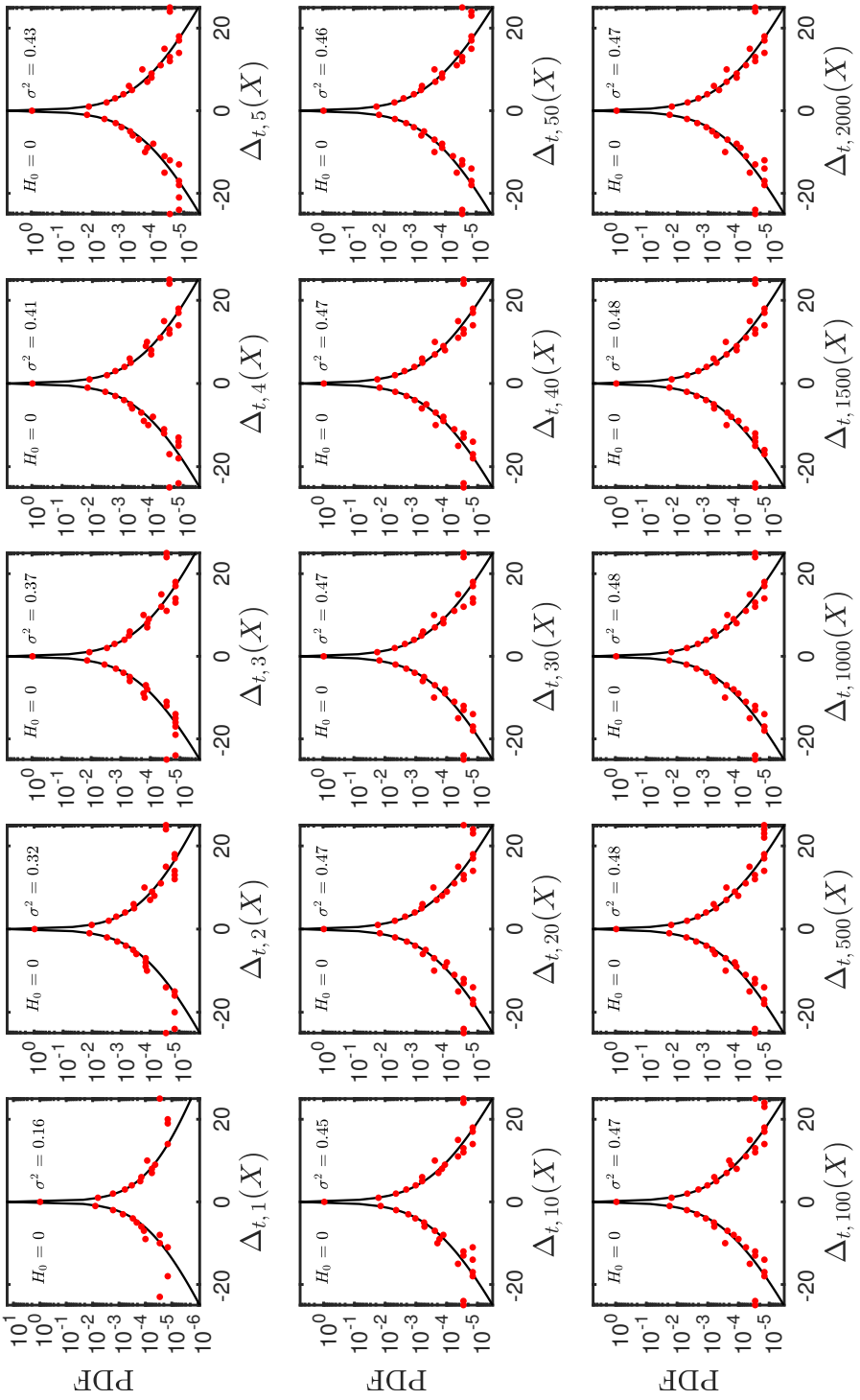

Figure B-17: Probability density function of the increments $\Delta_{t,u}$ of the rainfall time series recorded at gauge Quiba (RG9) for $u = \{1, 2, 3, 4, 5, 10, 20, 30, 40, 50, 100, 500, 1000, 1500, 2000\}$. The red dots represents the empirical PDF corresponding to the observations from the raingauge and the solid line represents the normal inverse Gaussian distribution for fitted to the rainfall data set. In each frame is indicated the value of null hypothesis H_0 (zero for the acceptance of H_0 and one for the rejection of H_0; both values for a 5% of significance level α). The null hypothesis states the data come from a normal inverse Gaussian distribution.

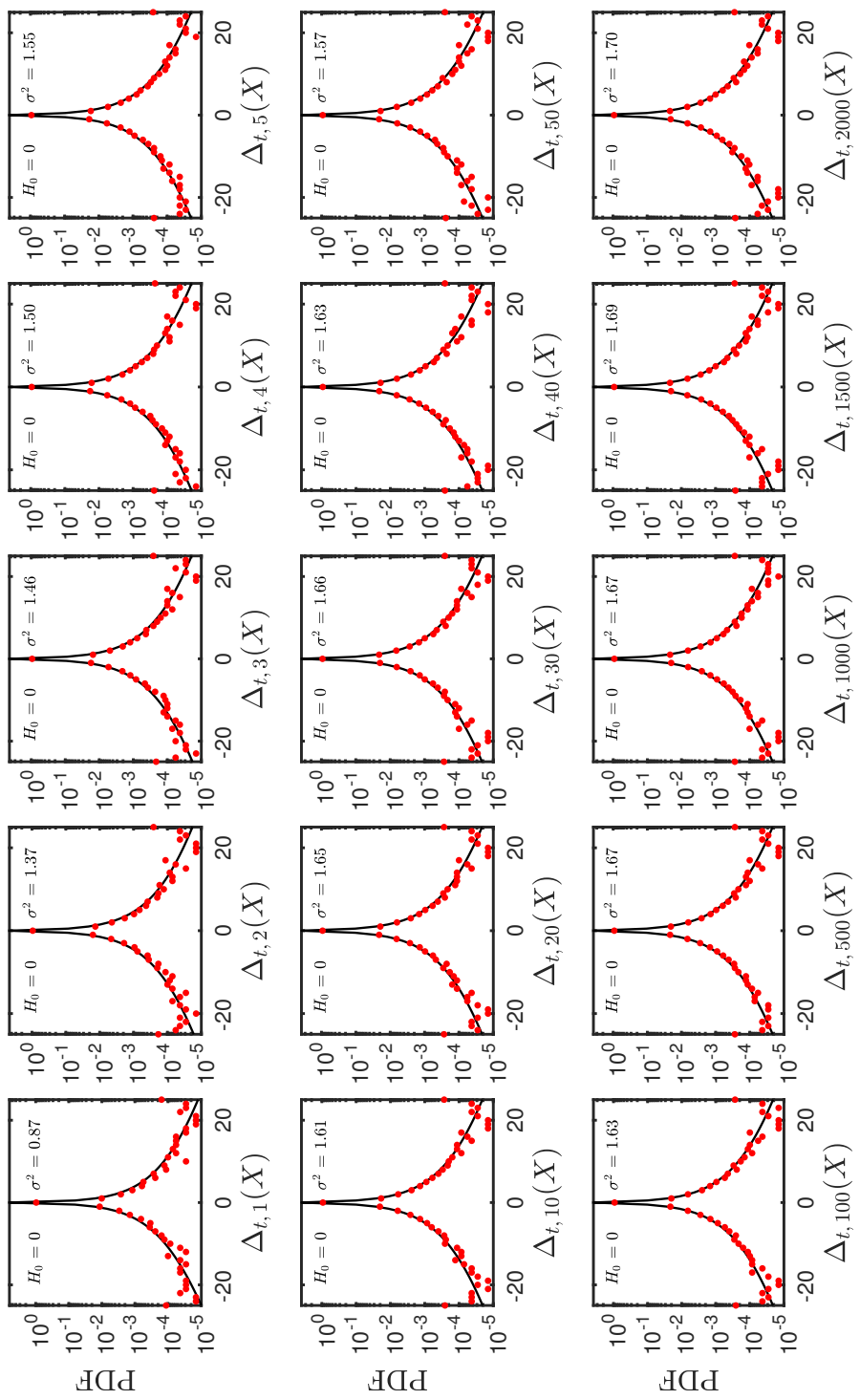

Figure B-18: Probability density function of the increments $\Delta_{t,u}$ of the rainfall time series recorded at gauge San Francisco (RG10) for $u = \{1, 2, 3, 4, 5, 10, 20, 30, 40, 50, 100, 500, 1000, 1500, 2000\}$. The red dots represents the empirical PDF corresponding to the observations from the raingauge and the solid line represents the normal inverse Gaussian distribution for fitted to the rainfall data set. In each frame is indicated the value of null hypothesis H_0 (zero for the acceptance of H_0 and one for the rejection of H_0; both values for a 5% of significance level α). The null hypothesis states the data come from a normal inverse Gaussian distribution.

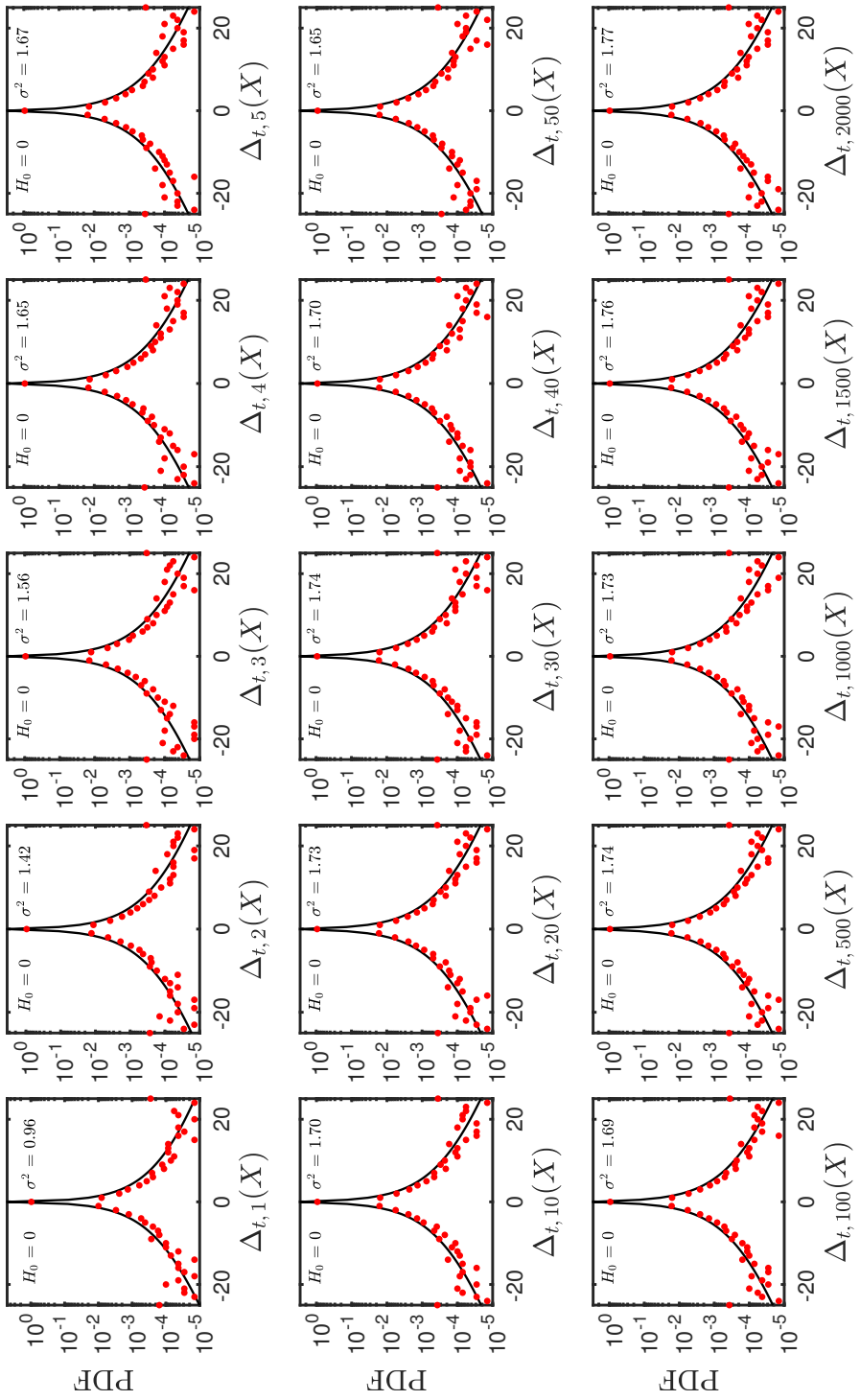

Figure B-19: Probability density function of the increments $\Delta_{t,u}$ of the rainfall time series recorded at gauge San Luís (RG11) for $u = \{1, 2, 3, 4, 5, 10, 20, 30, 40, 50, 100, 500, 1000, 1500, 2000\}$. The red dots represents the empirical PDF corresponding to the observations from the raingauge and the solid line represents the normal inverse Gaussian distribution for fitted to the rainfall data set. In each frame is indicated the value of null hypothesis H_0 (zero for the acceptance of H_0 and one for the rejection of H_0; both values for a 5% of significance level α). The null hypothesis states the data come from a normal inverse Gaussian distribution.

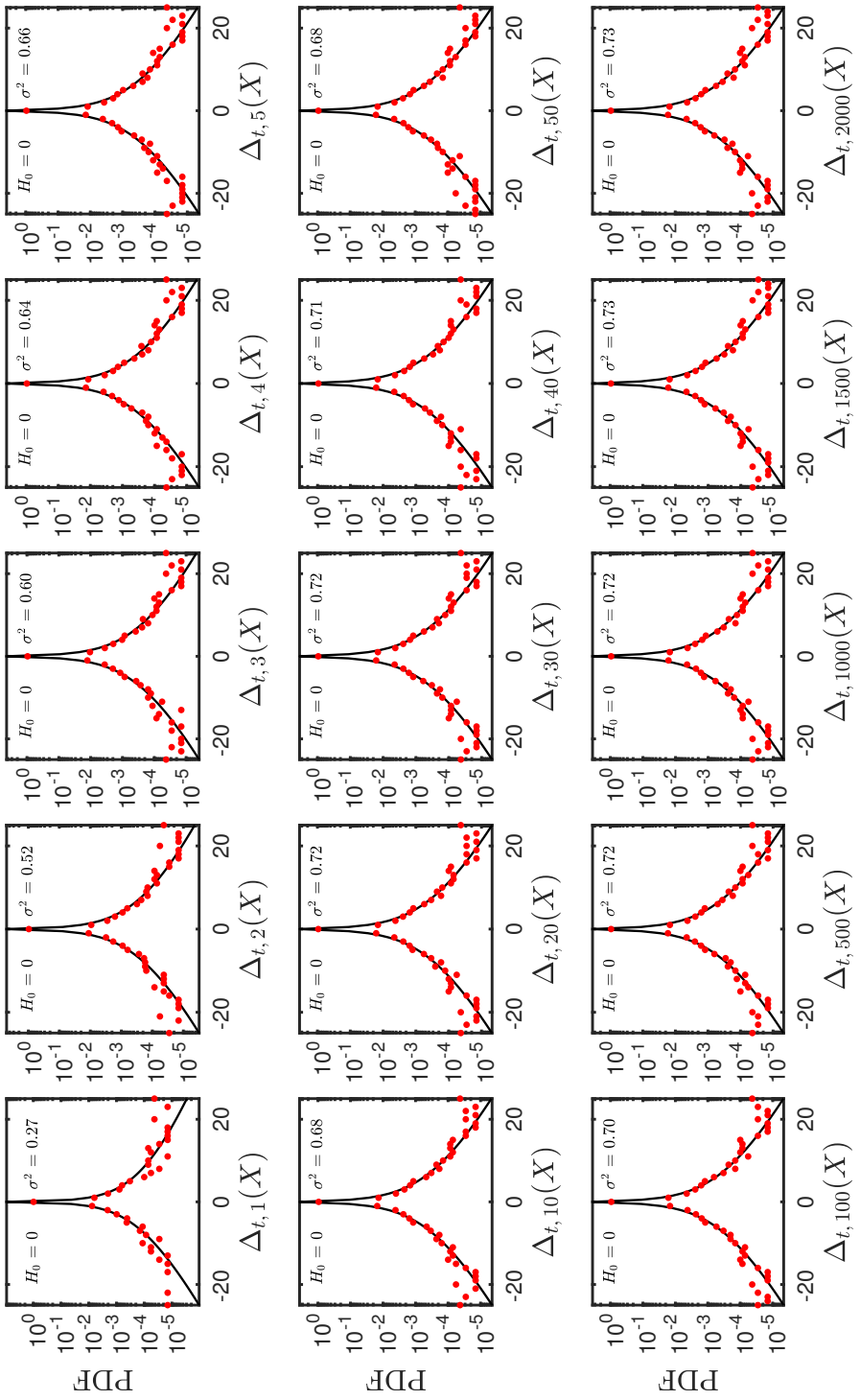

Figure B-20: Probability density function of the increments $\Delta_{t,u}$ of the rainfall time series recorded at gauge Santa Lucía (RG12) for $u = \{1, 2, 3, 4, 5, 10, 20, 30, 40, 50, 100, 500, 1000, 1500, 2000\}$. The red dots represents the empirical PDF corresponding to the observations from the raingauge and the solid line represents the normal inverse Gaussian distribution for fitted to the rainfall data set. In each frame is indicated the value of null hypothesis H_0 (zero for the acceptance of H_0 and one for the rejection of H_0; both values for a 5% of significance level α). The null hypothesis states the data come from a normal inverse Gaussian distribution.

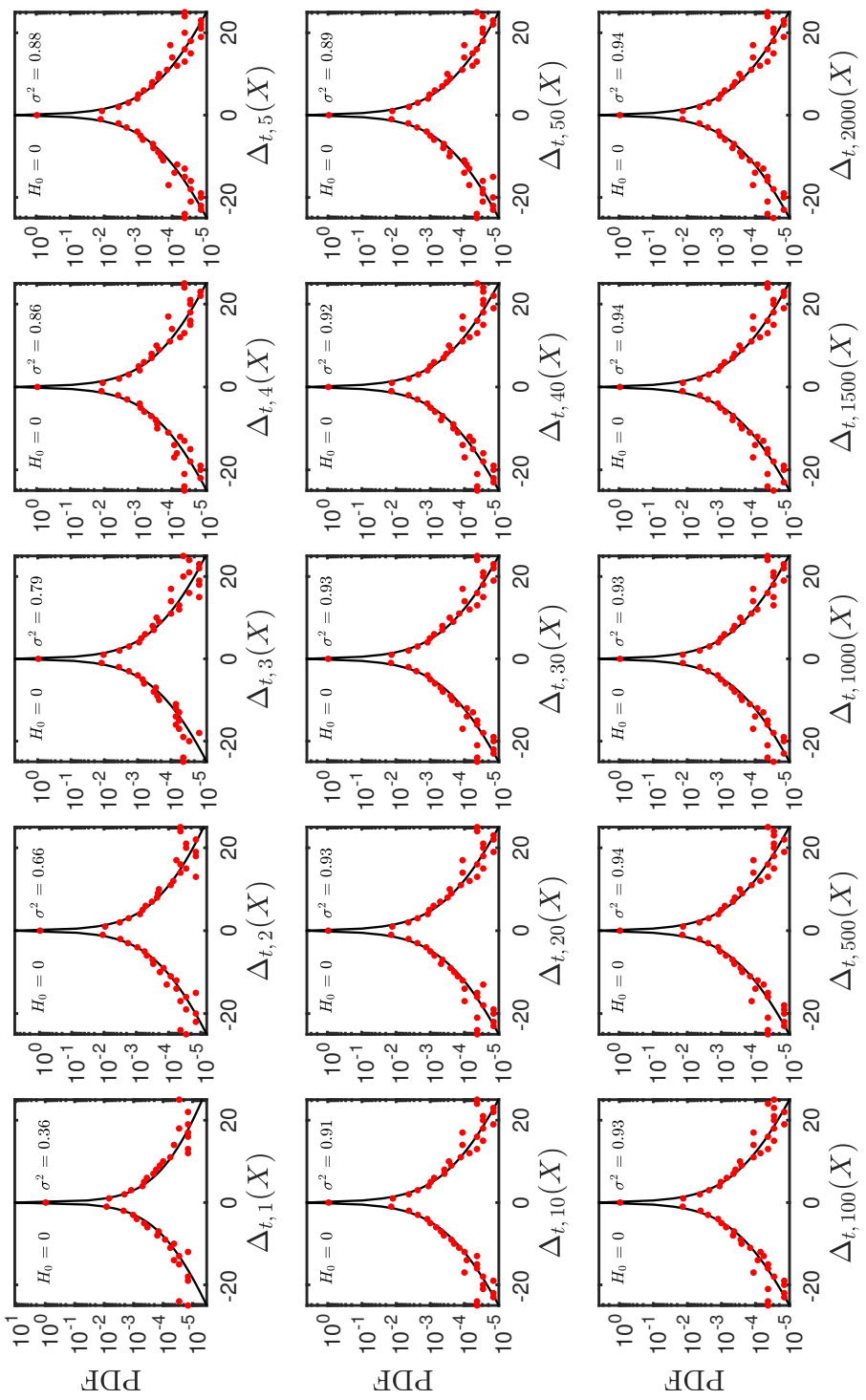

Figure B-21: Probability density function of the increments $\Delta_{t,u}$ of the rainfall time series recorded at gauge Serrezuela (RG13) for $u = \{1, 2, 3, 4, 5, 10, 20, 30, 40, 50, 100, 500, 1000, 1500, 2000\}$. The red dots represents the empirical PDF corresponding to the observations from the raingauge and the solid line represents the normal inverse Gaussian distribution for fitted to the rainfall data set. In each frame is indicated the value of null hypothesis H_0 (zero for the acceptance of H_0 and one for the rejection of H_0; both values for a 5% of significance level α). The null hypothesis states the data come from a normal inverse Gaussian distribution.

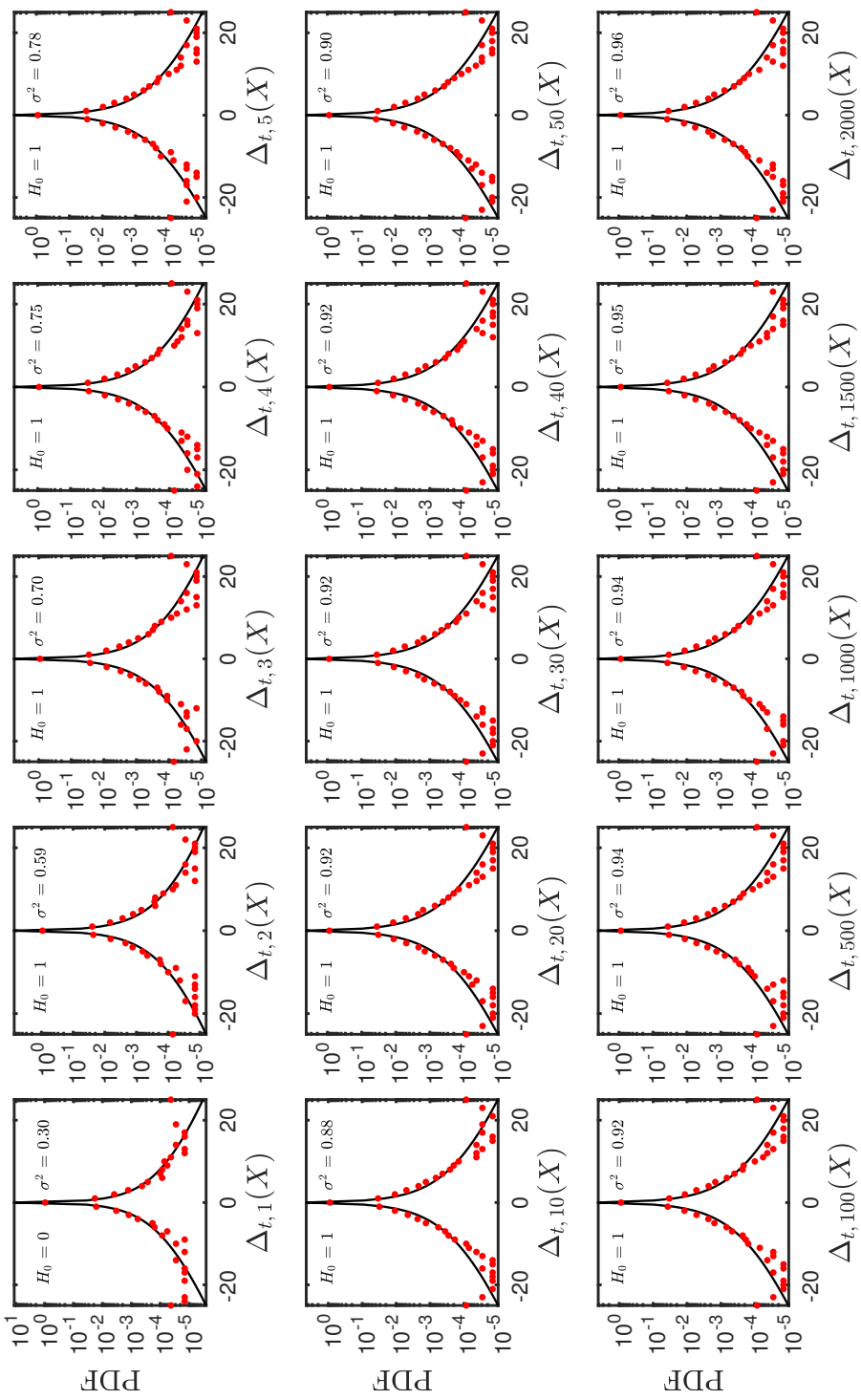

Figure B-22: Probability density function of the increments $\Delta_{t,u}$ of the rainfall time series recorded at gauge Teusacá (RG14) for $u = \{1, 2, 3, 4, 5, 10, 20, 30, 40, 50, 100, 500, 1000, 1500, 2000\}$. The red dots represents the empirical PDF corresponding to the observations from the raingauge and the solid line represents the normal inverse Gaussian distribution for fitted to the rainfall data set. In each frame is indicated the value of null hypothesis H_0 (zero for the acceptance of H_0 and one for the rejection of H_0; both values for a 5% of significance level α). The null hypothesis states the data come from a normal inverse Gaussian distribution.

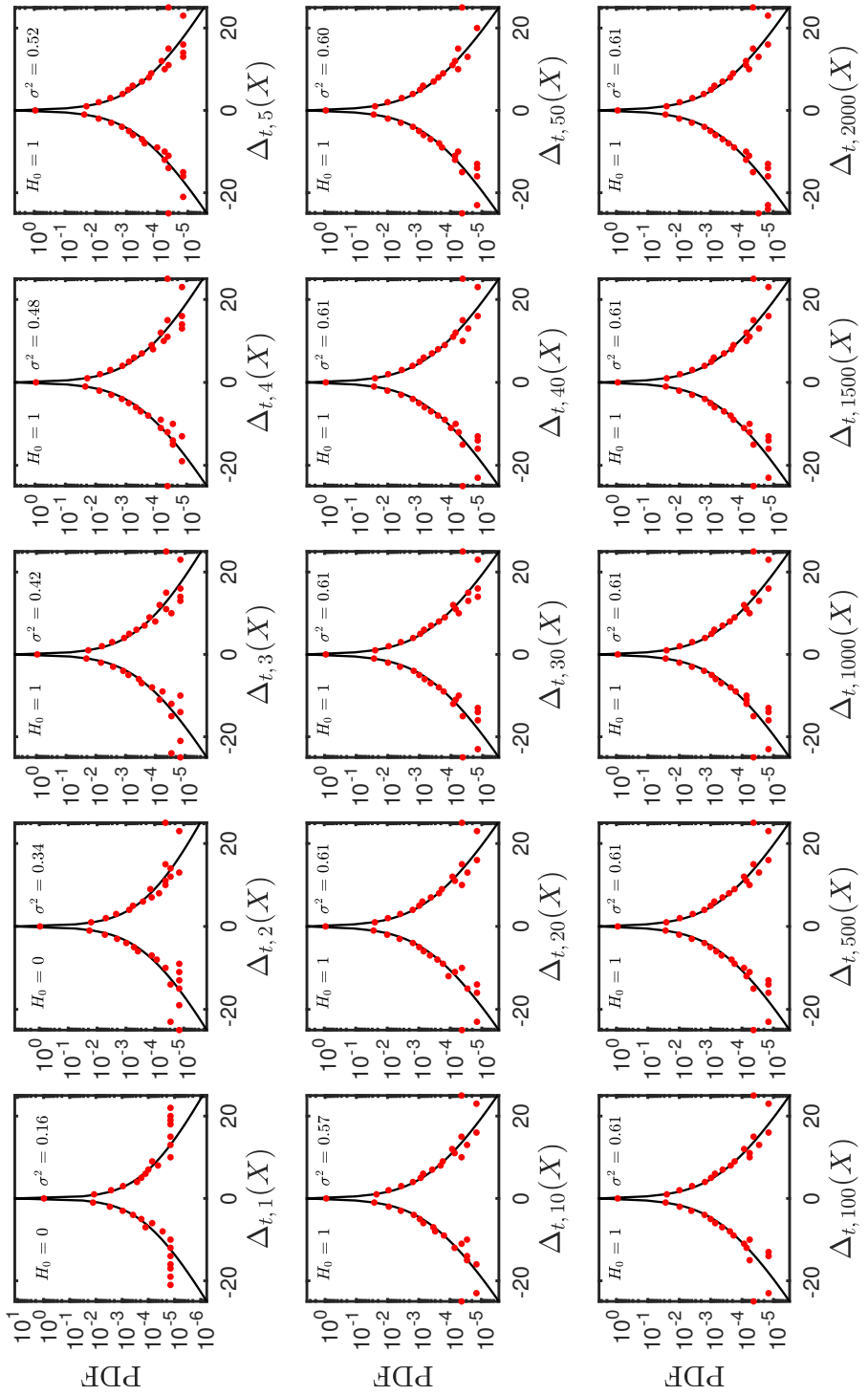

Figure B-23: Probability density function of the increments $\Delta_{t,u}$ of the rainfall time series recorded at gauge Une (RG15) for $u = \{1, 2, 3, 4, 5, 10, 20, 30, 40, 50, 100, 500, 1000, 1500, 2000\}$. The red dots represents the empirical PDF corresponding to the observations from the raingauge and the solid line represents the normal inverse Gaussian distribution for fitted to the rainfall data set. In each frame is indicated the value of null hypothesis H_0 (zero for the acceptance of H_0 and one for the rejection of H_0; both values for a 5% of significance level α). The null hypothesis states the data come from a normal inverse Gaussian distribution.

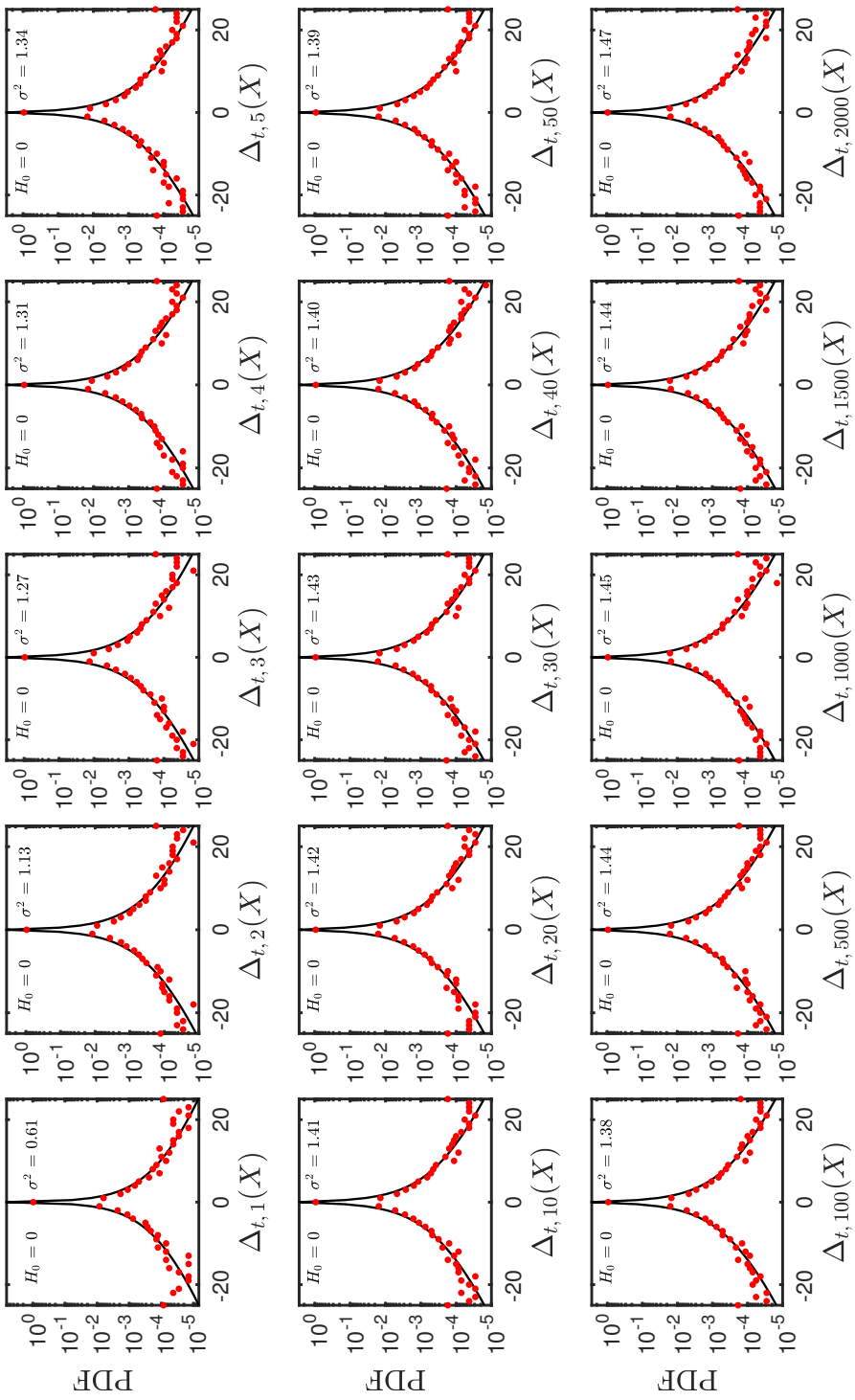

Figure B-24: Probability density function of the increments $\Delta_{t,u}$ of the rainfall time series recorded at gauge Usaquén (RG16) for $u = \{1, 2, 3, 4, 5, 10, 20, 30, 40, 50, 100, 500, 1000, 1500, 2000\}$. The red dots represents the empirical PDF corresponding to the observations from the raingauge and the solid line represents the normal inverse Gaussian distribution for fitted to the rainfall data set. In each frame is indicated the value of null hypothesis H_0 (zero for the acceptance of H_0 and one for the rejection of H_0; both values for a 5% of significance level α). The null hypothesis states the data come from a normal inverse Gaussian distribution.

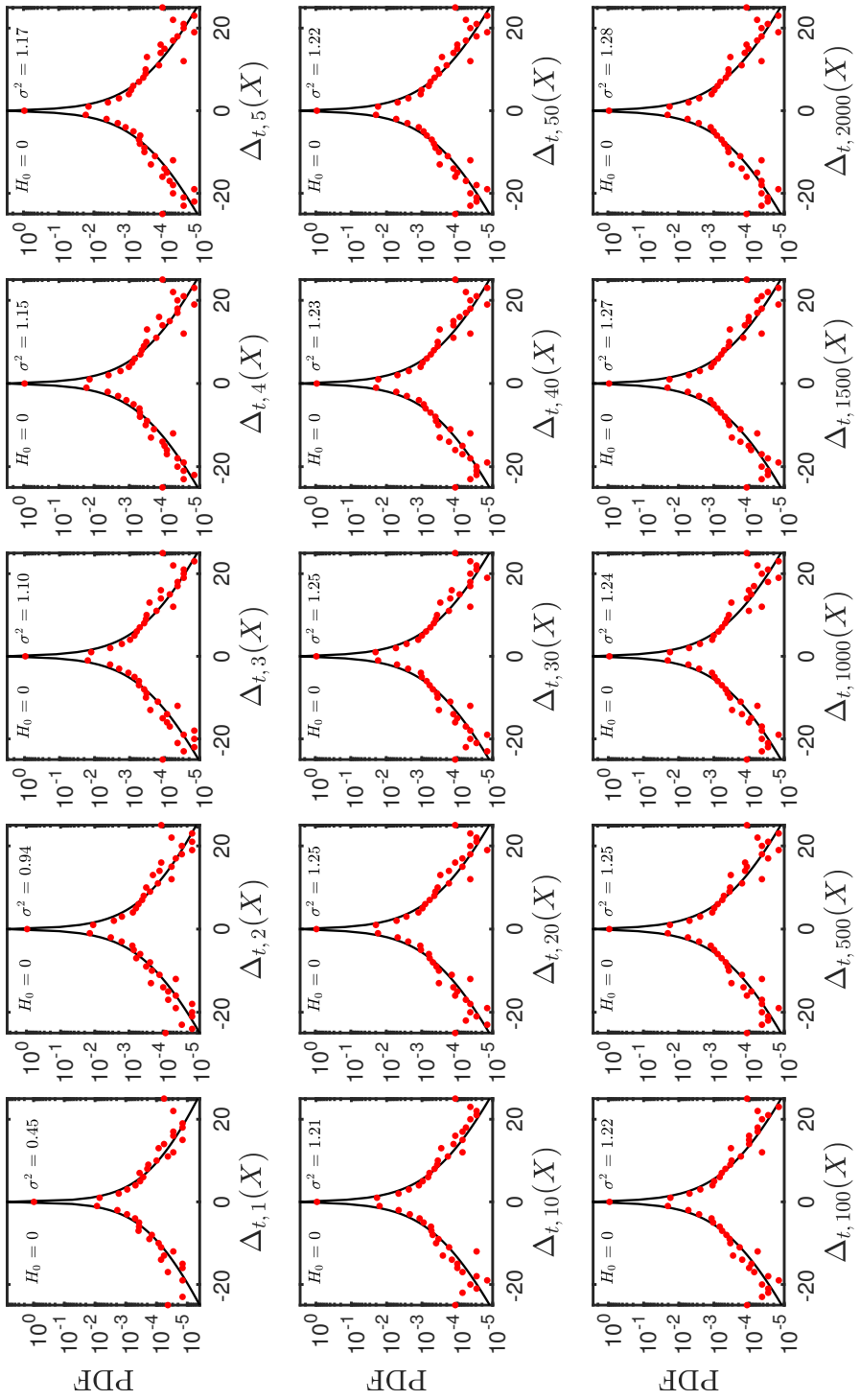

Figure B-25: Probability density function of the increments $\Delta_{t,u}$ of the rainfall time series recorded at gauge Vitelma (RG17) for $u = \{1, 2, 3, 4, 5, 10, 20, 30, 40, 50, 100, 500, 1000, 1500, 2000\}$. The red dots represents the empirical PDF corresponding to the observations from the raingauge and the solid line represents the normal inverse Gaussian distribution for fitted to the rainfall data set. In each frame is indicated the value of null hypothesis H_0 (zero for the acceptance of H_0 and one for the rejection of H_0; both values for a 5% of significance level α). The null hypothesis states the data come from a normal inverse Gaussian distribution.

C. Reflectivity Records from SIATA's Weather Radar

C.1. Space – Time Plots

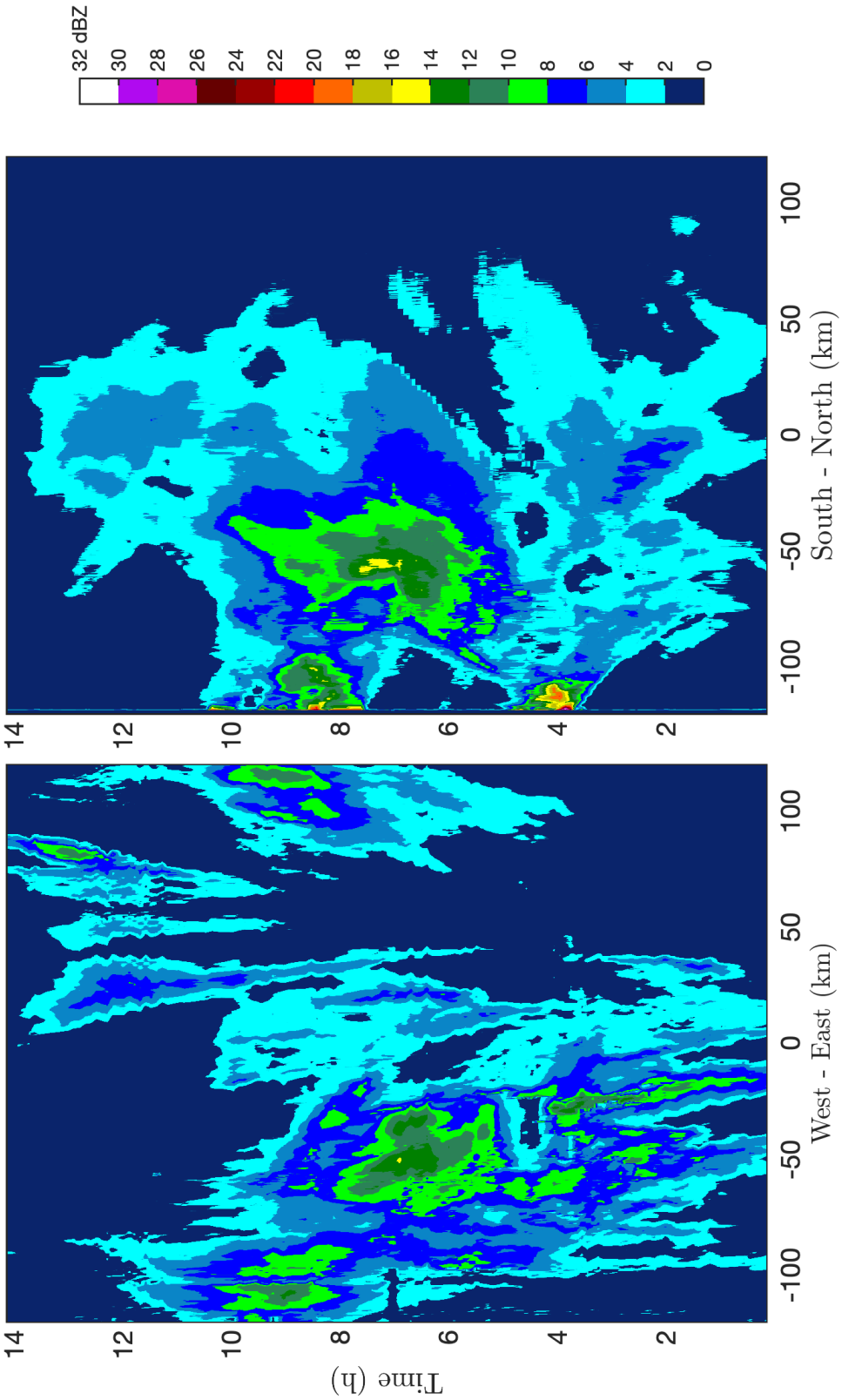

Figure C-1: Space-time diagrams for the reflectivity fields (Z) measured by the Early Warning System of Medellín and Aburrá's Valley (SIATA) on May 18th of 2018 from 00:00 to 14:00 h (GMT–5). At the left panel is shown the averaged values of each radar frame in the direction South–North and at the right panel is shown the averaged values of each radar frame in the direction East–West.

D. TRMM Rainfall Intensity

D.1. Plots of Spatial Statistics

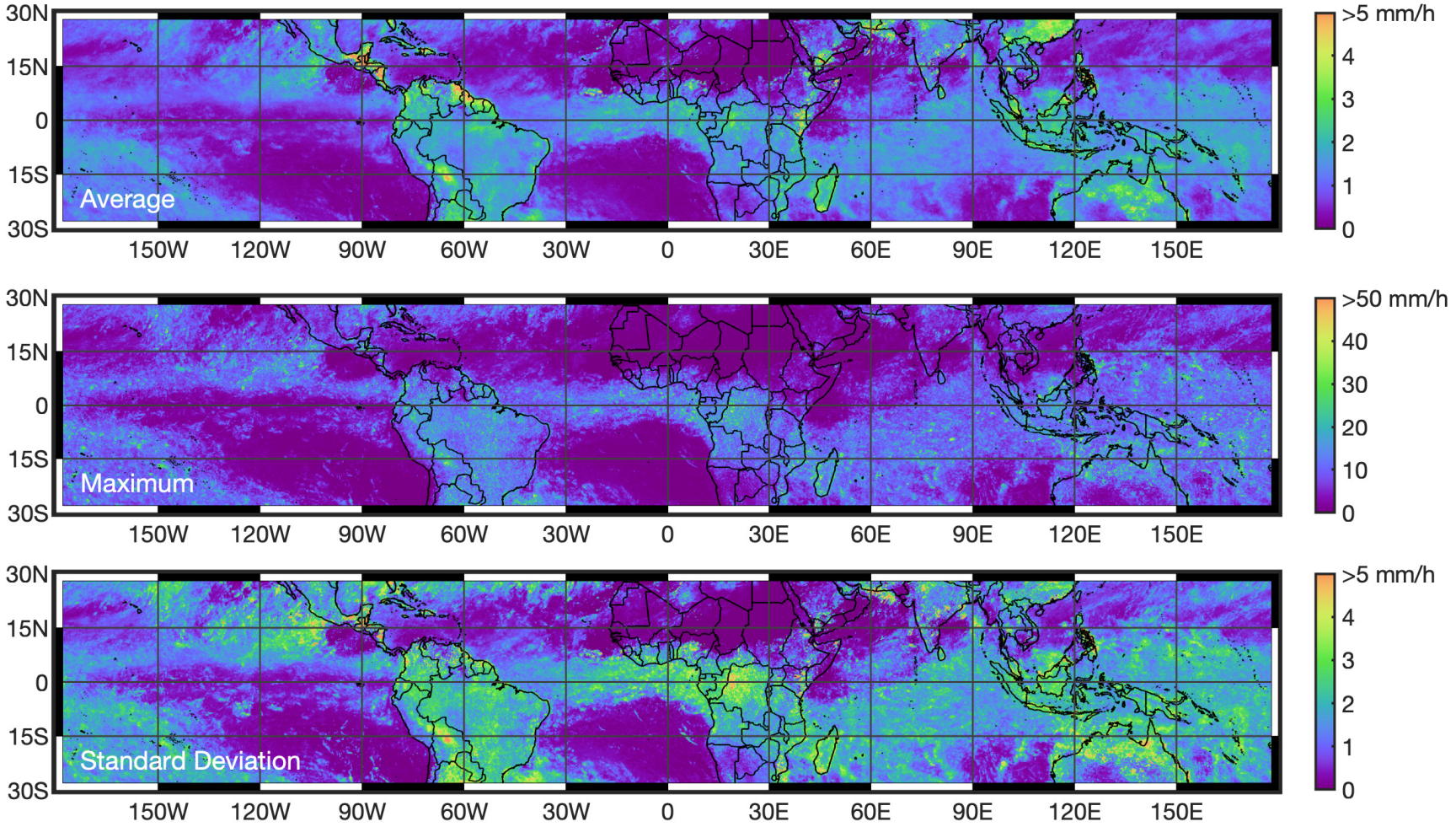

Figure D-1: Rainfall intensity fields for the period defined between January 1st to March 31st of 2015, which were measured by TRMM satellite mission (product 3B42; spatial resolution: 0.25°; time resolution: 3 h). The upper panel depicts the average value of rainfall intensity during the indicated period, the second panel depicts the maximum valued of rainfall intensity observed during the indicated period, and the third panel depicts the standard deviation for the selected records.

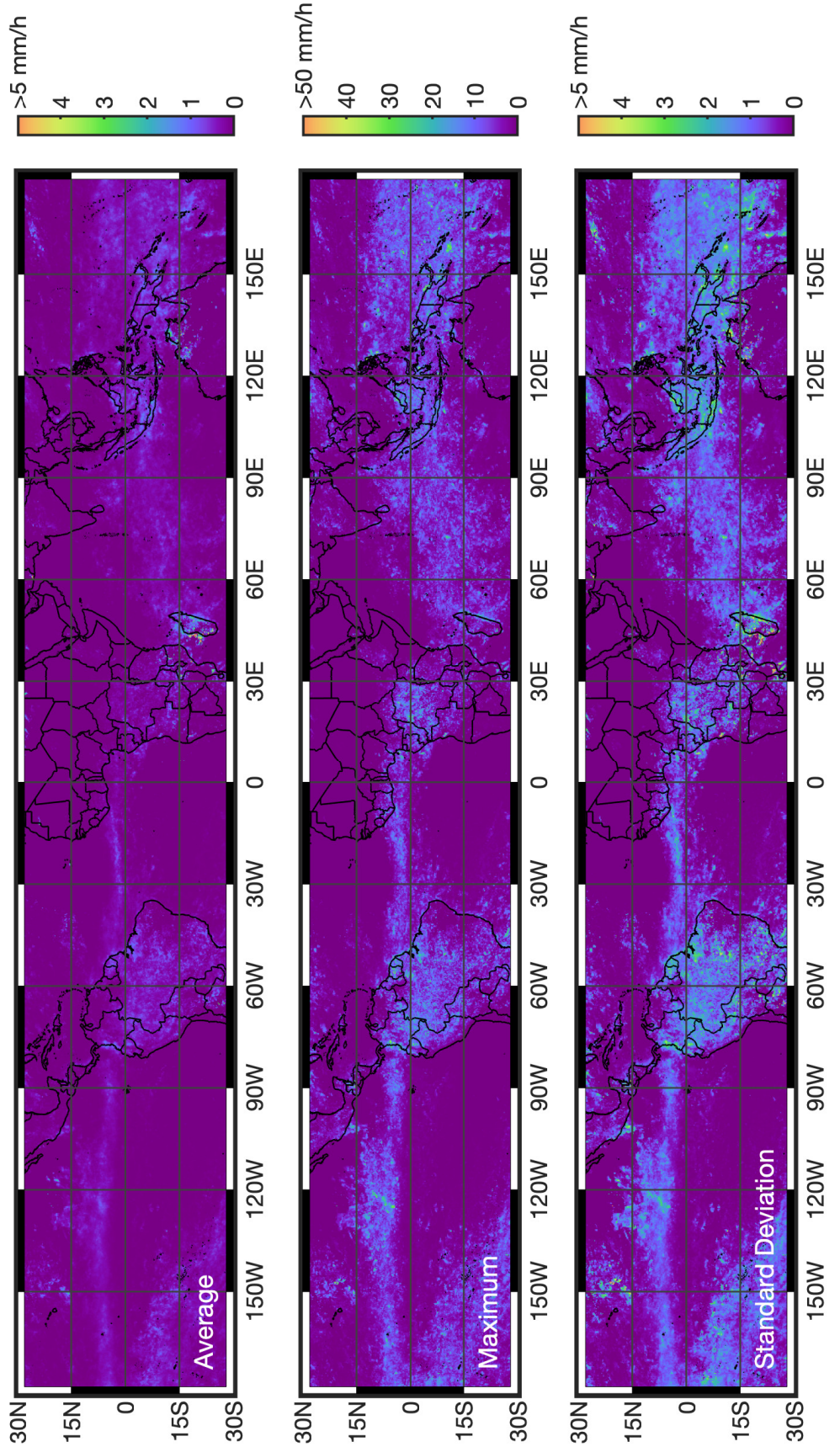

Figure D-2: Rainfall intensity fields for the period defined between April 1st to June 30th of 2015, which were measured by TRMM satellite mission (product 3B42; spatial resolution: 0.25°; time resolution: 3 h). The upper panel depicts the average value of rainfall intensity during the indicated period, the second panel depicts the maximum valued of rainfall intensity observed during the indicated period, and the third panel depicts the standard deviation for the selected records.

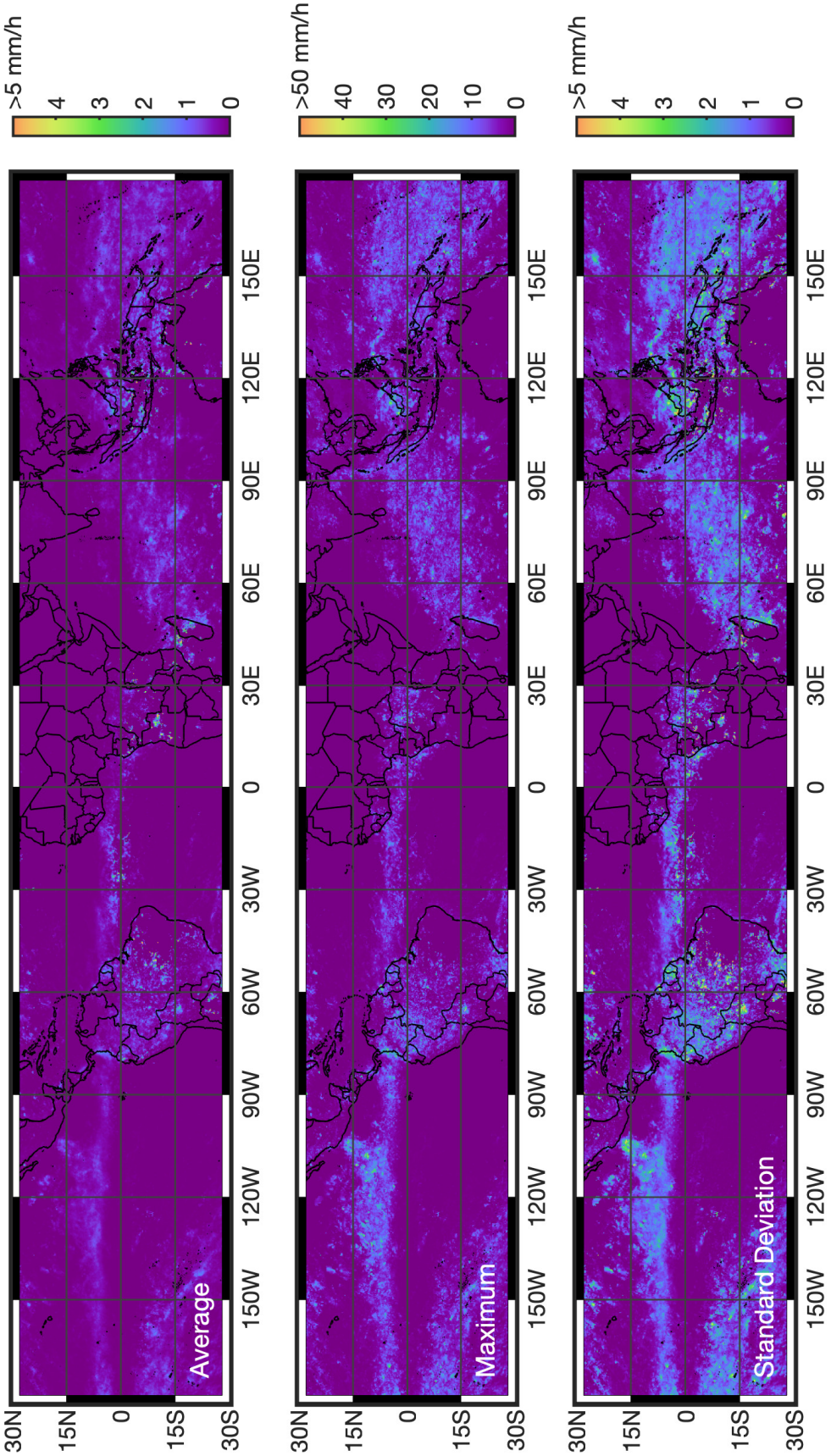

Figure D-3: Rainfall intensity fields for the period defined between July 1st to September 30th of 2015, which were measured by TRMM satellite mission (product 3B42; spatial resolution: 0.25°; time resolution: 3 h). The upper panel depicts the average value of rainfall intensity during the indicated period, the second panel depicts the maximum valued of rainfall intensity observed during the indicated period, and the third panel depicts the standard deviation for the selected records.

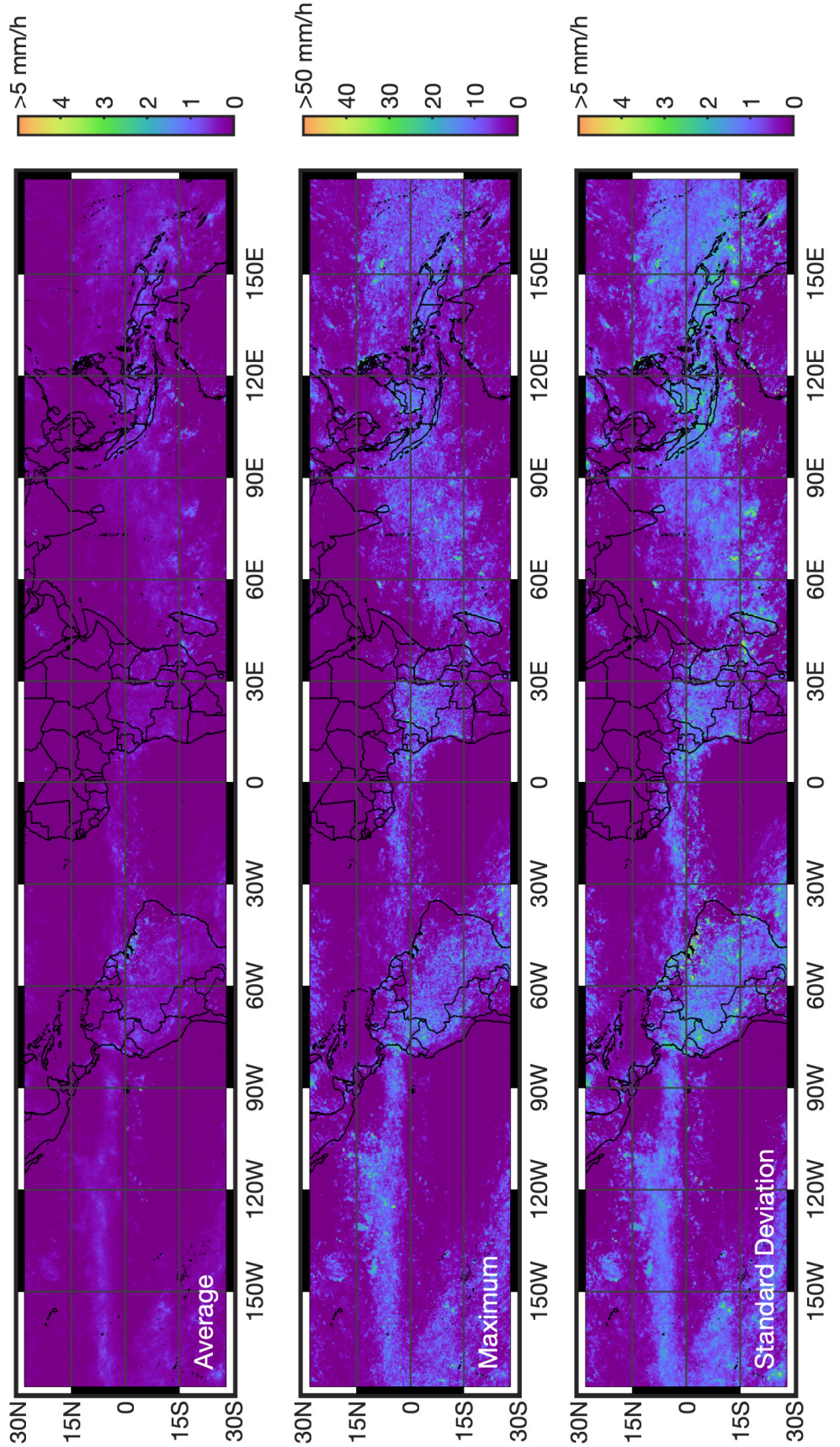

Figure D-4: Rainfall intensity fields for the period defined between October 1st to December 31st of 2015, which were measured by TRMM satellite mission (product 3B42; spatial resolution: 0.25°; time resolution: 3 h). The upper panel depicts the average value of rainfall intensity during the indicated period, the second panel depicts the maximum valued of rainfall intensity observed during the indicated period, and the third panel depicts the standard deviation for the selected records.

D.2. Space – Time Plots

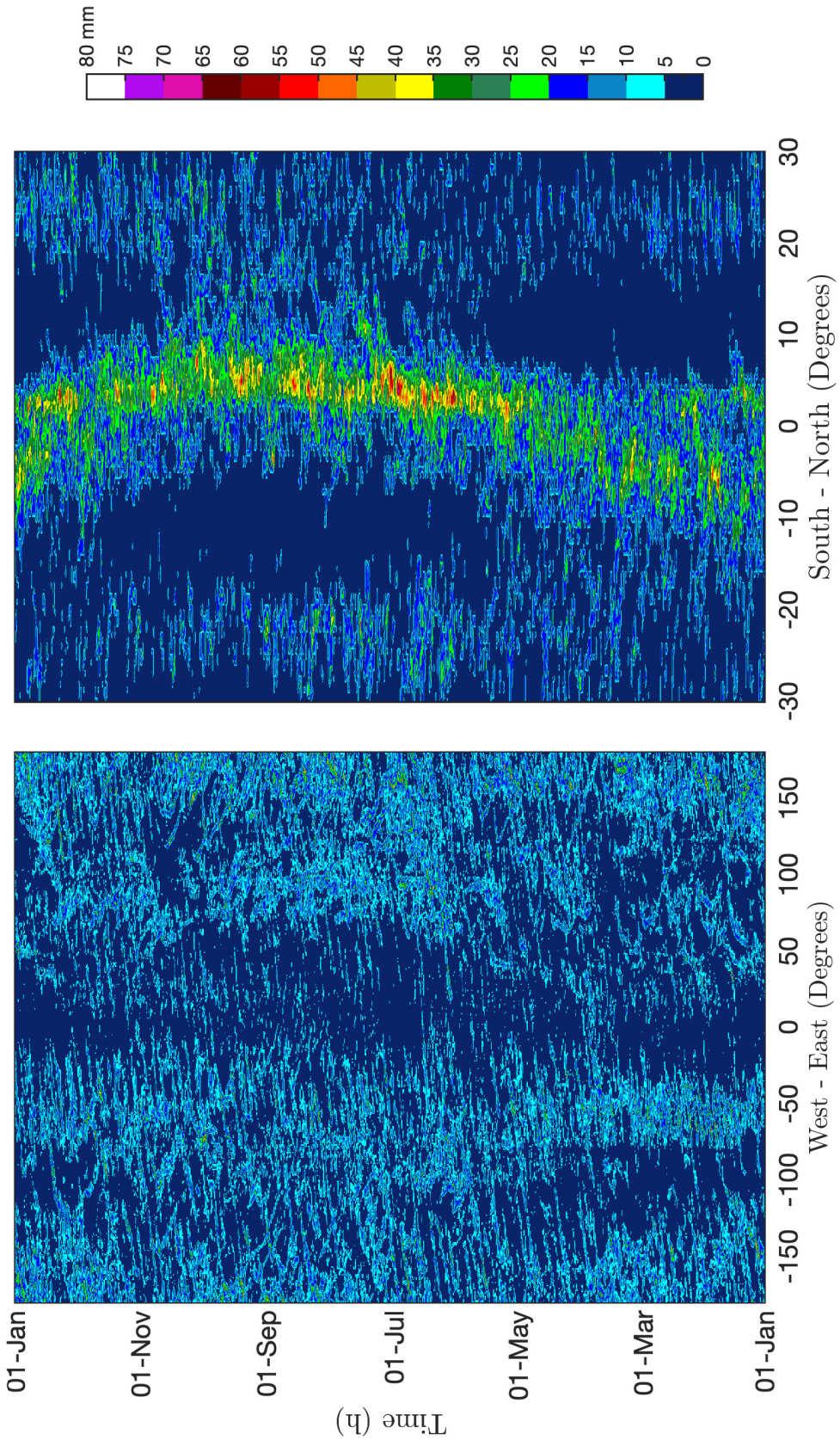

Figure D-5: Space–time diagrams for the rainfall intensity fields measured by the TRMM satellite mission in the year 2015 over the region bounded by the latitudes 30°S and 30°N. At the left panel is shown the averaged values of each observation in the direction South–North and at the right panel is shown the averaged values of each observation in the direction East–West.

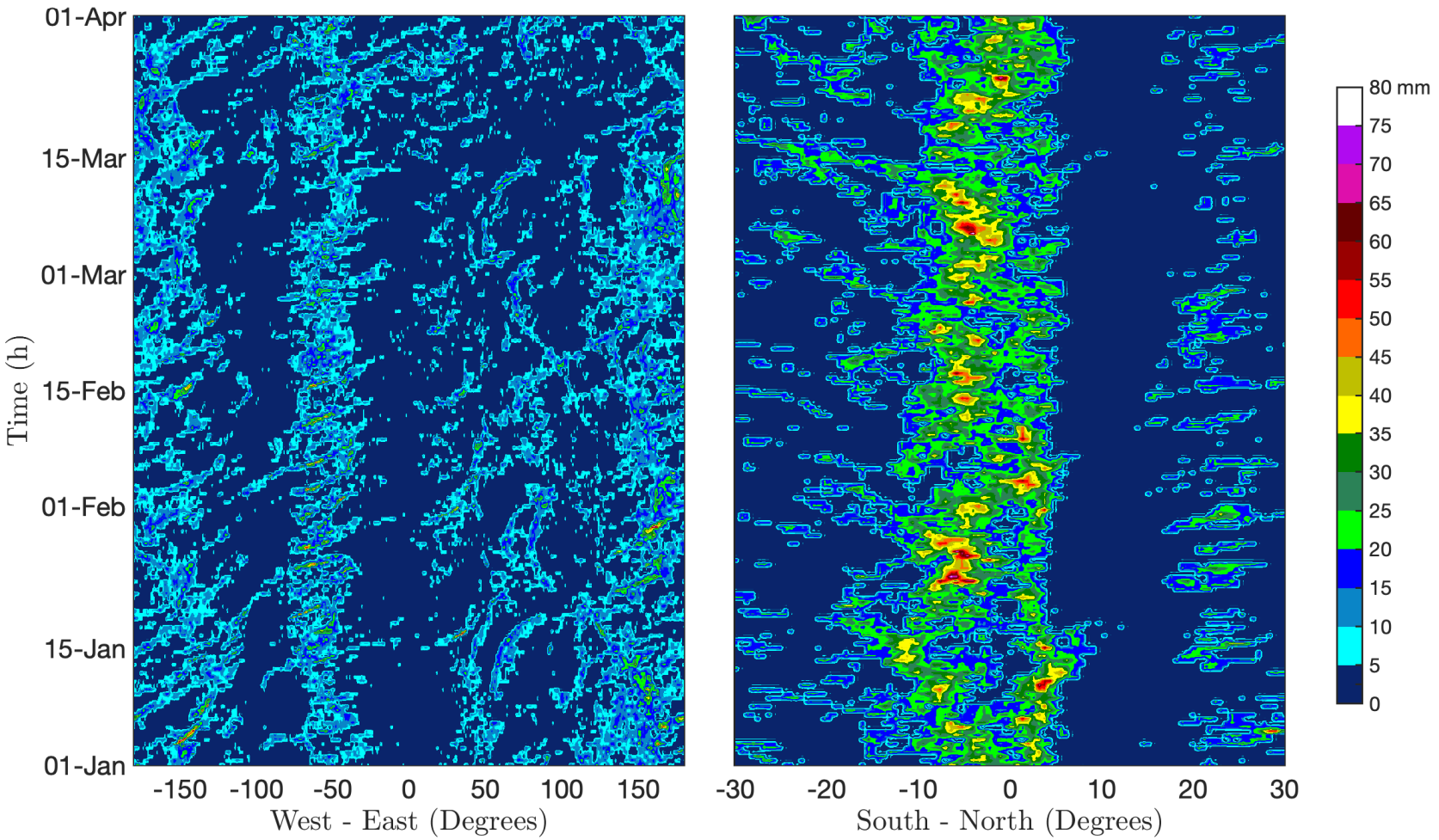

Figure D-6: Space–time diagrams for the rainfall intensity fields measured by the TRMM satellite mission in the first term of the year 2015 over the region bounded by latitudes 25°S and 25°N. At the left panel is shown the averaged values of the rainfall field in the direction South–North and at the right panel is shown the averaged values of the rainfall field in the direction East–West.

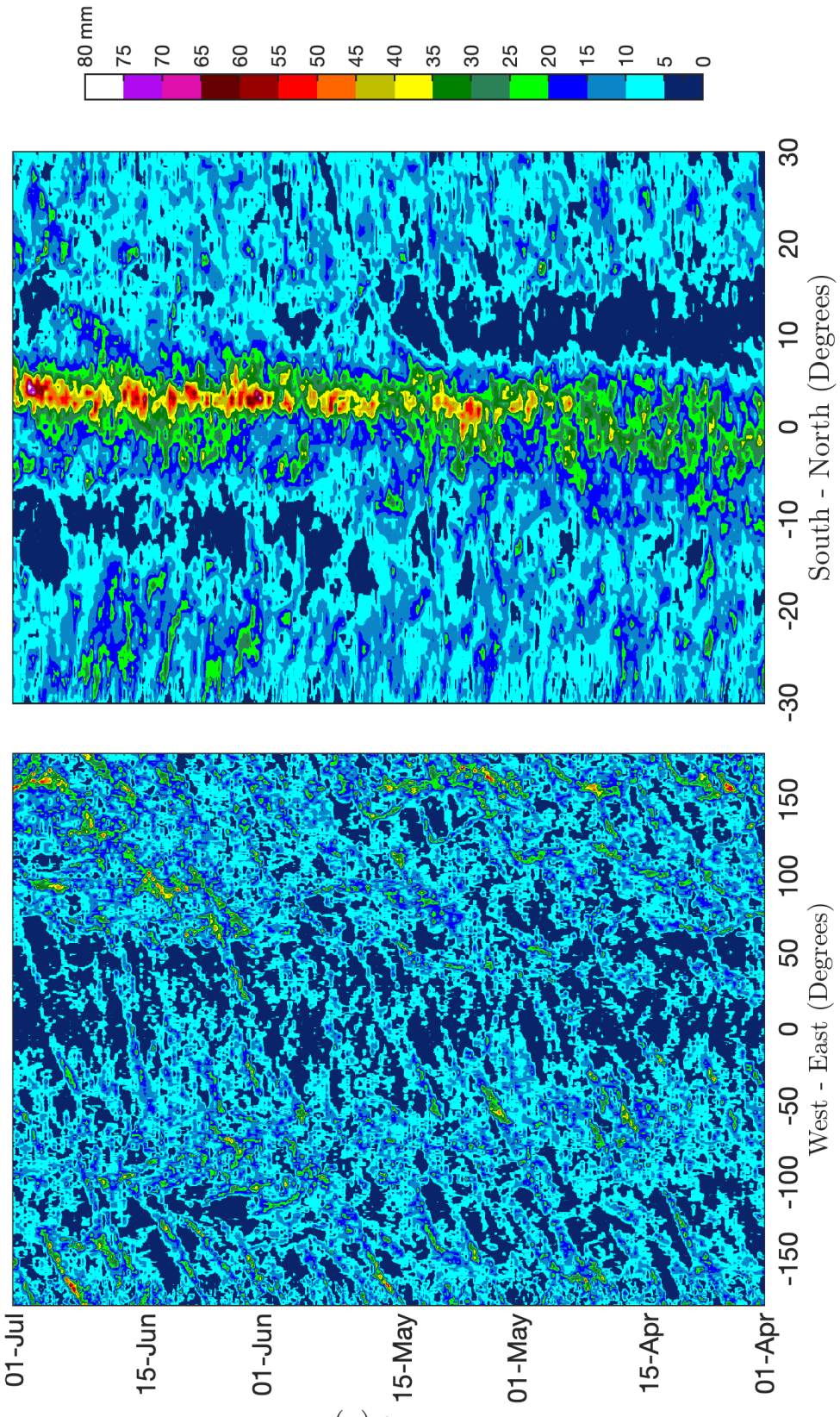

Figure D-7: Space–time diagrams for the rainfall intensity fields measured by the TRMM satellite mission in the second term of the year 2015 over the region bounded by the latitudes 25°S and 25°N. At the left panel is shown the averaged values of the rainfall field in the direction South–North and at the right panel is shown the averaged values of the rainfall field in the direction East–West.

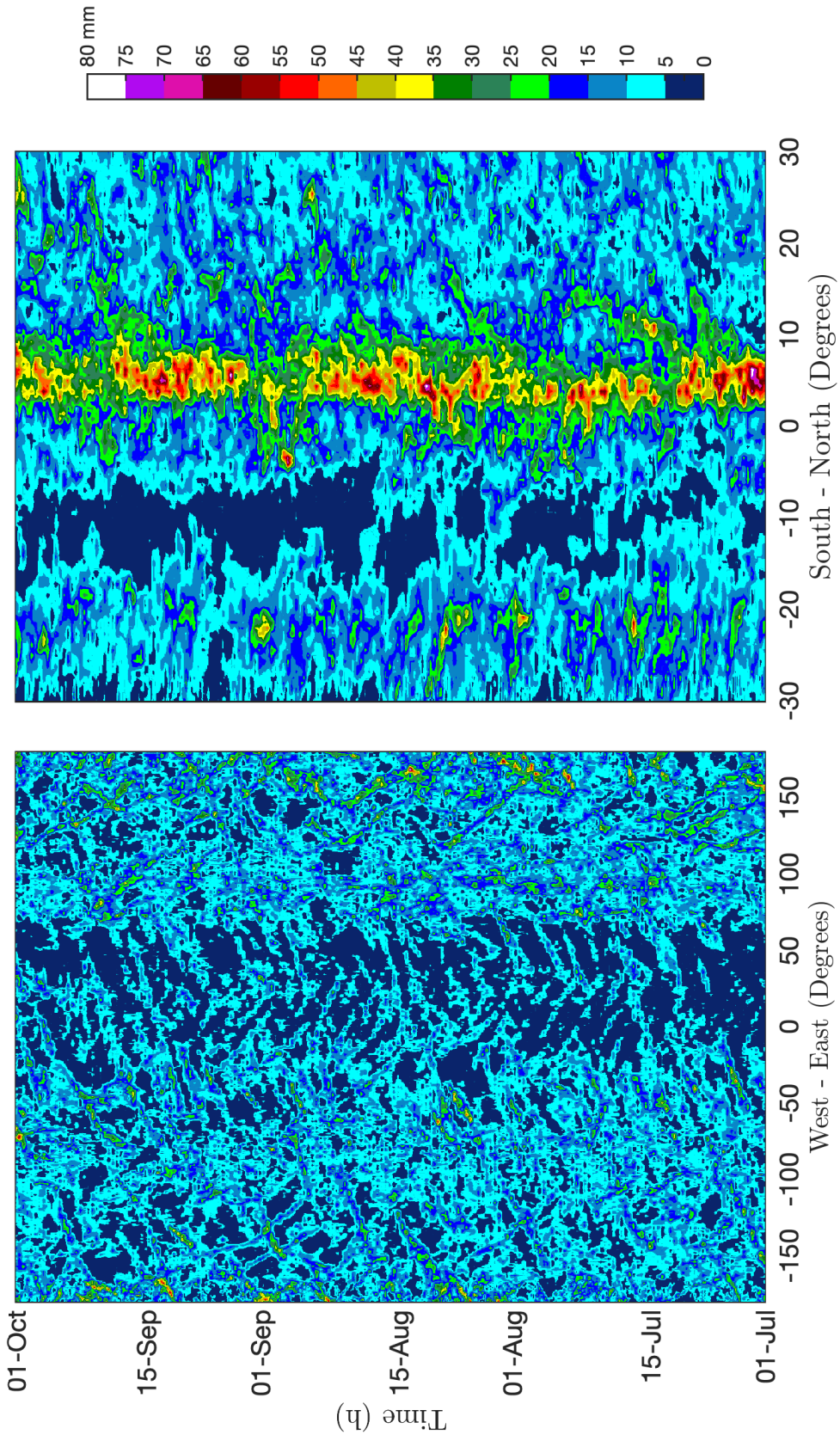

Figure D-8: Space–time diagrams for the rainfall intensity fields measured by the TRMM satellite mission in the third term of the year 2015 over the region bounded by the latitudes 25°S and 25°N. At the left panel is shown the averaged values of the rainfall field in the direction South–North and at the right panel is shown the averaged values of the rainfall field in the direction East–West.

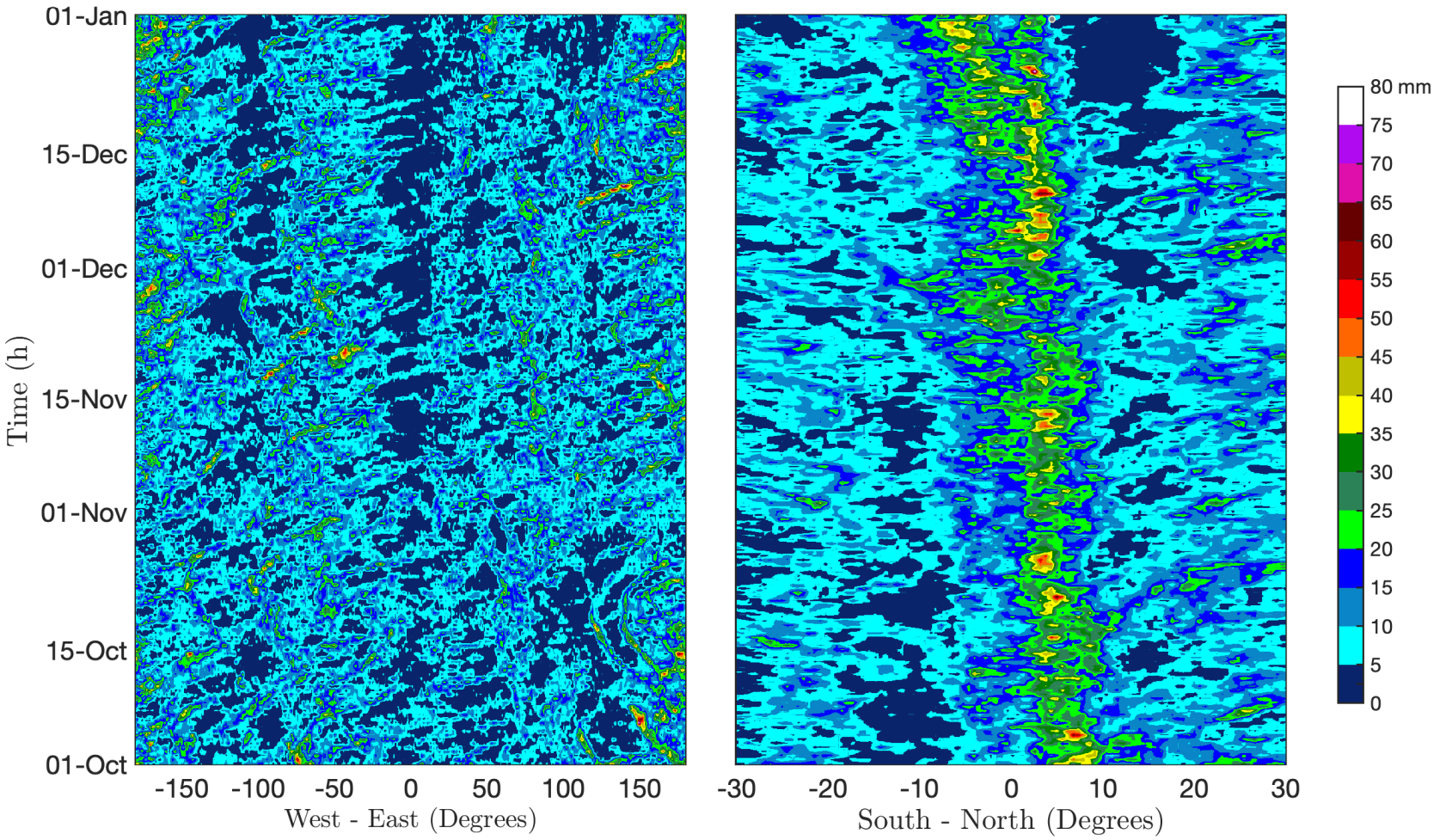

Figure D-9: Space–time diagrams for the rainfall intensity fields measured by the TRMM satellite mission in the fourth term of the year 2015 over the region bounded by the latitudes 25°S and 25°N. At the left panel is shown the averaged values of the rainfall field in the direction South–North and at the right panel is shown the averaged values of the rainfall field in the direction East–West.

E. Simulated Rainfall Patterns

E.1. Space-Time Plots

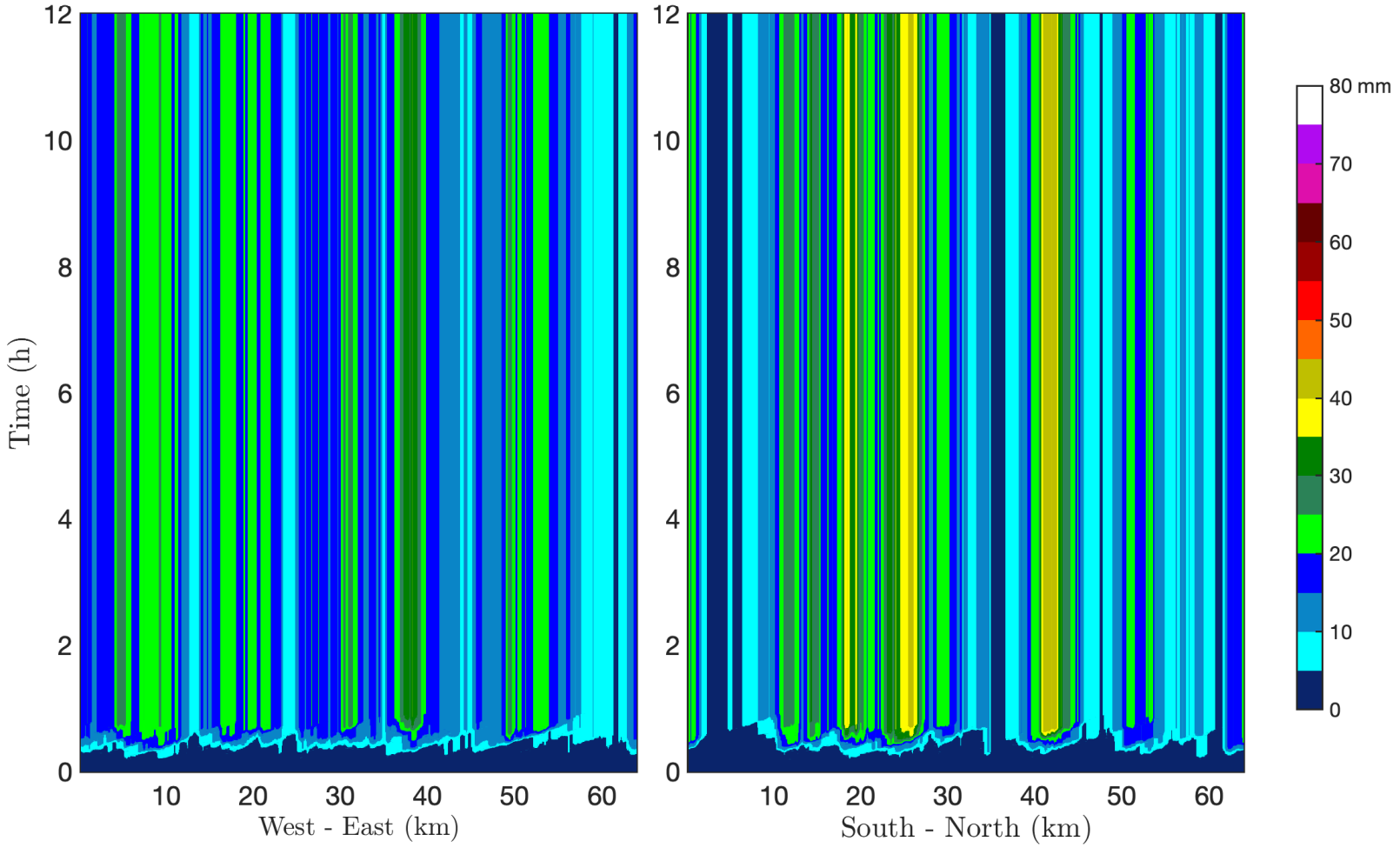

Figure E-1: Space–time diagrams for the average values of the simulated rainfall fields via Nordstrom & Gupta model [2003] which are shown at Figure 3-28. At the left panel is shown the averaged values of each rainfall field in the direction South–North and at the right panel is shown the averaged values of each rainfall field in the direction East–West.

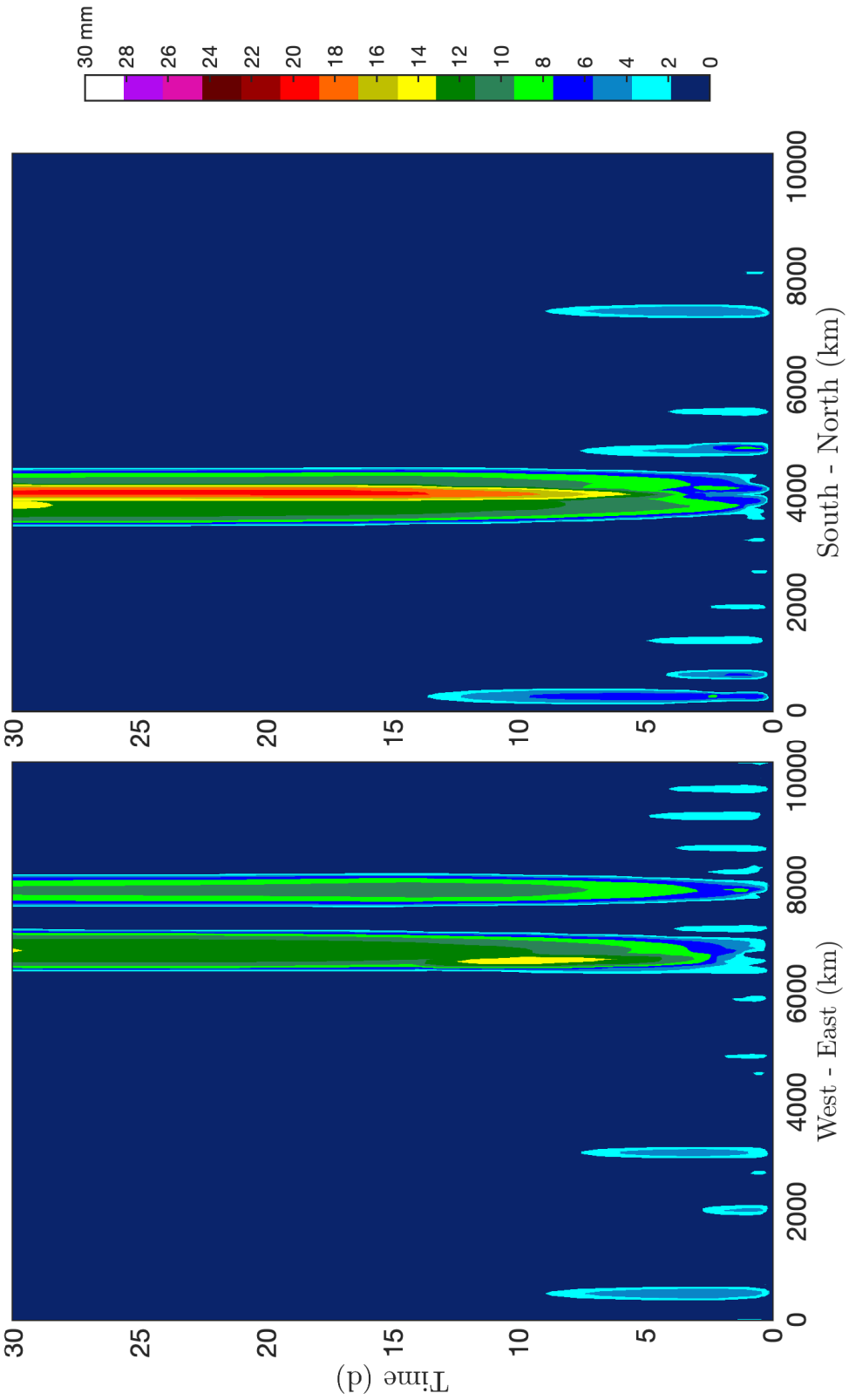

Figure E-2: Space–time diagrams for the average values of the simulated rainfall fields via Craig & Mack's model [2013] which are shown at Figure 3-36. At the left panel is shown the averaged values of each rainfall field in the direction South–North and at the right panel is shown the averaged values of each rainfall field in the direction East–West.

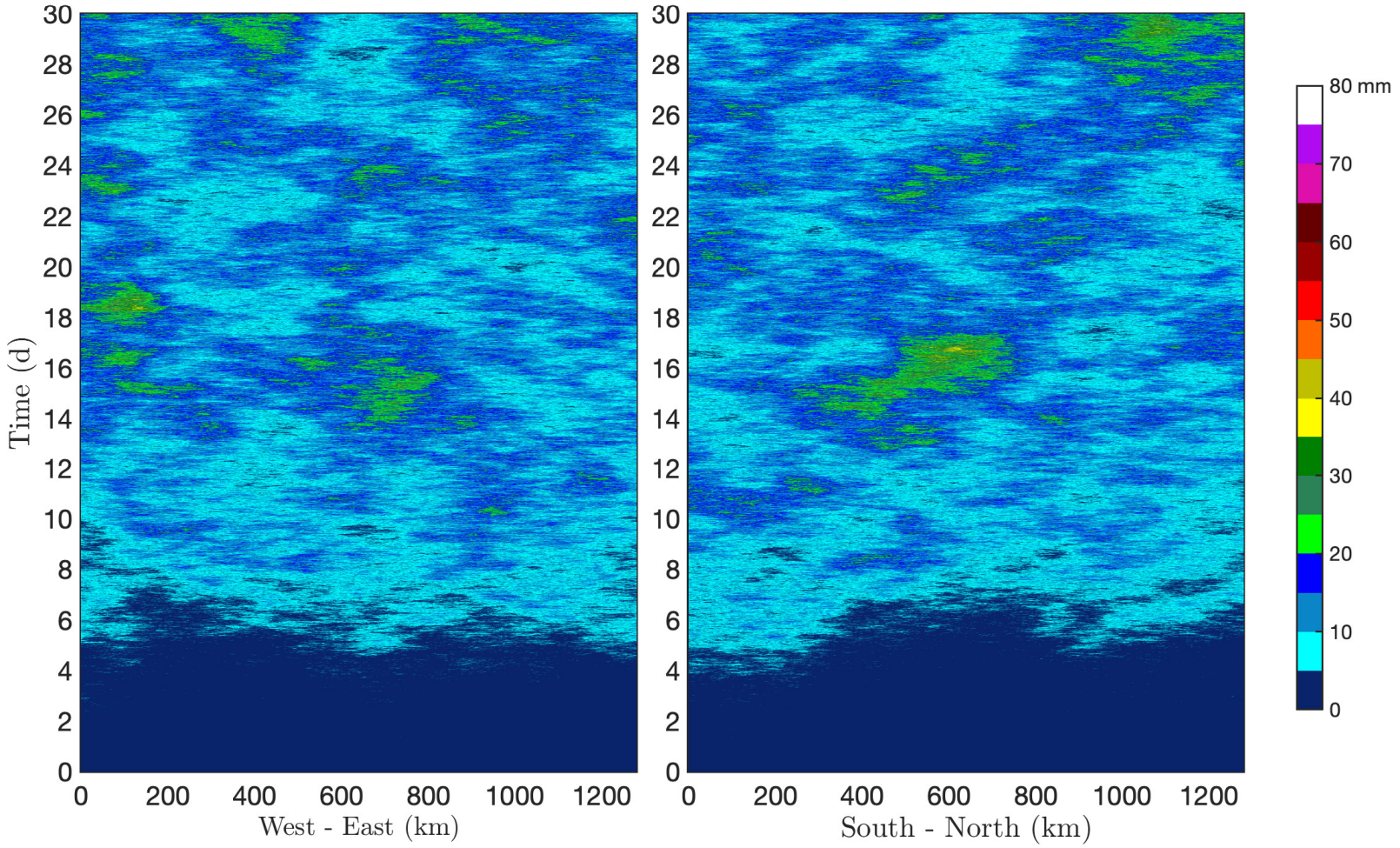

Figure E-3: Space–time diagrams for the average values of the simulated rainfall fields via Hottovy & Stechmann model [2015] which are shown at Figure 3-43. At the left panel is shown the averaged values of each rainfall field in the direction South–North and at the right panel is shown the averaged values of each rainfall field in the direction East–West.